Electric Power Transfer Concept for Improved Performance of Multi-spool Turbofan Jet Engine

Hossein Balaghi Enalou (BSc, MSc)

Submitted to the University of Nottingham for the degree of Doctor of Philosophy

January 2020

Acknowledgements

I would like to express my sincere gratitude to Allah (SWT) and Imam Mahdi (AJ) for giving me the strength and wisdom to persevere and complete this achievement satisfactorily.

I would like to express my deepest gratitude to my supervisor Prof. Serhiy Bozhko, for his full support and valuable guidance during the journey.

Moreover, special thanks are given to Dr. Patrick Norman and Prof. Pericle Zanchetta for sparing their time to be my examiners.

I am grateful to be funded by the University of Nottingham and the Clean Sky 2 Joint Undertaking under the European Union's Horizon 2020 research and innovation programme under grant agreement No 807081.

A million thanks to my friends and colleague, especially to Dr. Mohamed Rashed, Xiaoyu Lang, Dr. Seang Yeoh, Dr. Ponggorn Kulsangcharoen, Dr. Tao Yang, Dr. Christopher Hill, Ganeish Velmurugan, Fan Linhui, Chen Li and all other friends I have met during my PhD study.

At last but not least, I would like to express my heartfelt appreciation to my family, especially to my parents for their encouragement, understanding and support throughout my life. Also, I would like to thank my wife, Dr Najmeh Erfani for her love and encouragement on the way.

Finally, I would like to express my very profound gratitude to Mr GhulamHossein Heidari, Mr GolAli Abdullahi, Mr Hamid Akbari and Mr Abdolkhalegh and Rasoul Balaghi Enalou for their advice on the way. Although many others that contributed their time and expertise over the years remain nameless here, they are not forgotten.

Dedicated to Khadem of **Imam Reza** (A.S.)

Haj Ghulam Hossein Heidari

Abstract

Twin spool high-bypass turbofan engines are the dominant sources of propulsion for most civil aircraft. The shaft speeds in these engines are thermodynamically coupled even with no mechanical link between them. This coupling effect results in inevitable limitations on the engine design and performance, including mismatches in the performance of the compressors at low-speed conditions, that push for undesirable air bleeding requirements. Therefore, decoupling the shaft speeds can introduce remarkable improvements to engine performance, which leads to better fuel efficiency and hence reduced emissions.

A combination of solutions can offer new opportunities to address the mentioned coupling issue. These include the design trends towards the More Electric Engine (MEE) for the More Electric Aircraft (MEA), the boost in power electronics application, and introduction of new onboard Electric Power Systems (EPS) architectural paradigms. A multi-spool MEE can be equipped with an electrical machine connected to each of its shafts, which are connected via power electronics sharing a common high-voltage DC bus architecture. It is then possible to establish an "electrical bridge" to circulate the desired amount of power between the engine shafts, in order to decouple their speeds. This PhD research investigates the impact of the Electric Power Transfer (EPT) on the engine performance and introduces novel EPT-Adopted Designs (EPTAD) for the future MEA engines.

For this purpose, a 0-dementional engine model is developed by applying Inter-Component Control Volume (ICV) method, utilizing engine maps for CFM56-3 engine, thermodynamic rules and Newton's second law. Due to its inherent modularity and ease of implementation, various engines at different power ratings can be modelled, however, the engine maps are scaled since the engine maps are not readily available from the engine manufacturers. The proposed model includes the required shaft dynamics for studying power transfer via electrical machines, supported by the engine maps which are adequate to present the main thermodynamic behavior of the engine. Validating of results from simulation with engine performance data from literature highlights the fact that 0-D engine model is of enough accuracy for the purpose of power transfer.

The analytical analysis suggested a novel redesign of the engine by changing the power split ratio between the HPT and LPT to increase the HP speed at cruise condition. Results show that electric power transfer from the LP to HP shaft can further increase the HP speed at cruise condition which will increase the core pressure ratio and drive efficiency. Simulation results represent significant values of 0.27%, 0.64% and 1.4% of fuel consumption saving at cruise condition with electric power transfer for the baseline and redesigned engines with 500kW and 1150kW of EPT respectively. The flexibility of shaft speeds by the EPT system can also optimize engine performance both in terms of fuel consumption and surge margin for degraded engines. Moreover, electric power transfer from the LP to the HP shaft always increase surge margin of compressors, suggesting removal of the bleedings at low speed setting. It can also help to decrease more than 15% of fuel consumption at flight idle setting. Results show that during approach phase the engine fuel consumption can decrease significantly together with better thrust management for abrupt thrust recovery for flight maneuvers such go-around.

Finally, in order to enable better understanding and proof of the idea of power circulation between the engine shafts, an in-door engine emulator is constructed. The real-time engine model within dSPACE provides speed set-points for the induction machines on the LP and HP emulator spools which are coupled with two aircraft electric machines. Power transfer is realised between these machines through a single dc bus architecture. Similarity analysis is performed to enable real-time simulation by the engine emulator.

Claims and Novelty

In this thesis:

- A specialized 0-D transient and steady-state model is developed which enables analysis framework that includes modeling for the aerothermodynamics and inertia of the turbomachine and a full control system that enables optimization of the engine performance given electrical inputs. In addition, a detailed analytical twin shaft engine performance review is given for better insight for future studies on engine design.
- The state-of-the-art power generation architectures and the benefits of MEE concepts are reviewd and the performance of the baseline engine with EPT is analysed to show improvement in engine performance by reduced fuel consumption, and improve surge margin.
- A novel engine concept is introduced that is specifically designed to accommodate electric power transfer on the turbomachine shafts. The new architecture can reduce or eliminate the need for variable stator vanes or bleed valves. Significant improvement is achieved in fuel consumption at low and high power settings (up to 2%) and surge margin is increased at low power settings (up to 10%).
- A twin shaft engine emulator rig is constructed in order to show the feasibility of power transfer. A Hardware-in-the-Loop (HIL) setup is scaled by specialized real-time similarity analysis to run the engine model in a Real Time Platform (RTP).

List of Publications

The contents presented in this Thesis have been published or accepted in the following peer-reviewed journal articles and conference proceedings:

Journal Articles

[1] **H. B. Enalou**, E. A. Soreshjani, M. Rashed, S. S. Yeoh, and S. Bozhko, "A Detailed Modular Governor-Turbine Model for Multiple-Spool Gas Turbine with Scrutiny of Bleeding Effect," Journal of Engineering for Gas Turbines and Power-Transactions of the ASME, vol. 139, Nov 2017.

[2] **H. B. Enalou** and S. Bozhko, "Performance Improvement of Turbofans by Electric Power Transfer (EPT)," submitted to the ASME Journal of Turbomachinery.

Conference Papers

[1] **H. B. Enalou**, M. Rashed, P. Kulsangcharoen, C. I. Hill, and S. Bozhko, "Nonlinear aircraft engine model for future integrated power center development," in 2016 International Conference on Electrical Systems for Aircraft, Railway, Ship Propulsion and Road Vehicles & International Transportation Electrification Conference (ESARS-ITEC), 2016, pp. 1-5.

[2] **H. B. Enalou**, M. Rashed, P. Kulsangcharoen, S. Chowdhury, and S. Bozhko, "A Twin Spool Engine Emulator for the Study of Power Exchange Idea," in 2018 IEEE International Conference on Electrical Systems for Aircraft, Railway, Ship Propulsion and Road Vehicles & International Transportation Electrification Conference (ESARS-ITEC), 2018, pp. 1-8.

[3] **H. B. Enalou**, J.-M. Le-Peuvedic, M. Rashed, and S. Bozhko, "Potential Improvements in Turbofan's Performance by Electric Power Transfer," presented at the SAE 2018 The Aerospace Systems and Technology Conference, London Heathrow, 2018.

[4] **H. B. Enalou**, S. Bozhko, M. Rashed, and P. Kulsangcharoen, "A Preliminary Study into Turbofan Performance with LP-HP Power Exchange," in GPPS Global Power & Propulsion Society, Montreal, 2018.

[5] **H.Balaghi Enalou**, S. Bozhko, " Performance improvement of the CFM56-3 aircraft engine by electric power transfer," presented at the 13 th European Conference on Turbomachinery Fluid dynamics & Thermodynamics, April 8-12, 2018, Lausanne, Switzerland, 2018.

[6] **H. B. Enalou** and S. Bozhko, " The idea of power circulation between engine shafts for the MEE," presented at the MEA 2019 More Electric Aircraft Conference, February 6-7, 2019, Toulouse, France, 2019.

[7] X. Lang, T. Yang, **H. B. Enalou**, S. Bozhko, and P. Wheeler, "An Enhanced Power Generation Centre for More Electric Aircraft Applications," in 2018 IEEE International Conference on Electrical Systems for Aircraft, Railway, Ship Propulsion

and Road Vehicles & International Transportation Electrification Conference (ESARS-ITEC), 2018, pp. 1-6.

[8] X. Lang, T. Yang, **H. B. Enalou**, P. Wheeler, and S. Bozhko, "A Power Generation Center with Back-to-back Converter Considering Post-fault Operation for MEA Application," in *2019 22nd International Conference on Electrical Machines and Systems (ICEMS)*, 2019, pp. 1-6.

[9] X. Lang, T. Yang, **H. B. Enalou**, C. Li, S. Bozhko and P. Wheeler, "A Dual-Channel Enhanced Power Generation Architecture with Back-to-back Converter for MEA Application," *2019 IEEE International Electric Machines & Drives Conference (IEMDC)*, San Diego, CA, USA, 2019, pp. 1392-1397.

TABLE OF CONTENTS

Abstract I
Claims and Novelty III
List of Publications IV
List of Figures X
List of Tables XV
List of Acronyms XVI
List of Symbols XVIII
Chapter 1 Introduction 1
1.1 History of jet engines 1
1.2 Aim and Objectives 4
1.3 Structure of Thesis 5
Chapter 2 Jet Engine Technology 7
2.1 Jet engine technology overview 7
2.2 The more electric aircraft and engine (MEA & MEE) 12
2.3 Introduction into the concept of inter-shaft power exchange 16
2.4 Conclusion 20
Chapter 3 State-of-the-Art in Power Offtake 21
3.1 Power offtake configurations 22
3.1.1 HP Power Offtake (HP PO) 24
3.1.2 IP Power Offtake (IP PO) 25
3.1.3 LP Power Offtake (LP PO) 27
3.1.4 Multi-spool power offtake 28
3.2 Engine-EPS interface 32
3.2.1 Integrated Drive Generator (IDG) 32
3.2.2 Variable Speed Constant Frequency (VSCF) 33
3.2.3 Variable Frequency Generation (VFG) 34
3.2.4 Single dc bus EPS architecture 36
3.3 Power transfer methods 39
3.3.1 Power transfer through hydraulic transmission system 39
3.3.2 Power transfer through axial gear differential drive 41
3.3.3 Power transfer through a clutch assembly 42
3.3.4 Power transfer through an auxiliary air turbine 43

3.3.5 Power transfer through electric heater 44
3.3.6 Power transfer through electromagnetic clutch 45
3.3.7 Power transfer through electrical machines 46
3.4 Electrical Power transfer method: potential improvements into engine design and performance 48
3.5 Summary 52
Chapter 4 Development of Engine Model Suitable for EPT Concept Studies 53
4.1 Existing engine modelling methods 54
4.2 Introduction to ICV method 56
4.3 Component maps 59
4.4 Engine scaling 61
4.4.1 Shaft inertia scaling 62
4.4.2 Map scaling 62
4.5 Engine model modules 65
4.5.1 Shaft modules 66
4.5.2 CV module 67
4.5.3 Inlet duct 69
4.5.4 Fan 70
4.5.5 Compressors 72
4.5.6 Combustor 78
4.5.7 Turbines 79
4.5.8 Propelling nozzles 80
4.6 Control system 82
4.6.1 Fuel control system 83
4.6.2 Speed controller design 86
4.6.3 Variable geometry systems' control 88
4.6.4 Acceleration/deceleration control 89
4.7 Multi-spool engine performance 91
4.7.1 Thermodynamic coupling 91
4.7.2 Engine core matching 92
4.7.3 Pressure distribution throughout the engine core 93
4.8 Engine modelling in simulink 99

4.8.1 Numerical consistency 99
4.8.2 Initial condition 101
4.8.3 Model tuning/component matching 101
4.9 Engine model accuracy 101
4.10 Engine model uncertaintity 103
4.11 Model validation 104
4.12 Transient simulation results 108
4.13 Summary 112
Chapter 5 Electric Power Transfer 113
5.1 Engine performance criteria 113
5.1.1 Surge Margin (SM) 114
5.1.2 Overall efficiency 118
5.2 EPT impact on baseline engine's efficiency 122
5.3 Electric Power Transfer Adopted Design (EPTAD) 123
5.4 Simulation studies 125
5.4.1 Baseline engine at cruise condition 126
5.4.2 EPTAD engine with 1150kW of EPT (EPTAD-1150) 136
5.4.3 EPTAD engine with 500kW of EPT (EPTAD-500) 138
5.4.4 Off-design condition 140
5.4.5 VBVs schedule modification 141
5.4.6 Take off condition for EPTAD engines 146
5.4.7 Climb 148
5.4.8 Idle scenarios 150
5.5 Fuel consumption analysis 160
5.6 Summary 162
Chapter 6 Experimental Studies by Engine Emulation 164
6.1 Hardware-in-the-Loop (HIL) technique 165
6.2 Overview of gas turbine engine emulation systems 166
6.3 Twin shaft engine emulator setup 168
6.3.1 dSPACE 171
6.3.2 Drives 172

6.3.3 ControlDesk 173
6.3.4 Machines 175
6.4 Engine emulator dynamics 176
6.4.1 Similarity analysis 176
6.4.2 Engine model time scale 178
6.4.3 Electric power transfer emulation 180
6.4.4 Speed tracking performance 182
6.5 Experimental results 186
6.5.1 HP power offtake emulation (***p*30** idle) 187
6.5.2 Baseline engine's EPT emulation (Cruise) 190
6.5.3 EPTAD-500 engine's emulation 193
6.6 Summary 200
Chapter 7 Conclusions and Future Work 202
7.1 Achievements summary 202
7.2 Future works 205
Appendix A: Technical datasheet IM 208
Appendix B: Single dc bus architecture 209
References 211

List of Figures

Figure 1-1 Power supply for the conventional aircraft systems 3
Figure 2-1 Different Jet Engine Types 8
Figure 2-2 Jet engines' propulsive efficiency vs flight speed 8
Figure 2-3 Low and high-bypass turbofans 10
Figure 2-4 Turbofan's layout 11
Figure 2-5 The evolutionary application of electrical power in MEA 12
Figure 2-6 The conventional and more electric aircraft [38] 14
Figure 2-7 Comparison of a no-bleed engine (left) and the traditional bleed engine (right) 14
Figure 2-8 Initial conceptual design of MEE 16
Figure 2-9 Schematic diagram of a 2-spool, high bypass turbofan engine 18
Figure 3-1 Typical accessory gearbox 23
Figure 3-2 HP PO transmission system 24
Figure 3-3 IP power offtake of Trent 1000 26
Figure 3-4 Arrangement of the Starter/Generator on the dual drive shaft 29
Figure 3-5 Gear pitch circle diagram of the a summation gearbox 30
Figure 3-6 The Trent 500 MEE (Rolls-Royce University Technology Center, Strathclyde) 31
Figure 3-7 Larzac MEE configuration 31
Figure 3-8 IDG system 33
Figure 3-9 VSCF system using DC link 34
Figure 3-10 VSCF system using AC/AC converter 34
Figure 3-11 Simplified diagrams of electric distribution systems of B787 35
Figure 3-12 Configuration of single dc bus multi-source EPS 36
Figure 3-13 Constant power characteristic of motor drives with 38
Figure 3-14 Negative impedance characteristic of a CPL 39
Figure 3-15 Schematic of power transfer by hydraulic flow displacement machines 40
Figure 3-16 Schematic of power transfer by axial gear differential constant speed drive 41
Figure 3-17 Schematic representation of power transfer by clutch assemblies 42
Figure 3-18 Schematic of hydrostatic power transfer system 43
Figure 3-19 Schematic representation of power transfer by an auxiliary air turbine 44
Figure 3-20 Schematic representation of power transfer by electric heaters 45
Figure 3-21 Schematic representation of power transfer by electromagnetic clutch 46
Figure 3-22 Schematic power transfer by drivingly connected electrical machines 47
Figure 3-23 Schematic power transfer by embedded electrical machines 47
Figure 4-1 Twin shaft engine with gas-generator and free turbine 54
Figure 4-2 Block diagram of the twin-shaft gas turbine engine model 55
Figure 4-3 Structure of ICV modules 57
Figure 4-4 Compressor map 60
Figure 4-5 HPC map shifting peak efficiency line 64
Figure 4-6 Schematic of engine model in Simulink 65

Figure 4-7. Illustration of turbofan components with denoted engine stations 66
Figure 4-8 Solid rotor 66
Figure 4-9 Inertia module 67
Figure 4-10 CV module's block diagram 68
Figure 4-11 Denoted fan stations 71
Figure 4-12 Compressor, fan and turbine modules 73
Figure 4-13 Stall due to high angle of attack on stall 74
Figure 4-14 location of variable geometry systems on the CFM56-7B engine 76
Figure 4-15 VBVs' and VSVs' schedules 76
Figure 4-16 Combustor module 79
Figure 4-17 Corrected mass flow of turbines against engine Overall Pressure Ratio (OPR) 80
Figure 4-18 Close loop diagram of Engine-control system modules 83
Figure 4-19 Engine control system 85
Figure 4-20 Structure of the controllers 86
Figure 4-21 Speed-torque loop in speed control system 87
Figure 4-22 Pole zero location at different flight scenarios 88
Figure 4-23 VBVs and VSVs control system 88
Figure 4-24 Engine dynamics sequence 89
Figure 4-25 Fuel limit implementation 91
Figure 4-26 Corrected mass flow of turbines against engine Overall Pressure Ratio (OPR) 94
Figure 4-27 Corrected pressure ratio of turbines against engine Overall Pressure Ratio (OPR) 94
Figure 4-28 Settling speed, pressure ratio and mass flow for a compressor 95
Figure 4-29 Engine performance calculation flow chart (Choked nozzle) 96
Figure 4-30 Engine performance calculation flow chart (Choked LPT) 97
Figure 4-31 Engine performance calculation flow chart (Choked HPT) 98
Figure 4-32. Algebraic loops in Simulink 100
Figure 4-33 FAN operating line (steady-state idle to full throttle at ISA-SLS condition) 105
Figure 4-34 LPC operating line (steady-state idle to full throttle at ISA-SLS condition) 105
Figure 4-35 HPC operating line (steady-state idle to full throttle at ISA-SLS condition) 106
Figure 4-36 Measured and simulation results for shaft speeds 106
Figure 4-37 Simulation error for shaft speeds 107
Figure 4-38 SFC (steady-state idle to full throttle at ISA-SLS condition) 107
Figure 4-39 SFC error (steady-state idle to full throttle at ISA-SLS condition) 108
Figure 4-40 Shaft speeds, HPT exit temperature, SMs, $Wf/p30s$ (Burst-Chop maneuver) 109
Figure 4-41 FAN transient operating line (Burst-Chop manoeuvre) 110
Figure 4-42 LPC transient operating line (Burst-Chop manoeuvre) 111
Figure 4-43 HPC transient operating line (Burst-Chop manoeuvre) 111
Figure 5-1 Operation line on the HPC map with the effect of power transfer (cruise) 115
Figure 5-2 Operational speed line on compressor map 116
Figure 5-3 Operation line on the LPC map with the effect of power transfer (cruise) 117

Figure 5-4 Turbofan's core T-s diagram....118
Figure 5-5 Commercial aircraft gas turbine engine efficiency trend 119
Figure 5-6 Baseline and EPTAD engines' cruise and MTO operation points on the HPC map....124
Figure 5-7 Shaft speeds and turbine PSR vs EPT (cruise)....128
Figure 5-8. Core mass flow and $T48$ vs EPT (cruise) 129
Figure 5-9. Component and engine efficiency vs EPT (cruise)....130
Figure 5-10. Compressors pressure ratio and ($p30/p21$) vs EPT (cruise)....130
Figure 5-11. Fuel change and per-unit thrust vs EPT (cruise)....131
Figure 5-12. Available SM and ($Wf/p30$) vs EPT (cruise)....132
Figure 5-13 Fuel consumption change vs EPT, for various cruise conditions....133
Figure 5-14 Fuel consumption change at various EPT system efficiency 133
Figure 5-15 Fuel consumption change vs EPT for the degraded engine 135
Figure 5-16 Available SM vs EPT for the degraded engine 136
Figure 5-17 Shaft speed change vs EPT for EPTAD-500 engine 139
Figure 5-18 Cruise fuel consumption change for the EPTAD-500 engine 139
Figure 5-19 LPC's steady-state operating lines at ISA-SLS (baseline VBV schedule)....141
Figure 5-20 HPC's steady-state operating lines at ISA-SLS (baseline VBV schedule) 141
Figure 5-21 Control volume between the LPC and HPC....142
Figure 5-22 VBVs PI controller 142
Figure 5-23 VBV schedule for the baseline and EPTAD engines 143
Figure 5-24 Steady-state shaft speeds at ISA-SLS (re-scheduled VBVs) 143
Figure 5-25 LPC steady-state operating lines at ISA-SLS (re-scheduled VBVs)....144
Figure 5-26 HPC steady-state operating lines at ISA-SLS (re-scheduled VBVs) 144
Figure 5-27 LPC SM at steady-state operating lines at ISA-SLS (re-scheduled VBVs) 145
Figure 5-28 HPC SM at steady-state operating lines at ISA-SLS (re-scheduled VBVs)....145
Figure 5-29 Core pressure ratio at steady-state operating lines at ISA-SLS (re-scheduled VBVs)....146
Figure 5-30 Core mass flow at steady-state operating lines at ISA-SLS (re-scheduled VBVs) 146
Figure 5-31 Shaft speeds at 90% of MTO at ISA-SLS condition....147
Figure 5-32 Fuel consumption at 90% of MTO at ISA-SLS condition 148
Figure 5-33 Surge margins at 90% of MTO at ISA-SLS condition....148
Figure 5-34 Shaft speeds vs EPT at $p30$ Idle 152
Figure 5-35 Fuel consumption change vs EPT at $p30$ Idle 152
Figure 5-36 SMs vs EPT at $p30$ Idle....153
Figure 5-37 LP speed vs EPT during flight idle 154
Figure 5-38 Fuel consumption vs EPT during flight idle 154
Figure 5-39 SMs vs EPT during flight idle....155
Figure 5-40 Fuel consumption change vs EPT during taxing....156
Figure 5-41 SMs vs EPT during taxing 156
Figure 5-42 EPT values during TGL manoeuvre 157
Figure 5-43 HPT exhaust during acceleration from idle to full throttle setting....158

Figure 5-44 Shaft speeds during acceleration from idle to full throttle setting 158
Figure 5-45 Calculated thrust during acceleration from idle to full throttle setting 159
Figure 5-46 SMs during acceleration from idle to full throttle setting 159
Figure 6-1 Overview of CHIL 165
Figure 6-2 Overview of PHIL 166
Figure 6-3 System structure of the wind turbine emulator 166
Figure 6-4 System structure of the gas turbine emulator (single-shaft emulator) 168
Figure 6-5 Torque-speed block diagram of the emulator 168
Figure 6-6 Emulator's setup layout plan 170
Figure 6-7 Engine emulator components 171
Figure 6-8 dSPACE and its interface board 172
Figure 6-9 Induction machines' drive cabinet 173
Figure 6-10 Engine model control in ControlDesk environment 174
Figure 6-11 Monitoring in ControlDesk environment 175
Figure 6-12 Emulator's HP and LP testbeds 175
Figure 6-13 Schematic of emulator rig simulation modules 176
Figure 6-14 Time scale block for Simulink state blocks 180
Figure 6-15 Configuration of the engine emulator for electric power transfer 181
Figure 6-16 Control structure of the IM 181
Figure 6-17 Speed and torque communication between DSPACE and the emulator rig 183
Figure 6-18 Simplified block diagram of the engine emulator dynamics 184
Figure 6-19 Available power for acceleration and deceleration of the emulator shaft 185
Figure 6-20 Available torque for acceleration and deceleration of the emulator shaft 185
Figure 6-21 Emulator' HP shaft speed tracking performance (steps of 50% throttle at ISA-SLS) 186
Figure 6-22 q-axis current of the PMM from PMM's control board 187
Figure 6-23 Measured torque and corresponding scaled power from ControlDesk 188
Figure 6-24 Speed tracking performance of the HP shaft (scaling factor=20) 188
Figure 6-25 Speed tracking performance of the HP shaft (scaling factor=40) 189
Figure 6-26 Operating line of the LPC due to load steps ($p30$ idle) 189
Figure 6-27 Operating line of the HPC due to load steps ($p30$ idle) 189
Figure 6-28 HPC surge margin due to load steps ($p30$ idle) 190
Figure 6-29 Scaled LP and HP shaft power 191
Figure 6-30 Operating line of the LPC due to EPT (cruise) 191
Figure 6-31 Operating line of the HPC due to EPT (cruise) 192
Figure 6-32 Surge margins of the LPC and HPC due to EPT (cruise) 192
Figure 6-33 Fuel consumption change due to EPT at cruise condition 193
Figure 6-34 Emulator and EPT system power (MTO, EPTAD-500 engine) 194
Figure 6-35 Engine parameters (MTO, EPTAD-500 engine) 195
Figure 6-36 HPC map (MTO, EPTAD-500 engine) 195
Figure 6-37 LPC map (MTO, EPTAD-500 engine) 195

Figure 6-38 Emulator and EPT system power ($p30$ idle, EPTAD-500 engine) 196
Figure 6-39 Engine parameters ($p30$ idle, EPTAD-500 engine) 196
Figure 6-40 HPC map ($p30$ idle, EPTAD-500 engine) 196
Figure 6-41 LPC map ($p30$ idle, EPTAD-500 engine) 197
Figure 6-42 Emulator and EPT system power (Flight idle, EPTAD-500 engine) 197
Figure 6-43 Engine parameters (Flight idle, EPTAD-500 engine) 198
Figure 6-44 HPC map (Flight idle, EPTAD-500 engine) 198
Figure 6-45 LPC map (Flight idle, EPTAD-500 engine) 198
Figure 6-46 Emulator and EPT system power (Cruise, EPTAD-500 engine) 199
Figure 6-47 Engine parameters (Cruise, EPTAD-500 engine) 199
Figure 6-48 HPC map (Cruise, EPTAD-500 engine) 199
Figure 6-49 LPC map (Cruise, EPTAD-500 engine) 200
Figure B-1 Control structure of the PMM (Voltage control mode) 210

List of Tables

Table 3-1 Shaft speed twin spool engines 24
Table 4-1. GE scaling ratios 62
Table 4-2 LPC-HPC control volume variables at MTO and cruise condition 69
Table 4-3 CFM56-3 engine single cycle point at ISA-SLS condition 104
Table 5-1 SM uncertainty for the HPC 114
Table 5-2 Shaft speeds of the baseline and EPTAD engines 125
Table 5-3 Optimum flight and engine speed for 737 aircraft 127
Table 5-4 Comparison between the baseline and EPTAD-1150 engines 137
Table 5-5 Comparison between the baseline and EPTAD-500 engines at ADP 138
Table 5-6 Engine variables beginning of climb (100% throttle, 5kft, Mach=0.5) 149
Table 5-7 Engine variables top of climb (100% throttle, 35kft, Mach=0.75) 149
Table 5-8 Engine variables beginning of climb (85% throttle, 5kft, Mach=0.5) 150
Table 5-9 Engine variables top of climb (85% throttle, 35kft, Mach=0.75) 150
Table 5-10 Average fuel consumption for CFM56-3 engine for an 8-hours flight 161
Table 5-11 Weight analysis for an 8-hours flight of B737 with CFM56-3 engine 162
Table 6-1 Specifications of PMMs 176
Table 6-2 Mechanical parameters of the emulation system 182
Table 6-3 Steps of implementing EPT 190
Table 6-4 Electric power transfer scaling, EPTAD-500 engine 193
Table 6-5 Units of variables in dSPACE 194

List of Acronyms

0-D	Zero Dimensional
1-D	One Dimensional
2-D	Two Dimensional
3-D	Three Dimensional
AC	Alternating Current
AEGART	Aircraft Electrical Generation Active Rectifier Technology
ADP	Aerodynamic Design Point
AGB	Accessory Gearbox
AIPC	Advanced Integrated Power Centre
APU	Auxiliary Power Unit
ATP	Ambient Temperature and Pressure
CC	Combustion Chamber
CF	Constant Frequency
CFD	Computational Fluid Dynamics
CHIL	Controller Hardware-in-the-Loop.
CSD	Constant Speed Drive
CV	Control Volume
DC	Direct Current
DQ	Direct Quadrature
DSP	Digital Signal Processor
ECS	Environmental Control System
EEC	Electronic Engine Control
EOM	Engine Operation Mode
EPS	Electric Power System
EPT	Electric Power Transfer
EPTAD	Electric Power Transfer Adopted Design
FADEC	Full Authority Digital Engine Control
FOC	Field Oriented Control
FPGA	Field Programmable Gate Array
GE	General Electric
GSS	Grid-tie Source Sink
HIL	Hardware-in-the-Loop
HP	High Pressure

HPC	High Pressure Compressor
HPT	High Pressure Turbine
ICV	Intermediate Control Volume
IDG	Integrated Drive Generator
IGB	Internal Gearbox
IM	Induction Machine
ISA	International Standard Atmosphere
LP	Low Pressure
LPC	Low Pressure Compressor
LPT	Low Pressure Turbine
MEA	More Electric Aircraft
MEE	More Electric Engine
MTO	Maximum Take-Off
PHIL	Power Hardware-in-the-Loop
PI	Proportional plus Integral
PM	Permanent Magnet
PMM	Permanent Magnet Machine
PO	Power Offtake
RTD	digital Real-Time Platform
RTP	Real Time Platform
SAGB	Step Aside Gearbox
SLS	Sea-Level-Static
SM	Surge Margin
TGB	Transfer Gearbox
TGL	Touch-and-Go Landing
TIT	Turbine Inlet Temperature
VAC	Volts Alternating Current
VBVs	Variable Bleed Valves
VDC	Volts Direct Current
VFG	Variable Frequency Generation
VSCF	Variable Speed Constant Frequency
VSD	Variable Speed Drive
VSVs	Variable Stator Vanes
WIPS	Wing Ice Protection System

List of Symbols

C_P	Constant pressure heat capacity
E_{dc}	DC link voltage
$I_{d,q}^{ref}$	Three phase current reference voltage in dq frame
$L_{d,q}$	Machine inductance in dq frame
N_c	Corrected shaft speed
R_s	Stator resistance
T_E	Electromagnetic torque
T_L	Load torque
$V_{C,max}$	Maximum stator voltage magnitude
$V_{d,q}^{ref}$	Three phase voltage reference voltage in dq frame
V_{dc}	DC link voltage
V_{dc}^{ref}	DC link voltage reference
W_c	Inlet corrected flow
$i_{d,q}$	Three phase AC currents in dq frame
$i_{q,max}$	Maximum q axis current
m_{CV}	Mass of control volume
m_{CV}	Mass of control volume
$v_{d,q}$	Three phase AC voltages in dq frame
$\sigma_{r_{max}}$	Maximum centrifugal stress
ψ_m	Machine flux linkage
ω_r	Mechanical speed
A	Area
BPR	Bypass ratio
C	DC link capacitor
F	Thrust
FAR	Fuel to air ratio
H	Enthalpy
J	Shaft inertia
Ma	Mach number
N	Shaft speed
$N1$	LP shaft speed
$N2$	HP shaft speed
OPR	Overall pressure ratio

P	Power
PR	Pressure ratio
R	Individual gas constant
SM	Surge margin
T	Temperature/Torque
$TSFC$	Thrust specific fuel consumption
U	Internal energy
V	Volume of control volume
W	Mass flow
d	Diameter
k	Polytropic exponent
m	Scaling factor
p	Pressure
p	Machine pole numbers
v	Specific volume
γ	Specific heat ratio (adiabatic index)
δ	Non-dimensional inlet pressure
η	Efficiency
θ	Non-dimensional inlet temperature
θ	Electrical angle
π	Pressure ratio
τ	Time constant
ω	Speed

Chapter 1 Introduction

After substantial improvements in gas turbine design and manufacturing, they are widely used to power: aircraft, trains, ships, electrical generators, pumps, gas compressors and tanks. Jet engines have remained in the front line of aviation due to their high power density, high thrust, compact size and simple overall layout [1]. Jet engines have evolved from Jumo 004 with 1980lbf (9kN) of thrust in 1940s to contemporary state-of-the-art high bypass ratio turbofans, such as General Electric GE90 engine capable of providing up to 115,000lbf (510kN) of thrust [1]. The next Section discusses a historical overview of jet engines.

1.1 History of jet engines

The basic operational principles for all engines constitute three common components which are 1) the upstream rotating gas compressor, 2) the downstream turbine on the same shaft, and 3) the combustion chamber. The combustion chamber, also known as combustor, is located between the compressor and the turbine. The basis of gas turbine dates to 1870 when George Brighton, a mechanical engineer, introduced a constant pressure internal combustion engine. Germans made significant step during World War II. Hans Von Ohain developed the first workable gas turbine with axial compressors (in 1935) which was installed on fighter He178 in August 1939 which became the first operational jet aircraft. Independently, Britons produced the engine Power Jet W1, designed by widely recognized as “jet engine father” Frank Whittle with the patent initially offered in 1930. W1 has been employed to power Gloster E28/39 Aircraft in 1941. The W1 turbojet engine was capable of producing 1240lbf (5.6kN) of thrust at 17750 rpm [2]. Later in 1943, Junker’s Jumo 004 engines with

1980lbf (9kN) of thrust came into mass production which were used on jet fighter Me262 and on bomber Ar234 [3].

Following defeat of Germany in WWII and destruction of their factories, Britons became undisputed pioneers in jet engines. Their early designs used centrifugal compressors; however, these could not handle as much airflow as axial compressors on German engines. By sharing the Whittle's technology with the US, the General Electric Company was able to create the first US jet engine, the I-A. At the same time, British continued to develop their jet engines where Rolls-Royce initiated working on the Nene engine in 1944. Jet engine technology was then sold by Rolls-Royce to Pratt & Whitney and to the Soviets [4].

The next two decades witnessed breakthroughs in the jet engine development, where in 1950s, Pratt & Whitney introduced the dual-spool (low- and high-pressure spools) concept in J-57 engine, with the high pressure (HP) spool rotating faster. The second adoption was the production of turbofan engine by Rolls-Royce Conway in the 1960s [4]. The turbofan gains higher efficiency by having some of its thrust pass around the engine core rather than through it. In turbofans a fan is mounted on the low pressure (LP) spool.

Since then, the main technological efforts have been on improving metallurgy and manufacturing processes [5]. The major areas of development for turbofans can be broadly named as reaching higher pressure and temperature within the engine core and mounting larger fan to reach lower weight, fuel consumption, noise and emissions.

The More Electric Aircraft (MEA) technology introduced in 1990s, is one of the technologies that has been contributing to improvement of the aircraft. The MEA was initially the plan of certain military aircraft designers to decrease weight of the aircraft systems that were mostly operated by non-electrical power sources [6]. The advancements since 2000 in the field of: power electronic systems, fault-tolerant electric machines, electro-hydrostatic actuators, electrometrical actuators, and fault-tolerant electrical power systems have renewed the interest of the MEA to turn it into a modern trend to introduce new technologies in aviation industry [7, 8]. Successful achievements of these innovative ideas have contributed to the development of new systems for further reduction of: aircraft weight, equipment volume and overall fuel burn, hence less environmental impact and greener aviation [9, 10].

Figure 1-1 indicates the total non-thrust power is around 1.7MW for the conventional aircraft systems' supply, powered by a typical civil aircraft jet engine of the size of Rolls Royce IAE Model V2500 (i.e. A320 engine) with the estimated propulsion thrust equivalent to 40MW.

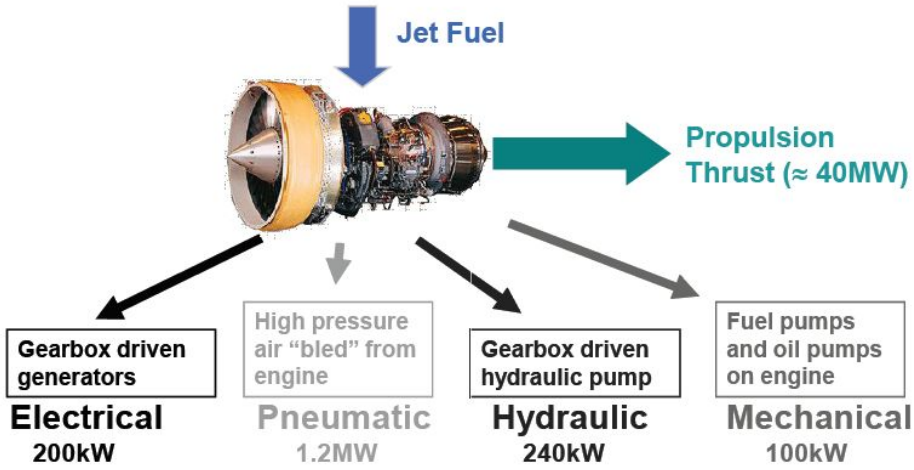


Figure 1-1 Power supply for the conventional aircraft systems [11]

With the advancements in electrical machine and power electronic technologies, if electricity is configured to be used as the common power transfer medium, the non-thrust power requirement, shown in Figure 1-1, will decrease to about 1MW, provided by emerging electrical generators [11].

Engines, as the essential part of the aircraft, are one of the main targets for the MEA development, while they are indirectly involved in electrification of other onboard systems. With the design trends towards the MEA, the More Electric Engine (MEE) has also pinpointed areas to push the boundaries of propulsion technology. This contribution has introduced a trend in remarkable improvements in designing quieter and more efficient engines.

The MEE trend has incorporated into the engine design mainly with more electrification of the engine control elements including: fuel system, oil system and engine actuation functions [12-14]. The development of electric machines and components with higher power to weight ratio, enables the installation of power optimized electric accessories instead of pneumatic and hydraulic systems [15]. Successful implementation of these changes have considerably simplified the interface between the MEE and the MEA, as a result contributing to the reduction in the weight and maintenance, and increase in the reliability of the engine [13].

There is no mechanical link between the engine shafts. This causes the inflexibility of shaft speeds which creates inevitable operation limitations in the engine, especially at

low speed conditions. In this case, any power transfer between shafts in order to decouple the shaft speeds can introduce remarkable improvements in engine design and performance.

Conventionally, electrical machines extract the non-propulsive power from the HP shaft of twin-spool engines [16]. However, the HP spool is typically limited to supplying low power for steady state loads [17]. The high amount of electric power required for the MEA has pushed the MEE from the single to multiple spool power extraction schemes. Power extraction in the MEE is realized through electrical machines mounted or connected to gearboxes on each of the main shafts of the engine. Having multiple shafts in turbofans, as sources of non-propulsive power, has resulted in introduction of innovative power systems. Power electronic converters, controlling the power generation, can accommodate an electrical bridge between the engine shafts. It is possible to exploit the electrical bridge to circulate desired amount of power between the engine shafts independent of their speeds. This Thesis investigates the impact of electric power transfer (EPT) on the baseline engine performance and introduces a novel EPT Adopted Design (EPTAD) of turbofans.

1.2 Aim and Objectives

This research aims to investigate the potential achievements of implementing highly innovative concept of bidirectional Electric Power Transfer between engine shafts through the electrical bridge for the future MEE.

In order to meet the aim of this research, the following objectives are defined:

#1: To review the potential concept via detailed literature review in the field.

The idea of power transfer has been suggested in 1993 [18], however, it has yet to be implemented in an engine. A detailed overview will be presented of the possible methods of power transfer and why these have not been practically implemented. Due to the continued advancements in electric machines and power electronic technologies, the idea will be re-scrutinized and presented as the EPT concept. For this purpose, a detailed overview of power generation architectures, benefits and liabilities of various methods of power transfer and how EPT can be accommodated into the new engine design schemes are to be investigated.

#2: To develop a multi-spool aircraft engine model suitable for EPT concept studies.

In order to assess the impact of EPT on overall performance of the aircraft, the engine and the electrical system will be modelled. The model should have sufficient accuracy and reasonable complexity, to be applied for different environmental conditions with flexibility on power exchange between engine shafts. The developed model will be validated with available field test results from real turbofan performance data.

#3: To investigate engine performance improvements by EPT.

The change in key performance variables of the engine at various flight scenarios such as: cruise, climb, ground and flight idle will be investigated by circulating power between the engine shafts. For this purpose, simulations will be performed on the developed model for the baseline engine. In order to integrate the EPT to further enhance engine performance, new conceptual designs are suggested and studied by the developed engine model.

#4: To construct an engine emulator to experimentally confirm the key outcomes of the study.

In order to investigate the feasibility of power transfer, a twin shaft engine emulator rig will be constructed to demonstrate the outcomes of simulations. A Hardware-in-the-Loop (HIL) setup will be stablished to run the engine model in a Real Time Platform (RTP). Two high speed induction machines will be used to emulate the two shafts of a twin-spool engine. The identified AEGART [19] electrical machines, coupled with the induction machines, will be used to realize power transfer between the engine shafts through their converters.

1.3 Structure of Thesis

This thesis is structured as follows:

Chapter 1 provides an insight into the background of jet engine and introduces the research question.

Chapter 2 presents an overview of design considerations for twin-shaft turbofans, from the preliminary engine designs up to the recent MEE design and ideas to be considered for next generation engines.

Chapter 3 represents an overview of the conventional and MEA power generation configurations and their interface with the engine shafts. A literature review is

conducted to cover various methods of power transfer to assess their efficiency and complexity. The latter part of this Chapter presents an outline of the possible achievements of power transfer for engine performance.

Chapter 4 develops the model for twin-spool turbofans in MATLAB®/Simulink® environment. Various engine modelling approaches are discussed, followed by selecting the Inter-Component-Volume (ICV) method. Using the ICV method, the engine components are detailed, with the relevant mathematical equations representing their performance. The component modules are integrated to derive a 0-dimensional engine model. A control structure for the engine is also presented which aims to establish the engine model as a controlled plant. The model is verified against real engine data of CFM56-3 engine. An assessment is presented for the validity of the derived model for the purpose of power transfer studies.

Chapter 5 performs preliminary analysis on the impact of power transfer on engine performance. Engine efficiency and surge phenomena are formulated to assess power transfer analytically. A re-design concept, which integrates power transfer into the design of future engines, is introduced to further utilize power transfer. Simulation results from the derived model on power transfer between engine shafts are presented. The achievements in terms of fuel consumption reduction and surge margin increase are reported for various flight scenarios.

Chapter 6 deals with the emulator design and construction to proof the feasibility of EPT concept. Due to lack of real engine for experimental setup, HIL techniques for emulation are discussed, focusing on gas engine emulators in the literature. The constructed engine emulator for this study is explained in detail and the collected experimental results are presented for power generation and electric power transfer.

Chapter 7 provides a conclusion of the Thesis and also presents possible future research work in this field.

Chapter 2 Jet Engine Technology

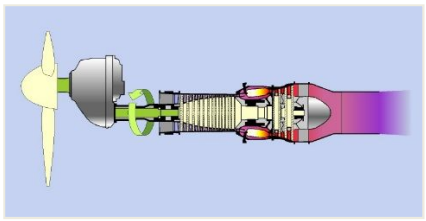
The noise and emission constraints imposed on the aerospace industry emphasize the need for improvement of propulsion technology; to accomplish ambitious overall aircraft fuel burn goals [20]. Among routes to fuel burn reduction, propulsion system supplier plays a paramount role; being responsible for increase in propulsion system efficiency. In this regard, any potential improvement of engine performance is important since the engine constitutes the primary source of power for propulsive and non-propulsive systems of the aircraft.

This Chapter presents an overview of engine developments, the recent MEE design and ideas to be considered for next generation engines.

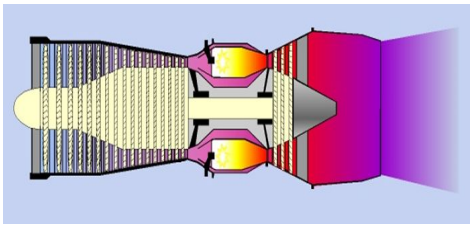
2.1 Jet engine technology overview

There are three types of jet engines based on how they create thrust namely; turboprop, turbojet and turbofan (see Figure 2-1). The main difference is due to the component which can be implemented to create thrust purely by a nozzle in turbojets or purely by a fan in turboprops or a mixture of them in turbofans [21].

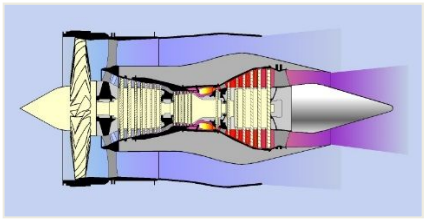
A turbofan can be thought of something between a turbojet and a turboprop, essentially consisting of a large ducted fan with a smaller diameter turbojet engine (known as turbofan core) mounted behind it. The core powers the fan and provides a portion of propulsion thrust. As shown in Figure 2-2, turbofans can fly at higher speeds with higher efficiencies when compared to turboprops, which provides maximum efficiency at speeds around 350mph (560km/hr).



Turboprop



Turbojet



Turbofan

Figure 2-1 Different Jet Engine Types [22]

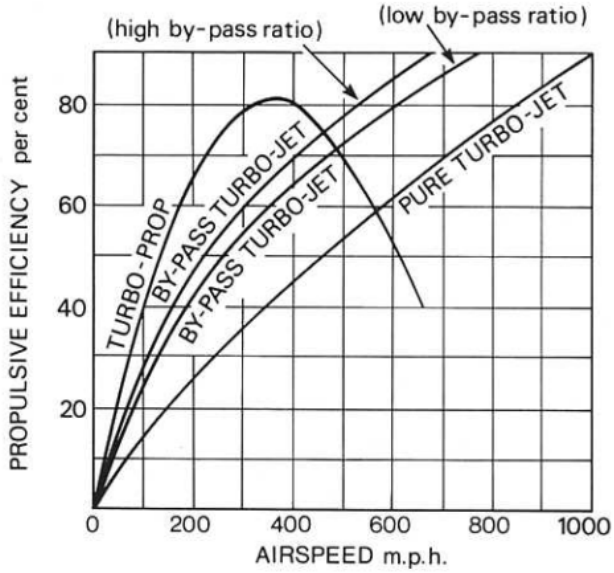


Figure 2-2 Jet engines' propulsive efficiency vs flight speed [23]

The emergence of turbofans was the result of addressing major drawbacks of turbojets such as high fuel consumption, high noise, high exhaust gas temperature, and low resistance to flameout phenomenon, which refers to extinguishment of flame in the combustor. The noise level in this engine type is reduced since a large mass of air (bypass duct) moves slowly whilst only a small mass of air goes through the core at much higher speed [24]. The bypass duct also cools down the engine and reduces the noise further.

Typically, extra turbine stages are mounted on a separate shaft (i.e. Low Pressure (LP) shaft) that rotates at a lower speed than the core shaft (i.e. High Pressure (HP) shaft). Aiming to increase the overall engine efficiency, a Low-Pressure Compressor (LPC) is implemented on the LP shaft to first pressurize the air before the High-Pressure

Compressor (HPC). In order to have an optimum operation point for compressors, the design speed of the compressor should be correlated with its design pressure which means higher speeds for high pressures. Practically, due to the complexity and maintenance costs, compressors are divided into LP and HP sections, the latter spinning faster [25, 26]. In fact, this is a way of increasing the air pressure ratio without causing any instability for the compressors. The engine efficiency improves by increasing the compressor pressure ratio (elaborated in Section 5.1.2).

It should be noted that the LP shaft cannot be linked to HP shaft mechanically; the LP to HP speed is not a fixed ratio where the compressor-turbine systems set the optimum performance speed. The airflow passing through the engine core provides the LP-HP thermodynamic coupling.

Some manufacturers prefer three spools solutions which can reach higher pressure ratio more efficiently in smaller engine. Comparing the GE [27] and Rolls Royce [22, 28] engines, designed for identical airframe specifications, the GEnx is a two spool arrangement with an overall pressure ratio of 43:1, a length of 4.9m and maximum take-off (MTO) thrust between 69.8klbf (310.5kN) and 76.0klbf (338.0kN) from released variants, whereas the Trent1000 engine has three spools enabling it to achieve a pressure ratio of 50:1, with a length of 4.7m and MTO thrust between 59.6klbf (265.1kN) and 81.0klbf (360.3kN) from released variants [29]. Twin spool engines are simpler, cheaper with lower maintenance cost, preferred for short haul operations whereas three spool engines are preferred for long haul flights where cost is more dependent on the fuel burn [22].

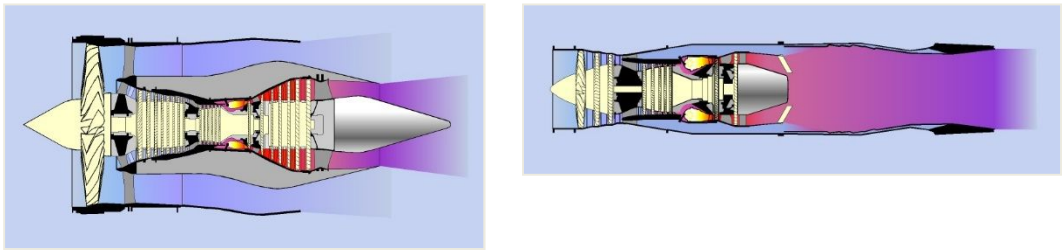
Turbofans are divided into two categories, known as low bypass and high-bypass turbofans, depicted in Figure 2-3. The term bypass ratio (BPR) is the ratio of the massflow of air bypassing the engine core, not mixing with fuel and burning, to the massflow of air that is passing through the core. Thrust is produced through a combination of these two portions working together as below;

$$Thrust = (W.V)_{core} + (W.V)_{bypass} \quad (2\text{-}1)$$

where W and V are massflow and outlet speed of the air for the bypass nozzle and combustion products for the core nozzle. Since the BPR of high-bypass turbofans is more than 5, around 80% of thrust is produced by the bypass nozzle. The impact of the outlet air speed ratio ($\frac{V_{bypass}}{V_{core}} \approx 1.3$) can be ignored compare to the massflow.

In comparison to the low-bypass turbofans, the high bypass ones have lower Thrust Specific Fuel consumption (TSFC), which refers to efficiency of an engine with respect to thrust output. TSFC can be defined as the fuel rate required to provide thrust, presented either in (g/s.kN) or (lb/hr.lbf).

The low-bypass turbofans are used for most modern military fighter engines due to high thrust-to-weight ratio, having more jet thrust relative to fan thrust. Conversely, high-bypass turbofans are preferred for most commercial aviation jet engines for good fuel efficiency and reduced noise, having considerably more fan thrust than jet thrust. They are usually most efficient at the cruise speed of most large airliners, 500-550mph (800-885km/h) [4, 25].



High bypass turbofan Low bypass turbofan

Figure 2-3 Low and high-bypass turbofans [30]

High-bypass turbofan is the dominant source of propulsion for most of civil aircraft. Figure 2-4 is a schematic diagram of a 2-spool, high-bypass turbofan engine with an unmixed exhaust [30]. The major engine components of a turbofan can be named as inlet duct, fan, bypass duct, booster (LPC), inter-compressor bleeds, HPC, cooling bleeds, fuel metering system, combustion chamber, High Pressure Turbine (HPT), Low Pressure Turbine (LPT) and discharge nozzles. The HPT drives the HPC on the HP shaft and the LPT drives the fan and LPC on the LP shaft. For three spool turbofans, the LPC is replaced by the Intermediates Pressure Compressor (IPC), driven by Intermediate Pressure Turbine (IPT), mounted on a separate Intermediate Pressure (IP) shaft.

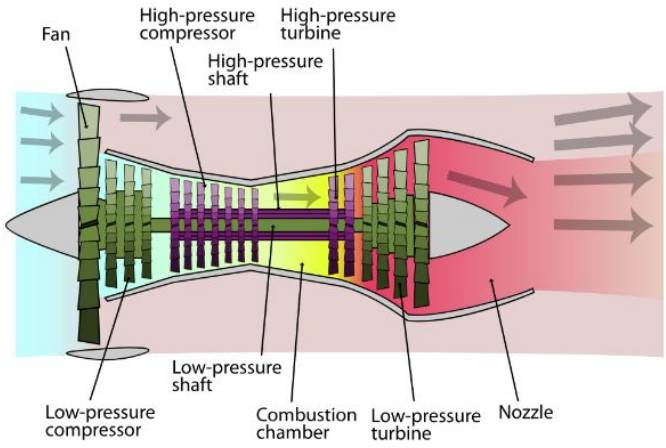


Figure 2-4 Turbofan's layout [30]

The high-bypass turbofan's performance is optimized for cruise condition which is normally considered Aerodynamic design Point (ADP) of the aircraft mission. For longer flights most of an aircraft's fuel is consumed during cruise. The engine shaft speeds are matched to keep the air massflow balanced between the LPC and HPC to avoid compressor surge [31]. One of the most critical threats to an engine is compressor surge. Surge phenomena is elaborated in Section 4.5.5.1. Surge can lead to mechanical damage to the compressor blades and the thrust bearings due to large fluctuations of airflow and direction of forces on the rotor. Surge margin is defined as an index referring to the gap between the operating point and surge incidence; higher surge margin means higher compressor stability. Surge margin is defined in detail in Section 4.3.

For operation at shaft speeds below cruise ones, the compressors keep the airflow within the limits to prevent surge occurrence. Methods to address the surge problem at low-speed settings include compressor air bleed at the intermediate stage, variable geometry compressor and multi-spool compressors or combinations of them. On a twin-spool engine, the air control systems include:

- the variable bleed valve (VBV) system (or surge bleed system) at the LPC exit
- the variable stator vane (VSV) system for the HPC
- and bleed valves at certain stages of the HPC

Variable geometries are elaborated in Section 4.5.5.2.

Irrespective of size, the efficiency of a turbofan is notoriously poor at low shaft speed settings. This is because of the way in which the engine operates at low shaft speeds. Moreover, the wide range of engine operation adds significant complexities to the

engine design. New technologies linked to the MEA and the MEE concepts [14, 32] can provide significant mitigations to the issue due to offered design flexibilities.

2.2 The more electric aircraft and engine (MEA & MEE)

The MEA as a modern trend in aviation is expected to optimize the total aircraft package, by replacing three individually optimized but collectively sub-optimized secondary power systems (electric, hydraulic and pneumatic) with one globally-optimized electrical system [14]. This has resulted in continuous increase of on-board electric power demand as shown in Figure 2-5, hence, development of highly efficient, reliable and safe electrical energy generation channels that provide high-quality power for on-board loads, many of which are flight-critical [10].

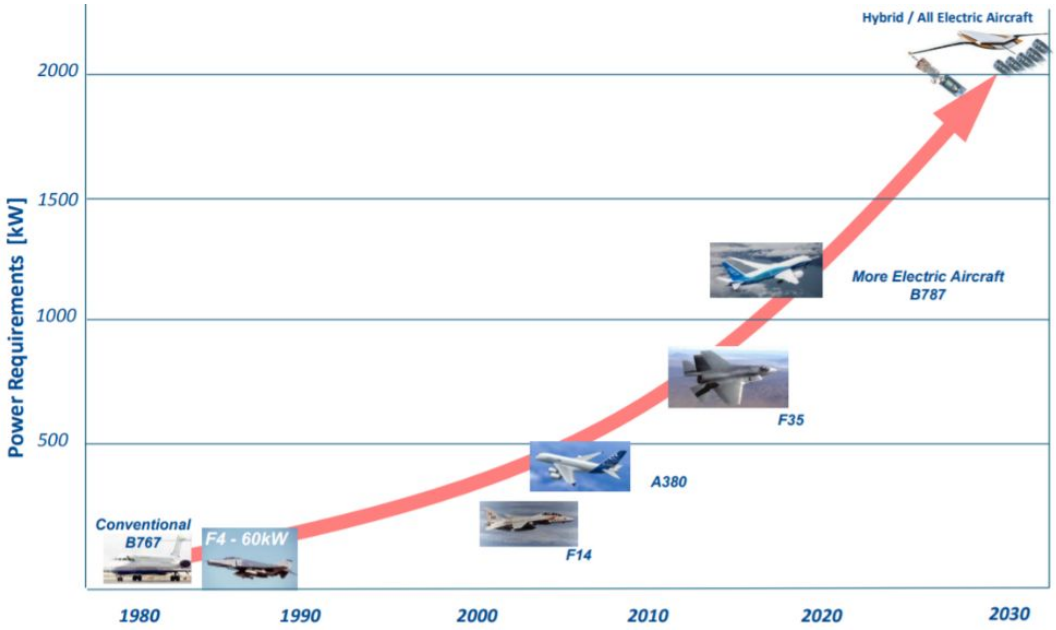


Figure 2-5 The evolutionary application of electrical power in MEA [33]

Having been equipped with 4 of 40kVA generators, Vickers VC10 built 50 years before the Airbus A380, is recognized as the pioneer of the MEA [11]. Contemporarily, the B787 Dreamliner has brought the concept of MEA into practice, implementing; electric engine start and electric driven hydraulic pumps, highly expanded electrical systems, electric air conditioning, cabin pressurization systems and electric wing ice protection while the pneumatic bleed system has been eliminated [33].

One of the most significant achievements from the MEA is the concept of an integrated system that combines engine starting and electrical power generation functions, referred to as starter-generator (S/G) system. By such integration, significant

advantages in terms of overall weight and volume is achieved. In this scheme, the same electrical machine provides the ability to smoothly accelerate the engine for start-up process. When the engine starts, it extracts mechanical power, converting it to electrical one for supplying onboard loads. Conventionally, starter turbine, running with air supplied by compressors of either a ground cart or Auxiliary Power Unit (APU) is used to drive the engine shaft up to a self-sustaining speed. In the new scheme, electrical power is supplied by either a ground facility or the APU to the S/G. B787 has implemented the S/G function using electrical machines mounted on the accessory gearbox (AGB) [34]. The electrical machine can be mounted directly on the shaft without the AGB and can be controlled by a dedicated Power Electronic Converter (PEC). In spite of the main challenge of embedded S/G, which is operating at temperatures in excess of 330°C, a demonstrator has been developed in 2008 [35] which is further discussed in this Chapter.

Another outstanding achievement brought by the MEA is electrical Environmental Control System (ECS). Particularly, the ECS consumes up to 75% of the energy consumed for the aircraft systems [36]. In electrically powered ECS onboard, the air is taken directly from the atmosphere, fed to electric compressors and heat exchangers. With this new technology, the main proportion of customer bleed from the engine has been eliminated, thus, moving toward bleed-less engine with higher efficiency [34]. Figure 2-6 depicts the considerable involvement of the MEA into the engine design.

As discussed above, the bleed-less engine needs to provide electric power to replace pneumatically powered predecessors for the electric ECS and electric Wing Ice Protection System (WIPS). As it is shown in Figure 2-7, removing the requirement of air bleed from the compressors has a significant impact on the engine design. Following this, the engine starting is also facilitated only electrically. Bleed-less engine causes a significant increase in the mechanical power offtake from the engine via the generators with a maximum peak value of more than 800kW for Trent 1000 engine [22, 28, 37].

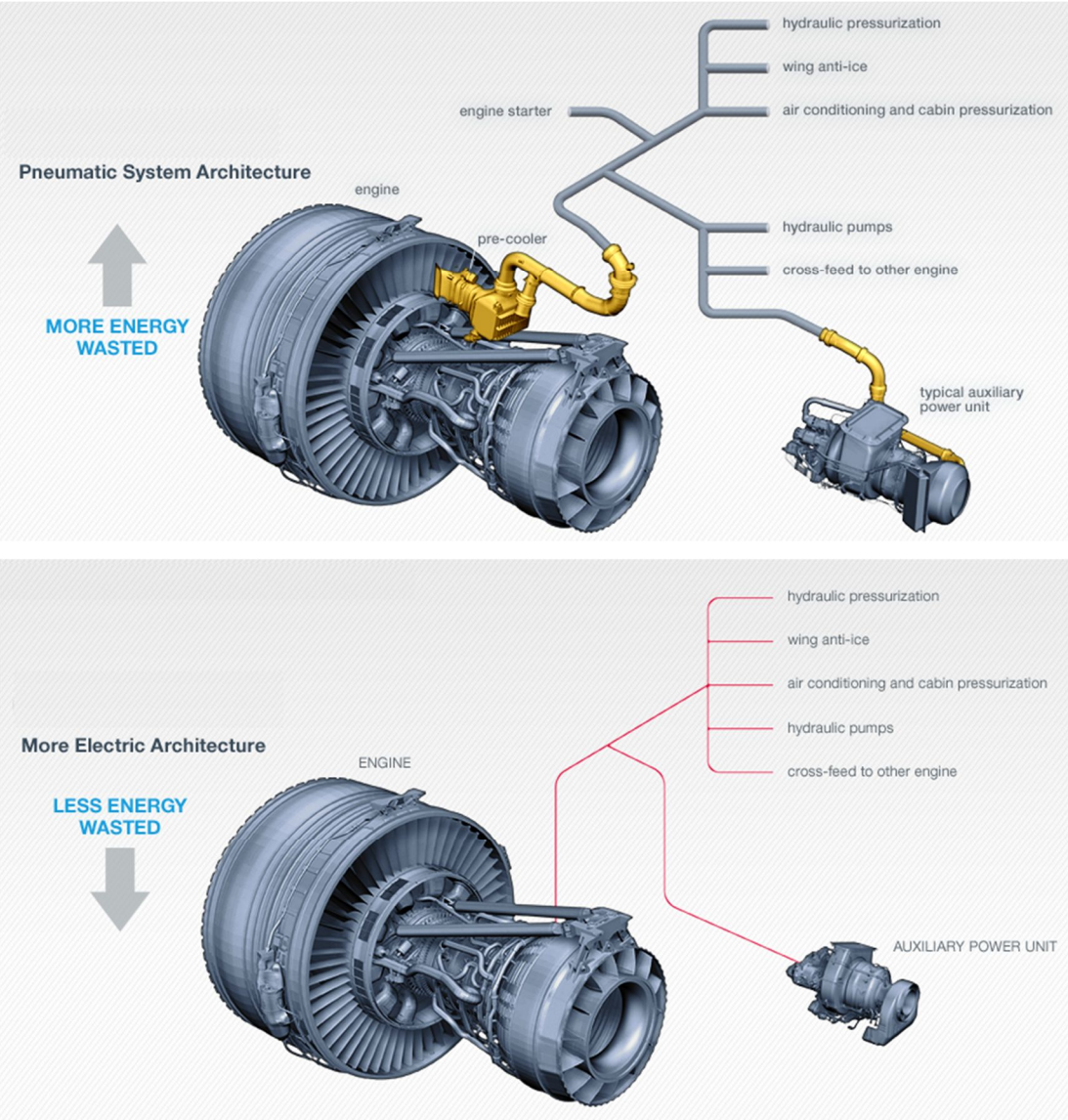


Figure 2-6 The conventional and more electric aircraft [38]

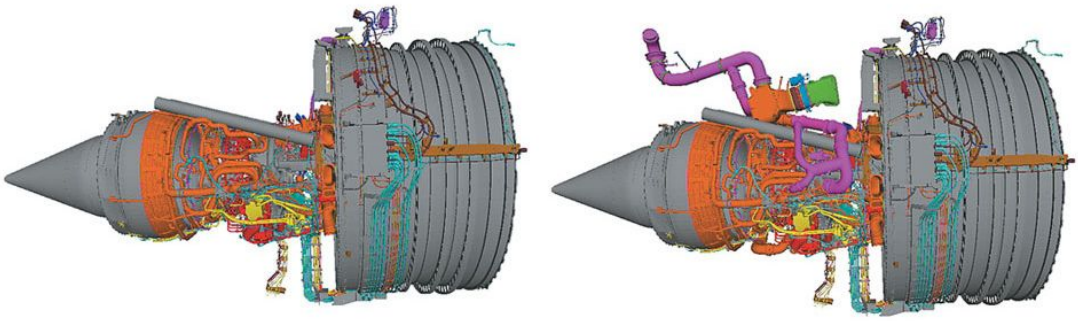


Figure 2-7 Comparison of a no-bleed engine (left) and the traditional bleed engine (right) [34]

Recently, the A380 and B787 have both taken advantage of more electric technologies in different ways, such as; in the A380, the hydraulically powered flight control actuation system has been partially replaced by electrically powered actuator units,

while the B787 has taken a bigger step by embracing the bleed-less engine technology, powering the ECS and WIPS electrically.

The MEE, as one of the main targets for the MEA, utilizes recent innovations in electrical motors, motor controllers and power electronics into the engine design by replacing conventional engine accessories, such as AGB-driven pumps, hydraulic actuators by electrically-powered pumps and Electro-Mechanical Actuators (EMAs) [8, 13, 39]. In order to raise overall efficiency of the engine, the MEE system has adopted two approaches;

- AGB elimination
- bleed-less operation

The complex AGB will be replaced by the electrical pumps and EMAs, which are powered from the generators on a simpler gearbox or embedded on the engine shafts. The technologies for embedded generators is largely developing [12].

Conventional AGB-driven fuel pump system is replaced with electric motor driven fuel pumps. In the new system, the inefficient bypass mechanism of the excess flow and Air-Cooled Oil Coolers (ACOCs), which waste fan discharge air, are eliminated. This improves engine efficiency by reducing power extraction [32]. The MEE fuel system, closely cooperating with full authority digital engine control (FADEC), can significantly reduce the fuel burn of engines and CO2 emissions from the aircraft. It can also improve the safety, reliability and maintainability of the engines [39].

Although both the A380 and B787 have taken big steps toward the MEA, neither A380 nor B787 is fitted with a MEE. There is no MEE that is in-service, or close to be in service today [12]. However, the benefits and issues related to the implementation of the MEE are under extensive investigation. A work has been undertaken by Rolls-Royce and the European Union funded Power Optimised Aircraft (POA) Programme partners in integrating the prototype units on a demonstrator engine and seeking to prove the concepts of more-electric technology whilst providing a better understanding of the requirements and design challenges for a future MEE [13, 35, 40]. The initial conceptual design prepared in 2004 is shown in Figure 2-8, where most of it has been met by today as shown in Figure 2-8.

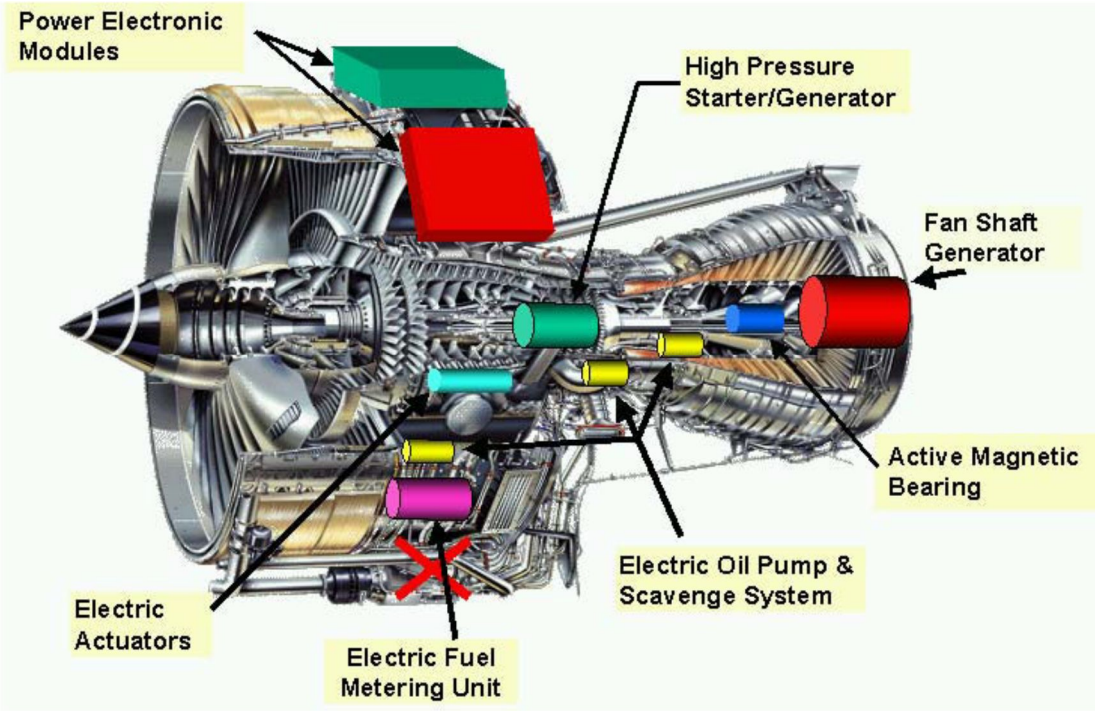


Figure 2-8 Initial conceptual design of MEE [13]

Among new technologies, the MEE have mainly focused on the engine systems. However, there is a great chance to optimize engine performance by power circulation between the engine shafts, since there is at least one electrical machine on each of the MEE shafts. The next Section provides an overview of this idea.

2.3 Introduction into the concept of inter-shaft power exchange

The compressor-turbine sets of turbofans are designed to be matched to operate most efficiently with the inlet flow at cruise condition [31, 41]. It is a complicated task to control turbofans, because there is no mechanical link between the two shafts. The whole engine's control system performance must be accomplished by regulation of the fuel and airflow. The engine components are thermodynamically coupled so that the shaft speed variations bind to each other from idle to full power setting. The shaft speeds at design condition are set to make compressors' flow match with each other. However, at off-design condition the inevitable inflexibility of shaft speeds due to thermodynamic coupling causes mismatches in the performance of compressors [31]. This enforces the implementation of handling bleeds between the LPC and HPC to regulate the flow and to avoid surge in the compressors. Consequently, the engine operates in a sub-optimal condition during low speed settings at flight phases, such as

taxiing and descent. Handling bleeds diverts some of the core airflow to the bypass duct of the engine (see Figure 4-14); making the engine fuel inefficient and also causing inconsistent thrust with the flight mission at low speed settings [31, 42, 43]. In this case, any solution which can help decouple the shaft speeds is highly desirable. Moreover, there is a possibility that the engine operation will shift from its desired design point, either after the assembly of all components due to deviated tolerances or degradation after aging. The engine will experience a decrease in its efficiency and safety margins due to this shift. Normally, the HP shaft components are more likely to wear out due to higher speed and pressure operation conditions when compared to the LP ones [44-48]. The engine efficiency can be retrieved by power circulation between the shafts and by changing the operating point of the HP shaft components independently from the LP ones.

Furthermore, excessive safety margins of each of the compressors at various flight scenarios can lead to fuel inefficiency. With the ability to circulate power between shafts; the optimum operation point for the whole engine, adequate safety margins and lowest possible fuel consumption can be established.

Prior control schemes of MEE elaborated in multi-spool power extraction have attempted to optimize engine performance by splitting the high-power demand on the two spools. As a novel idea, in order to further optimize and enhance engine performance there is a possibility to transfer power between the shafts given that there are electrical machines on both HP and LP shafts. The inter-shaft power transfer is expected to make the engine lighter and less costly [14]. The main expectations from this configuration are;

- fuel burn reduction at off-optimum conditions
- increase in engine stability margins
- compatible thrust with flight mission.

Power transfer has been suggested during 1990-s [18] and diverse methods such as; implementation of hydraulic transmission system with hydraulic pumps and motors, multi speed transmission systems with clutch assemblies, auxiliary air turbines, electric heaters and magnetic gearboxes have been considered. However, they have never come into practice due to low efficiency and complexity (discussed in Section 3.3).

Remarkably, an electric bridge can be created as shown in Figure 2-9, to circulate power between the shafts independent of their speed provided that the MEE is equipped with electrical machines connected to each of the HP and LP shafts. Prior control schemes elaborated in multi-spool power generation (more in Section 3.1.4) have mainly focused on optimization of engine performance by splitting the power extraction on the spools. However, the power can also be transferred between the engine shafts to further optimize and enhance engine performance. This idea is thoroughly investigated in this Thesis.

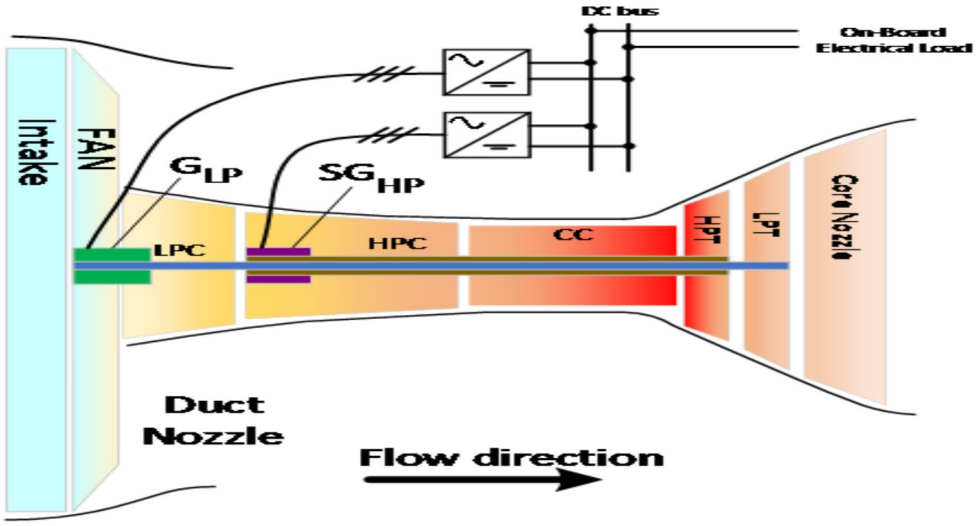


Figure 2-9 Schematic diagram of a 2-spool, high bypass turbofan engine

This configuration, which will be able to decouple shaft speeds to certain degree, depending on power capability of the electrical channel, is expected to;

- improve the engine design

The baseline (i.e. existing) engine design is faced with many constraints due to the thermodynamic coupling of the engine components. With the contribution of the EPT system in engine design, the shaft speeds can be manipulated to decrease these constraints. Novel EPT adopted design (EPTAD) will be suggested in this Thesis.

- provide optimized operation for baseline engine design depending on Engine Operation Mode (EOM)

The engine is designed for a wide range operation with optimum performance at cruise condition. However, with the baseline design the engine is non-optimal in other EOMs. This concept improves the performance of the engine at off-design conditions.

- increase the stability margin of the engine

In order to keep the engine's safe operation, stability margins for the compressors are to be considered and monitored continuously to predict any malfunction. The decrease

in the stability margin is, however, inevitable at some EOMs for the baseline design due to the thermodynamic coupling effect. The flexibility provided by the power transfer provides an opportunity to increase stability margins. Moreover, by power transfer the boost in temperature can be handled to avoid exceeding the temperature limit in a more manageable way during fast acceleration.

- improve overall efficiency, reliability, availability and maintainability with engine aging

Engine performance deteriorates with its aging. Differences in conditions of operation leads to different components degrading at different levels which then results in mismatches between them. Power transfer can manipulate the shaft speeds to find the most optimum point of operation for the engine. With aging, core components are more susceptible to degrade due to higher temperature, speed and pressure condition. Depending on the type of degradation, the core speed can be decreased or increased to make the operation of core components closer to their optimum point while keeping them in the safety margin.

- reduce the fuel burn during low speed settings

The engine operates at low speed settings at some manoeuvres such as ground and flight idle. The minimum allowable HP shaft speed is normally set as the limit for the engine operation in these modes; this may lead to excessive fuel burn and thrust which is not favourable. Power transfer can mitigate this problem by decreasing the throttle while keeping the minimum HP shaft speed.

- help faster recovery of thrust in case of abrupt thrust demand

For manoeuvres such as go-around, abrupt thrust recovery is required which is limited by the engine constraints. Power transfer can keep the engine prepared for fast acceleration while also keeping the fuel consumption at lower level.

- transfer wind-milling power from the LP to HP shaft for engine restart

During a windmilling event, the considerable amount of power extracted from the large LP fan can be transferred to the HPC in order to attempt to start the engine.

- feed power to the fan in a hybrid electric engine concept

In hybrid propulsion systems, the fan can receive power not only from the LP turbine but also from multiple sources such as batteries. Power transfer from the HP shaft can also contribute into the new hybrid engine designs.

- manipulate shaft speeds to overcome surge incidence

The EPT system can manipulate the compressor speeds to overcome the surge incidence. Once the surge phenomenon happens, the LP and HP shaft speeds experience severe changes within a short period of time. This can be handled relatively with the help of the quick response of electrical machines.

The possible achievements briefly discussed above are elaborated in Section 3.4. The proposed EPT concept can be broadly applied not only for jet engines but also for ship engines, ground-based power generation gas turbines and other multi-spool engines. Certainly, the concept will lead to an increased weight and volume of the engine. This should be the subject of aircraft-level optimization, including the impact of proposed system on aircraft's overall propulsion efficiency.

After the brief introduction into the EPT, the next Chapter reviews the state-of-the-art aircraft power systems and discusses the implementation of EPT system in more detail.

2.4 Conclusion

This Chapter presents a brief overview of the engine technology development up to the future MEE. The motivations for EPT between the engine shafts to improve engine performance is also discussed and realization of EPT through electrical machines on each shaft of the MEE is described briefly.

Chapter 3 State-of-the-Art in Power Offtake

Aircraft engine is primarily a thrust source for aircraft with a range of total propulsive power from 0.5MW for 9-seats to 22MW for 150-seats aircraft [49]. At the same time, the engine is the prime mover for non-propulsive systems which represent approximately 5% of total fuel consumption of the flight [11, 50]. This highlights the fact that in order to optimize the performance of aircraft systems, one should see the whole picture of the engine and non-propulsive systems.

The MEA concept, adapted during the last four decades; has allowed for a better control, monitoring, fault tolerance, decreased maintenance cost and increased overall reliability for the propulsive and non-propulsive systems [51]. This is mainly due the replacement of hydraulic and pneumatic systems with electrical systems. The MEA's concern is the electrification of aircraft systems which were conventionally hydraulic, pneumatic or mechanical. In this aspect, the main difference between a conventional aircraft and a MEA for an engine manufacturer, is the ratio of electrical power extracted by generators to overall power extraction from the engine [52]. Along with this, engine designers are continuously pushing forward for optimization of engine performance to fit into the MEA requirements in the highly competitive market.

The MEE concept; as the companion of MEA, is mainly focused on accommodating new engine systems to benefit the engine from the electric power generated by the engine-mounted generators.

This Chapter provides a literature review of conventional and MEA power extraction configurations; while also considering their interface with the engine shafts. The latter part of this Chapter presents an outline of the purpose of this study which is the idea of power transfer between engine shafts as a possible future configuration to improve the MEE's performance.

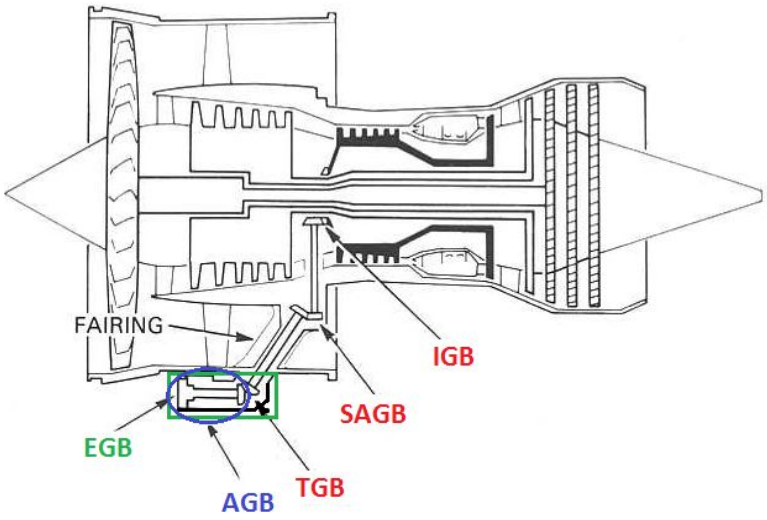
3.1 Power offtake configurations

Aircraft are exploiting various non-propulsive systems for a safe operation while keeping passengers' comfort. These so-called secondary power systems have been continuously optimized, considering the trade-offs between structural, aerodynamic, electronic and mechanical aspects. These systems are typically driven by a combination of various power types such as hydraulic, pneumatic, electrical and mechanical, all extracted from the engine. The term power offtake (PO) is referred to the whole power for mechanism and functional systems that are extracted from the engine core [37]. Pneumatic power is extracted from the engine by the bleed air from the compressor stages whereas hydraulic and electrical power are extracted from the engine shaft through the AGB. Systems which are normally connected to the AGB include;

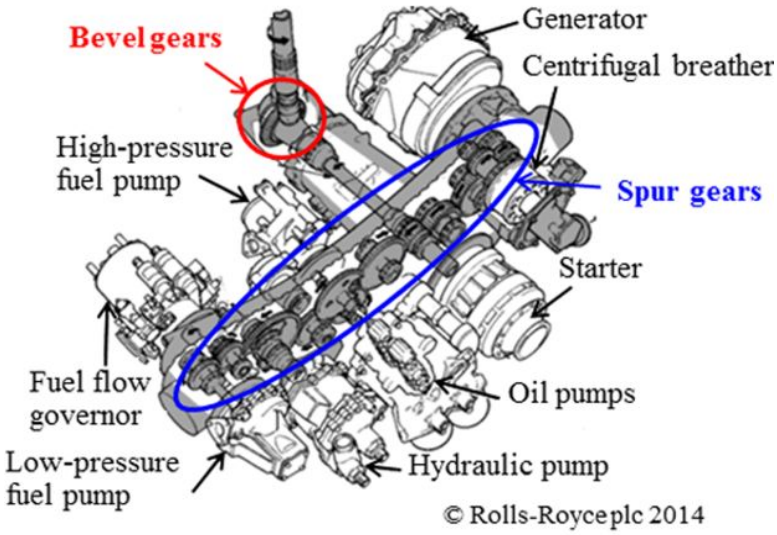
- aircraft main electrical generators to supply power for on-board loads
- aircraft hydraulic pumps to power on-board 3000psi hydraulic systems
- engine electrical generators to supply electrical power for engine systems
- engine fuel hydraulic pumps
- engine lubrication hydraulic pumps
- and an engine oil breather

Figure 3-1 shows a typical AGB where the bevel gears (i.e. Transfer Gearbox (TGB)) are connected to the engine shaft through a Step Aside Gearbox (SAGB) and Internal Gearbox (IGB) [23]. It should be noted that one of the main objectives of the MEE is removal of the AGB by directly mounting the electrical machines on the engine shafts within the engine core [13].

The electrical generator of the HP shaft also functions as a starter of the engine with external power supply either from the APU, other engine's generator or on ground source.



a) Aero-engine



b) AGB

Figure 3-1 Typical accessory gearbox [53]

In order to have a better assessment, the amount of PO is expressed as a fraction of the corresponding shaft's turbine power. For instance, in the Trent 1000 engine, the amount of PO is 500kVA which is almost 30% of the power produced by the IPT at idle setting [37]. The limit for PO to shaft power for each of the engine shafts depends on several factors that are mainly defined by the costumer; such as operability, minimum and maximum value of thrust, overhaul intervals, etc. [37]. For a 2-shaft or 3-shaft engine; load requirements, idle setting, engine weight, fuel burn, starting performance, thermodynamic and mechanical aspects, secondary air system features and noise are the main players for the selection of the PO level from each shaft. Designers normally end up in trade-off studies at the expense of weight, cost and

reliability with constraints such as the core size requirement, transient behaviour, available safe margins, etc. [37].

The AGB has been conventionally mounted on the HP shaft of the engines. Former engines are less affected by HP PO due to low percentage of PO to shaft power. The higher power demand of the MEA have motivated the designers to consider PO from other shafts, albeit with new challenges and limitations. In this Section, various PO configurations such as, HP PO, IP PO and multi-spool PO are introduced.

3.1.1 *HP Power Offtake (HP PO)*

The HP shaft speed is high and relatively constant with maximum to minimum ratio of 1.5-2.5, compared to that of LP shaft with maximum to minimum ratio of 5-6, presented in Table 3-1 for some engines. Table 3-1 shows the HP and LP shaft speed values for modern twin shaft engines. HP_{max}/HP_{min} and LP_{max}/LP_{min} are the ratio of maximum to minimum speed of the HP and LP shafts respectively.

Table 3-1 Shaft speed twin spool engines [16]

Engine series	Aircraft	LP speed (100%)	HP speed (100%)	LP_{max}/LP_{min}	HP_{max}/HP_{min}
GP7200	A380	2467	10998	6.1	1.9
CFM56	B737	5175	14460	5.2	1.8
GEnx-2B67	B747-8	2560	11377	6.7	2.3
GE90	B777	2261	9331	6.1	1.7

In fact, the HP shaft is a reasonable choice of mechanical power source to drive electrical generators, no matter which electrical architecture is employed. In addition, it is much more efficient to start the engine by rotating the HPC for which the generator can act as a starter as discussed in Section 2.2. An illustration of the HP PO though the AGB is shown in Figure 3-2.

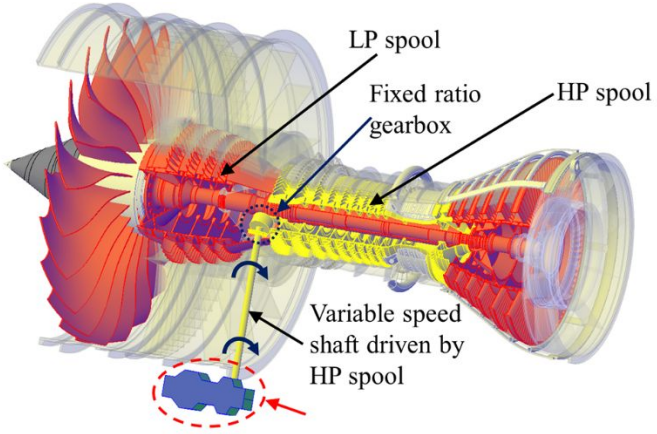


Figure 3-2 HP PO transmission system [16]

However, drawing power from the HP shaft imposes a slowdown in the HP speed. For this reason, HP PO is limited to avoid compressor instability most notably during flight and ground idle due to high PO to shaft power, and transient conditions due to lower surge margin [54].

The surge problem during high PO demands can be mitigated by increasing the engine speed and bleed which is elaborated in Section 5.1.1. This solution, however, can increase both the fuel burn rate and the residual thrust, which refers to the undesirable thrust during idle setting. The residual thrust would not allow the aircraft to descend quickly enough, thus lengthening the descent phase (which is a fuel inefficient operational combination) or resulting in a significantly higher than normal airspeed during descent (steeper pitch angle) [55].

The high level of HP PO requires an oversized HPT and a redesign of the pressure ratio split between the compressors [37, 56]. Oversized HPT affects the engine core size compatibility, air system related issues and other constrains such as HPC/IPC surge margin, generator speed, overhaul intervals, minimum and maximum thrust etc. [37]. In general, oversized HPT is not the ideal solution since it causes low engine efficiency at off-design engine speeds.

3.1.2 *IP Power Offtake (IP PO)*

The significant increase in PO for the MEA is one of the main design aspects when it comes to selection between geared 2-shaft vs. 3-shaft engine configurations. Power extraction from each shaft affects the secondary systems of the engine including: the internal air system, bleedings, oil and electric systems [37].

Higher levels of PO, with the maximum of 750kW per engine for Trent 1000 engine [37], has led to an alternative architecture where the AGB is driven through the IP spool instead of the HP spool for a three-spool engine, as shown in Figure 3-3.

Engine operability and fuel consumption are the major benefits of IP PO in the three-spool design. The key advantage of the IP PO system is that the requirement of bleeding has been lifted which results in fuel burn reduction during approach and idle settings. In addition, the engine operability is much less affected by high amount of IP PO, since the IPC is on downstream side of the HPC. In fact, in this configuration the decrease in IPC speed due to PO improves the IPC surge margin and does not affect the HPC surge margin [57]. The IP shaft speed variation range is around 2:1 which

makes the generator design less challenging than LP PO with speed variation range of approximately 5:1.

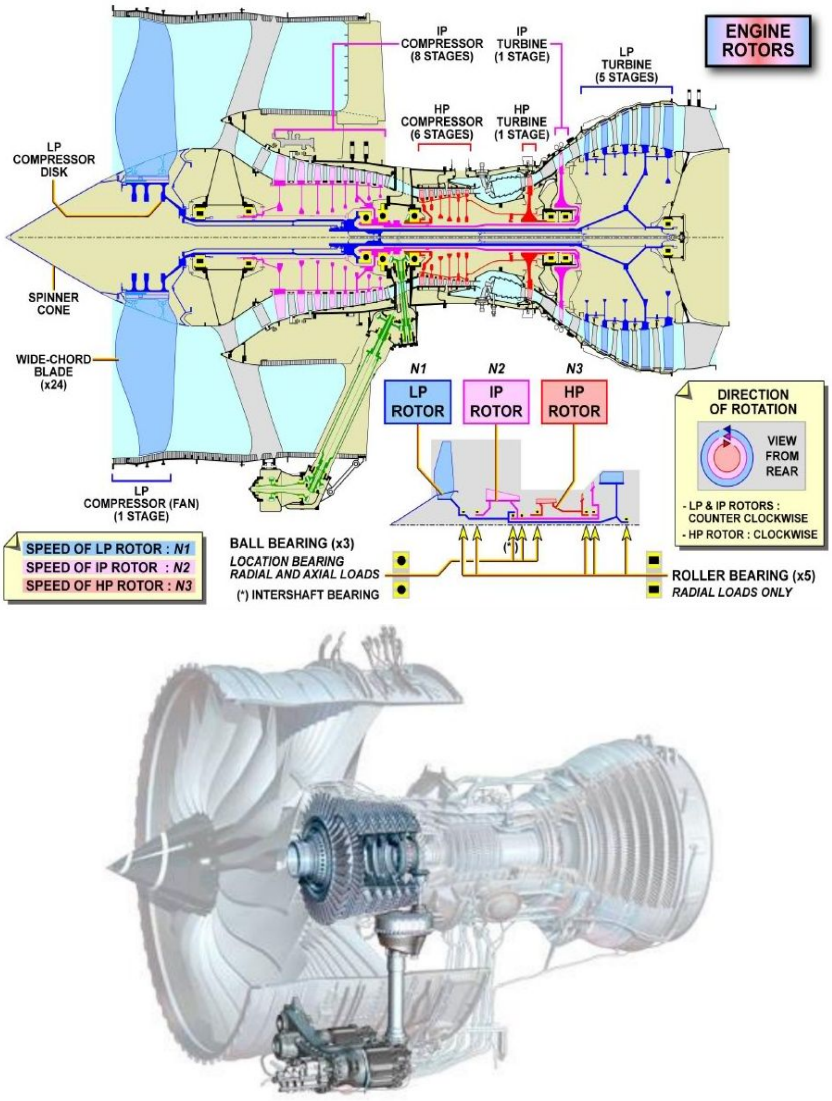


Figure 3-3 IP power offtake of Trent 1000 [28]

Incorporating to the MEA concept, the services which were traditionally powered by pneumatic bleed air such as the ECS are now driven electrically in B787. The main consequence of this shift is the high amount of IP PO, which replaces the bleeding system for the pneumatic system usage. In bleed-less engines, no air is extracted from the compressor stages for onboard usage, increasing the overall engine efficiency (1-2% for Trent 1000 in B787) [34]. It should be noted that the bleed-less engine still requires handling bleeds for compressor stability especially at low speed settings [42]. The benefits obtained from the IP PO when compared to the HP PO are [37]:

- meeting the increased PO requirements
- reducing fuel burn for low range missions

- decreasing idle setting (reduced break wear)
- reducing noise during approach
- and enabling wider operability range

In the Trent 1000 bleed-less engine, the amount of PO from the IP spool is 500kVA which is almost 30% of the power produced by the IP turbine at idle setting [37]. This is a significant amount of the overall turbine power and therefore any increase beyond this amount will have a significant effect on engine matching.

3.1.3 *LP Power Offtake (LP PO)*

In order to power larger loads of the MEA; power can be extracted from the LP spool of the multiple-spool engines, which carries a high amount of power for the fan. The LPC operates in a lower load regime, making it much less susceptible to surge.

The HP PO reduces the surge margin of both the HPC and LPC, while the LP PO increases the LPC surge margin and keeps the HPC surge margin at its baseline value. The effect of PO on surge margins of the LPC and HPC is discussed in detail in Section 5.1.1. In general, it is always preferable to extract power from the shaft of the first compressor in the flow direction, for the sake of compressors' surge margin.

An analytical study in [58], on the performance model of a twin-shaft high BPR turbofan with thrust of 20-30klbf, shows the superiority of LP offtake in terms of TSFC, compatible thrust, surge margin and thrust response. The LP offtake leads to higher efficiency due to the higher efficiency of the LPT.

However, the LP PO is yet to be implemented due to the challenges below:

- Wide range and low values of the LP shaft speed results in complexity of the generator design. The LP speed ratio exceeds 5:1 (see Table 3-1) for high-bypass turbofans [59]. The better performance of the engine can be eroded by the LP generator weight penalty.
- The operating efficiency and sizing of components such as hydraulic pumps and electric generators are severely affected with the wide speed range. Being designed for design speed, these components operate in sub-optimal condition at off-design condition.
- LP PO decreases LP shaft speed and thus its pressure ratio. Due to the change in pressure difference of the LP blades with the casing, sealings which are

designed for minimum pressure values might be affected in the way that the direction of flow changes.

- For high-bypass turbofans, very low fan pressure ratio at idle setting does not adequately increase the temperature across the fan to be able to remove the ice growth on stators and Variable Inlet Guide Vanes (VIGVs) [37].
- The generator on the fan shaft (LP shaft) cannot be used as a starter. In order to pressurize the air with the LPC, much higher power is required compared to that of the HPC due to the lower pressure ratio. Even if the LPC reaches its maximum speed, its outlet pressure ratio is still very low to start the combustion with. Moreover, the fan is connected to the LP shaft; which draws high power to rotate while bypassing the air to the duct, which is unnecessary for the engine to start.

For the reasons above, multi-spool PO is suggested which is discussed in the next Section.

3.1.4 *Multi-spool power offtake*

Neither the HP nor the LP can be relied on to be the single source for high levels of PO due to operational limits such as surge margin of compressors, generator speed, minimum speed for idle performance, minimum and maximum thrust, etc. As a result, exploiting various shafts (the LP and HP for twin-shaft engines) in a multi-spool PO configuration has been under extensive investigation [35, 58, 60-66].

In a multi-spool configuration; the LP generator can be physically attached to the LP spool in many locations, including the fan drive nosecone and the LPT tail cone [14, 35, 67, 68]. The HP and LP generators can also be embedded on the shaft into the core of the engine, combined with the Active Magnetic Bearings (AMBs) in the colder side of the engine (i.e. compressor side). This will also allow the hydraulics to be replaced with electric motor/hydraulic pump assembly [13, 14].

Multi-spool PO is expected to mitigate the negative impacts on engine performance in comparison when compared to the single shaft HP PO architectures [58]. By multi-spool PO, engine speed variation is split between multiple shafts. This decreases the adverse effect of severe speed reduction of single shaft PO. As a result, flow matching between compressors is less affected, as well as engine stability and surge margin. The narrower speed variations also leads to improved life of the engine for transient load cycles [69].

To implement multi-spool PO, one generator can be connected to both LP and HP shafts through summation gearboxes, with power split ratio imposed by shaft speed ratios. In another configuration, generators can be independently connected to each shaft to extract power with adjustable power split ratios. The next Section presents these two configurations.

3.1.4.1 Dependent multi-spool PO

To tackle the wide speed range of LP PO, various configurations have been offered, including multi speed gear assembly on the LP shaft or between the LP and HP shafts [56, 70-73] and implementation of a clutch between the generator and LP shaft [74]. Essentially, power transmission from the LP shaft to the generators through a mechanical transmission requires a multi-speed transmission system. The reliability of this system is not guaranteed because it is complicated. It also requires multiple gears which adds high additional weight to the engine.

In a dual drive booster turbofan architecture suggested in [75], as it is shown in Figure 3-4 and Figure 3-5, a summation gearbox is implemented to extract power from both the HP shaft, shown in purple, and the LP shaft, shown in blue, to drive the LPC, shown as green, and the starter/generator [56].

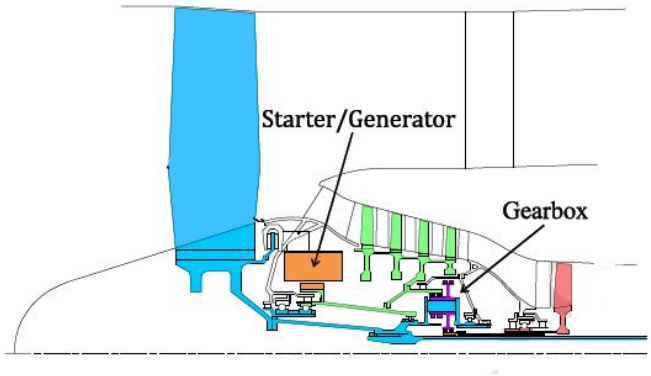


Figure 3-4 Arrangement of the Starter/Generator on the dual drive shaft [56]

An epicyclic gear system is situated between the fan and the HPC, as shown exemplarily in Figure 3-4. In the contra-rotating configuration, the HP shaft drives the sun gear and the LP shaft drives the planet carrier, while the LPC and the generator are both driven by the annulus gear. Figure 3-5 is a diagram of the gear pitch circles showing the directions of rotation. The higher spool speed with a narrower range of variation makes this configuration more suitable for electrical machines rather than for one separate LP generator.

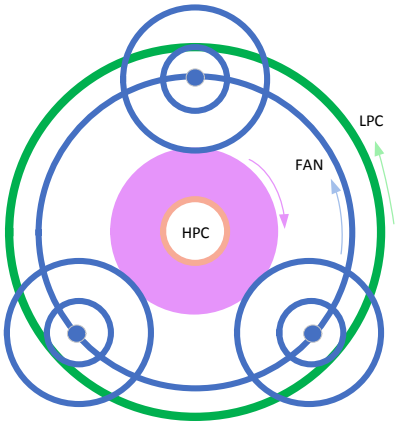


Figure 3-5 Gear pitch circle diagram of the a summation gearbox [56]

In particular, the core compressors (LPC and HPC) are less affected since both shafts are contributing to power offtake, which allows higher power offtakes and provides more flexibility during engine design and operation. Additionally, there is a potential to use the new configuration as a hybrid gas turbine-electric engine [76] where electrical power boost is applied during critical flight phases. Some of the challenges of dependent multi-spool PO are listed below:

- In case of any damage to the gearbox, LPC's performance will deteriorate, which will cause instabilities to other compressors, decreasing the reliability of this configuration.
- In this configuration power split ratio is a function of the LP and HP speeds for the whole operation range, enforcing some undesirable constraints on engine performance. The optimum performance of this configuration depends on the choice of the gear ratio to a very high degree, which is chosen for one operation point, leaving sub-optimal operation for off-design conditions.
- During severe engine transients, the HP shaft speed accelerates faster than the LP one which may deteriorate the performance of handling bleeds, leading to compressor instabilities.

3.1.4.2 Independent multi-spool PO

Generators can extract power from the engine shafts independently, either mounted directly or through AGBs. Since there are separate generators on the HP and LP shafts, power offtake can be split between engine shafts in a more manageable and reliable way.

Independent multi-spool PO has not yet been commercialized on a civil aircraft in operation. It has been demonstrated on a Trent 500 MEE in [35] where a 120kW switched-reluctance generator is connected to the LP shaft through a 1:4.5 ratio gearbox and a 150kW permanent magnet embedded motor/generator is directly connected to the HP shaft (shown in Figure 3-6).

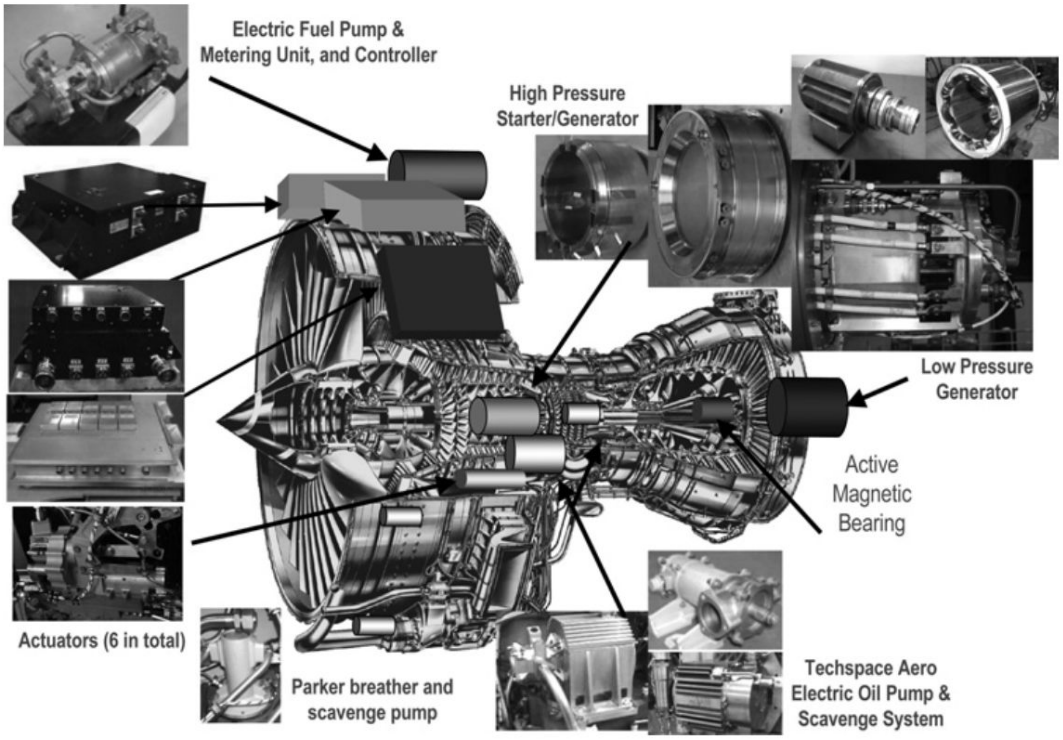


Figure 3-6 The Trent 500 MEE (Rolls-Royce University Technology Center, Strathclyde) [35, 40]

A demonstrator has also been set up on a Larzac 04 C5 jet engine, schematically shown in Figure 3-7 [15]. This demonstrator has been developed for detailed research on the independent multi-spool PO.

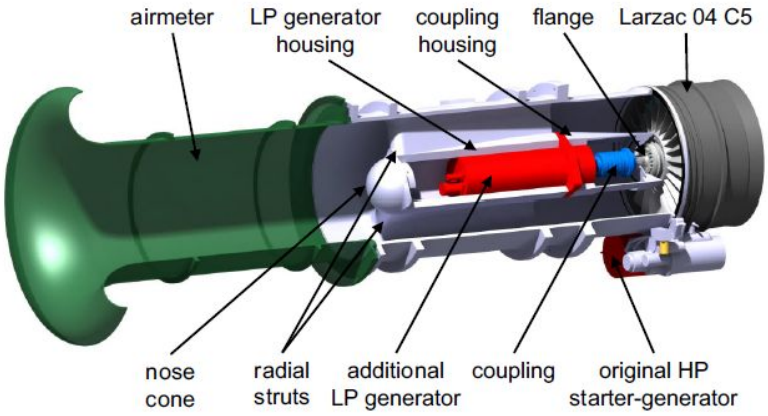


Figure 3-7 Larzac MEE configuration [15]

Among various methods of power supply from the engine, independent multi-spool PO architecture provides power extraction management between the shafts in a

controllable way. This increases the operation flexibility (operability) both for the engine and power generation systems [55] which makes this architecture a suitable choice for the future MEE. Apart from these superiorities, independent multi-spool PO enables power transfer between the shafts, which is the focus of this study.

After reviewing various available ways of power offtake, in terms of the source of shaft power extraction, it is of paramount importance to review the interaction of PO with the onboard loads. For this purpose, the next Section aims to discuss various architectures between the engine and MEA loads.

3.2 Engine-EPS interface

When it comes to the design of electrical PO architecture, it should be noted that engine shaft speeds are not constant; varying from idle to full engine power setting, while many of the aircraft loads are operating at a constant frequency. Hence, either the shaft speed is adapted to a fixed-speed shaft, of a constant-speed generator or a variable-speed generator feeds power to the converters to provide; wild frequency, constant frequency, or DC power, as desired, and to further include inherent levels of redundancy that is reliable to ensure safe operation [16, 50, 77].

Starting from the1960s, AC generation took over DC, due to higher power requirement for the aircraft and AC generation privileges, such as better reliability and power density at higher operating voltages. In 1959, the standard of three-phase 115/200 Volts Alternating Current (VAC) at 400 Hz was stablished by the US Air Force (MIL-STD-704) which has not changed until today for both civil and military aircraft [16, 50].

The generations of mediums between the engine shaft and power generation outputs have been; Constant Speed Drive (CSD), Integrated Drive Generation (IDG), Variable Speed Constant Frequency (VSCF) and Variable Frequency Generation (VFG). These are discussed in the next Sections.

3.2.1 *Integrated Drive Generator (IDG)*

To provide Constant Frequency (CF) generation, which is usually three-phase 115 VAC at 400Hz, the traditional approach provides constant speed for the AC generator shaft depending on pole numbers (e.g. 24000rpm for 2-pole generators for Boeing 777 [78]). A variable ratio hydro-mechanical transmission gearbox known as Constant

Speed Drive (CSD) was installed between the synchronous generator and the engine shafts in the 1960s for B707 with a power density of 0.88kVA/kg (typical value for CSD + generator systems) [16, 79, 80].

The bulky, heavy and expensive CSDs were replaced with the Integrated Drive Generator (IDG) in the 1970s which integrated the generator and CSD into a single unit with shared lubrication and a cooling system within a common housing with a considerable shift in power density to 1.5kVA/kg [16, 81].

Figure 3-8 depicts the IDG system schematic which has been the most common architecture for conventional aircraft, such as A320, A330, A340, B747, B757, B767, and B777, providing constant frequency power in the range of 40-120kVA per channel [16, 82]. The complex constant speed drive is the key component of the IDG and is connected to the turbofan HP shaft, through the fixed ratio IGB and SAGB (see Figure 3-1).

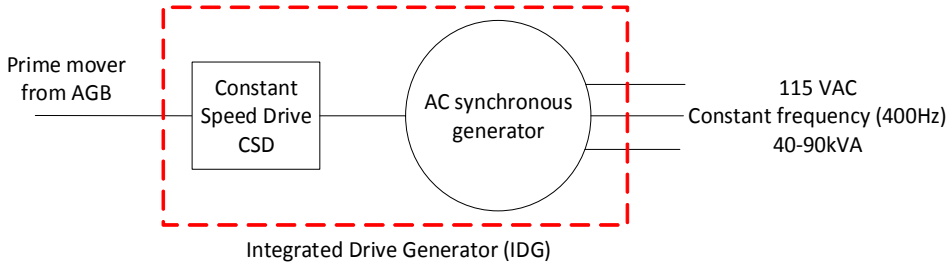


Figure 3-8 IDG system

3.2.2 *Variable Speed Constant Frequency (VSCF)*

The need for frequent maintenance and noticeable weight and size are the main drawbacks of the constant speed transmission systems which leads to the removal of CSD or IDG, by the introduction of Variable Speed Constant Frequency (VSCF) generation [10, 83, 84]. Generators without the need for the complex constant speed drive are simple, efficient, more reliable, require less maintenance, and have lower spare costs than the traditional IDGs [34]. In this configuration, the generator is connected to the engine shaft through fixed speed ratio IGB and SAGB. The variable frequency of the generated power can be regulated for CF loads with Power Electronic Converters (PECs) through two well-stablished configurations [34].

In the first configuration, a DC link is implemented between the variable frequency AC generation, and the constant frequency AC loads through rectifiers and inverters (shown in Figure 3-9). The DC link can also supply power for other DC loads at different voltage level through DC-DC converters [10]. This layout was put to practice

on the MD-90 and B777 aircraft for the two 20kVA back-up generators; there is a fixed 2.86:1 speed ratio between the engine HP shaft (with nominal speed of 9333rpm) [85] and the variable speed generator (with nominal speed of 23763rpm) [84].

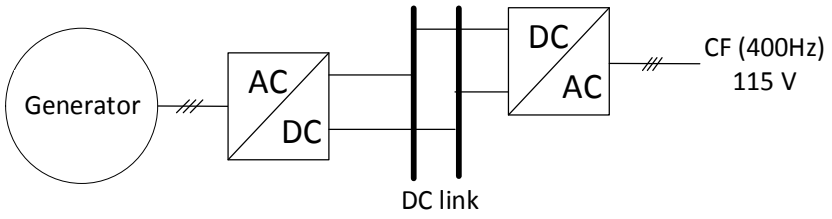


Figure 3-9 VSCF system using DC link

In the second configuration, the medium between the variable and constant frequency AC systems is an AC/AC converter, either cycloconverter or matrix converter, which; It has been implemented on fighter aircraft such as the F-18 and the F-117A [50, 77]. The reliability of the convertors in these configurations is of paramount importance since they are on the critical path of power supply to electrical loads of the aircraft.

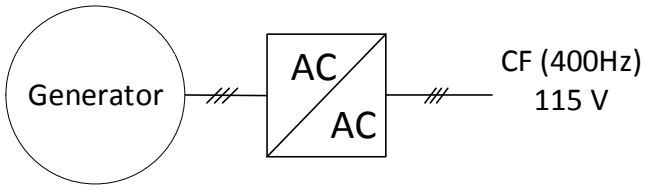


Figure 3-10 VSCF system using AC/AC converter

3.2.3 *Variable Frequency Generation (VFG)*

Recently, the Variable Frequency Generation (VFG) has been implemented in a so-called hybrid voltage electrical system [34]. In this configuration, the generators are directly connected to the engine through fixed-ratio IGB and SAGB and therefore, they operate at a variable frequency (360 to 800Hz) proportional to the engine speed [34].

VFG is used to power the resistive loads while the locally distributed PECs are inevitable for constant frequency loads in this configuration. In the B787, the main electrical power generation relies on four 250kVA VFGs (two per each main engine), while the A380 uses four 150kVA VFGs (one per engine) [16].

The hybrid ac/dc system consists of the following voltage types: 235VAC, 115VAC, 28Volts Direct Current (VDC), and ±270VDC. As a consequence of the new no-bleed MEA architecture, the 235VAC and the 270VDC voltage types are added to the traditional 115VAC and 28VDC voltage types, allowing a greatly expanded electrical

system generating which generates a capability of twice as much electricity as previous Boeing airplanes [34].

The 235VAC 360-800Hz output of generators directly powers the frequency insensitive loads such as wing ice protection, galley ovens, and cargo heaters. At the same time, it is converted to 270VDC by Auto-Transformer-Rectifier Units (ATRUs). The 270VDC system supports a handful of large-rated adjustable speed motor drives required by the MEA. These include cabin pressurization compressor motors, ram air fan motors, the nitrogen-generation-system compressor used for fuel-tank , and large hydraulic pump motors. The majority of airplane electrical equipment, being either 115VAC or 28VDC, are supported through auto-transformer or transformer rectifier units from the generator outputs as well [34].

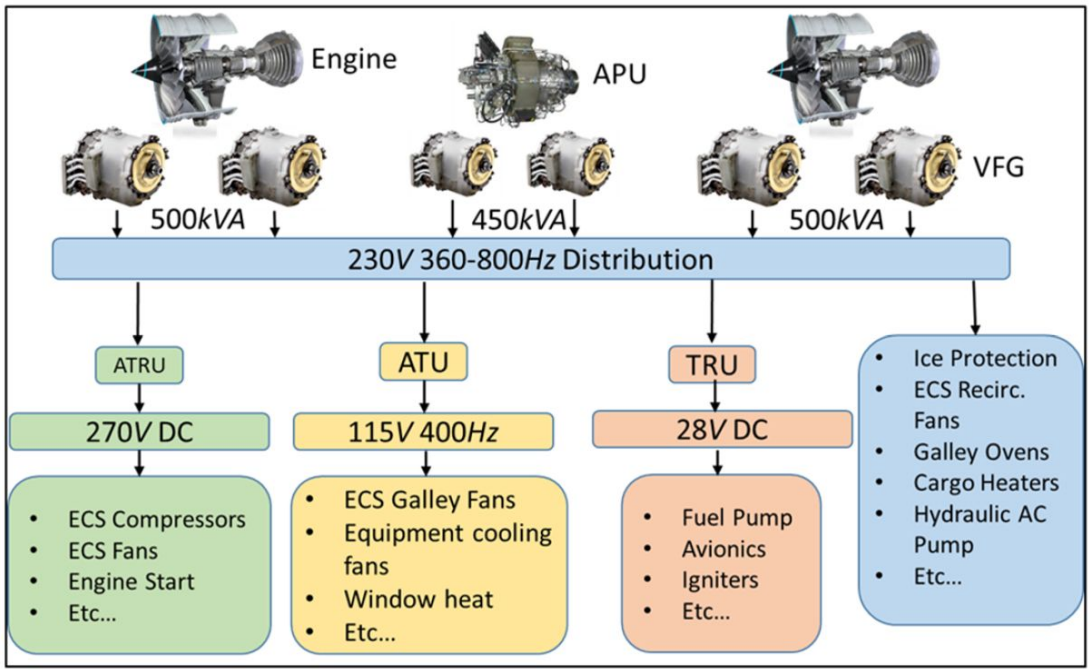


Figure 3-11 Simplified diagrams of electric distribution systems of B787 [16]

The distribution topologies discussed above including; AC, DC and hybrid frequency are still under scrutiny to be more optimized for the MEA in terms of weight, efficiency, reliability and lower cost. Electric Power system (EPS) architectures with DC distribution network is one of the promising trends for the MEA research studies, among which single DC bus architecture with multiple paralleled generation sources is being widely considered [16].

3.2.4 *Single dc bus EPS architecture*

Given that multi-spool power generation is from multiple shafts, operating at different speeds in a wide range, and with different frequencies, various architectures have been proposed in the literature [86-89]. Note that in a typical EPS, the generators, as a rule, are not allowed to be paralleled. Among all, a dc distribution network can easily handle parallel operation of multiple dissimilar electrical sources with potential benefits in terms of total weight, efficiency, availability and cost in comparison to the existing architectures [90]. In this architecture, PECs convert all the motor/generator outputs to a single high-voltage DC output through a supervisory controller to share the load between the sources [89-92]. The DC power can then be exported to transmission systems around the airframe [14]. In this configuration; HP and LP generators operate in parallel to transfer the power to the DC bus through AC/DC bidirectional converters as shown in Figure 3-12.

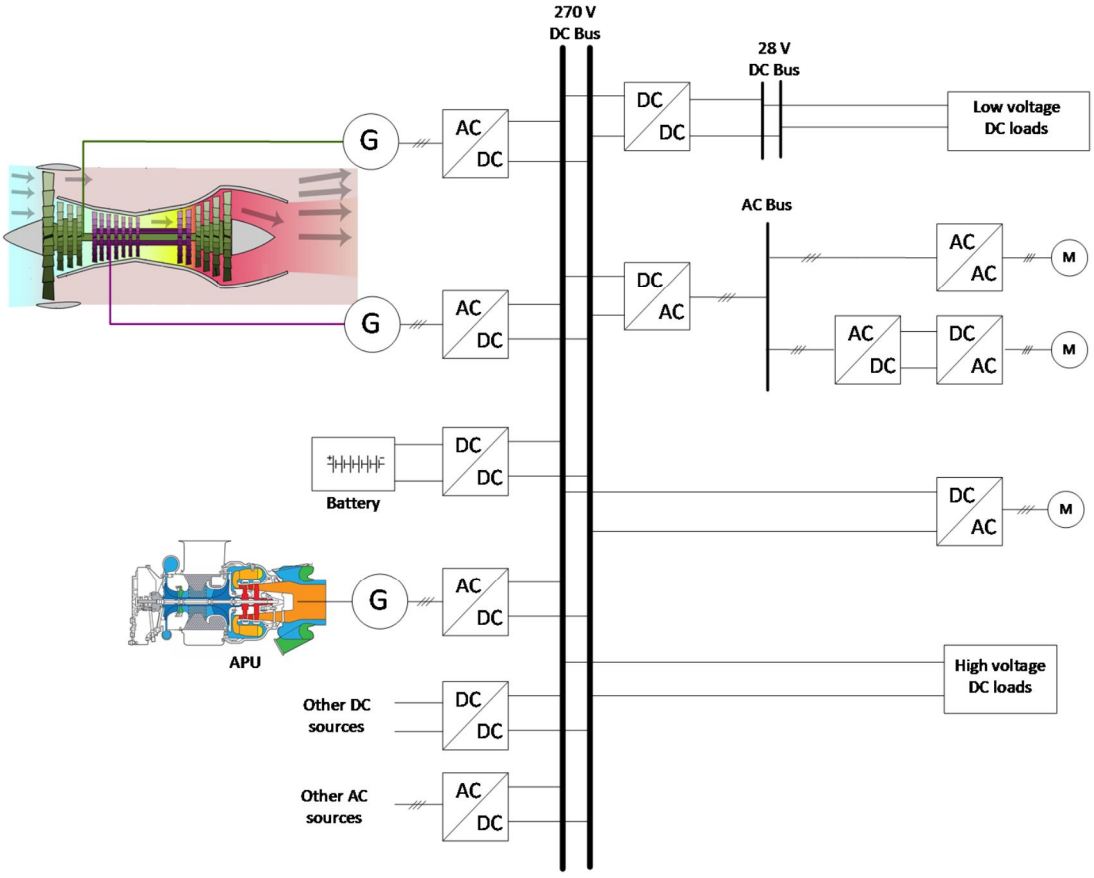


Figure 3-12 Configuration of single dc bus multi-source EPS [92]

The possibility to integrate new sources to the system such as energy storage devices is also a privilege as it helps to level power demands so that the generators' weight is reduced and the system availability is improved [93]. Moreover, for ground starting of

the engine, the DC bus can be fed from auxiliary supplies such as APU [55]. It should be noted that the airframe loads and their architectures is out of scope of this study. In this thesis a single separate dc bus has been employed for the purpose of EPT.

3.2.4.1 Control and stability of the single dc bus architecture

Having been fed from multiple sources of power, the DC bus shown in Figure 3-12 requires a stable voltage level, normally 270Volt with PO management from different sources [90]. A control system helps achieve this due to its load sharing ability between the sources. Similar to DC microgrids [94], there are three main load sharing methods from communication point of view as: centralized, decentralized and distributed control which are discussed in the following.

a) centralized control

In this approach, loads and sources communicate with a central controller through a digital communication link [94]; where master/slave approach is widely implemented within the central controller. One of the modules, normally the source with the largest capacity or highest reliability, can be chosen as the master to control the voltage of DC bus controller while the remaining modules can share the current as slaves [95].

b) decentralised control

Local measurements are employed to implement independent regulation with local controllers. There is no centralised controller and link between local controllers in this approach [94]. As a common practice, droop control is applied in decentralised control method, since each parallel module independently relies on local measurements and controllers [96]. A virtual resistance, also known as droop gain or constant, is added to the closed-loop of the controllers to realise desired power or current sharing between parallel sources. The references can be created either in I-V droop or P-V droop as follows:

$$I_i^* = \frac{V_{dc}^* - V_{dc}}{k_{dI}} \tag{3-1}$$

$$P_i^* = \frac{V_{dc}^* - V_{dc}}{k_{dp}} \tag{3-2}$$

where I_i^* and P_i^* are the output current and power of the droop controller, i.e., the reference value for the converter #i; V_{dc}^* is the reference value of DC voltage; k_{dI} and k_{dp} are the droop coefficients in current- and power-based droop controllers, and V_{dc} is the voltage of the dc link.

The conventional droop control discussed above is a primary control structure. Secondary control structure can be added for voltage restoration to improve load sharing performance [90, 97].

c) distributed control

In this approach, there is no central controller whereas neighbouring controllers locally communicate among themselves through a communication line. Due to the lack of direct communication between all sources, a consensus algorithm is installed to provide secondary control. The consensus is a simple protocol, to provide observation of the whole system for local controllers [94, 98]. For instance, in [98], a dc voltage observer, which receives information from neighbouring generators, is developed in a dynamic consensus to correct the voltage reference for local controllers. Also, a current regulator is employed, which compares the local current with the neighbours and removes current sharing error.

In a single dc bus architecture with parallel sources, following an outage of one or more converters, the remaining ones should be able to handle the resulting power deficit in an appropriate proportion. Therefore, for the sake of reliability, it is desirable that all converters participate in voltage control of the DC-link by receiving properly modified set values of DC-link voltage in decentralised control [96].

3.2.4.2 Stability

Typical loads of the MEA EPS include constant impedance loads, constant current loads, and constant power loads (CPLs). CPLs are the main concern for the stability of the single dc bus architecture due to their destabilizing effect [99]. If there is only one corresponding torque value for every speed value of an AC motor, then for rigorous speed regulation, the DC/AC inverter is considered a CPL for the DC bus as shown in Figure 3-13.

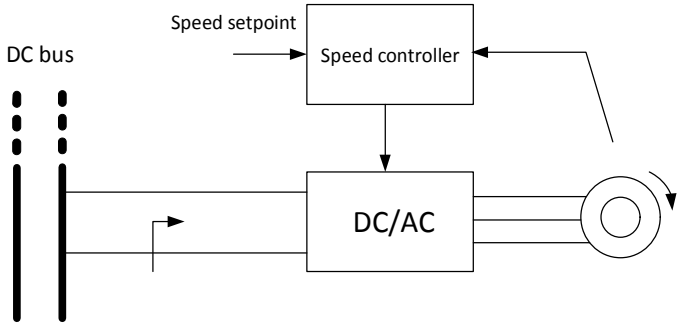


Figure 3-13 Constant power characteristic of motor drives with [100]

Figure 3-14 shows the V-I characteristic of a tightly controlled motor drive system with constant power characteristic. As it can be seen, the slope of the tangent line at the operating point is negative, hence representing negative equivalent small-signal resistance (negative incremental resistance) [96].

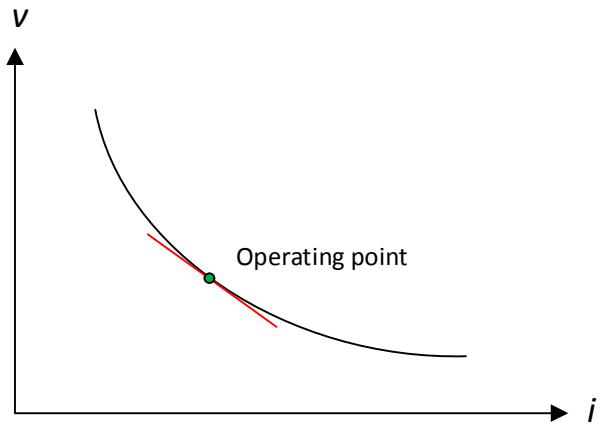


Figure 3-14 Negative impedance characteristic of a CPL

The negative incremental impedance characteristics of the CPLs can lead to interaction problem among subsystems, and deterioration of system stability and power quality. The candidate control system should be scrutinized to guarantee stable operation of the EPS within a wide range [96].

The control and stability studies of this architecture has mainly focused on power offtake from generators on both HP and LP shaft [90-92, 96]. While, the control system can provide the great potential of power transfer between the shafts which is the main focus of this thesis. Power transfer as one of the targets of the MEE [14] is discussed in the next Section.

3.3 Power transfer methods

The idea of power transfer has always been highly desirable for the engine designers [18, 41, 69, 72, 101-103] due to reasons some of which mentioned in the previous Section. Various transmission means including; hydraulic, pneumatic and electrical systems have been suggested in the literature which are discussed in the next Section.

3.3.1 *Power transfer through hydraulic transmission system*

A hydraulic transmission system is suggested in [18], to transfer power between the shafts of a three-spool engine. The system is composed of flow displacement machines operable as pumps or motors connected to each shaft with fluid supply communication

to define a hydrostatic transmission system. The starter, either pneumatic or electric, is connected to the HP shaft in this configuration.

With reference to Figure 3-15, the transmission comprises of three hydraulic flow displacement machines 62, 64 and 66, each one is drivingly connected to an engine spool, through the gearboxes 42, 76 and 78. All three machines are arranged in fluid supply communication to define a hydrostatic transmission system. The machines are of the type which may be operated in a positive displacement mode as a pump, converting mechanical work input into pressurized hydraulic output, and in a negative reverse mode as a motor, converting pressurized hydraulic input into mechanical work output. These machines are commonly found in hydrostatic transmission systems [18].

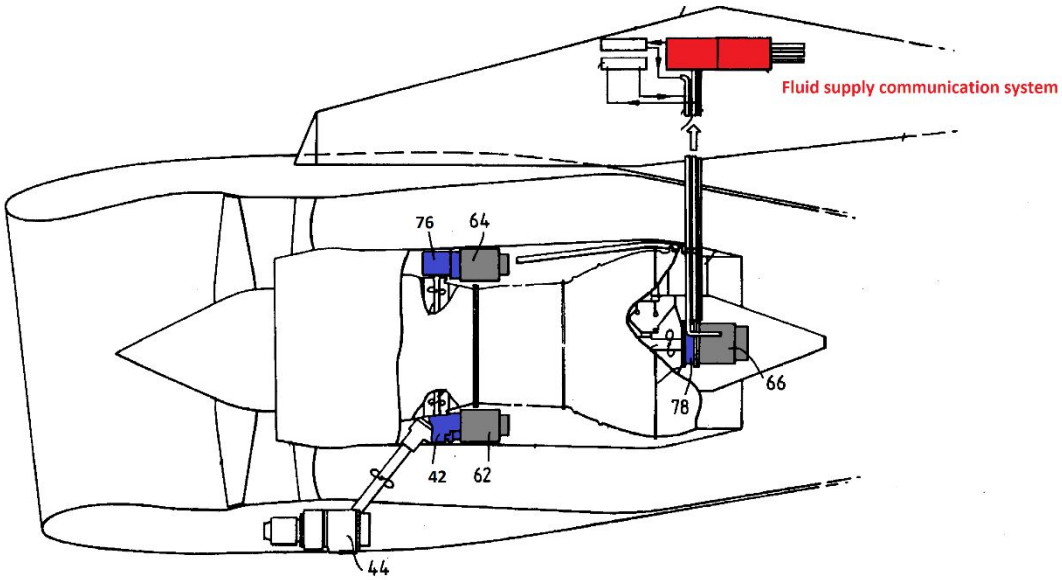


Figure 3-15 Schematic of power transfer by hydraulic flow displacement machines [18]

Hydraulic transmission systems offer high specific power, i.e. transmitted power per unit of the total weight of elements. It is also relatively simple to control and protect the system in a wide range with a fast response due to a low moment of inertia.

However, the main drawback of the hydraulic drive is relatively low efficiency and high energy losses during transmission of fluid over long distances. On top of that, the dependence of the system characteristics on operating conditions such as oil temperature and pressure make the hydraulic transmission systems less reliable. For instance, the viscosity of the working fluid depends on the temperature, or low pressure can cause cavitation in the hydraulic system or discharge of dissolved gases from the liquid. Sensitivity to contamination of the working fluid and the increase in fluid leaks due to deterioration of moving parts makes high maintenance culture imperative for

these systems. These reasons seem enough for this method not to be implemented on the engine.

3.3.2 *Power transfer through axial gear differential drive*

In this configuration, a differential gearbox is responsible for the power transfer. A so-called axial gear differential constant speed drive [18] is implemented between the engine shafts, which is similar to the CSDs in performance. A differential drive allows two different speed inputs to be mechanically summed to produce a single-speed output. It is accompanied by the hydrostatic transmission to control the speed similarly to the CSDs. The suggested configuration is arranged in a way that two of mechanical ports of the differential gear are connected to two of the engine shafts, and the third port is connected to the hydrostatic transmission output shaft. The hydrostatic transmission systems provide an infinitely variable drive ratio for the differential gear. These drives are configured in that most of the power passing through them is passed through a differential gear arrangement depending on the speed ratio of the shafts, while a small proportion is used to drive an internal variable speed hydrostatic transmission system for the speed-torque control purpose.

The transmission comprises the axial gear differential constant speed drive 172 together with shafts 174 and 176, which connect the axial gear differential 172 to gearboxes 162 and 170, respectively as shown in Figure 3-16.

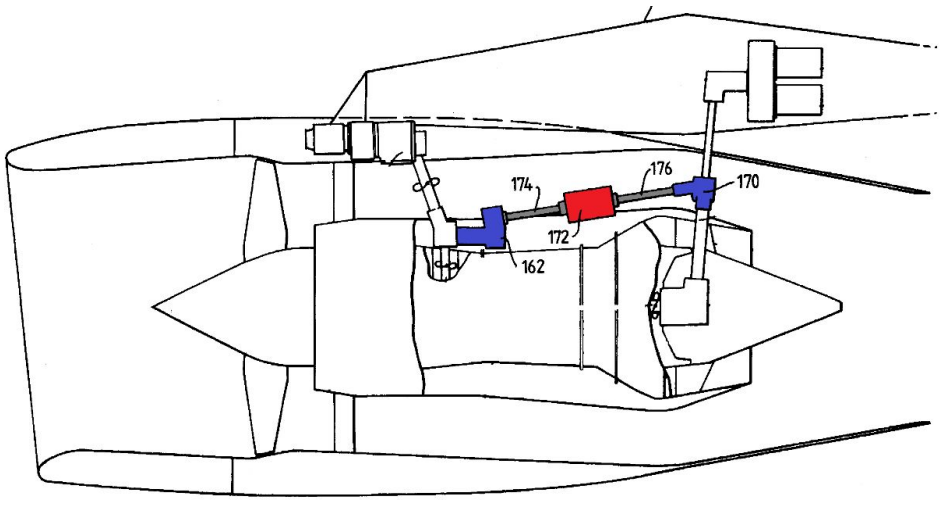


Figure 3-16 Schematic of power transfer by axial gear differential constant speed drive [18]

The LP shaft speed variation over a wide range increases the complexity of the transmission system. On top of that, as discussed in the previous Section; gearboxes

are heavy, prone to wear, and the inefficient hydrostatic transmission machines make the system more challenging.

3.3.3 *Power transfer through a clutch assembly*

In this configuration, clutch assemblies are provided so that the drive between the engine spools can be selectively engaged and disengaged. As shown in Figure 3-17, a clutch assembly is provided in a drive shaft so that the HP and IP spool may be selectively engaged and disengaged. Likewise, a second clutch assembly is provided in drive shaft so that the HP and LP spools may be selectively engaged and disengaged. For a three-spool engine, engagement of the HP and IP shafts and disengagement of the LP and HP shafts may improve the engine ground start and part load performances, while engagement of the LP and HP shafts and disengagement of the HP and IP shafts may improve the engine relight performance after a flameout. In addition to this, because of the engagement of the clutch assemblies, the PO through accessory gearbox can be split between the engine shafts, depending on the power transfer direction between the shafts.

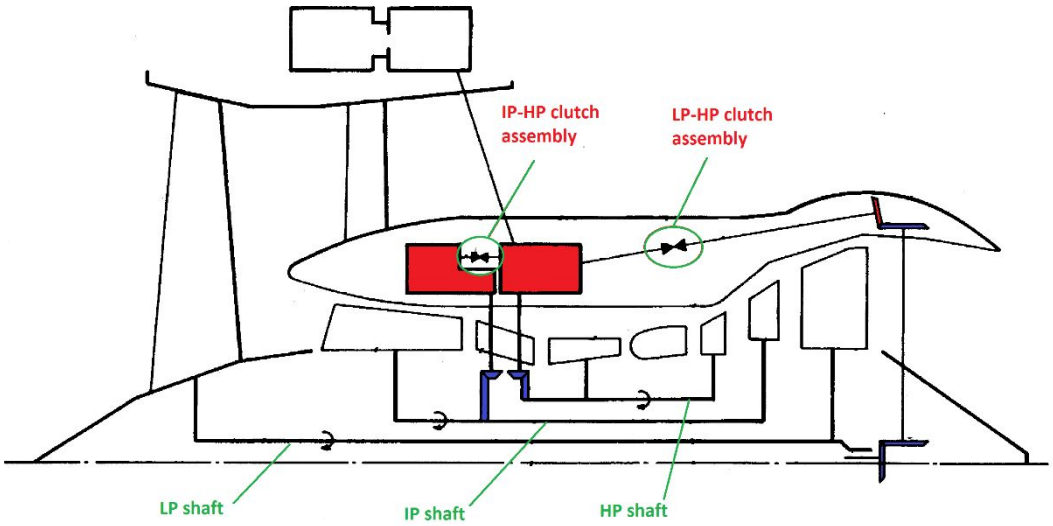


Figure 3-17 Schematic representation of power transfer by clutch assemblies [18]

In a similar fashion, the suggested system in [72] which is, shown in Figure 3-18, includes a hydrostatic power transfer system that includes a hydraulic pump 154 and a hydraulic motor 156 coupled to the LP and HP turbines, respectively. The systems additionally include a mechanical and electrical load shifting/loading sharing system that use clutches 166-1 and 166-2, and gear assemblies 160 to share and/or shift load between the turbines.

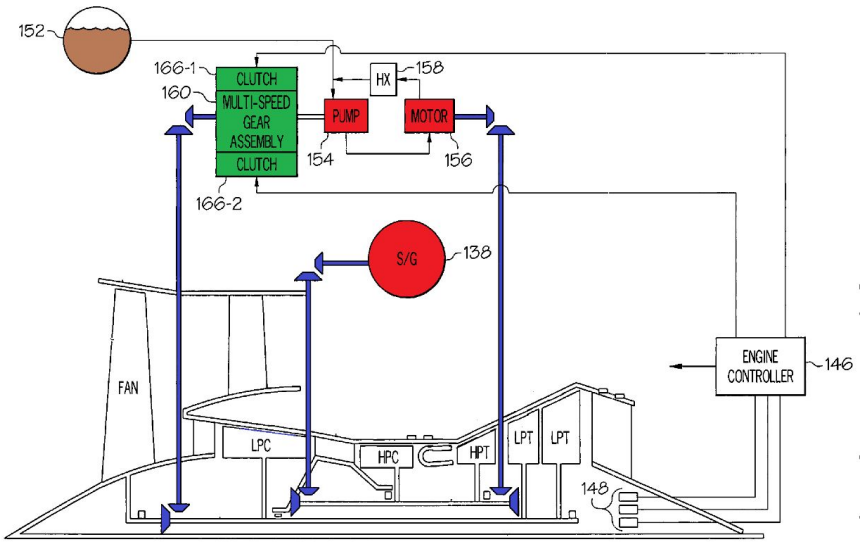


Figure 3-18 Schematic of hydrostatic power transfer system [72]

However, mechanical engagement of the clutch assembly couples the engine shafts, which adds certain performance constraints and complexity so that the whole engine design in terms of components' matching is affected. The other issue with this configuration is that the direction and amount of power transfer cannot be controlled and can vary depending on the engine operation point. Clutches are also prone to excessive wear which decreases its reliability and increases its maintenance costs.

3.3.4 *Power transfer through an auxiliary air turbine*

An auxiliary air turbine can assist power transfer between the shafts; by exchanging high-pressure air between compressors on different shafts or the compressor and the fan duct. The transmission system, shown in Figure 3-19, comprises an auxiliary air turbine 230 drivingly connected to the engine accessory gearbox 44. The auxiliary turbine includes an inlet which receives flow from the downstream end of the IPC through the ducting 234. A bleed flow control valve 238 is positioned so that the compressor discharge air may be bled selectively from the engine to drive the turbine. Accordingly, the transmission system enables power to be selectively transferred from the IP to HP spool by selective operation of the valve.

The bleed flow is normally dumped to the bypass flow, which decreases the cycle efficiency. This configuration enables the utilization of bleed flow at a low-speed operation to increase the speed and flow capacity of the HPC and thereby improve engine performance.

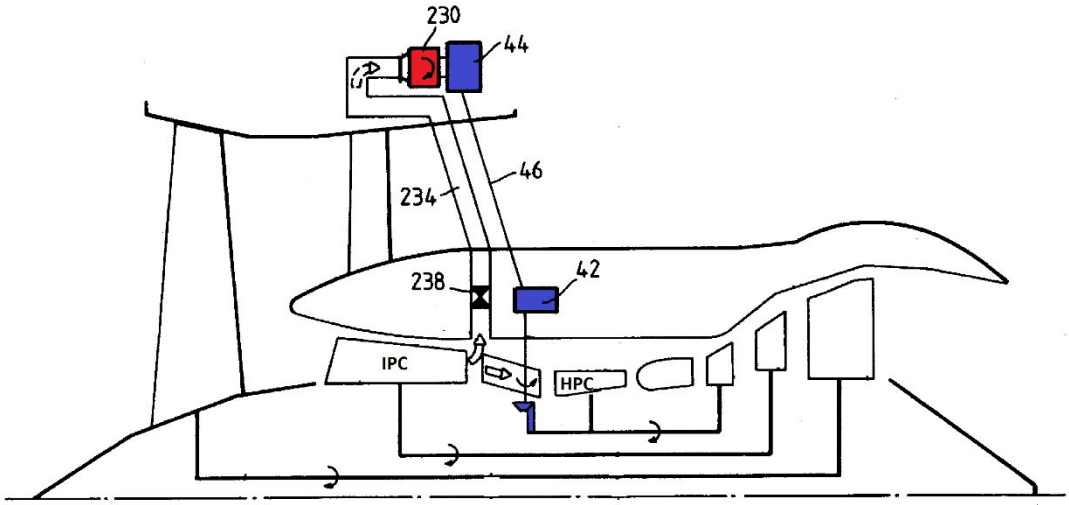


Figure 3-19 Schematic representation of power transfer by an auxiliary air turbine [18]

This configuration has been suggested for power circulation between the IPC and HPC. Power extraction from the IPC bleed air is expected to increase the efficiency, while if the air is bled from the HPC for this purpose, not only can it decrease the engine efficiency, but it can also disturb the matching between the compressors, causing compressor instabilities.

Moreover, the pressure and mass flow of the LPC bleed is not that high to provide a significant amount of power. Due to low air pressure, the power to weight ratio of the air turbine will be low, which makes this configuration not an ideal design for power transfer.

3.3.5 *Power transfer through electric heater*

To transfer power between the shafts, an apparatus is offered in [103], comprising of electrical generators rotationally connected to engine shafts and electrical heaters adapted to heat gases in the gas path. The heaters are electrically connected to the generators while also being controlled to add a specific amount of heat to the gas path. The heaters can be mounted before the turbine path, to increase the inlet temperature to the turbines, to extract more power from the associate turbine. They can also be mounted after the turbines, to increase exhaust gas temperatures to boost the engine thrust similar to an afterburner.

As it is illustrated in Figure 3-20, the electrical generators 32 and 30 are coaxially mounted on the LP and HP shafts 26 and 28, respectively and are electrically connected to one or more electrical heaters 34 and 36, located around the core gas path and the bypass gas path, such that heat developed by the heaters is transferred to the gas in the

gas path. The heaters 34 and 36 are preferably resistive heaters, which are provided to surround the annular gas path.

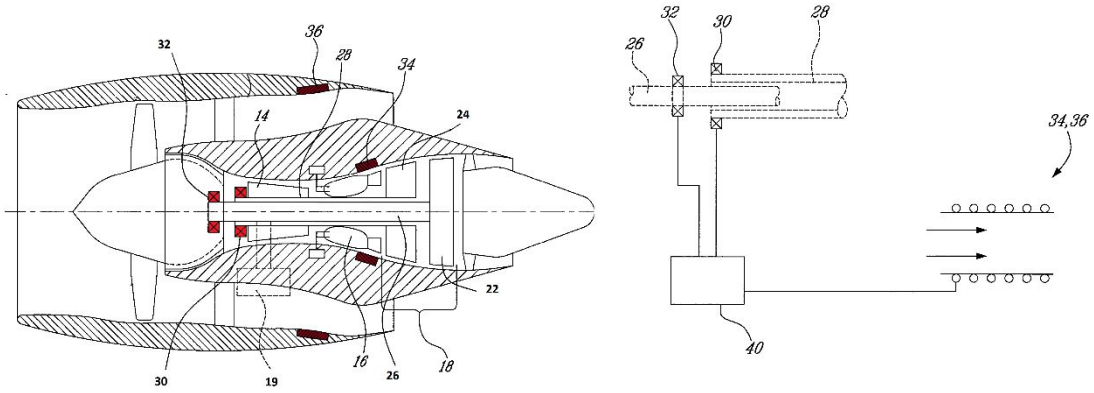


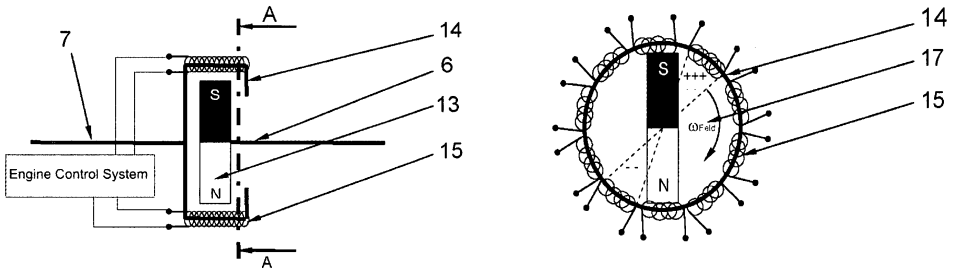
Figure 3-20 Schematic representation of power transfer by electric heaters [103]

The efficiency of this configuration is also under question since it is changing pure kinetic energy to potential energy which should be converted to kinetic energy at low efficiency on the turbine blades. One of the main concerns about this configuration is also the design of heaters, to evenly distribute the heat in the gas flow. It seems the only possible solution is to distribute the resistive loads in the gas path section which causes pressure drop for the hot gas flow. Other than that, even if the heaters are distributed on the casing; they will affect the gas path clearances, which is also undesirable.

3.3.6 *Power transfer through electromagnetic clutch*

Gearless power transmission in a broad speed range can be implemented by applying the electromagnetic gear system concept. The clutch element on one of the shafts is a coil ring with several individually, annularly arranged coil sections, engaged by a magnet provided on the other shaft. The coils are sequentially activated by a power electronic system, at a specific frequency to create a frequency-controllable rotary field. Power can be transmitted between shafts, in a controllable manner, irrespective of the shaft speeds, with the rotary field [104].

As illustrated in Figure 3-21, the LP shaft gear train 7 is connected to the HP shaft gear train 6 via an electromagnetic clutch 10 for non-contact torque transmission. The electromagnetic clutch comprises a magnet 13 on the side of the HP shaft and a coil ring 14, with a multitude of coil sections 15 on the side of the LP shaft. Activation of the coil sections 15, or the frequency of the rotary field 17 generated by coil sections, is controlled via the power electronic system [104].



A-A section view

Figure 3-21 Schematic representation of power transfer by electromagnetic clutch [104]

These coils are on the rotating shaft, which imposes the implementation of brushes to be connected to the supply from power electronics outputs. To transfer a high amount of torques, the coils current should be high enough. Brushes are prone to wear and need regular maintenance. Therefore, this system is not of high reliability.

3.3.7 *Power transfer through electrical machines*

As it is shown in Figure 3-22, the transmission system comprises of an electrical machine 202 drivingly connected to the engine's accessory gearbox 44, an electrical machine 204 drivingly connected to the gearbox 182 and an electrical machine 206 drivingly connected to the engine's LP spool via gearing 208. The electrical machines 202, 204 and 206 together with their mechanical drive can be replaced with electrical machines 222, 224 and 226, respectively, directly mounted on the corresponding shaft as shown in Figure 3-23.

The machines may be adapted to operate as a generator or motor. They are electrically connected to a control unit 210 via separate lines 212, 214 and 216. Initially offered in [18], the control unit 210 comprises switchgears, adapted to isolate each of the machines 202, 204 and 206 from the transmission. In this configuration, by operating one machine as a generator and another machine as a motor, power can be selectively transferred between the engine shafts.

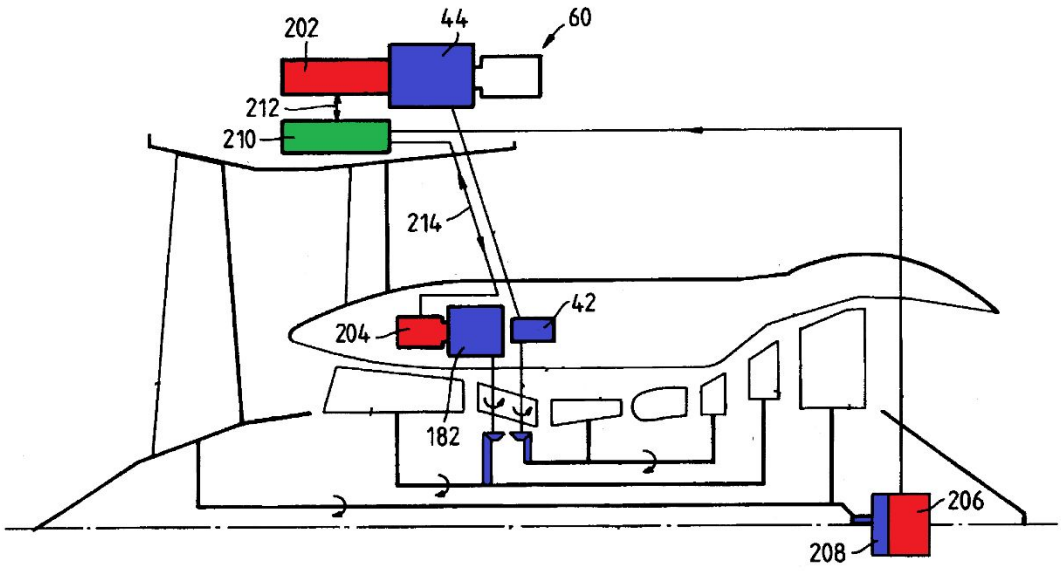


Figure 3-22 Schematic power transfer by drivingly connected electrical machines [18]

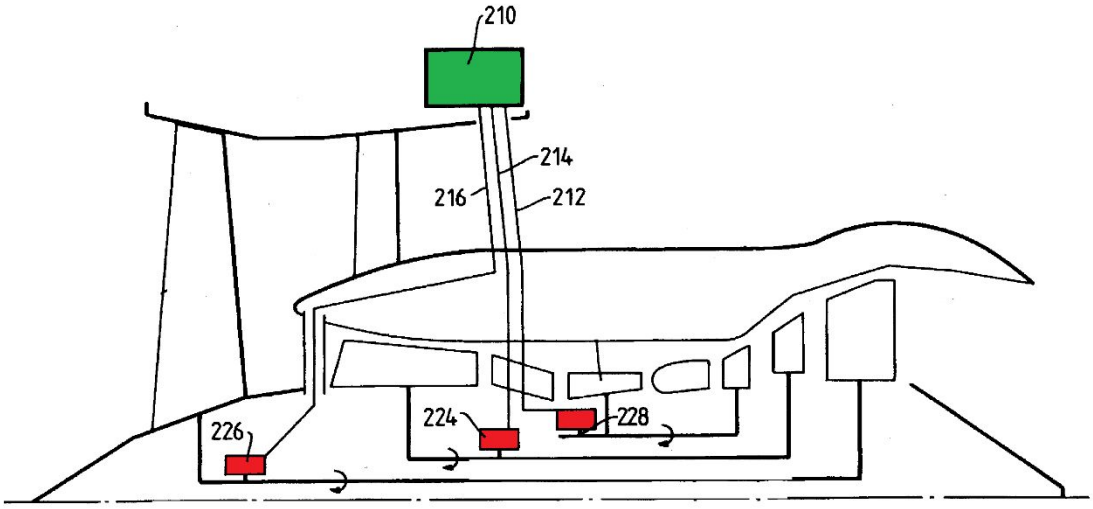


Figure 3-23 Schematic power transfer by embedded electrical machines [18]

With the boost in power electronics technology along with the MEA trend, various topologies have been suggested for multi-spool power generation with electrical machines on various shafts. This enables power transfer between engine shafts similar to the configuration shown in Figure 3-23. Circulation of the desired amount of power between engine spools, independent of their speeds can be easily handled by using PECs within a common high-voltage DC bus configuration, discussed in Section 3.2.4.

3.4 Electrical Power transfer method: potential improvements into engine design and performance

Among different methods of power transfer discussed in the previous Section, electrical power transfer through electrical machines on each shaft provides the highest flexibility, reliability, controllability and efficiency, mainly due to the use of electrical systems instead of hydraulic and pneumatic ones. The principal added feature of this configuration to the MEE is decoupling of shaft speeds to some degree, depending on the amount of transferred power to shaft powers. This provides the potential to not only improve the performance of the baseline engine design but also contribute to the design of future engines. In this aspect, power transfer between engine shafts is expected to:

- contribute into new design of the engine;

More power can be drawn from the HPT than the LPT in the EPT adopted design (EPTAD) if the turbine section of the engine is re-designed. Power transfer from the LP to HP shaft can further improve the efficiency and compressor stability during cruise condition, while power transfer from the HP to LP shaft during MTO is required to keep the engine within its operational limits. This is one of the main contributions of this Thesis, elaborated in Section 5.3.

The HP shaft would be constantly braked by the HP shaft alternator which, in other terms, means keeping the HP speed higher than its baseline value. An oversized HP turbine could mean a faster acceleration of the HP shaft, which of course precedes the acceleration of the LP shaft. It also means that the HP turbine can be optimized for a smaller speed range.

- optimize compressors' performance to have higher efficiency with adequate surge margin;

The engine efficiency correlates with the core compression ratio. However, normally the surge margin limits the maximum available pressure ratio of the engine. Due to the thermodynamic coupling for the broad range of operation, designers consider excessive surge margin at design condition to meet the requirements of off-design condition. This is fuel inefficient and creates incompatible thrust with the flight mission. Power transfer can decouple shaft speeds and manipulate the engine operating points to a more desirable condition [69].

- manage the thrust to make it compatible with the flight mission;

Power transfer between the fan shaft and the core shaft can help increase thrust during take-off and decrease it during descent and taxing. Thrust management can decrease excessive application of brakes during taxing and is desirable for various flight scenarios such as continuous descent.

- remove Variable Stator Vanes (VSVs) and Variable Bleed Valves (VBVs);

Variable-geometry systems including VBVs or VSVs for the compressors are used at low-speed settings to control the core airflow and to avoid instability of the compressors [42, 101]. The main drawback of bleeding is its negative impact on the engine cycle efficiency, in addition to their complexity, cost and considerable weight. The bearings and other movable components of them are also prone to wear. Thus, an alternative to variable-geometry methods is highly desirable. Power transfer can potentially control compressors' working points during low speed and transient operation by re-scheduling the compressor speeds. This can result in the removal of some or all of the handling bleed valves and/or variable guide vanes, making the engine lighter and less costly [101].

- enable power extraction from windmilling engines;

During a windmilling event, the LP generator can extract power from the fan. Being exposed to the incident airflow during descent makes the fan a wind turbine in itself. Having a substantially larger diameter than the HP spool, the fan mounted on the LP shaft is an ideal candidate to extract a substantial amount of power from the air rushing through the fan blades [69]. HP compressor is less conducive to rotate sufficiently for a windmill start [69]. The extracted power from the fan shaft can be fed to the HP shaft for the engine to restart [61]. It can also be useful as emergency power for aircraft's critical systems such as flight control. This will make the Ram Air Turbine (RAT) unnecessary for emergency power generation [105].

Windmilling can also happen when aircraft are parked in windy areas with their gas turbine engines shut down. Windmilling is generally undesirable for an engine which is not in operation, because of the rotation speeds that could excite the natural frequencies of the shaft, causing vibration issues. Moreover, potentially long periods of rotation of the rotor without lubricating oil can damage the bearings [106].

- improve engine starting and relighting;

During periods of extinguished engine operation, the additional load imposed by the accessories on the HP shaft reduces the free rotational speed of the HP spool, thereby

the airflow through the core engine [18]. This can be troublesome for the MEA with high PO values; while by transferring power to the HP shaft and help rapid engine acceleration or relight this drawback can change to an advantage.

Engines are started through rotation of the HPC to up to 10% of its speed, where the optimal fuel to air ratio can be achieved for combustion, and the shaft speed becomes self-sustained with combustion [50]. Once the HP shaft is self-sustained, it does not need any power from the HP electrical motor. At this point, the products of combustion over the LPT blades, rotate the LP shaft to drive the LPC and the FAN. After a specific amount of HP speed, the engine is not allowed to go for higher speeds unless the LP shaft reaches some levels of speed. However, due to high inertia of the LP shaft, this may take some time which delays the start-up process or even sometimes fails it. In this case, power can be transferred to the LP shaft, to help speed it up, thus having a faster and more reliable engine start-up. For a three-spool engine, start-up power distribution between the IPC and HPC can contribute to a more efficient and faster engine starting as well.

- help faster acceleration and deceleration of the engine;

The acceleration rate is critical for flight scenarios such as go-around or touch-and-go. The main constraints for engine acceleration and deceleration rates are; over-temperature, over-speed and low surge margins. Power transfer between engine shafts is expected to handle engine limits for faster manoeuvres. Unlike conventional engine controllers, which typically rely on the control of fuel rate of the engine, power transfer can result in a more immediate adjustment of the gas turbine compressor speed, which adjusts the airflow and pressure through the gas generator.

- help the engine core to withstand severe transients;

The gas turbine engine must be designed to withstand transient speed and temperature conditions, these are encountered when sudden changes occur to the load on the generator, fan, or propeller. For instance, multi-spool engines are suffering from over-speed after load rejection, which is mainly due to the excessive core airflow and low HP shaft inertia [107]. With power transfer between the shafts, the compressor speed and airflow can be quickly adjusted to avoid exceeding the engine limits. This can reduce the severity and duration of the transient conditions, resulting in decreased operation and reliability problems [108].

- help the engine to overcome surge incidence;

Once the surge phenomenon happen, the shaft speeds experience severe changes within a short period. Through power transfer, the shaft speed changes can be handled to manage the airflow of the HPC, to overcome the surge phenomena. The quick response of the electrical machines is faster than variations of the shaft speeds and airflow during surge. In this case, EPT can be utilized to overcome the surge incidence.

- manage engine start-up and performance at very high or low ambient temperatures;

Engines are normally designed to operate safely within a wide range of climates (weather and altitude of the flights). Normally, deviations from this condition affects the performance for which precautions are considered. These limits affect engine efficiency and available thrust. For instance, during a hot day or at high altitudes, the available thrust is decreased noticeably, up to a point that sometimes the flight is cancelled due to short runway. Very low temperature also affects the compressors' operating line by shifting them closer to the surge line [101]. With power transfer, there is a possibility to increase the available thrust without exceeding the engine limits.

- manage high PO amount from the MEE;

Power transfer allows controlling of power flows within the engine; between the engine and the airframe. With the possibility of EPT, new architectures can be introduced to manipulate power offtake between the engine shafts. The redundancy of power offtake is higher within these architectures, where multiple power sources with multiple paths are connected to the common DC bus.

- decrease the technical requirement on the HP spool alternator;

If the HP shaft speed range becomes narrower by EPT, the design of HP section of the engine including the HPC, HPT and HP generator can be optimized. This may increase LP speed variation slightly. However, the LP shaft speed changes over a wide range, which does not lead to any significant further improvements nor degradations of LP component efficiencies.

- collaborate with the future hybrid propulsion concepts;

Energy storage systems and other external power sources such as APU can be closely incorporated into the power transfer concept [109]. In the future hybrid propulsion systems, power can be fed to the LP shaft, to rotate the fan as well. It's the same case when one of the engines fails.

3.5 Summary

This Chapter provides an overview of the prior to state-of-the-art PO configurations. Overall, this Chapter reviews the items below:

a) the impact of PO from engine shafts
b) the development of power generation architectures
c) the single dc bus architecture and opportunity of electric power transfer between the engine shafts
d) suggested methods for power transfer including hydraulic, pneumatic and gear transmission systems
e) and expected opportunities provided by the EPT system for improvement of baseline engine performance and contribution into future designs.

In this regard, the key target of this Thesis is to investigate the impact of power transfer on engine performance and propose new conceptual designs. The oppurtinites which can be analysied include the thermodynamic aspects of the engine performance such as fuel consumption reduction and surge margin increase by the EPT. For this purpose, a specialized 0-D transient and steady-state analysis model with adequate degree of accuracy and flexibility is developed in the next Chapter. The model includes modeling for the aerothermodynamics and inertia of the turbomachine and a full control system that enables optimization of the engine performance given electrical inputs.

Chapter 4 Development of Engine Model Suitable for EPT Concept Studies

To study the effect of the proposed power exchange method on engine performance, an aircraft engine model with an adequate degree of accuracy is required. The developed model should include detailed shaft speed modules to be able to interact with the model of the electrical machines. Moreover, it should contain the nonlinear thermodynamic behaviour of a multi-spool engine. This enables the study of power transfer impact on engine performance in terms of fuel consumption and stability margins. The developed engine model should also present adequate engine dynamics; real-time simulation is to be used in the development of the engine emulator.

In this Chapter, the existing approaches in engine modelling are elaborated, to find the appropriate method for this study. Considering the engine dynamics required for the purpose of this study, together with the targeted application of the model for the engine emulator, the Inter Component Volume (ICV) approach is selected in MATLAB/Simulink® software environment. The ICV method provides modularity in order to customise the model for performance simulation of various engines.

To make the foundation for the model, the ICV method is introduced, various engine parts are briefly overviewed and their sub-models are presented. Afterwards, the implementation of the engine model in MATLAB/Simulink® is discussed. The proposed 0-dimensional model is then validated with real engine data and the model performance is assessed. This model appears to perform well, providing a case study for other researchers who may want to replicate such an analysis based upon the cited works.

Normal operation of the engine from idle setting to full throttle can be investigated by the developed engine model. The model also includes the VBVs, however, sub-idle performance can not be investigated in the developed model.

4.1 Existing engine modelling methods

Nowadays, Research and Development (R&D) sectors of all engine manufacturers consider engine modelling as an essential tool when it comes to minimization of costs in their quest towards optimizing an engine performance. The existence of accurate simulations alongside real field testing is necessary at different stages of design and development of an engine. Before bringing a new idea into reality, models have substantial advantages in comparison to real, full-scale prototypes. The accuracy of a model is normally accompanied with its complexity which is a drawback for simulation speed. Nevertheless, the application determines the degree of accuracy and complexity of the model. For each application, there are vital dynamics which cannot be ignored and they are bases of the model.

The dynamics of single shaft gas turbines have been modelled as a linear system in [110-112]. Similarly, a parameterized model based on the single-shaft Rowen model [112] has been developed in [113, 114] for a twin-shaft gas turbine, which is shown in Figure 4-1. This type of engine configuration is normally used for twin-shaft microturbines, wherein a Gas-Generator (GG), consisting of a compressor, combustion chamber and turbine, set on one shaft, provides the hot exhaust to drive a Free Turbine (FT), which can be coupled with a generator or a propeller as loads.

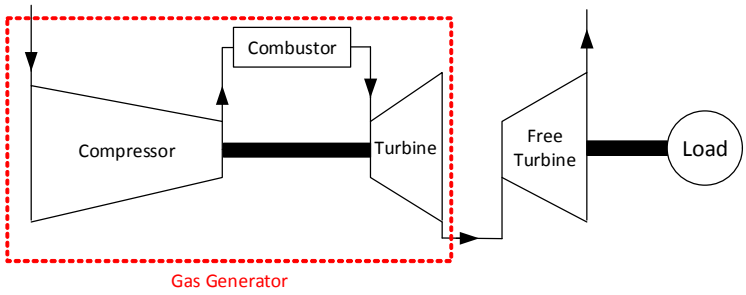


Figure 4-1 Twin shaft engine with gas-generator and free turbine

Figure 4-2 illustrates the block diagram of the model including three control loops: the FT speed control (i.e. speed governor), the acceleration control and the GG speed control. The model is composed of first-order transfer functions, accounting for delays of the fuel system, combustor and a torque function of the FT [113].

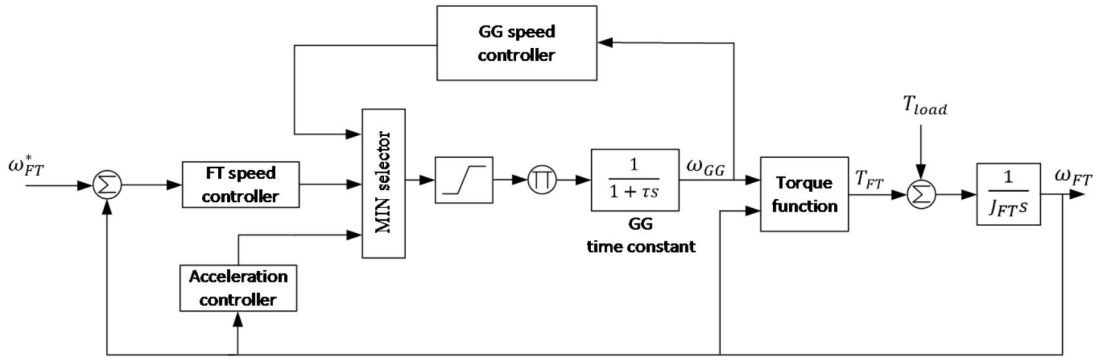


Figure 4-2 Block diagram of the twin-shaft gas turbine engine model [114]

However, the nonlinear model is required for multiple spool turbofans due to the nonlinear behaviour of the thermodynamic coupling between compressor-turbine sets. Depending on the application of the model, it can be 0-dimensional (0-D), one-dimensional (1D), two-dimensional (2D) or three-dimensional (3D).

The 0-D model includes modules of engine elements as a "blackbox" without adding any physical dimensional parameter. These modules present the thermodynamic behaviour of the component. Also, inertia modules stand for the engine shafts' dynamics. It is generally accepted that a 0-D simulation is sufficient for dynamic performance modelling and controller design which include shaft speed and gas path related effects [31, 115-119]. Added transient features such as heat soakage and tip clearance control can make this model applicable for transient gas-path-related studies. There are several commercial software as 0-D performance models for multi-spool engines such as GasTurb [120], GSP [121] and T-MATS [122] developed by Netherland's National Aerospace Laboratory (NLR), GasTurb GmbH and NASA respectively. These models are, however, compiled codes without access to their details. In this case for any new option in the model, their developers should be asked to customize their software for the desired study. Furthermore, the model is a "black box" where all the engine parameters are not accessible. This highlights the need to develop a generic model.

For this purpose, the iterative approach is proposed in [119, 123, 124], which is commonly used by the stated commercial software. In an iterative approach, the number of state variables is equal to the number of shaft inertias which leads to a quasi-steady state simulation. Using this approach, all other performance data are calculated through thermodynamic laws as well as an iterative solver to reduce the flow continuity errors between components. The main drawback of this approach is that iteration adds a significant amount of noise due to the fluctuation of the variables, which is limited

by the solver tolerance band. In this case, virtual filters with adequate lag should be considered on the desired variables for transient studies. Engine stability issues cannot be analysed due to the perturbations produced unless the virtual filters are implemented [31, 125].

For the transient operation, the mass flow entering a component is not equal to that leaving it, where the density of the flow is changing with time. This phenomenon has a second-order effect during transient manoeuvres especially for large volumes such as the combustion chamber and the fan duct. The approach is called "aero-thermodynamic model" [126], also known as Inter Component Volume (ICV) [115] method that proposes to add storage volumes between executive components to account for real physical gas storage volumes of the components in an engine. The crucial parameter for this approach is the size of volumes between components which limits the permissible time step of the solver. The ICV approach has been selected for this study in order to avoid fluctuations when designing the engine emulator (in Chapter 6). Moreover, ICV method is quite simpler and faster for transient simulation [116], on top of that provides real-time simulation opportunity.

4.2 Introduction to ICV method

In the ICV method, components are treated as volume-less lumped blocks together with storage volumes (control volumes) between every two executive components (see Figure 4-3). The operating point of the components is dictated by the state variables obtained from the surrounding control volumes. The flow properties of the components are also fed to the derived first-order differential equations within the control volume, accounting for the imbalance of the state variable over time. Therefore in the ICV method, there are several closed loops [126].

The proposed 0-D model constitutes component (compressors and turbines), control volume, inertia and combustor modules. It is essential to maintain mass, momentum, and energy conservation between these modules. Within each component module, the inputs are inlet pressure; P_{in}, backpressure; P_{out}, inlet temperature; T_{in} and shaft speed; N (see Figure 4-3). This data is then used to find the performance point of each respective component. Components including fan, compressors and turbines are represented by maps in which corrected mass flow and adiabatic efficiency, are indexed by corrected shaft speed and pressure ratio (see Figure 4-4). Outlet

temperature and power can be obtained by having inlet mass flow, efficiency, and implementing thermodynamic laws for open systems, including conservation of mass and energy. This is discussed in detail in Section 4.5.

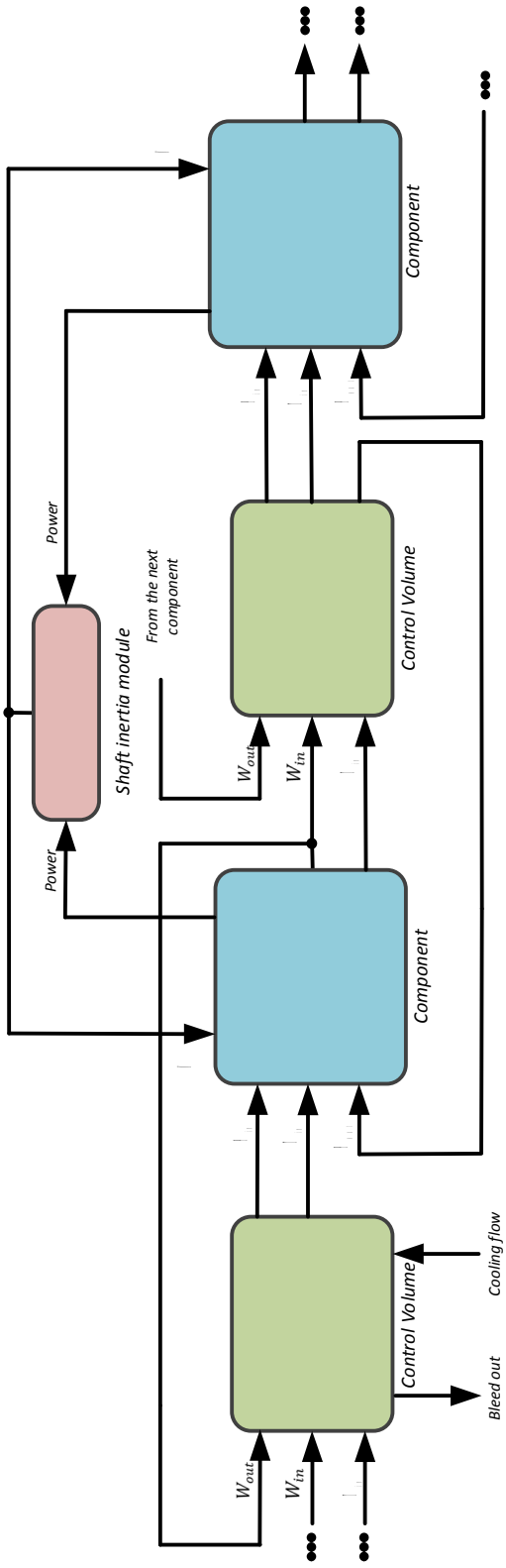


Figure 4-3 Structure of ICV modules

In the Control Volume (CV) module shown in Figure 4-3, a volume is assumed to be an open thermodynamic system in which thermodynamic laws are applied to calculate state variables. The state variables for the control volumes are pressures between executive components. No work is done on the fluid in the CV modules, due to fixed boundaries of the open system of the CV modules. Heat transfer is also assumed to be zero in the model. In this case, the change in internal energy (ΔU) of the flow is zero through the CV modules as below:

$$\Delta U = Q - W = 0 \tag{4-1}$$

where Q is the heat applied to the system and W is the work done by the system. Outlet pressure of the control volumes are assumed to be state values when applying CV analysis. The change in mass inside the CV is calculated using:

$$\frac{dm_{CV}}{dt} = \dot{m}_{in} - \dot{m}_{out} \tag{4-2}$$

where m_{CV} is the mass of the CV and $\dot{m}_{in}$ and $\dot{m}_{out}$ are inlet and outlet mass flows. Pressure, temperature and volume of the mass inside the CV are related by using the ideal gas law as below:

$$pV = m_{CV}RT \tag{4-3}$$

where p and V are pressure and volume of the CV and R is the specific gas constant. Pressures and temperatures are total amounts including the kinetic energy of the gas. By using (1) and (2), assuming no temperature gradient in the control volume [116, 126] the outlet pressure can be determined as:

$$\frac{dp}{dt} = \frac{\dot{m}_{in} - \dot{m}_{out}}{V/_{RT}} \tag{4-4}$$

Equation (4-4) accounts for the dynamic due to the flow through the volumes between engine components.

In reality, components have their own physical gas storage volumes that cause a lag in flow transfer within them. The volume over the temperature (V/T) for each control volume determines the magnitude of the time constant between components which directly affects the stability of simulation. To investigate the engine dynamics accurately, the solver time step should be at least 10 times less than the smallest time constant within the model [125].

The imbalanced torque between components of each shaft leads to acceleration or deceleration, which after integrating over time yields the shaft speeds. The shaft inertia modules use Newton's second law for this purpose, which is explained later in this Chapter. The control volume module's structure is the same for all storage volumes between components.

4.3 Component maps

The nonlinear behaviour of the compressors and turbines can be modelled with the help of Computational Fluid Dynamics (CFD) in a 2D or 3D simulation. It can also be modelled on the mean line of the blade rows in a 1D simulation, by implementing turbomachinery and thermodynamic rules [127]. However, these models are not only very complex and time-consuming, but also the blade data is a confidential asset of the manufacturer, which is not accessible. Luckily, turbomachinery components within their family; either axial compressors, radial compressors, turbines or pumps follow the same trend as a lumped system for their off-design performance. Once the geometry of these machines is fixed at design condition, their "map" for the off-design performance is generated through detailed component modelling and tests. Maps, which represent the significant correlation of the compressors and turbines [31, 128, 129], are the most critical requirement of the 0-D modelling [130].

It is important to make the component maps independent of the inlet condition for a fixed geometry. A wide range of inlet condition is experienced by the engine components due to the altitude or front component delivering the inlet flow at different condition. The effect of inlet temperature and pressure variations are employed by correction factors, $(\sqrt{\theta}/\delta)$ and $(1/\sqrt{\theta})$ for the inlet massflow and machine speed respectively. θ and δ are non-dimensional values, calculated by the ratio of the inlet temperature and pressure over their values at ISA Sea Level Static (SLS) (e.g. $101.325\ kPa$, $288.15\ °K$) as below:

$$\theta = \frac{T_{t\ inlet}}{288.15} \tag{4-5}$$

$$\delta = \frac{P_{t\ inlet}}{101.325} \tag{4-6}$$

The corrected flow and speed and flow are then:

$$W_c = W_{inlet}\sqrt{\theta}/\delta \tag{4-7}$$

$$N_c = N/\sqrt{\theta} \tag{4-8}$$

Relative corrected speed is then defined as:

$$N_{c,rel} = \frac{\frac{N}{\sqrt{T_{in}}}}{\left(\frac{N}{\sqrt{T_{in}}}\right)_{design}} \tag{4-9}$$

which is a value between 0 to 100.

The typical form for the maps is to plot the pressure ratio (back-pressure to inlet pressure) against the inlet mass flow for various constant corrected speeds, illustrated in Figure 4-4. Constant efficiency contours, also known as efficiency islands, are plotted on the same map. Maps are plotted only for the stable region of their operation below the border between stable and unstable operation, known as surge line. Normally, the steady-state operating line is off the surge line, with enough so-called surge margin which is defined as:

$$SM = \frac{PR_{surge} - PR_{operating}}{PR_{operating}} \tag{4-10}$$

where PR stands for pressure ratio.

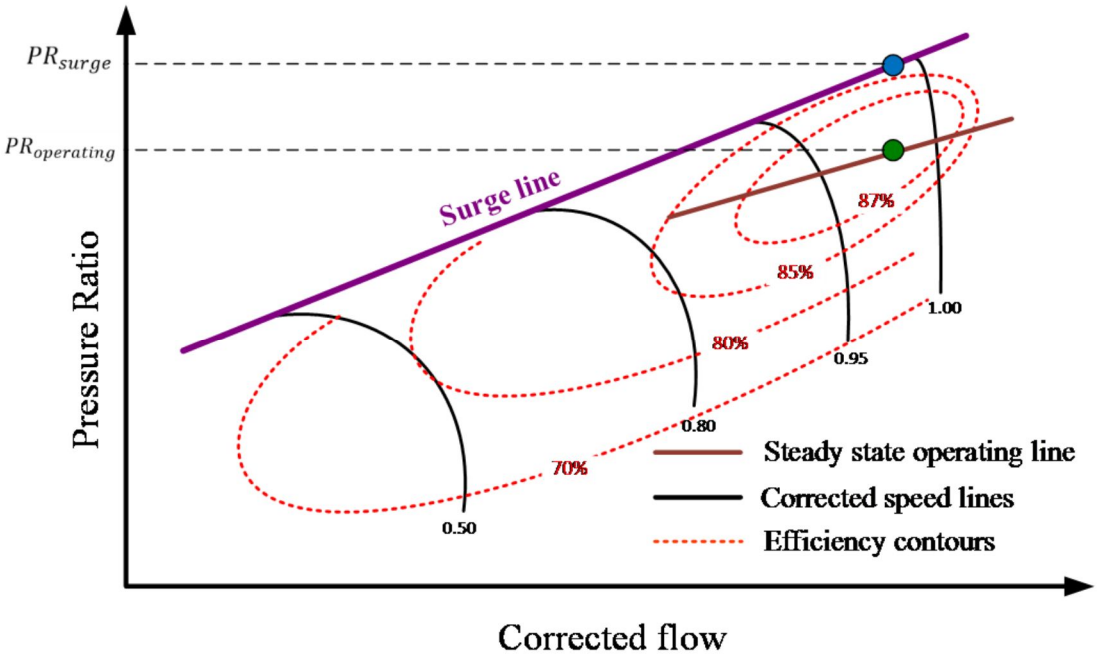


Figure 4-4 Compressor map

It is also a common practice to use total temperature and pressure instead of the static values, to make the data independent of the inlet air velocity, due to aircraft speed. For an aircraft engine, this is done at the inlet to the fan map, where there is a significant

speed of airflow, due to the aircraft speed at around 80% of the sound speed (Mach=0.8). Assuming isentropic conversion of velocity head to pressure head, the total temperature is a function of the static temperature, T_s, and Mach number, Ma, as below [131]:

$$T_t = T_s\left(1 + \frac{\gamma - 1}{2} Ma^2\right) \tag{4-11}$$

where; γ is the ratio of the specific heats. The total pressure is then:

$$P_t = p_s\left(\frac{T_t}{T_s}\right)^{\frac{\gamma-1}{\gamma}} \tag{4-12}$$

where; p_s is the static pressure of the flow [131].

4.4 Engine scaling

The engine model consists of physical rules including thermodynamic, Newton laws, and component maps for the off-design simulation purpose. As mentioned previously, component maps are not readily available since they are confidential documents of the engine manufacturers. Luckily, it is a standard practice to scale an existing map to a new one with a different set of design point parameters for initial design purposes [128]. This provides the opportunity to have the conceptual design of engines with a wide range of thrust, starting from 9,500lbf (42kN) to 12,000lbf (53kN) of thrust class for business jets to 110,000lbf (490kN) for wide-body jets. Due to the lack of component maps for this project, scaling has also been implemented after selecting the target engine to study.

In GE philosophy [132], scale factor is defined as the ratio of the components' diameters. The engine is then scaled based on the principle that its rotational speed should be simultaneously increased or decreased. This produces similar aerodynamical and mechanical behaviour of compressors and turbines and keeps the same levels of temperature, pressure, blade angles, stress, pressure ratio and efficiency. As presented in Table 4-1, linear dimensions vary directly as the scale factor; shaft speed varies as the inverse of that ratio to keep the rotary component's tip speeds constant. The airflow and power vary with the square of the scale factor, and the weight varies with the cube of the scale factor [132].

Table 4-1. GE scaling ratios [132]

Scale factor	0.5	1	2
Pressure Ratio	1	1	1
Efficiency	1	1	1
Shaft Speed	2	1	0.5
Flow Velocities	1	1	1
Mass flow	0.25	1	4
Power	0.25	1	4
Weight	0.125	1	8
Stresses	1	1	1
Tip Speed	1	1	1

4.4.1 *Shaft inertia scaling*

Shaft inertia is the most complex parameter to be scaled. Assuming constant length to diameter ratio, it is proportional to the diameter by power 5 as below:

$$J \propto d^5 \tag{4-13}$$

The maximum centrifugal stress, $\sigma_{r_{max}}$ on the rotor is proportional to the diameter and shaft speed by power 2 as below:

$$\sigma_{r_{max}} \propto d^2\omega^2 \tag{4-14}$$

Centrifugal stress is the main stress in high speed rotary equipment. To keep the centrifugal stress at the same level, equations (4-13) and (4-14) yields to the relation below between the shaft inertia and rotational speed.

$$J \propto \left(\frac{1}{\omega}\right)^5 \tag{4-15}$$

Bearing in mind that the rotary component tip speeds are the same, the inertia can be scaled by the value of mass flow as below:

$$J \propto (W_{air})^{2.5} \tag{4-16}$$

Different variables of the target engine can be used as shown in Table 4-1 to scale the shaft inertia. However, a discrepancy is expected, due to the variety of factors involved in engine design. The value of shaft inertia is not involved in steady state results.

4.4.2 *Map scaling*

In order to avoid significant errors in map scaling, the geometry of target component should be the same as the component with available map, where at least, the type of compressor and the number of its blade rows should be the same. Scaling is normally implemented by gas turbine companies at the preliminary phase of a new machine

design. The most straightforward technique, to derive the map from an existing map is through applying constant factors as below;

$$W_{new} = C_W W_{ex} \tag{4-17}$$

$$PR_{new} = C_{PR}(PR_{ex} - 1) + 1 \tag{4-18}$$

$$eff_{new} = C_{eff} eff_{ex} \tag{4-19}$$

where "ex" and "new" stand for the existing and new map. W, PR, and eff are the massflow, pressure ratio and efficiency of the map correspondingly, and C_W, C_{PR} and C_{eff} are their scaling coefficient respectively.

This results in acceptable accuracy if pressure ratio and efficiency of the component are not largely scaled, i.e. with C_{PR} and C_{eff} around (1 ± 0.2). Otherwise, for substantial scale factors, Kurzke and Riegler in [128] have performed a statistical analysis of many compressor maps that were taken from open literature and from MTU in-house data bank, which then led to a new compressor map scaling procedure. Having considered the hidden correlations and trends in compressor maps, the new scaling procedure is comprised of the following steps:

1- Calculation of characteristics for original and new maps

At first, the average characteristic data including pressure ratio at 50% of design mass flow, $(PR_{rel})_{50\%W}$, and corrected mass flow at 80% of design corrected flow, $\left(W_{c,Range}\right)_{80\%W}$, are extracted from the map. The relative corrected flow and pressure ratio are also defined based on the reference mass flow, $W_{c,ref}$, and reference pressure ratio, Π_{ref} as below:

$$W_{c,rel} = \frac{W_c}{W_{c,ref}} \tag{4-20}$$

$$\Pi_{rel} = \frac{PR - 1}{PR_{ref} - 1} \tag{4-21}$$

Then statistical analysis in [128] shows that, for axial compressors the following correlations are a good compromise:

$$(PR_{rel})_{50\%W} = 0.1961 + 0.8ln(PR_{ref}) \tag{4-22}$$

$$(W_c/N_c)_{50\%W} = 1.1037\, PR_{ref}{}^{-0.2223} \tag{4-23}$$

$$\left(W_{c,Range}\right)_{80\%N} = 0.1751\, e^{-0.1042 PR_{ref}} \tag{4-24}$$

By knowing the design (i.e. reference) pressure ratio and mass flow of the target map, the values of $\left(W_{c,Range}\right)_{80\%W}$ and $(PR_{rel})_{50\%W}$ can be found from the equations (4-22) and (4-24).

2- Modifying mass flow for each speed line;

At the second step the massflow of speed lines is adjusted. The maximum massflow is kept unchanged to abide the correlation $W_{c,max} = f(N_c)$, while the mass flow values are modified for each speed line as below:

$$W_{c,new} = W_{c,max} - \frac{(W_{c,Range})_{80\%N,new}}{(W_{c,Range})_{80\%N,orig}}(W_{c,max} - W_{c,orig}) \quad (4\text{-}25)$$

Figure 4-5 compares the original and scaled map characteristics by plotting the relative pressure, PR_{rel}, against the relative flow, $W_{c,rel}$ for the scaling factor of 4.

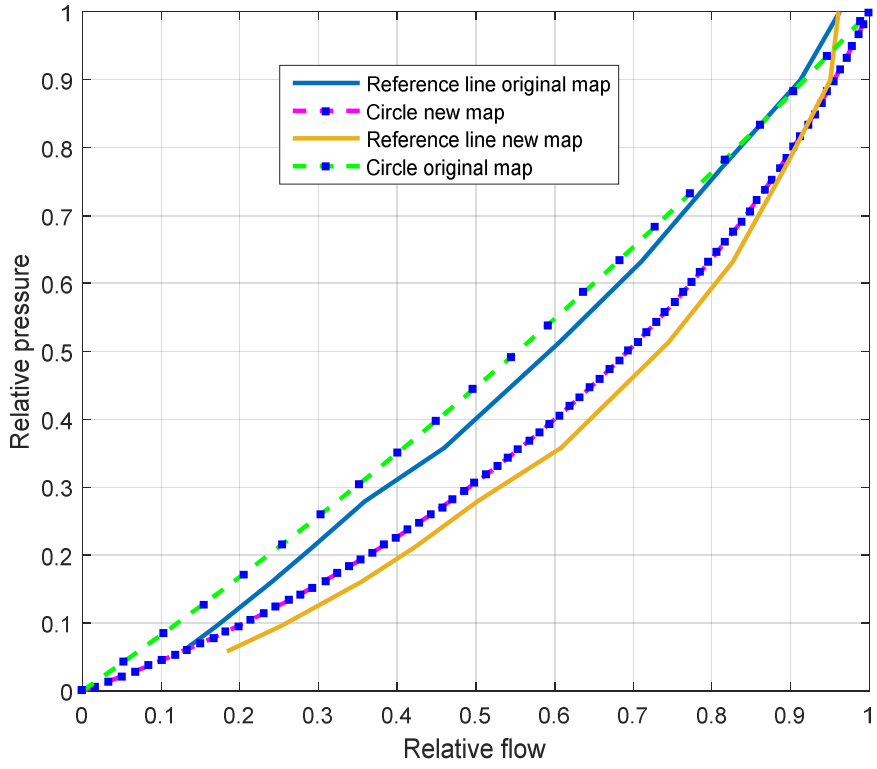


Figure 4-5 HPC map shifting peak efficiency line

By modifying the mass flow for each speed line, the efficiency contours move to new operating points as well. Efficiency is scaled in a way that, the efficiency for all points remains the same as in the original map. Finally, the new surge line is found in a way that, the surge margin relative to the reference line is retained.

In the third scaling step, the speed values associated with the off-design speed lines are modified such that the correlation between pressure ratio and speed is correct. More details can be found in [128].

4.5 Engine model modules

The ICV method has been implemented in the MATLAB/Simulink® environment. The engine modelled in this project is a multi-spool turbofan. The engine duct sub-systems are in order of flow direction; the intake manifold, the fan, the duct CV, and the bypass nozzle. The core sub-systems are in order of flow direction; the fan-LPC CV, the LPC, the LPC-HPC CV, the HPC, the Combustion Chamber (CC), the HPT, the HPT-LPT CV, the LPT, the LPT-Core nozzle CV and the core exhaust nozzle. In addition to these sub systems, there are also shaft inertia blocks. The engine model is illustrated schematically in Figure 4-6 where the green connection lines are exchanging power-speed information between sub systems, while the blue lines are exchanging flow properties, including mass flow, pressure and temperature between corresponding sub systems.

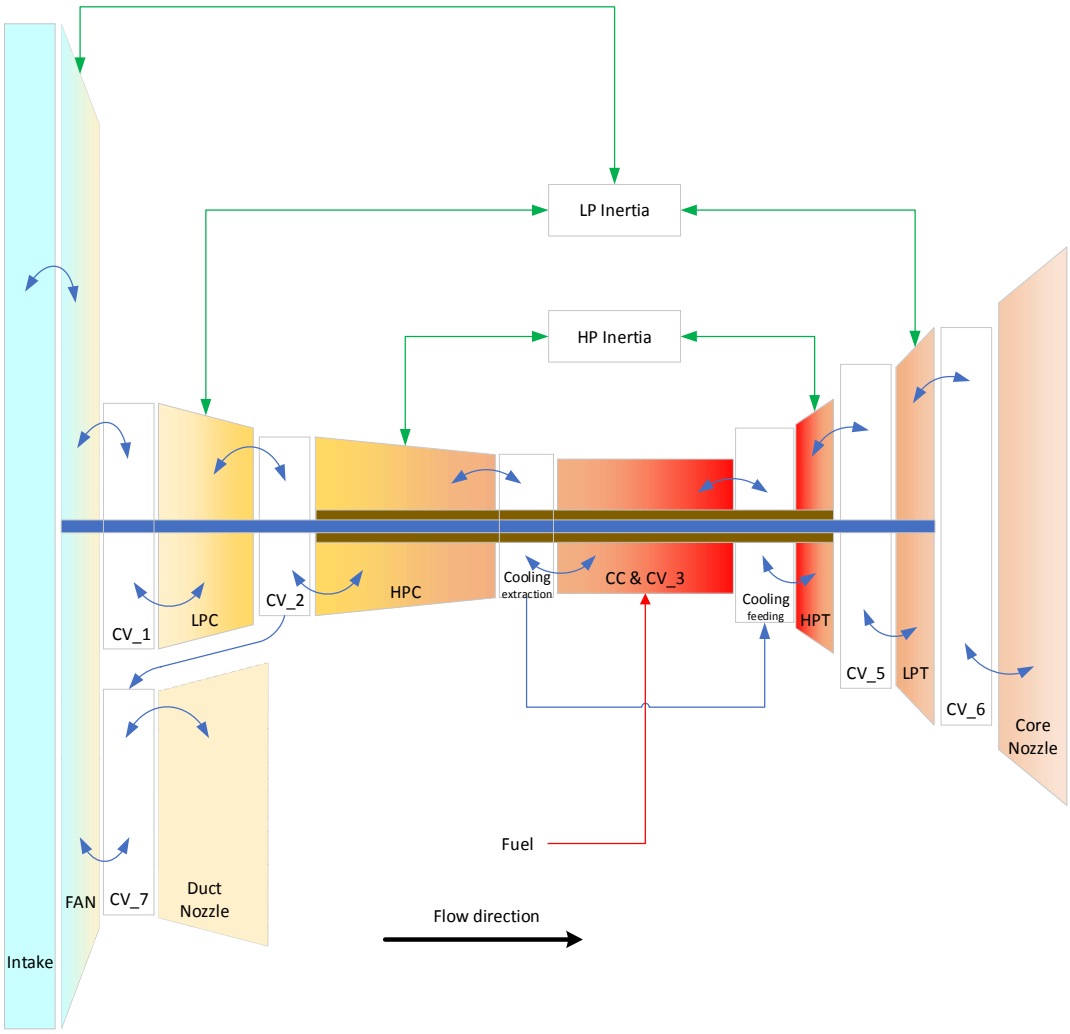


Figure 4-6 Schematic of engine model in Simulink

Equations for mass/momentum/energy conservation are applied within each subsystem. As it can be seen in Figure 4-6, the engine components are all coupled thermodynamically and any fraction of change in fuel injection affects the operation points of all components. Each module has specific features contributing to the dynamics of the engine. It should be noted that all variants of this model are in the International Systems of Units (SI); if required, these can be changed to other systems of units. As it can be seen, the model is modular which means it can be modified for other engine configurations by simply replacing the data of the target engine such as component maps, shaft inertias, nozzle area and LHV of the fuel. In the following Sections, each module will be further elaborated. The typical numbering system for turbofans in [107] has been implemented (see Figure 4-7), to identify a location by its dedicated number.

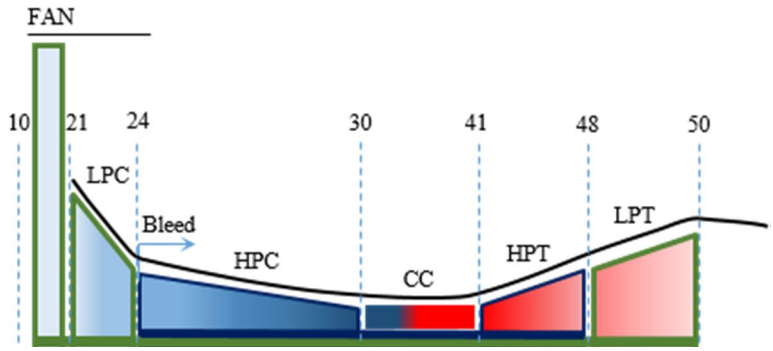


Figure 4-7. Illustration of turbofan components with denoted engine stations

4.5.1 *Shaft modules*

Torque generated by the HPT and LPT are required to drive the HPC on the HP shaft, and the LPC and FAN on the LP shaft respectively.

Figure 4-8 shows the torques which are imposed on the rotor by the turbine (T_{GT}), the compressor and the electrical machine (T_{Load}).

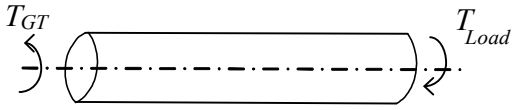


Figure 4-8 Solid rotor

In order to study the performace of the engine in terms of fuel consumtion and surge margin, dynamic resonance and torsional behaviour of the rotor can be ignored in the model. If the turbine rotor is assumed to be solid, Newton's second law gives:

$$T_{GT} + T_{Load} = J\dot{\omega} \tag{4-26}$$

where J is the rotor moment of inertia and ω is the shaft speed. The relation between power and torque is shown below:

$$P = T\omega \tag{4-27}$$

Rearranging (4-26) by using (4-27), ω can be determined, this is shown in Figure 4-9.

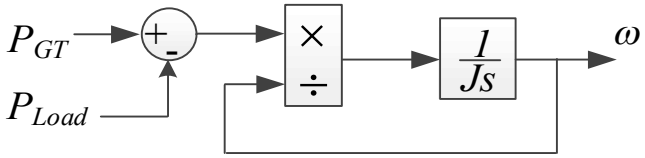


Figure 4-9 Inertia module

The engine model interacts with the electrical machine model through the shaft modules. Assuming that in the MEE, there is at least one electrical machine connected to each shaft, either through gearboxes or being mounted on the engine shaft, equation (4-26) is rewritten for the HP and LP shafts as shown below:

$$P_{HPT} - P_{HPC} + P_{EHP} = J_{HP}\omega_{HP}\dot{\omega}_{HP} \tag{4-28}$$

$$P_{LPT} - P_{FAN} - P_{LPC} + P_{ELP} = J_{LP}\omega_{LP}\dot{\omega}_{LP} \tag{4-29}$$

where P_{ELP} and P_{EHP} are power from electrical machines for LP and HP shafts.

4.5.2 *CV module*

The CV modules of the engine model account for the mass flow balance between executive compressors, turbines, cooling and bleeding flows. From equation (4-4), each CV module can be represented as an integrator. The state variables are pressure values in the control volumes as an open thermodynamic system. In order to consider the outlet flow temperature due to cooling and bleeding flows, a simple mixing block is considered to give the exit temperature as:

$$T_{out} = \frac{W_{in}c_{p,in}T_{in} + W_{bleed}c_{p,bleed}T_{bleed} + W_{cooling}c_{p,cooling}T_{cooling}}{W_{out}c_{p,out}} \tag{4-30}$$

In this case the block diagram of CV modules is shown in Figure 4-10.

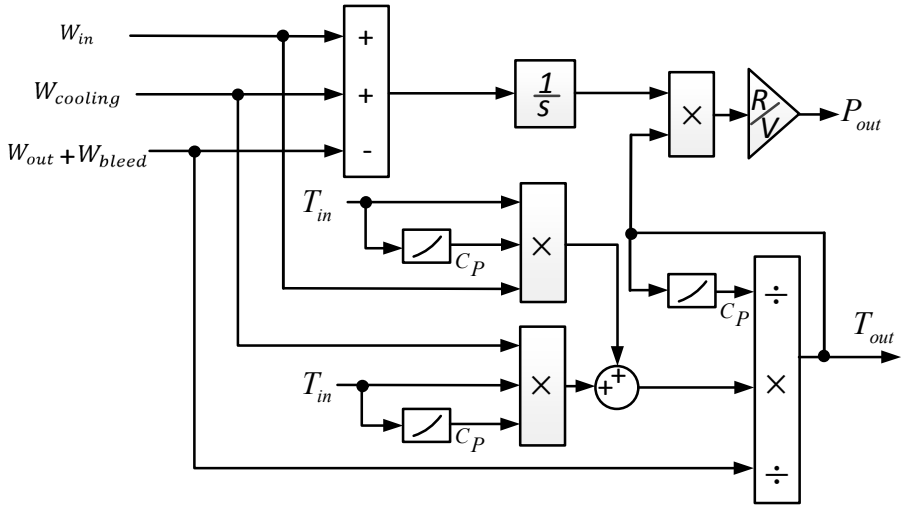


Figure 4-10 CV module's block diagram

The following discussion presents an analytical view of the CV modules. If the cooling flows, bleeding flows and pressure drops are ignored and the core fan map is integrated into the LPC map, equations below present the engine model's dynamic behaviour:

$$W_{Fan} - W_{LPC} - W_{ductNoz} = \left(\frac{V}{RT}\frac{dp}{dt}\right)_{13} \tag{4-31}$$

$$W_{LPC} - W_{HPC} = \left(\frac{V}{RT}\frac{dp}{dt}\right)_{24} \tag{4-32}$$

$$W_{HPC} - W_{HPT} = \left(\frac{V}{RT}\frac{dp}{dt}\right)_{30-41} \tag{4-33}$$

$$W_{HPT} - W_{LPT} = \left(\frac{V}{RT}\frac{dp}{dt}\right)_{48} \tag{4-34}$$

$$W_{LPT} - W_{coreNoz} = \left(\frac{V}{RT}\frac{dp}{dt}\right)_{50} \tag{4-35}$$

Basically, control volumes act as a capacitor where volume size, V, determines the time constant of pressure states in equations (4-31) to (4-35). If the transfer function of the control volume is stated as below:

$$\frac{W_{out}}{W_{in}} = \frac{1}{1+\tau_V s} \tag{4-36}$$

by assuming the outlet flow of the control volume to be proportional to its pressure, the lag associated with the flow in the control volumes, can be approximated by the following equation [133, 134]:

$$\tau_V = \frac{P_0}{W_0} V \frac{\partial}{\partial P}\left(\frac{1}{v}\right) \tag{4-37}$$

where V, P_0, W_0 are volume, the average pressure and massflow and $\frac{\partial}{\partial P}\left(\frac{1}{v}\right)$ is the density change due to pressure changes, at the temperature of control volume. The following

is an example calculation of the time constant for the control volume between the LPC and HPC ($V = 0.1m^3$) at MTO and cruise condition for which the variables are given in Table 4-2.

Table 4-2 LPC-HPC control volume variables at MTO and cruise condition

Variable	MTO	cruise
Mass flow	$52\ kg/s$	$13.6\ kg/s$
Temperature	$371°K$	$299°K$
Pressure	$220.2kPa$	$55.78kPa$

By considering the air thermodynamic characteristic tables in [131] to find $\frac{\partial}{\partial P}\left(\frac{1}{v}\right)$ at desired engine temperature, τ_V is calculated as below:

at MTO: $\tau_V = \frac{220.2\times10^3}{52} \times 0.1 \times 1.031 \times 10^{-5} = 0.0044\ s$

at cruise: $\tau_V = \frac{55.78\times10^3}{13.6} \times 0.1 \times 1.031 \times 10^{-5} = 0.0047\ s$

As shown before, the time constant is very small and can be ignored. However, pressure states should be included in the model, to find pressure values between components and avoid unreal fluctuations, compared to iterative approach discussed in Section 4.1.

4.5.3 *Inlet duct*

The inlet duct for high-bypass turbofans is of a fixed divergent shape. It helps to smooth the air flow into the fan and compressors to avoid compressor instability due to flow distortions [24].

The standard correlations between altitude and ambient temperature together with the deviation from ISA condition gives the ambient temperature and pressure at each altitude. Using flight Mach number then yields the flight velocity and the total engine inlet conditions T_1 and p_1 from equations (4-11) and (4-12).

The total temperature through the inlet remains constant since no thermodynamic work is done on the flow. The changes of the total pressure through the inlet, however, cannot be ignored. The term pressure recovery has been defined to account for these losses due to the wide variety of factors such as the shape of the inlet, the speed of the aircraft, the airflow demands of the engine, and aircraft manoeuvres [135]. The recovered pressure after the losses on the inlet surface or flow separations in the duct is measured by the inlet efficiency factor n_i as [122]:

$$p_2 = n_i p_1 \tag{4-38}$$

For the engine model in this thesis, the values of n_i are inserted by a map from the gas turbine model developed by NASA (TMATS) [122].

4.5.4 *Fan*

The fan of a high bypass turbofan is normally a single stage, low hub-to-tip ratio, low pressure compressor with significant radial variations in performance [136]. Air that passes through the fan is divided between two streams: the primary flow to the engine inner section, which is known as the core flow and the secondary flow known as bypass flow, which is discharged via an annular duct that surrounds the engine core. The core flow is mainly used for engine combustion while the bypass flow is responsible for about 80% of thrust for high-bypass turbofans, depending on the BPR [137]. The ratio between the duct and core mass flows is known as BPR as shown below:

$$BPR = \frac{W_{duct}}{W_{core}} \tag{4-39}$$

A significant proportion of the power output of the LPT is consumed by the fan for high bypass turbofans. Therefore, an accurate fan model is highly desirable to keep the model consistent with the real engine performance. Fan module can be named as the most controversial part of the model, due to the flow split after it and the noticeable variation of flow regime from its hub to tip. It can be set up in several ways among which, there are four main approaches in the literature.

For the first generation of 0-D engine models, the fan used to be represented as a one-dimensional component map, for which a single corrected mass flow determines the fan inlet airflow. The same downstream conditions, including the pressure ratio and efficiency are applied to both the core and bypass flow [138]. In this approach, the bypass mass flow-pressure loop determines the fan pressure ratio, and thus the inlet corrected flow to the fan. Then, the core flow is determined by deducting the duct flow from the fan entry flow, while keeping the BPR constant at its design value.

In order to be more accurate, the core pressure ratio and efficiency values should be derived from those of the outer stream, using the design ratios as below [139]:

$$\eta_{21} = \eta_{13}\left(\frac{\eta_{21}}{\eta_{13}}\right)_{design} \tag{4-40}$$

$$\frac{p_{21}}{p_2} = 1 + \left(\frac{p_{13}}{p_2} - 1\right)\left(\frac{\frac{p_{21}}{p_2} - 1}{\frac{p_{13}}{p_2} - 1}\right)_{design} \tag{4-41}$$

where stations 2, 21 and 13 correspond to the fan inlet, duct flow and core flow respectively as it is shown in Figure 4-11.

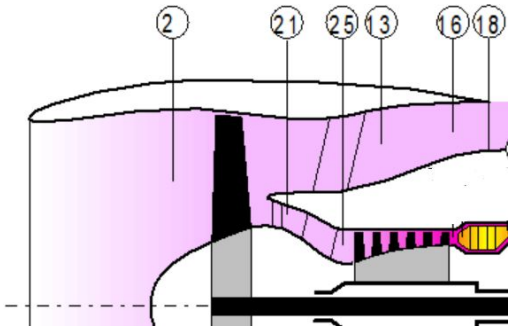


Figure 4-11 Denoted fan stations [139]

A rough estimation can be given as the pressure ratio of the core flow is equal to the bypass flow for low-bypass turbofans, and around 80% of it for the high-bypass turbofans [139].

In the second approach, having the same corrected speed, the correlations between corrected mass flow and pressure ratio for the core and duct section, are set with two, separate, dedicated, one-dimensional component maps for the core and the bypass sections of the fan. In this case, core and duct flow are independent in mass flow-pressure loops, while being coupled with the engine LP core section in speed-torque loop [125]. For this approach, separate core and bypass maps might be provided by the engine manufacturer. If not, the fan map can be scaled into two maps for the core and bypass flow, depending on the design point of the core and bypass flow.

In other approaches, knowing the fact that the flow is not uniform, [138, 140] have implemented 1-D model by producing a fan-radial-profile characteristic to split the map. This approach needs a fan blade profile data to perform the 1-D flow analysis.

In the last approach; for some engines, the fan core flow compression effect is included in the booster map, while the fan map is exclusively for the bypass flow. In this case, the inlet condition to the booster is the same as the fan inlet [136].

Specific Fuel Consumption (SFC) differs by less than 2% between the most simple method 1 and the latter with radial profiles [136]. In the developed model, depending on the available maps, either two separate maps are scaled from the fan map, or the fan core compression is integrated into the booster map.

Once the fan's corrected mass flow, pressure ratio and efficiency are provided from the fan maps, the outlet temperature is derived as [131]:

$$T_{out} = T_{in}\left[\frac{\pi^{R/C_P} - 1}{\eta_C} + 1\right] \quad (4\text{-}42)$$

where; η_C is the efficiency and π is the pressure ratio of the fan ($^{p_{out}}/_{p_{in}}$). R and C_p are determined from thermodynamic tables for the mean temperature of inlet and outlet flow [31]. The required power to drive the fan, P_{Shaft}, can also be calculated as:

$$P_{Shaft} = \dot{m}C_p(T_{in} - T_{out}) \quad (4\text{-}43)$$

The fan module's block diagram is shown in Figure 4-12.

4.5.5 *Compressors*

The high temperature airflow does not release energy through turbines, unless it is pressurized. For this reason, following the fan, the core flow is compressed via compressor stages which consist of rotating vanes and stationary stators, in series. Compressors are of two types: axial and radial (centrifugal).

From Bernoulli's Principle, the total energy at a given point in a fluid is composed of the energy associated with the movement of the fluid (i.e. kinetic head), energy from static pressure in the fluid (i.e. pressure head), and energy from the height of the fluid relative to an arbitrary datum (i.e. elevation head) [131]. The axial compressors used in most modern jet engines consist of several stages, in which the rotor increases the absolute velocity of the fluid and the stator converts absolute kinetic head of the fluid into pressure head by diffusing action. Centrifugal compressors, commonly used in simple or old gas engines, have the same working principle where the radial airflow is deflected to a diffuser to increase the pressure. Engines can have the so-called "mixed compressor" design, in which a single-stage centrifugal compressor is after a multi-stage axial unit, driven by single or multi-spool shafts [141].

As can be seen in Figure 4-12, the component module for the compressors, fan and turbines are similar in structure, while having different maps and equations. In the modules, pressure ratio and shaft speed determine the mass flow from the corresponding map and non-dimensional values from equations (4-5) to (4-8). Afterwards, the outlet temperature and power consumption are calculated from equations (4-42) and (4-43), for the fan and compressors and equations (4-52) and (4-53), for the turbines in the ideal gas law module. The C_p function is as below [31];

$$C_p = 0.99 + 0.24 \times TZ - 1.85 \times TZ^2 + 6.08 \times TZ^3 - 8.89 \times TZ^4 + 7.10 \times TZ^5 - 3.23 \times TZ^6 + 0.79 \times TZ^7 - 0.08 \times TZ^8 \quad (4\text{-}44)$$

where: $TZ = \frac{T_{inlet}+T_{outlet}}{1000}$

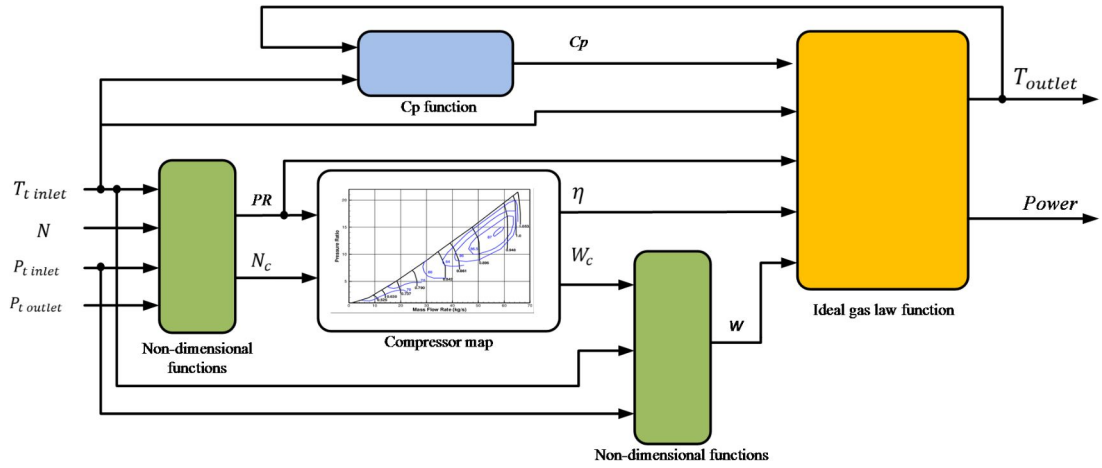


Figure 4-12 Compressor, fan and turbine modules

To model the engine, relight and start-up, detailed sub-idle component maps are required. Maps for the sub-idle region can be created simply by pure mathematical process, which is of low accuracy [142, 143]. The new methods that have a physical background such as a locked rotor [144] also need detailed information of the compressor.

4.5.5.1 Compressor stall and surge

Compressors are prone to two major instabilities as surge and stall [23, 25, 31, 43], which are sometimes interpreted with the same meaning but they are distinctly different. Stall is the partial breakdown of airflow affecting a single blade or a small group of blades but not the whole compressor. It is caused by air approaching a blade (or blades) at an angle greater than the stalling angle. As shown in Figure 4-13, by plotting the flow speed triangle between the rotor radial speed, U, and absolute flow velocity entered the rotary blades row from the exit of stationary blades, V, angle of attack, α, is defined as the angle between the rotary blade cord line and relative flow speed, V_r. If the rotor speed, U, does not keep up with the flow speed, V, then the angle of attack, α, increases at low flow velocity or high rotor speed. For α beyond the stall angle, the airflow tends to separate from the blade, creating a turbulent wake, downstream of the blade [145]. The wake may diminish through the next couple of

blades in the flow direction or affect several blades rearwards. The front rows of a compressor are more susceptible to stall since, they receive the airflow from the previous component, where the airflow may not be matched with their speed properly.

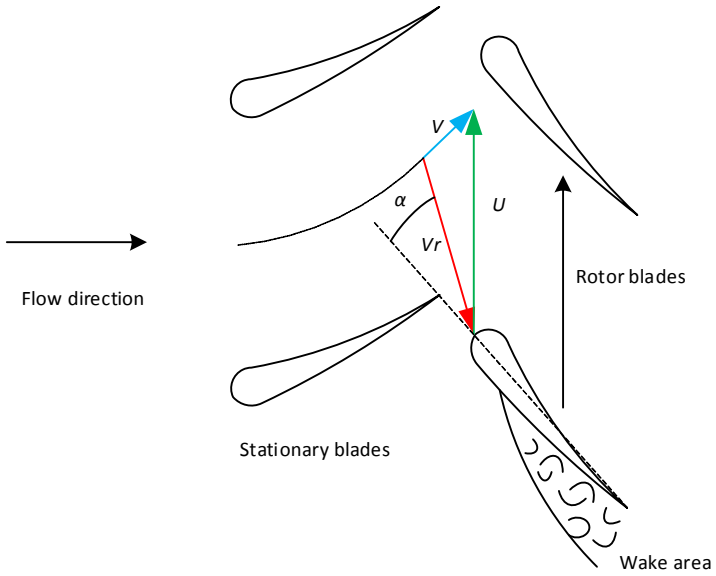


Figure 4-13 Stall due to high angle of attack on stall

If the downstream pressure of the compressor increases too much, it acts as a blockage, causing a total breakdown of the airflow and stall all over the compressor blades, accompanied by reversal of the airflow. This phenomenon is referred to as surge, if severe, it can result in violent reversal of the compressed air or even combustion products from the air intake (watch [146]). In spite of stall, following an increase in backpressure of the compressor, the angle of attack of rear blades increases first, leading to their stall. This further reduces the airflow, progressing stall to front rows and subsequently the stall cascades all over the compressor. Eventually, the pressure in the compressor falls, allowing the reversal flow of the-high pressure downstream air or combustion products [23].

4.5.5.2 **Variable geometry systems**

The compressors of a commercial turbofan engine are designed for optimum operation at the aerodynamic design point (ADP), which is the operating condition during the cruise flight phase. For operation on power settings below cruise power, the compressors need systems that keep the airflow within the limits and prevent stall and surge. Methods to lift the surge problem at low-speed settings include the use of compressor air bleed at the intermediate stage, use of variable geometry compressor,

and use of multi-spool compressors or combinations of them. To ensure this, on a twin-spool engine the air control systems are as follows:

- the variable bleed valve (VBV) system (or surge bleed system) at the exit of the LPC
- the variable stator vane (VSV) system for the HPC
- bleed valves at certain stages of the HPC.

Within a compressor, the first rows of blades are more susceptible to stall where the ability to control the airflow is less when compared to that of rear rows of blades. The rear blades receive the flow from subsequent rows with a more efficient angle of attack, while the front ones are facing the flow delivered from the previous component, which might not be matched properly. Variable geometry systems are employed in compression part of the engine; to vary the angle of the incoming airflow, it is required to ensure that the angle of attack of the first row of rotors is always less than their stalling angle. Variable Stator Vanes (VSVs) are implemented at the inlet, and Variable Bleed Valves (VBVs) are located downstream or at intermediate stages of a multi-stage compressor. VSVs and VBVs systems are scheduled against shaft speeds for off-design, low-speed operational conditions. Figure 4-14 shows VBVs and VSVs on the CFM56-7b engine.

At low speed, VSVs are closed to change the inlet flow angle, thus reducing the inlet flow passed by the front stages of the compressor. This affects the compressor map, in a way that the referred speed lines are shifted approximately horizontally on the compressor map. In this way, for given mass flow and pressure ratio, the surge line rises and the compressor speed increases. The working line does not change, since it is set by downstream components, however, the compressor operating point moves toward higher speeds where higher efficiency is expected [31, 37, 42].

Inter-stage VBVs affect the map and working line due to the change in the internal compressor geometry and bleeding a proportion of the airflow. Conversely, if VBVs are located downstream of the compressor, the working line experiences a downward step, to increase the available surge margin on the same map [31, 147].

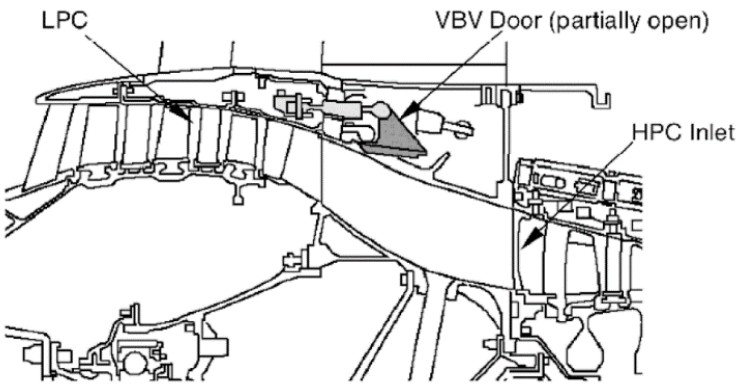


Figure 4-14 location of variable geometry systems on the CFM56-7B engine [42]

Due to unavailability of compressor maps for inter-stage VBVs, their impact is not considered in the model, while downstream VBVs module is modelled as an open loop reduction in mass flow, scheduled against either HP or LP corrected speed. The extracted flow from downstream CV of the VBVs are fed to the CV of the duct. VBVs are normally scheduled against HP speed as it is shown in Figure 4-15.

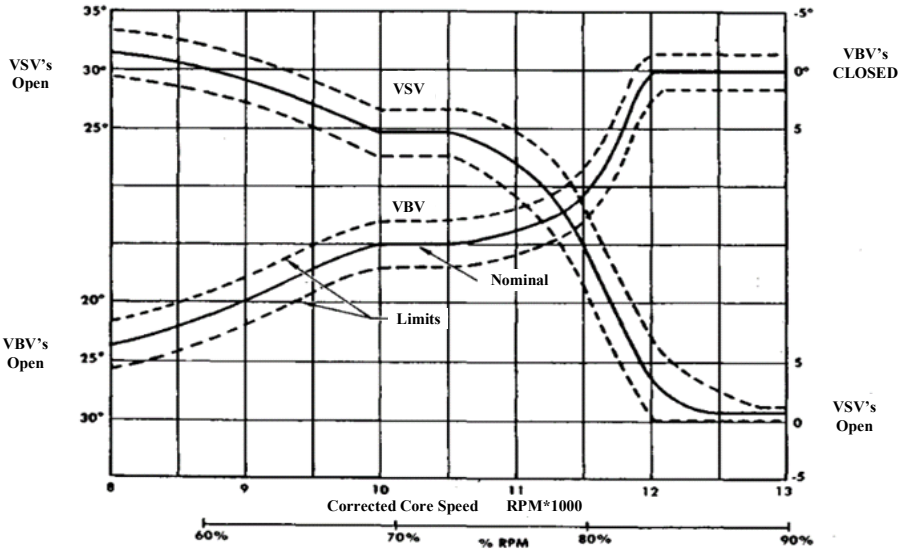


Figure 4-15 VBVs' and VSVs' schedules [148]

The effect of closing the VSVs, which shifts the whole compressor map, is not included in the developed model. One map covers the whole operation range due to lack of maps for various VSV opening.

4.5.5.3 Anti-surge bleed valves

Surge can also happen due to shock-induced separation (i.e. shock stall) as a consequence of high-speed airflow. The compressor cross-section decreases from front to rear stages to compensate for the reduction in flow's specific volume. This helps to

keep the flow velocity constant to have the optimum performance at design compressor speed. At compressor low speeds of operation with lower compression efficiency, however, the rear stages' section area is not enough to pass the excessive airflow. In this case, the flow speed reaches sound speed in their throat (Mach number=1), leading to choke and flow separation. The flow breakdown develops to the front stages as well, due to further reduction of compression efficiency.

To avoid this phenomenon, during engine start-up surge valve bleed normally circulate the airflow from the rear stages to the front stages or dump the airflow to the duct [149]. These effects are not modelled in this study due to the lumped nature of the compressor module.

4.5.5.4 **Customer bleeds**

Customer bleeds refer to the bleeds normally taken for pneumatic requirements such as anti-ice system or Environmental Control Systems (ECS) [42]. Some part of the bleeding, typically from the HPC downstream also supplies pressurized air for turbine blades cooling. Since the cooling flow can be up to 11% of the engine core airflow, it represents a significant role in mass continuity of the model [120, 122]. The customer bleeds for series engines changes from 12.5% to1.95% for engine operation mode from low idle to MTO [150]. The amount of customer bleed for ECS and anti-icing bleed also differs significantly from conventional to the MEA. For instance, Boeing's aircraft, B787, has implemented an all-electric ECS (AE-ECS), eliminating any customer bleed [34].

The costumer bleeds for turbine cooling have been modelled by extracting the required flow from the downstream CV of the corresponding compressor and feeding it to the CV before the corresponding turbine. For pneumatic usages, it is modelled just as an extraction of the flow.

It should be noted that in the MEA costumer bleeding is eliminated from the engine. However, the bleeding has been included in the model for the purpose of verification of the engine model against real data from a convensional engine.

4.5.6 *Combustor*

Combustion chamber, known as combustor for gas turbines, is located between HPC outlet and turbine inlet. Fuel is added to the combustor to increases the pressurized airflow's temperature at approximately constant pressure.

Although combustor efficiency decreases slightly at part load near idle and very high altitude, it is assumed to be constant for the engine model. Depending on the design, pressure losses of 2% to 5% due to friction and heat addition are seen.

In modern combustors, combustion is comprised of three zones as below [31]:

- a 'primary zone' to enable a sufficient mixture of the injected fuel with the air to facilitate combustion and flame stabilisation
- a secondary zone to complete the combustion by injecting further air
- a tertiary zone for injecting the remaining air to tune the exit air temperature compatible with turbine constraints

For 0-D modelling, these zones are merged into a control volume to account for the mass balance between the HPC outlet, and HPT inlet and fuel injected into the combustor. The energy balance is also included implementing second thermodynamic rules as following.

By assuming no heat and work on the combustor volume, the change in internal energy of control volume $\dot{U}$ can also be calculated as:

$$\dot{U} = H_{in} - H_{out} \tag{4-45}$$

where; U and H are internal energy of the control volume and flow enthalpy respectively. U and H are calculated as follows:

$$U = m_{CV} C_v T \tag{4-46}$$

$$H = W C_p T \tag{4-47}$$

where; C_v and C_P are specific heat at constant volume and pressure respectively. The energy released by fuel burning is obtained by the equation below:

$$H_f = W_f \eta LHV \tag{4-48}$$

where W_f is fuel mass flow and LHV is the Lower Heating Value of fuel. Using equations (4-46)-(4-48) and assuming negligible variation of the mass percentage in the control volume ($\frac{m_{CV}}{W_{in}}$), the outlet temperature can be given as:

$$\frac{dT}{dt} = \frac{H_{in} + H_f - H_{out}}{m_{CV} C_v} \tag{4-49}$$

At steady state condition equation (4-49) gives the relation below for the outlet temperature:

$$T_{41} = \frac{FAR.LHV + (c_pT)_{30}}{(1+FAR)(c_p)_{41}} \tag{4-50}$$

where FAR is fuel to airflow ratio as below;

$$FAR = \frac{W_f}{W_{air}} \tag{4-51}$$

By assuming the outlet temperature to be the same as combustion temperature, the block for combustor CV constructed based on equation (4-49) is shown in Figure 4-16.

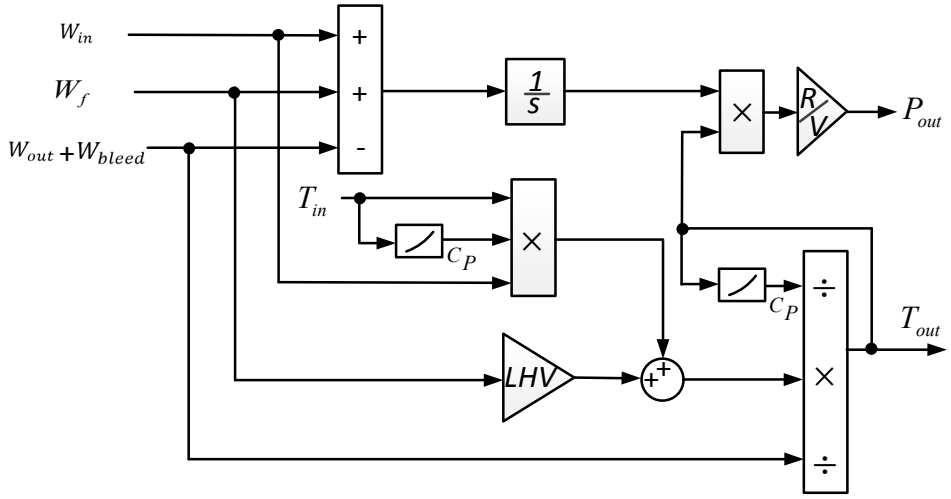


Figure 4-16 Combustor module

In the model, heat soakage is considered in the combustor and a lag from fuel being injected to releasing heat in a combustor in the order of 1–2 milliseconds are employed to calculate the heat soakage effect. As a rough estimation, a reduction of 30% is expected for the effective over-fuelling, i.e. fuel burnt rather than fuel metered, during an acceleration transient [31].

4.5.7 *Turbines*

The high-temperature pressurized airflow expands though turbine blades to produce power to drive corresponding compressors. Pressure head or velocity head converts the enthalpy of the high-temperature flow into torque on the turbine shaft in reaction or impulse turbines respectively. Within the stationary blades, the pressure head converts to velocity head, which cannot exceed the sound speed. If flow velocity reaches sound speed (Mach=1), the corrected flow hits its maximum value, then the turbine is called choked turbine. The Overall Pressure Ratio (OPR) of an engine is

defined as the ratio of HPC exit pressure over the fan inlet pressure. The corrected mass flow over the OPR for the High and Low-Pressure Turbines (HPT and LPT) are plotted in Figure 4-17 which shows the fact that HPT is normally choked for most of the operating range of a turbofan.

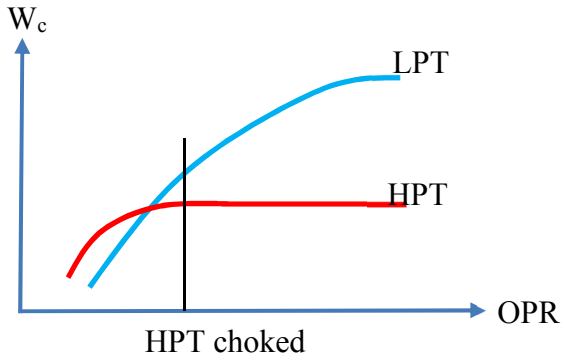


Figure 4-17 Corrected mass flow of turbines against engine Overall Pressure Ratio (OPR)

In a similar fashion to compressor modules, once the corrected mass flow, pressure ratio and efficiency are provided from the turbine map, by applying the conservation equations, the outlet temperature of the turbine is given by:

$$T_{out} = T_{in}\left[1 + \eta_T\left(\pi^{R/C_P} - 1\right)\right] \quad (4\text{-}52)$$

where η_T is the efficiency and π is the pressure ratio of the turbine (p_{out}/p_{in}). R and C_p are determined from thermodynamic tables for the mean temperature of inlet and outlet flow of the turbine. The output power of the turbine, P_{Shaft}, can also be calculated as:

$$P_{Shaft} = \dot{m}C_p(T_{in} - T_{out}) \quad (4\text{-}53)$$

The cooling flow through turbine blades is mixed with the main airflow, in the control volume prior to the corresponding turbine.

4.5.8 *Propelling nozzles*

For a turbofan with an unmixed exhaust system, there are a core and a bypass propelling nozzle. The bypass increases the flow, which has low temperature and velocity, improving propulsive efficiency. The exhaust system can also be comprised of a mixer to combine the hot core flow and the cold flow of the duct before a standard propelling nozzle. Typically, separate nozzles are employed for turbofans in subsonic civil aircraft due to lower weight and cost against a better thrust and SFC gain, coupled with a lower level of noise of the mixer [31]. Separate nozzles have been modelled for the purpose of this thesis.

Similar to turbines, if the flow speed reaches sound speed (Mach=1), the nozzle is called choked. The degree of choking of a propelling nozzle is affected by flight Mach number. Typically, over the operating range of a high bypass turbofan, the core and bypass nozzles are unchoked. In this case, the gas (air for the bypass and combustion products for the core) is expanded to the ambient pressure through converging nozzles and accelerated to subsonic flow at the nozzle throat. The throat area regulates the amount of flow that can be exhausted through the nozzle.

Nozzle modelling is one of the main parts of the engine model, because not only are they responsible for creating thrust but also, they determine the operating point of other components since they are at the engine downstream. Throat areas of both the propelling nozzle and stator nozzles of turbines set the mass flow through the engine and the maximum pressure at the HPC exit [151].

For a gas undergoing an isentropic expansion through a nozzle:

$$\frac{{p_0}^{k-1}}{{T_0}^{k}} = \frac{{p_{exit}}^{k-1}}{{T_{exit}}^{k}} \tag{4-54}$$

where; p_0 and T_0 are stagnation pressure and temperature to account for non-negligible gas velocity of the inlet flow.

The efficiency of a nozzle, η_n, is defined as the ratio of the actual kinetic energy produced to theoretical maximum assuming isentropic process. The expansion through the nozzle is not perfectly isentropic due to inevitable frictional losses, causing a mixture of isentropic and isothermal, known as polytropic [131]. The polytropic exponent, k, is then;

$$k = \frac{\gamma}{\gamma - \eta_n(\gamma - 1)} \tag{4-55}$$

where; γ is the adiabatic index. The gas acceleration rate depends on the nozzle back pressure, p_{out}, which limits the final exit velocity as below:

$$Ma = \frac{2}{k-1}\left[\left(\frac{p_0}{p_{exit}}\right)^{(k-1)/k} - 1\right], \qquad Ma \leq 1 \tag{4-56}$$

where; p_{exit} is the atmospheric pressure, p_{atm}, if calculated Mach number is less than unity. For the converging nozzle, Mach number cannot exceed unity, giving outlet pressure as below;

$$p_{exit} = p_0\left(\frac{2}{(k+1)}\right)^{k/(k-1)} \tag{4-57}$$

The flow rate through the nozzle with the speed above is then:

$$\dot{m} = \frac{AMap_0\sqrt{k/(RT_0)}}{[1+(k-1)Ma^2/2]^{(k+1)/[2(k-1)]}} \tag{4-58}$$

The net thrust on the airframe, produced by the jet of exhaust gas with higher speed than that of the aircraft, is comprised of pressure and velocity terms as below:

$$F_T = (p_{exit} - p_{amb})A_{exit} + \dot{m}_{jet}(V_{jet} - V_{air}) \tag{4-59}$$

where; V_{jet} and V_{air} are absolute exit velocity of the nozzle and the airspeed of the aircraft respectively. Typically, at cruise conditions Ma is less than unity, for which inlet and exit pressures are equal to atmospheric pressure, leading to zero pressure thrust. Moreover, since total pressure and temperature have been used, considering the airspeed into the pressure rise at the inlet, V_{air} is equal to zero and p_{amb} is the total pressure at the inlet. Propulsive power is also defined as:

$$P_p = F_T V_{jet} \tag{4-60}$$

and Thrust Specific Fuel Consumption, TSFC, is defined as the ratio of the fuel flow, $\dot{m}_{fuel}$, to the thrust:

$$TSFC = \frac{\dot{m}_{fuel}}{F_T} \tag{4-61}$$

which is as commonly illustrated in $\left({}^{gr}/_{(kN.s)}\right)$ in the order of 10.

4.6 Control system

The engine model requires a full control system which includes the shaft speed control while keeping the engine within its safe operation margin in terms of maximum temperature and surge margin. With the advancements in electronics, the control system of the aircraft engine turned into the Full Authority Digital Engine Control (FADEC) system [50] which keeps the engine running at maximum possible efficiency while providing smooth, stable operation of the engine throughout the flight envelope. The modelling emphasis is on considering sufficient control features meeting the dynamics required for the study, so simplification of FADEC is expected.

The electronic sensors, typically 6 to 7 [152], collect the information such as air density, throttle (Power Lever Angle (PLA)), engine temperature and pressure at various locations. FADEC analyses the signals and then provide the actuators with

control commands, such as fuel flow, VBVs and VSVs position to regulate the engine operation. Since thrust is not measurable, a power management module translates the required thrust, expressed in throttle or PLA, into the engine shaft speed either N1 (LP shaft speed) or N2 (HP shaft speed) after consideration of atmospheric condition. For a high bypass turbofan, the fan speed correlates with the thrust, due to fan's 80% contribution into thrust. Figure 4-18 depicts the closed-loop diagram of the engine model, including the control system and the engine modules.

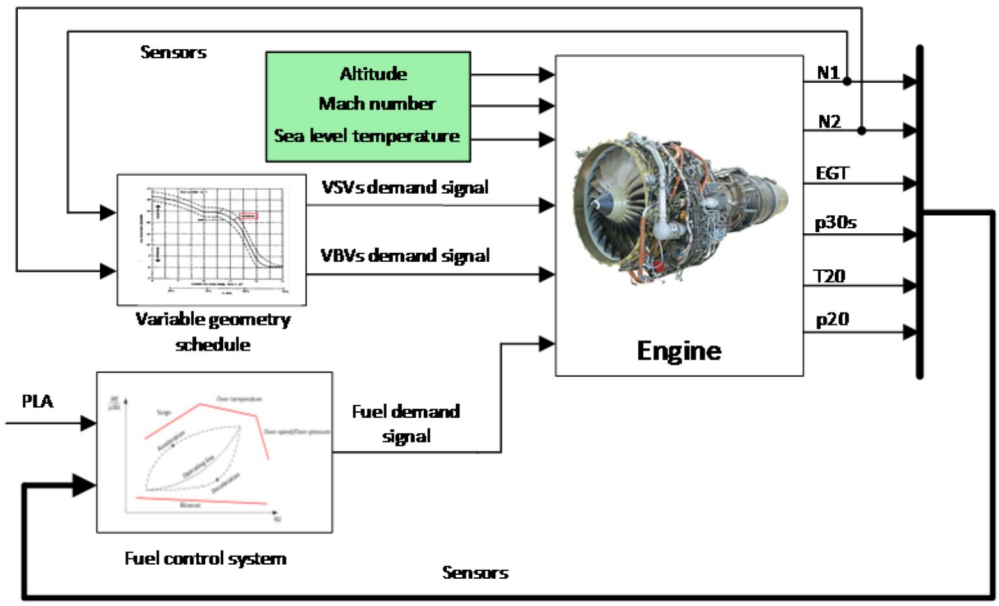


Figure 4-18 Close loop diagram of Engine-control system modules

4.6.1 *Fuel control system*

The main task of engine governor is fuel control. Typically, in mechanical systems, the maximum achievable efficiency is restricted by at least one of the operational limits. For an engine, while seeking for operation at maximum possible efficiency, at least one of the engine components meets its critical mechanical or thermal limits. The control ensures the engine performance within the permissible operating limits under a range of environmental conditions for requested throttle. The governor carries out subsidiary tasks to keep the engine within the high availability and reliability area of the operation. It is also responsible to run-up (start) and restart the engine.

Due to slow dynamics of the engine compared to that of the electrical system and simplicity, PI controller is implemented in the model. The control structure is a bump-less override control in which several Proportional and Integral (PI) controllers are used. A diagram of the proposed model's closed-loop control logic is provided in Figure 4-19.

In order to avoid exceeding structural limits of the rotor's maximum speed and maximum Turbine Inlet Temperature (TIT), limit controllers are employed. Additional limit controllers are implemented to maintain adequate surge margin for the compressors. The minimum fuel level is also defined to prevent combustor blowout. Minimum and maximum flow (MIF, MAF) are functions of altitude and HP shaft speed to prevent lean blow-out and surge phenomenon, respectively. Surge margin and TIT cannot be measured, so they are evaluated by other variables which are explained in this Section.

The inputs to the system from sensors include; shaft speeds (N1 and N2), pressure and temperature at the fan inlet, LPC exit and HPC exit, and Exhaust Gas Temperature (EGT). The sensors are taken as first-order lags, with the bandwidth of 10-25 rad/s.

The control system is comprised of the main controller, receiving thrust set-point in terms of either N1 or N2 from the power management system. Power management receives the PLA and determines the N1 or N2 required for demanded thrust. The output of the main controller is then compared with Min/Max controllers for which the minimum and maximum levels are scheduled against the altitude and environmental temperature. W_f is also fed back to all the limit controllers in order to clamp the integral terms of the controllers and track the output of the other activated controller, thus preventing the accumulation of a significant error when other controllers are active.

Figure 4-20 shows the structure of the controllers in the model. Usually, PI control is sufficient for engine control [152]. This control system is valid for almost all modes of operation except run-up and restart of the engine. The fuel command, $Y_{min/max}$, is backtracked to each of the controllers to avoid wind-up phenomena. The controllers are tuned for low, at high-speed settings for ground and high-altitude operation, by using a linear engine model around the operation point. The gains for PI controllers are scheduled against altitude, where at high altitudes, the engine response is slower due to low air density [21].

The fuel transfer system has been modelled as a simple lag time constant based on equation (4-36), representing the delay due to fuel transfer mainly in the fuel pipes, valves and actuators.

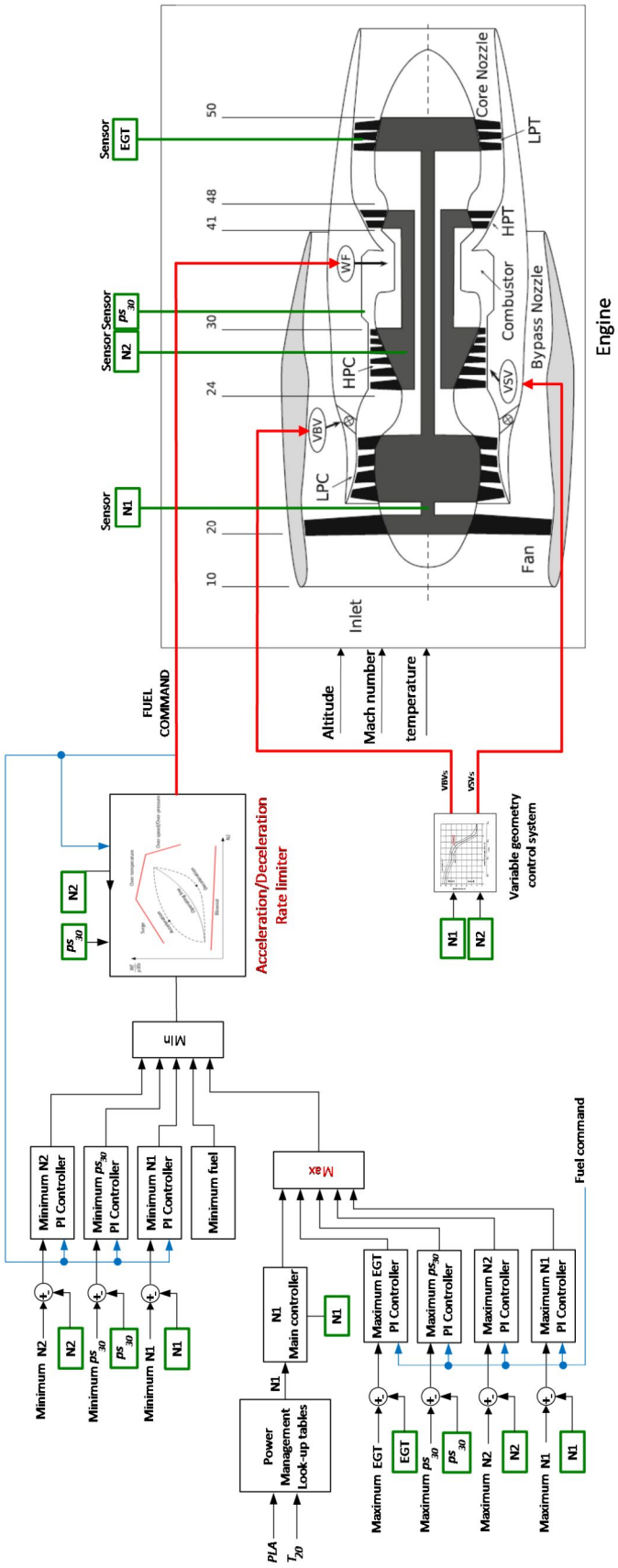


Figure 4-19 Engine control system

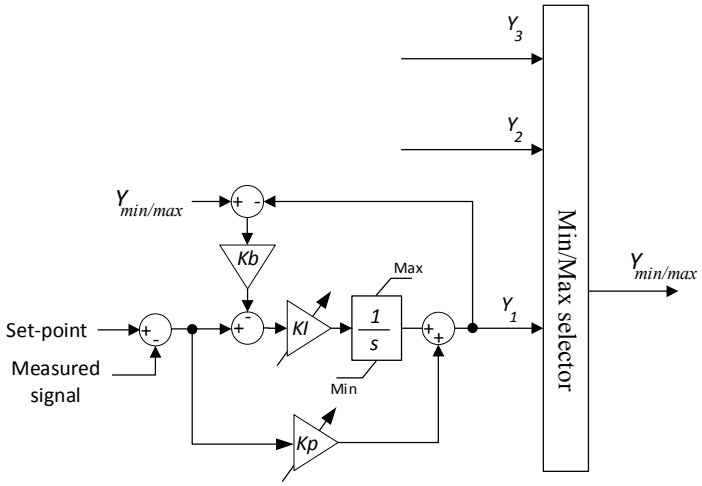


Figure 4-20 Structure of the controllers

4.6.2 *Speed controller design*

Considering the component maps in which the mass flow is a function of component's speed and pressure ratio, equations (4-31) to (4-35) for the CV modules is rewritten as below:

$$f_1\left(\frac{p_{13}}{p_{10}},\omega_{LP}\right).\left(\delta/\sqrt{\theta}\right)_{10}-f_2\left(\frac{p_{24}}{p_{21}},\omega_{LP}\right).\left(\delta/\sqrt{\theta}\right)_{10}-W_{ductNoz}=\left(\frac{V}{RT}\frac{dp}{dt}\right)_{13} \tag{4-62}$$

$$f_2\left(\frac{p_{24}}{p_{21}},\omega_{LP}\right).\left(\delta/\sqrt{\theta}\right)_{10}-f_3\left(\frac{p_{30}}{p_{24}},\omega_{HP}\right).\left(\delta/\sqrt{\theta}\right)_{24}=\left(\frac{V}{RT}\frac{dp}{dt}\right)_{24} \tag{4-63}$$

$$f_3\left(\frac{p_{30}}{p_{24}},\omega_{HP}\right).\left(\delta/\sqrt{\theta}\right)_{24}-f_4\left(\frac{p_{41}}{p_{48}},\omega_{HP}\right).\left(\delta/\sqrt{\theta}\right)_{41}=\left(\frac{V}{RT}\frac{dp}{dt}\right)_{30-41} \tag{4-64}$$

$$f_4\left(\frac{p_{41}}{p_{48}},\omega_{HP}\right).\left(\delta/\sqrt{\theta}\right)_{41}-f_5\left(\frac{p_{48}}{p_{50}},\omega_{LP}\right).\left(\delta/\sqrt{\theta}\right)_{48}=\left(\frac{V}{RT}\frac{dp}{dt}\right)_{48} \tag{4-65}$$

$$f_5\left(\frac{p_{48}}{p_{50}},\omega_{LP}\right).\left(\delta/\sqrt{\theta}\right)_{48}-W_{coreNoz}=\left(\frac{V}{RT}\frac{dp}{dt}\right)_{50} \tag{4-66}$$

where δ and θ are non-dimensional inlet pressure and temperature values defined in equations (4-5) and (4-6), and f_1, f_2, f_3, f_4 and f_5 presents the nonlinear mass flow functions from the fan, LPC, HPC, HPT and LPT maps respectively.

By using the equations (4-28) and (4-29) for power consumption and generation by the compressors and turbines, the power-speed loop for the HP and LP shafts also gives the equation below:

$$\left(W_c\left(\frac{\delta}{\sqrt{\theta}}\right)_{41}T_{41}\eta_T c_p\left(\left(\frac{P_{48}}{P_{41}}\right)^{R/c_P}-1\right)\right)_{HPT}-\left(W_c\left(\frac{\delta}{\sqrt{\theta}}\right)_{24}T_{24}\frac{1}{\eta_C}c_p\left(\left(\frac{P_{30}}{P_{24}}\right)^{R/c_P}-1\right)\right)_{HPC} \tag{4-67}$$
$$=\left(J\omega\frac{d\omega}{dt}-P_{EHP}\right)_{HP}$$

$$\left(W_c\left(\frac{\delta}{\sqrt{\theta}}\right)_{48} T_{48}\eta_T c_p\left(\left(\frac{P_{50}}{P_{48}}\right)^{R/c_P}-1\right)\right)_{LPT} -\left(W_c\left(\frac{\delta}{\sqrt{\theta}}\right)_{10} T_{10}\frac{1}{\eta_C}c_p\left(\left(\frac{P_{24}}{P_{10}}\right)^{R/c_P}-1\right)\right)_{LPC}$$
$$-\left(W_c\left(\frac{\delta}{\sqrt{\theta}}\right)_{10} T_{10}\frac{1}{\eta_C}c_p\left(\left(\frac{P_{13}}{P_{10}}\right)^{R/c_P}-1\right)\right)_{LPC} = \left(J\omega\frac{d\omega}{dt}-P_{ELP}\right)_{LP} \quad (4\text{-}68)$$

The nonlinear equations from (4-62) to (4-68) highlight the thermodynamic coupling between pressure and temperature at various engine stages as functions of HP and LP shaft speeds. In order to design the speed controllers, due to very fast dynamics of pressure and temperature states compared to slow dynamics of shaft inertia, they can be ignored by assuming $\frac{dp}{dt}=0$ in control volumes in equations (4-62) to (4-66). In this case, equations (4-67) and (4-68) are linearized to design the controller. Figure 4-21 shows the speed-torque loops of the LP and HP shafts where the LPT, LPC, HPT and HPC are functions of both LP and HP speed and also fuel as shown in equations (50), (4-67) and (4-68).

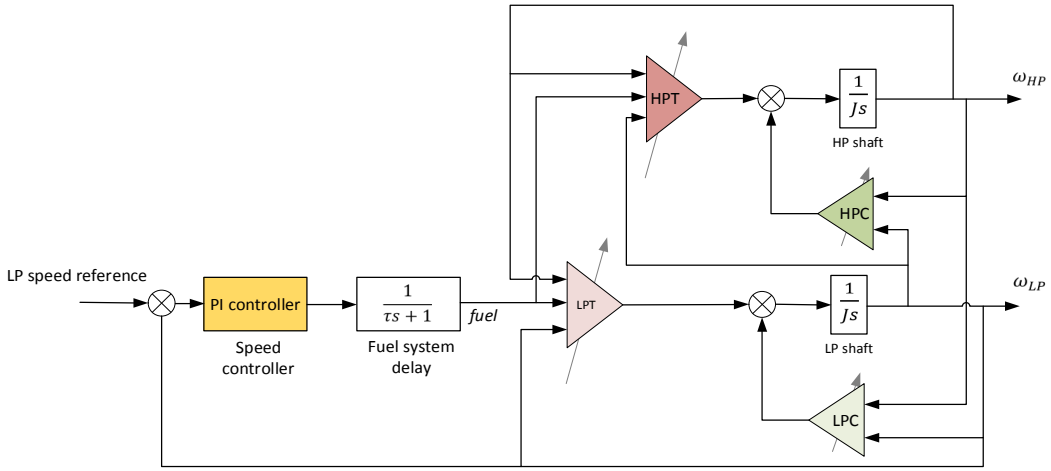


Figure 4-21 Speed-torque loop in speed control system

The linearized models at various condition are as below:

ISA-SLS MTO condition ($\omega_{LP}=100\%$)

$$\begin{bmatrix}\dot{\omega}_{LP}\\ \dot{\omega}_{HP}\end{bmatrix}=\begin{bmatrix}-5.82 & -0.16\\ -0.02 & -0.88\end{bmatrix}\begin{bmatrix}\omega_{LP}\\ \omega_{HP}\end{bmatrix}+\begin{bmatrix}187.98\\ 152.90\end{bmatrix}W_f \quad (4\text{-}69)$$

ISA-SLS idle condition ($\omega_{LP}\cong 50\%$)

$$\begin{bmatrix}\dot{\omega}_{LP}\\ \dot{\omega}_{HP}\end{bmatrix}=\begin{bmatrix}-2.97 & -0.32\\ -0.01 & -1.25\end{bmatrix}\begin{bmatrix}\omega_{LP}\\ \omega_{HP}\end{bmatrix}+\begin{bmatrix}165.23\\ 170.68\end{bmatrix}W_f \quad (4\text{-}70)$$

cruise condition at 39kft ($Mach\cong 0.8$, ($\omega_{LP}\cong 90\%$))

$$\begin{bmatrix}\dot{\omega}_{LP}\\ \dot{\omega}_{HP}\end{bmatrix}=\begin{bmatrix}-0.75 & -0.11\\ -0.00 & -0.39\end{bmatrix}\begin{bmatrix}\omega_{LP}\\ \omega_{HP}\end{bmatrix}+\begin{bmatrix}198.30\\ 165.14\end{bmatrix}W_f \quad (4\text{-}71)$$

descent condition at 39kft ($Mach \cong 0.8$, ($\omega_{LP} \cong 50\%$))

$$\begin{bmatrix}\dot{\omega}_{LP}\\ \dot{\omega}_{HP}\end{bmatrix} = \begin{bmatrix}-0.81 & -0.09\\ -0.00 & -0.35\end{bmatrix}\begin{bmatrix}\omega_{LP}\\ \omega_{HP}\end{bmatrix} + \begin{bmatrix}166.13\\ 175.23\end{bmatrix} W_f \tag{4-72}$$

Figure 4-22 shows a pole-zero map at various operation point, calculated from equations (4-69) to (4-72). The pole-zero locations of the system are changing, while the slowest pole-zero sets are at high altitude. For this reason, the PI gains of the PI controller are scheduled against altitude linearly. The controllers should be fast enough to avoid over-speed, due to the lag in the engine response. The close loop bandwidth of shaft speeds depends on the shaft inertia and altitude.

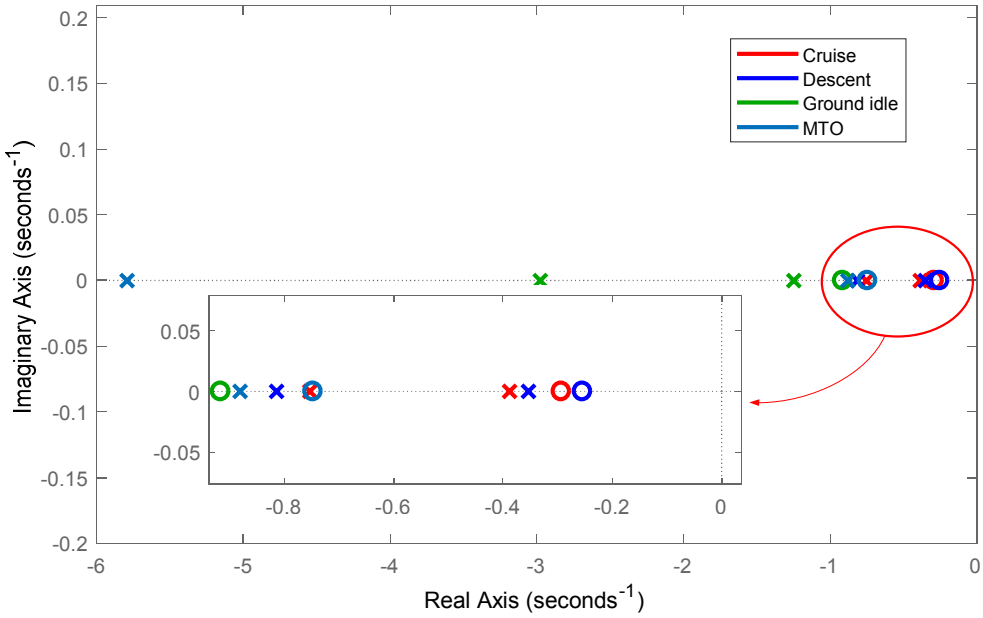


Figure 4-22 Pole zero location at different flight scenarios

4.6.3 *Variable geometry systems' control*

As already discussed in Section 4.5.5.2, VBVs and VSVs are implemented in order to prevent stall and surge of compressors and increase the engine efficiency at low-speed operation. They are normally scheduled against either HP or LP speed. An open-loop scheduled controller sends the command to the actuator of these systems, which is typically modelled as a first-order transfer function [119]. τ is in the order of 0.1 seconds.

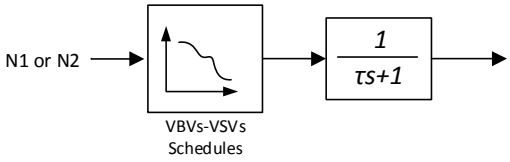


Figure 4-23 VBVs and VSVs control system

4.6.4 *Acceleration/deceleration control*

In order to have a vision of the engine dynamics, Figure 4-24 illustrates the sequences of engine dynamics. At transients, any change of fuel rate directly influences the produced power in turbines, so that the shaft speeds change to modify the mass flow and consequently create HPC upstream pressure up to the equilibrium point.

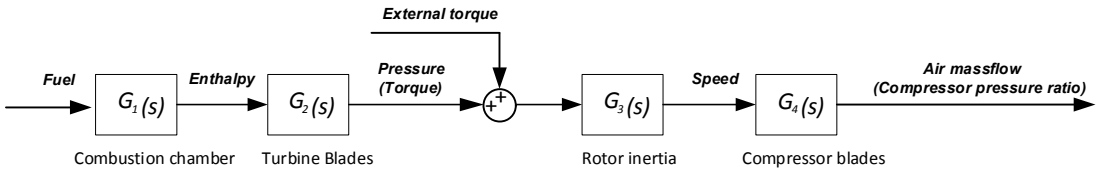


Figure 4-24 Engine dynamics sequence

In an increasing order, G2 and G4 are of the order of engine length/flow speed $\approx 10^{-2}$ sec; G1 is limited by the fuel flow time constant $\approx 10^{-1}$ sec; then over-speed, over-temperature and surge margin limit the acceleration time constant, G3, in the order of 1-10 sec [21]. Time constants of G2 and G4 can be ignored compare to G1 and G3 where the dynamics are slower due to the fuel system and inertia lag. VSVs and VBVs schedules and their actuator time constants are also in the order of 10^{-1} sec.

As is shown in Figure 4-25, following an increase in fuel, T_{41} increases before the HPC speed and HPC flow due to the shaft inertia. It is later discussed in the next Section, according to the engine matching, by an increase in T_{41}, HPC outlet pressure experiences a rise while the speed follows this with a delay. As a result, the operating line during acceleration moves up, closer to the surge line, shown in Figure 4-25. While during deceleration, the pressure drops faster than the speed due to the delay between combustion temperature and shaft speed increase.

For the LPC, the operating line depends on the inertia of both LP and HP shaft speeds. If the LP shaft inertia is considerably more than HP shaft inertia, then the increase in the HPC speed before that of the LPC results in the HPC swallowing the airflow more than its steady-state value and causing a lower operating line of the LPC during acceleration.

Moreover, during acceleration, due to the delay between fuel injection and HPC mass flow, the Fuel to Air Ratio (FAR) increases drastically, and as a result, T_{41} hits its maximum limit. Also, during severe deceleration of the engine, there is a probability of "lean blowout" [153], since the fuel drop is before airflow drop causing the FAR to reduce lower than its steady-state value.

The compressor output pressure gradient is a proper indicator of the likelihood of surge phenomenon. However, pressure readings are noisy, therefore deriving pressure gradient is very challenging. Luckily, at any operation point, the pressure gradient, δp, is a function of HPC outlet pressure, p_{30}, fuel, T_{41} and N2. The airflow entering the combustion chamber can be given as;

$$W_{air} = \frac{p_{41s}}{RT_{41}} AV \tag{4-73}$$

where p_{41s}, T_{41} and V stands for static pressure, temperature and velocity of the flow at combustor exit, and A and R represent the exit area and specific gas constant. If equation (4-73) is multiplied by the fuel flow, W_f, with the assumption of no pressure drop in the combustor, it results in FAR as;

$$FAR = \frac{W_f}{W_{air}} = \frac{W_f}{p_{30s}} \frac{RT_{41}}{Av} \tag{4-74}$$

Temperature measurement is usually accompanied by a significant amount of delay, while T_{41} can be translated into the fuel due to very small combustion delay. Typically, the value of W_f/p_{30s} at different core speeds is relatively easy to measure, which can be a representative of the FAR and the outlet pressure gradient [153]. Therefore, for engine control systems, the maximum permissible value of W_f/p_{30s}, scheduled against core compressor speed, limits the fuel command as it is shown in Figure 4-25. At lower, medium and high core speeds, the engine is protected against surge, over-temperature and over-speed by maximum permissible W_f/p_{30s} as an acceleration rate limit, and for the full speed range the lower limit of W_f/p_{30s} is defined to avoid combustor blowout during deceleration of the engine (see Figure 4-25).

Redundant limit controllers have also been considered for over-speed, over-temperature and over-pressure, due to the importance and probability of them at any core speed.

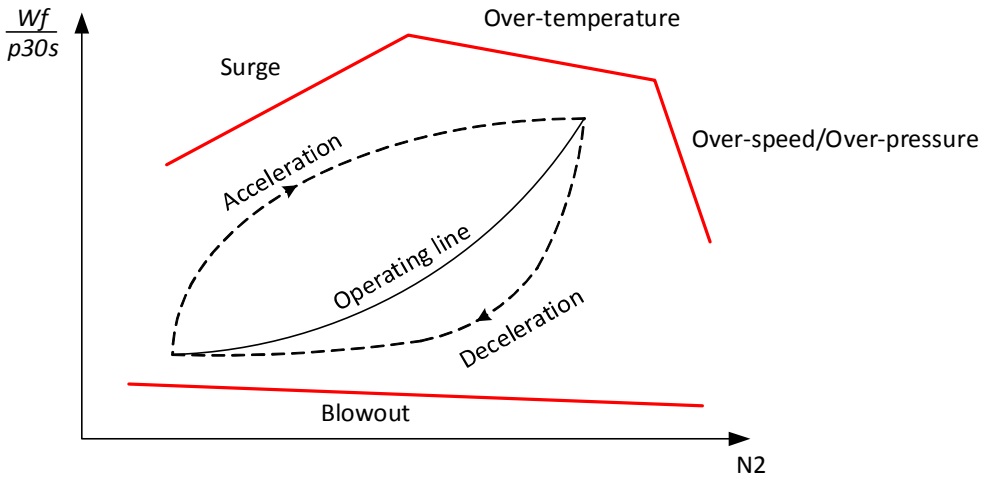


Figure 4-25 Fuel limit implementation [152]

4.7 Multi-spool engine performance

After discussing engine components behaviour independently, the engine performance is discussed in this Section. The thermodynamic coupling of the engine components is elaborated, followed by the core matching and pressure distribution across the engine core.

4.7.1 *Thermodynamic coupling*

There is no mechanical link between the shafts, while the core airflow creates thermodynamic coupling between shaft speeds. This coupling causes many of inflexibilities for the engine performance at the off-design condition, which is expected to be improved by the EPT.

Since the whole engine with two shafts is thermodynamically coupled, any change in fuel affects the output temperature of the combustion chamber, and as a result, the engine performance adapts with this variation. Similarly, any change in the speed of the LP or HP spool by the EPT affects the engine performance, which is the case during power exchange between shafts.

By ignoring the temperature change across the control volume between the LPC and HPC, the change in pressure is calculated using:

$$\frac{dp_{24}}{dt} = \frac{RT}{V}(W_{LPC} - W_{HPC} - W_{BLD}) \tag{4-75}$$

where W_{BLD} is the bleeding flow between the LPC and HPC, V and T are the volume and temperature of the control volume, and R is the specific gas constant [131]. After

ignoring flow dynamics and using equation (4-7), the relation below shows the thermodynamic coupling between the compressors' pressure ration and their mass flow.

$$W_{c,LPC}\frac{p_{21}}{p_{24}}\sqrt{\left[\left(\frac{(p_{24}/p_{21})^{R/Cp}-1}{\eta_c}\right)+1\right]}=W_{c,HPC}+W_{c,Bleed} \tag{4-76}$$

By using the equations (4-42), (4-43), (4-52) and (4-53) for power consumption and generation by the compressors and turbines, the power-speed loop for the HP and LP shafts gives the equation below:

$$\left(W_c c_p P_{41}\sqrt{T_{41}}\eta_T\left(\left(\frac{P_{48}}{P_{41}}\right)^{R/C_P}-1\right)\right)_{HPT}-\left(W_c c_p P_{24}\sqrt{T_{24}}\frac{1}{\eta_C}\left(\left(\frac{P_{30}}{P_{24}}\right)^{R/C_P}-1\right)\right)_{HPC} \tag{4-77}$$
$$=\left(J\omega\frac{d\omega}{dt}+P_{offtake}\right)_{HP}$$

$$\left(W_c c_p P_{48}\sqrt{T_{48}}\eta_T\left(\left(\frac{P_{50}}{P_{48}}\right)^{R/C_P}-1\right)\right)_{LPT}-\left(W_c c_p P_{21}\sqrt{T_{21}}\frac{1}{\eta_C}\left(\left(\frac{P_{24}}{P_{21}}\right)^{R/C_P}-1\right)\right)_{LPC} \tag{4-78}$$
$$-\left(W_c c_p P_{10}\sqrt{T_{10}}\frac{1}{\eta_C}\left(\left(\frac{P_{13}}{P_{10}}\right)^{R/C_P}-1\right)\right)_{LPC}=\left(J\omega\frac{d\omega}{dt}+P_{offtake}\right)_{LP}$$

The inlet condition to the HPC is subject to the performance of the LPC by the term $P_{24}\sqrt{T_{24}}$, in equation (4-77), affecting the HP shaft matching between the HPC, combustor and HPT. On the other hand, the inlet condition of the LPT depends on the performance of the HPT due to the term $P_{48}\sqrt{T_{48}}$, in equation (4-78), which makes the performance of the LP shaft coupled with the HP shaft.

4.7.2 *Engine core matching*

The fact that the engine components are coupled suggests that it would be worthwhile to study engine components matching between the LP and HP shaft components. The matching between the LPC and HPC is mainly a function of their speed ratios at different scenarios. In other words, speed of the HPC should be matched with that of LPC one, to be able to swallow the flow delivered by the LPC to adjust p_{24} for both the LPC and HPC, as shown in equation (4-75) . Higher amounts of p_{24} cause surge for the LPC.

The speed ratio is a function of turbine power split ratio $\left(\frac{P_{HPT}/(P_{HPT}+P_{LPT})}{P_{LPT}/(P_{HPT}+P_{LPT})}\right)$ wherein usually it is around 60/40 at cruise condition (Aerodynamic Design Point (ADP)) [37]. While designed for the ADP, later in this Section it is shown that turbine power split ratio is mainly an established function of the HPT and LPT corrected flow rates and the combustion temperature for the rest of operation range. The power generated by the HPT and LPT depends on the pressure ratio of them. The pressure distribution throughout the engine core is discussed in the next Section.

4.7.3 *Pressure distribution throughout the engine core*

The core nozzle (hot nozzle) with other components including the turbine nozzles set the back-pressure of the HPC, by virtually acting as a downstream restrictor to the flow [2]. The HPC upstream pressure determines the flow rate into the front of the engine at settled compressor speeds. For an engine, the capacity for nozzles can be defined as below:

$$C_{Nozzle} = \frac{W_{50}\sqrt{T_{50}}}{P_{50}} \tag{4-79}$$

Considering equation (4-79), nozzle capacity reaches its maximum value once Mach=1, which is the case at high flight speeds due to the ram rise in the air intake. At this condition, flow is choked, and capacity is given in the equation below:

$$C_{Nozzle} = \frac{AMa\sqrt{k/(R)}}{[1+(k-1)Ma^2/2]^{(k+1)/[2(k-1)]}} \tag{4-80}$$

Knowing the fact that the area between every two blades of HPT or LPT act like a nozzle, their capacities can be demonstrated similar to equation (4-79), as equal to their corrected mass flow as below:

$$C_{HPT} = \frac{W_{41}\sqrt{T_{41}}}{P_{41}} \tag{4-81}$$

$$C_{LPT} = \frac{W_{48}\sqrt{T_{48}}}{P_{48}} \tag{4-82}$$

The corrected mass flow over the EPR for the HPT and LPT are plotted in Figure 4-17, which shows the fact that HPT is usually choked for most of the operating range of a turbofan. Typically for a turbofan, the nozzle unchokes first, followed by the LPT and then HPT at lower engine Overall Pressure Ratio (OPR). The following discussion emphasizes the impact of the corrected flow of the HPT and LPT on the turbine power

split ratio. As it is shown in Figure 4-27, the shape of the relative pressure ratio for the HPT and LPT is established mainly based on their corrected flow. Different modes of operation are discussed in the following.

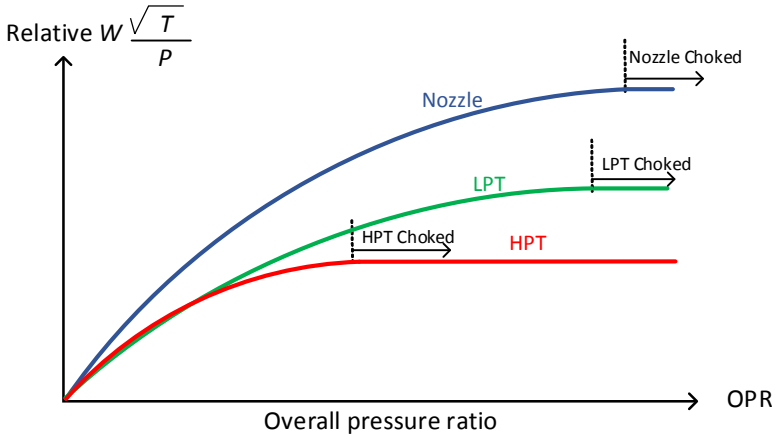


Figure 4-26 Corrected mass flow of turbines against engine Overall Pressure Ratio (OPR)

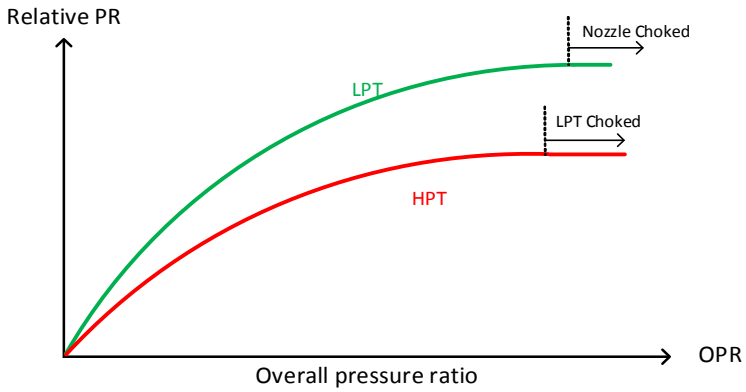


Figure 4-27 Corrected pressure ratio of turbines against engine Overall Pressure Ratio (OPR)

4.7.3.1 Choked nozzle, LPT and HPT

When the nozzle is in a choked state, the inlet pressure is independent of the nozzle operation point. While the constant capacity of the nozzle imposes a constraint on the capacity of the nozzle and turbines, the compressor-turbine sets find a settling equilibrium point. In order to start discussing the equilibrium point, the mass flow provided by the compressor side is assumed to be known, as shown in Figure 4-29.

By having the core mass flow and the value of $\frac{W\sqrt{T}}{P}$ on the HPT map, the combustion temperature determines P_{41}. By ignoring cooling flows, the equations (4-79) and (4-82) give the equation below:

$$\frac{C_{LPT}}{C_{Nozzle}} = \frac{P_{50}}{P_{48}}\sqrt{\frac{T_{48}}{T_{50}}} \tag{4-83}$$

From equation (4-83), for the LPT, $\frac{T_{48}}{T_{50}}$ is also a function of $\frac{P_{48}}{P_{50}}$. Therefore, the LPT expansion ratio, $\frac{P_{48}}{P_{50}}$, remains constant and the same applies for the HPT expansion ratio, $\frac{P_{41}}{P_{48}}$. Knowing the expansion ratio and core mass flow, the produced power by turbines is determined, it highlights the fact that in this mode of operation, turbine power split ratio of shafts is a function of HPT and LPT corrected flows.

Moreover, for the determined value of W_{Bleed}, the compressors rests on the speed, to produce the assumed mass flow to set the equilibrium speed, $N_{C,s}$ as shown in Figure 4-28. Any change in p_{24} affects the mass flows of the LPC and HPC in two different directions, since it changes their pressure ratios in different ways.

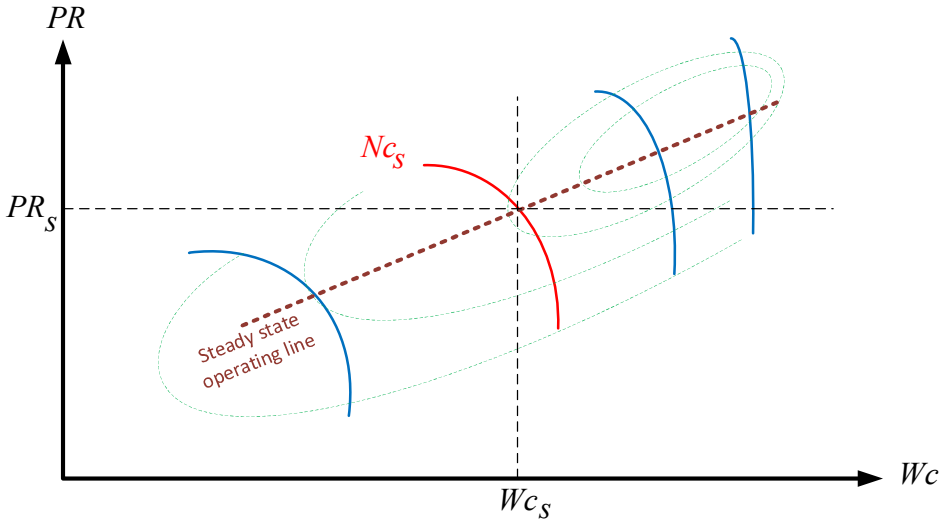


Figure 4-28 Settling speed, pressure ratio and mass flow for a compressor

The flow chart for the discussion above is presented in Figure 4-29. In this case, the whole turbine side acts as a lumped system by ignoring the CV's very fast dynamic compare to that of shafts. The turbine side receives the core flow as input and feeds back the produced power irrespective of shaft speeds. While the operating point of the HPC and LPC changes the compressor speed and mass flow to reach a pressure ratio to satisfy the equations (4-77) and (4-78) for the power equilibrium.

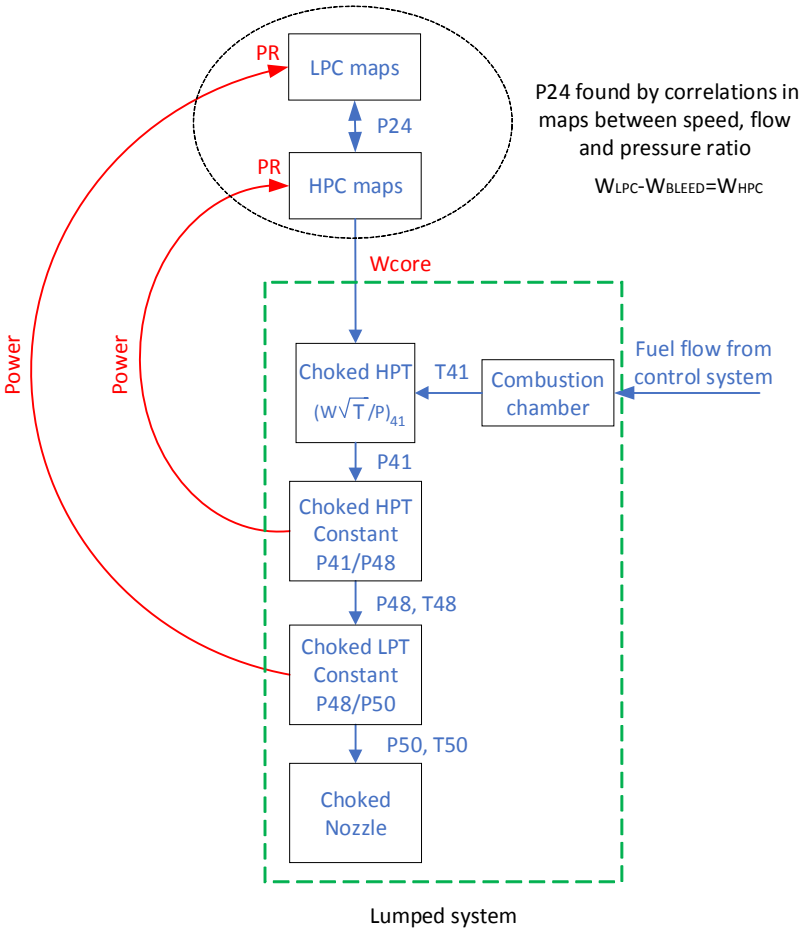


Figure 4-29 Engine performance calculation flow chart (Choked nozzle)

4.7.3.2 **Choked LPT and HPT**

In the case of the unchoked nozzle and the choked LPT and HPT, both C_{HPT} and C_{LPT} are constant. By ignoring bleedings, core mass flow can be assumed the same for all components across the engine core, so the equation below is obtained;

$$\frac{C_{HPT}}{C_{LPT}} = \frac{P_{48}}{P_{41}}\sqrt{\frac{T_{41}}{T_{48}}} \tag{4-84}$$

From equation (4-52) for the HPT, $\frac{T_{48}}{T_{41}}$ is also a function of $\frac{P_{48}}{P_{41}}$. Therefore, the HPT pressure ratio, $\frac{P_{48}}{P_{41}}$, and temperature ratio, $\frac{T_{48}}{T_{41}}$, remain constant.

By knowing the combustion temperature, T_{41}, T_{48} is determined due to the fixed $\frac{T_{48}}{T_{41}}$. This gives P_{48} by the equation (4-84) for the LPT, and thus the value of P_{41} is also determined due to fixed value of $\frac{P_{48}}{P_{41}}$. On the other hand, by solving equations (4-57) and (4-58) the upstream pressure, P_{50}, and temperature, T_{50}, are determined by the environmental temperature and downstream pressure of the nozzle.

In this case, as it is shown in Figure 4-30, irrespective of the HP shaft speed, HPT acts as a lumped system where the input is the core flow and feeds back the produced power. However, the pressure ratio of the LPT is imposed by the HPT and nozzle. In this case, the pressure ratios and thus turbine power split ratios are mainly functions of HPT and LPT corrected flows.

As a result, by knowing the pressure ratio and core flow, the LP shaft speed is imposed by the LPT. Hence, the operation point of LPT is coupled with the LPC and HPC to settle down on a steady-state speed to have consistent core mass flow and satisfy power equilibrium between the compressor-turbine sets. The discussion for the distribution of pressure and temperature between the LPC and HPT is like the Section 4.7.3.1.

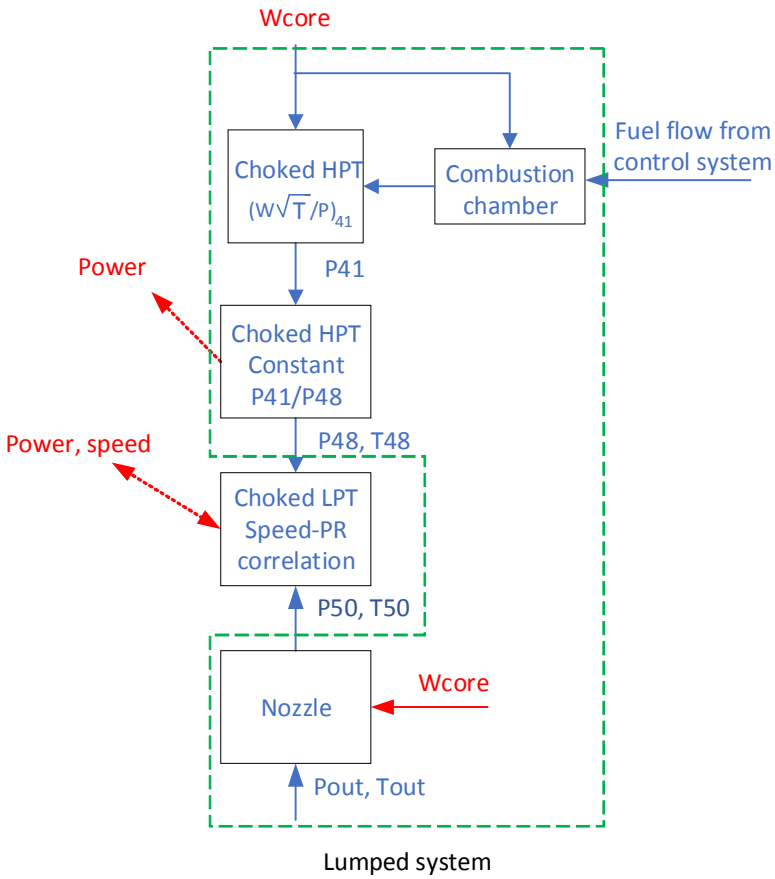


Figure 4-30 Engine performance calculation flow chart (Choked LPT)

4.7.3.3 **Choked HPT**

For most of the flight envelope, the nozzle and LPT are unchoked while HPT is choked, as shown in Figure 4-17. In this case, the performance of all engine components is coupled through shaft speeds as it can be seen in Figure 4-31. In this case, the LPT downstream pressure and HPT upstream pressure are functions of the

engine core flow. While P_{48}, which determines the pressure ratio of the HPT and LPT and thus the power split ratio between them is mainly a function of the corrected flow of the LPT. If the capacity of the LPT increases, it can accept more mass flow, which decreases P_{48} in the control volume between the HPT and LPT similar to equation (4-75). Decrease in P_{48} increases the turbine power split ratio. In this case, the corrected flow of the LPT plays the main role in power split ratio of the turbines and in order to modify the engine design value of turbine power split ratio this parameter is changed later in this study.

The discussion for the distribution of pressure and temperature between the LPC and HPT is similar to Section 4.7.3.1.

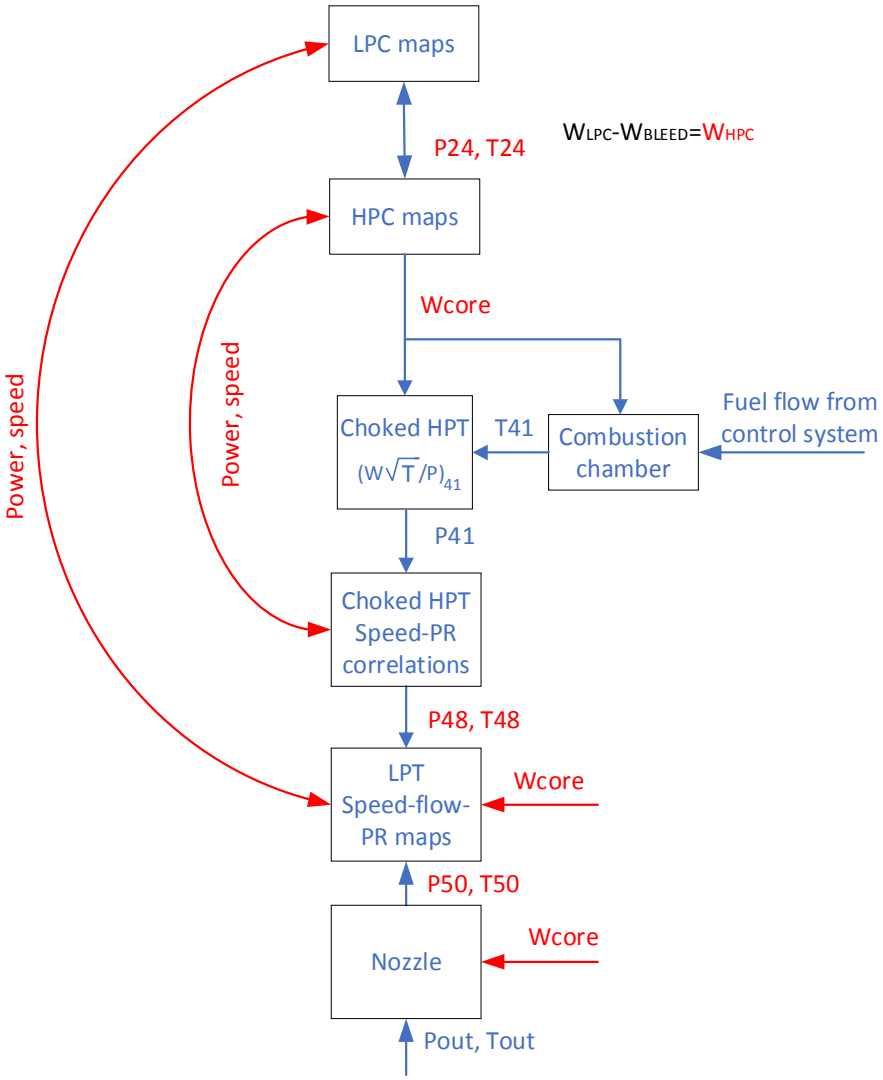


Figure 4-31 Engine performance calculation flow chart (Choked HPT)

4.8 Engine modelling in simulink

After having an analytical overview of engine performance, this Section presents the engine model in Simulink, followed by simulation results. As it is shown in Figure 4-6, the engine model in Simulink is comprised of modules which are coupled through mass flow-pressure and speed-power loops. The engine model states include pressure in control volumes and shaft speeds, where for each there are dedicated integrator blocks. Modelling in Simulink can be implemented either in continuous- or in discrete-time domain. Discrete simulation is preferred since there is a control on the time step size in order to avoid divergence in simulation.

4.8.1 *Numerical consistency*

The inlet mass flow to the component is obtained from the component map. After subtracting the bleedings within the compressor, it gives the outlet mass flow of the components as well. As shown in Figure 4-32, the mass flow is directly fed back to the previous control volume for pressure state calculation (equations (4-31) to (4-35)), creating a so-called algebraic loop. In a Simulink model, an algebraic loop occurs when a signal loop exists with only direct feedthrough blocks within the loop. Direct feedthrough means that Simulink needs the value of the block's input signal to compute its output at the current time step. Such a signal loop creates a circular dependency of block outputs and inputs in the same time-step. It results in an algebraic equation that needs solving at each time-step, adding computational issues to the simulation [154].

On the other hand, the outlet pressure of the subsequent control volume is also directly fed back to the component for outlet mass flow calculation, creating another algebraic loop. In order to eliminate the pressure-flow algebraic loops coloured as red lines in Figure 4-32, a unit delay block, z^{-1}, for the discrete domain is implemented. The same analysis applies for the power-speed loop coloured in green in Figure 4-32.

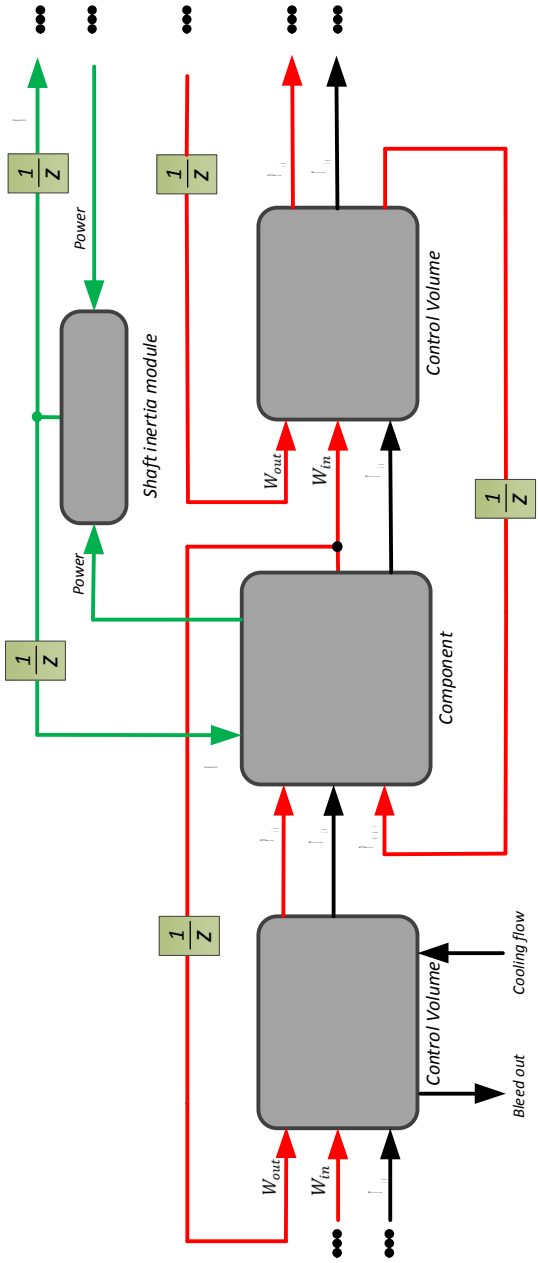


Figure 4-32. Algebraic loops in Simulink

In the ICV method, the max time step size of simulation is limited by the volume size of CVs. From equations (4-31) to (4-35), time step should be of reasonable value to avoid the ratio (V/dt) causing instability, due to dp or affecting simulation speed severely. However, due to the complexity of the engine model, it is not easy to quantify the permissible time step size analytically. In this case, the max time step size should be reduced up to the point that the fluctuation of engine variables around their operation point becomes less than 0.1%. This seems to make the fluctuation low enough compared to the changes made by the EPT on the engine variables.

4.8.2 *Initial condition*

Due to the usage of several lookup tables, representing component maps of the engine model, the initial condition is of paramount importance in order to avoid divergence of the operating point at the onset of simulation. The outlet condition of each module is the inlet condition of the next module within the feedforward nature of ICV method where in case of inappropriate initial condition the errors of each module can accumulate and cause out-of-range operation for at least one of the modules. Note that the model can reach a stable operating point provided that the initial condition is approximately correct (within 10 %) of the target stable operating point. Typically, the design condition is used as an initial condition for the state variables.

4.8.3 *Model tuning/component matching*

The available compressor maps are scaled to the design point of a specific engine (e.g. CFM56-3). After scaling, each module should be tuned at its design point in terms of mass flow, temperature, speed, and pressure. Following this, the engine core components including the HPC, combustor and HPT, are integrated. The pressure values of control volumes are not expected to vary if the mass flow of each module is tuned properly to make it consistent with the modules before and after integration. Once the pressure ratio, temperature and mass flow values are tuned, the power equilibrium in the shaft inertia modules produces the design speed.

Having two compressor-turbine sets on HP and LP shaft, their performance should be matched for the whole operating range of the turbofan. At low-speed settings, the engine performance should be within the acceptable operating range on the compressor maps considering the effect of variable geometries such as VBVs and VSVs.

4.9 Engine model accuracy

The engine model presented in this study is based on physical rules, however during the modelling process around their design point. Assumptions are mainly for so-called second-order phenomena [31], which affects engine transient response while steady-state variables are not expected to deviate considerably. The steady-state results are validated against their equivalent test results' counterparts later in this Chapter.

The main simplifications for engine modelling are as following:

- using generic maps instead of real engine maps

As already discussed in Section 4.4, generic maps are scaled to be used instead of real engine maps. The maps are tuned for design speed with less than 0.2% of error, however there is up to 5% error at low-speed settings specifically for the engine core components such as the HPC and HPT. Typicallly for conceptual studies such as the EPT impact on engine performace, the error up to 30% is acceptable.

- heat soakage simplification

For steady-state operation of a gas turbine, there is negligible net heat transfer between the gas path and the engine carcass. During engine transients, however, there are significant net heat fluxes between the working fluid and the engine metal [31]. Heat is transferred as the carcass soaks to a new temperature, where the amount of heat soakage depends on the mass of each component, size of each component, the speed of the transient manoeuvre and the magnitude of the temperature change [155]. This net heat transfer from the working fluid to the metal is termed heat soakage and has a significant effect on engine performance [31].

For example, due to an acceleration from idle to full power or thrust the engine carcass must soak to a new higher steady-state operating temperature, which absorbs typically 30% of the excess fuel energy. Among conventional engine components, the combustor has the largest effect, due to its large surface area, thermal mass and temperature changes [31]. Heat soakage has not been modelled since component geometric data, real thermal masses and heat transfer coefficients are not normally known to great accuracy. The latter must be calculated from correlations based on parameters such as Reynolds number and Prandtl number and are difficult to evaluate accurately. In this thesis, all heat soakage is considered to take place in the combustor, and a time constant is used to calculate the heat soakage versus time.

- geometry changes

During a transient manoeuvre, minor engine geometry changes may occur, such as tip clearances increasing during acceleration due to casing thermal growths being faster than the rotary components. It is a change of engine geometry which affects component behaviour and hence the non-dimensional relationships on the component maps [31]. Changing tip clearances and inter-stage heating may significantly lower the surge line, depending on the design of the compressor. The changes to the compressor map are of second-order and are ignored for the simple transient performance model of this study [31, 117].

- pressure losses

Pressure loss mainly happens within the combustion chamber, fan duct and nozzles. For combustion chamber, 5% of pressure loss has been assumed and, for the nozzles, an efficiency of 98% has been considered [120].

- control system delays and lags

The detailed control structure, including delays and time constants need to be provided by control system component manufacturers [31]. In this thesis, the controller is a typical PI controller and first-order lag to consider delays to model the control system.

- heat transfer within multi-stage components

During engine transients, the net heat transfer affects the gas temperature through the component, which in turn disturbs stage matching, as it changes the referred speed and hence flow capabilities of the rear stages. For this study, a single map is used to model a multi-stage component such as an axial flow compressor. Therefore, second-order effects upon the map during transients are not modelled.

- inlet distortion

Inlet flow distortions are non-uniformities in either temperature, pressure or swirl, which primarily influences compression system stability. They can impact the performance in the form of an efficiency degradation as well. In the available literature, the effect ranges between 1-5% [24]. The effect of inlet distortion has not been considered in the developed model.

- Reynolds number influences

A compressor map is set up at a reference Reynolds number. With rising altitude, the ambient pressure falls and thus the Reynolds number decreases. Below a critical Reynolds number, the viscosity causes boundary layers to grow which, as a result reduces efficiencies and mass flow and affect the ideal non-dimensional parameter of the map [117]. This effect has not been considered in the model. The effect of compressibility has also been ignored since it is applicable for supersonic jet engines.

4.10 Engine model uncertaintity

The 0-D model suffers from various simplifications, while the level of accuracy is still accepted due to the noticeable impact of power transfer between shafts on engine performance. The ideal gas laws are sufficient to describe the steady-state operation

within 0.1% of actual conditions for design condition and within 1% for off-design condition, whereas for transients the error might be up to 30% [31]. However, for this study, the effect of power transfer is compared with the baseline engine model.

4.11 Model validation

The engine model has been validated for multi-spool turbo-generator, for steady-state and transient performance by the author of this thesis in [107]. This Section presents the performance validation using an example of CFM56-3 engine. Generic component maps from [120] have been scaled in such a way that they fit the cycle point of the CFM56-3 engine at ISA-SLS condition, presented in Table 4-3.

Table 4-3 CFM56-3 engine single cycle point at ISA-SLS condition

	Temperature (°K)	Pressure (kPa)
FAN inlet	288	101
LPC exit	371	220
HPC exit	786	2445
HPT inlet	1520	2318
LPT inlet	1135	598

HP spool speed	14335 rpm
LP spool speed	4835 rpm

In order to validate the engine model, simulation results are compared with the correlation test report data of the CFM56-3 engine from [137, 147]. FADEC can not be validated in this study due to lack of required data.

Figure 4-33, Figure 4-34 and Figure 4-35 show acceptable agreement between the simulation results with the test data for the fan, LPC and HPC operating lines for the steady-state test from idle to full throttle setting at ISA-SLS. The engine maps include the pressure, mass flow and temperature (obtained from efficiency) data of engine. Therefore, the agreement between the simulation and correlation test report in Figure 4-33 to Figure 4-35 can be interpreted as the agreement of performance data, including pressure, mass flow and temperature.

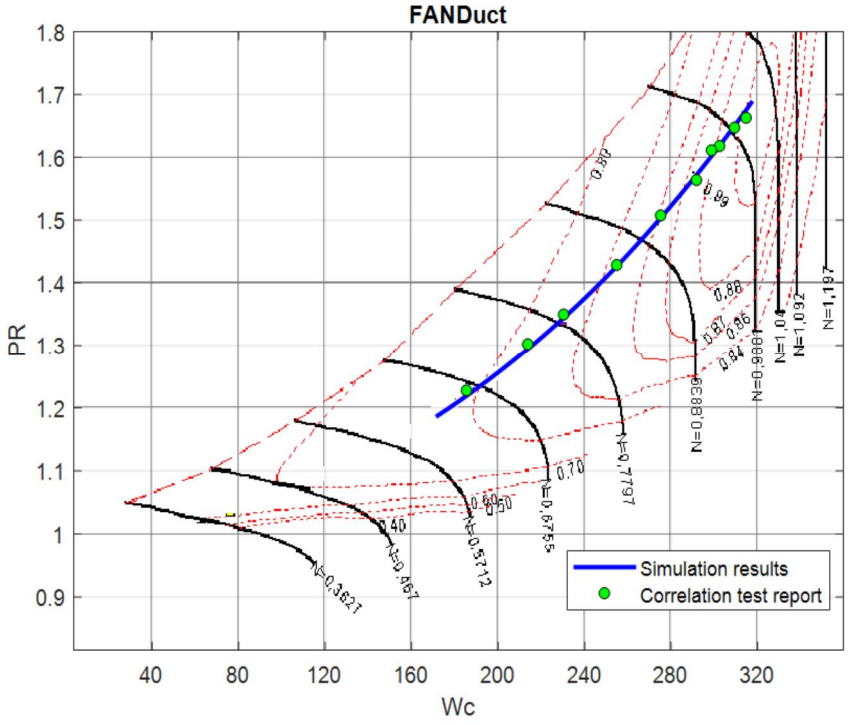


Figure 4-33 FAN operating line (steady-state idle to full throttle at ISA-SLS condition)

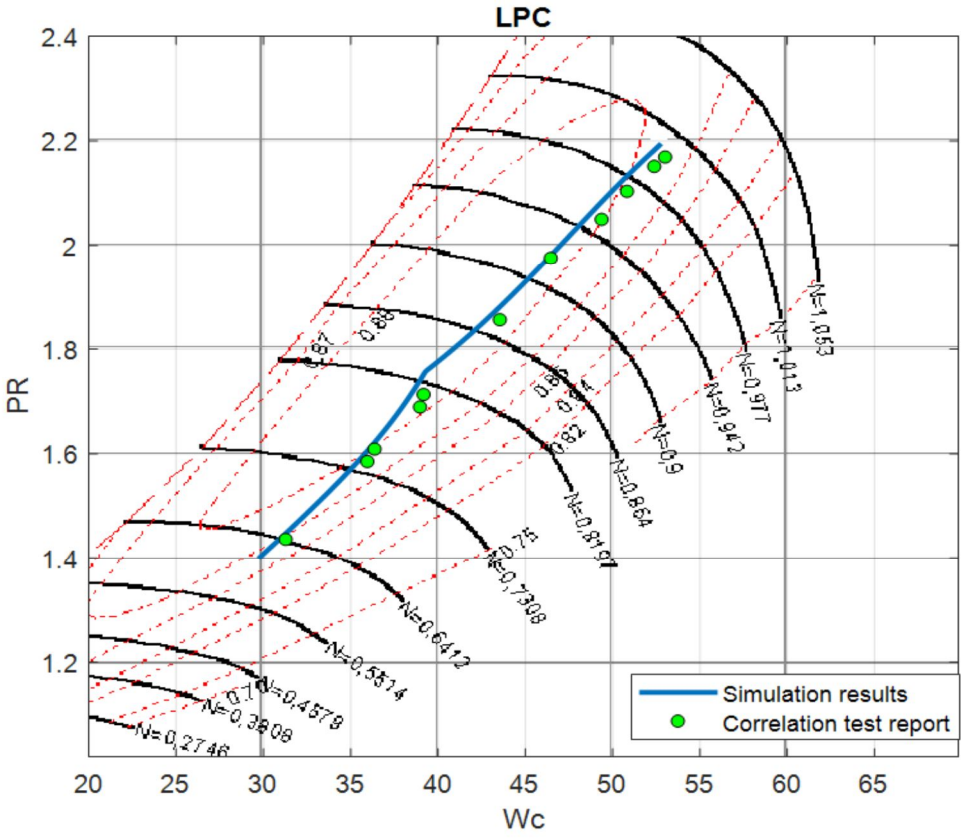


Figure 4-34 LPC operating line (steady-state idle to full throttle at ISA-SLS condition)

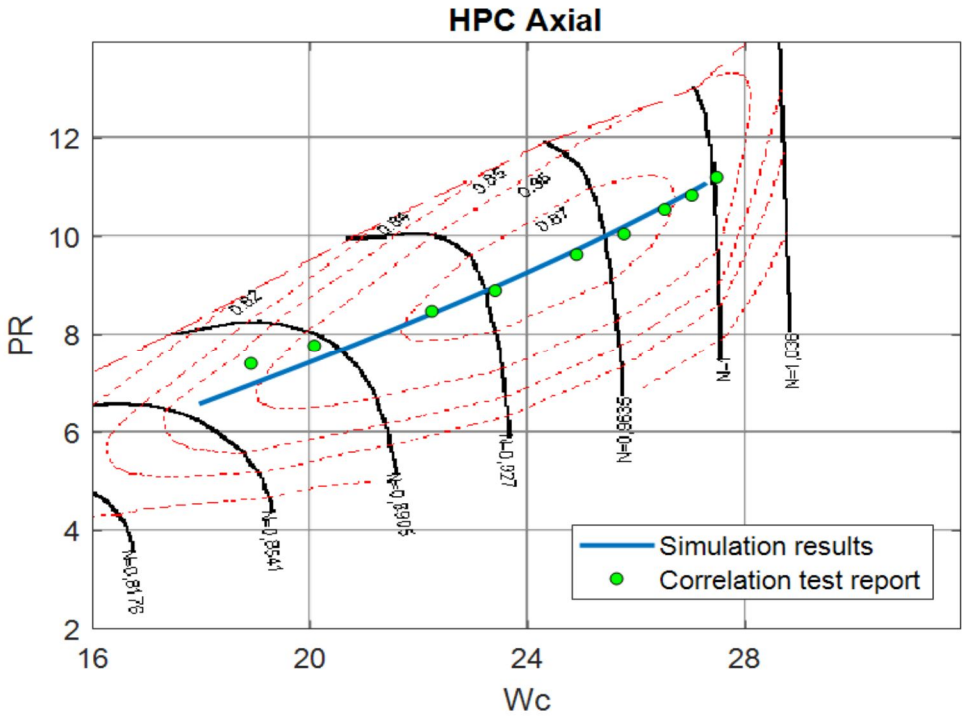


Figure 4-35 HPC operating line (steady-state idle to full throttle at ISA-SLS condition)

Results for LP and HP shaft speeds and their corresponding simulation error compared to the correlation test report are plotted in Figure 4-36 and Figure 4-37. HP speed mimics the engine behaviour with a high degree of accuracy with an error of less than 0.8%, and the LP speed error is less than 2.2%. The maximum error happens at low-speed settings due to use of the single generic map at various VBV and VSV openings.

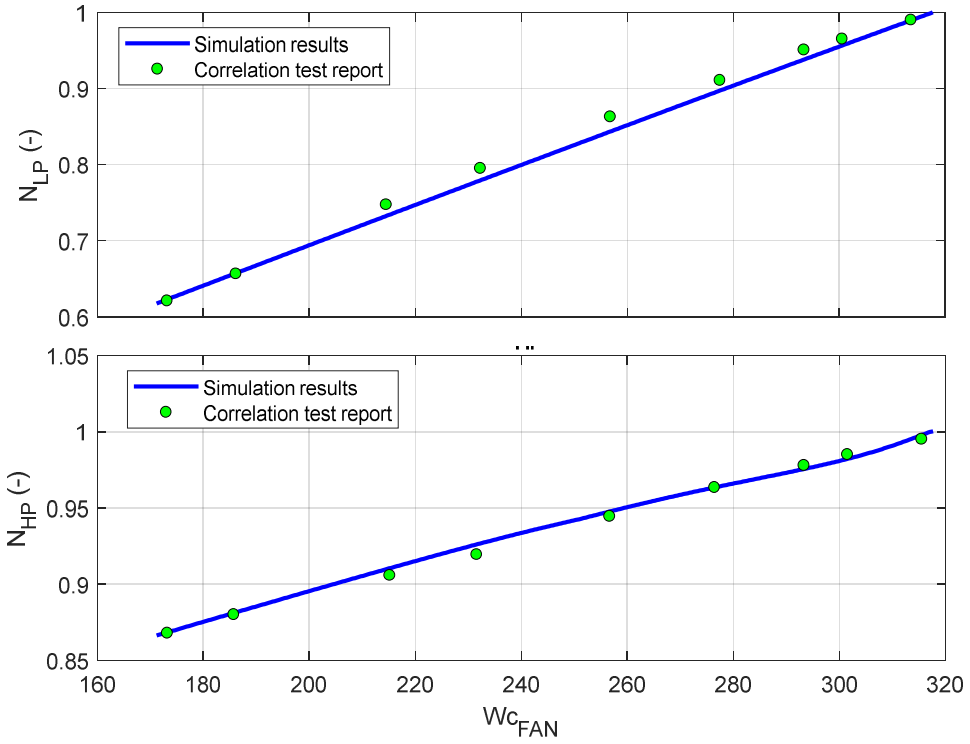


Figure 4-36 Measured and simulation results for shaft speeds

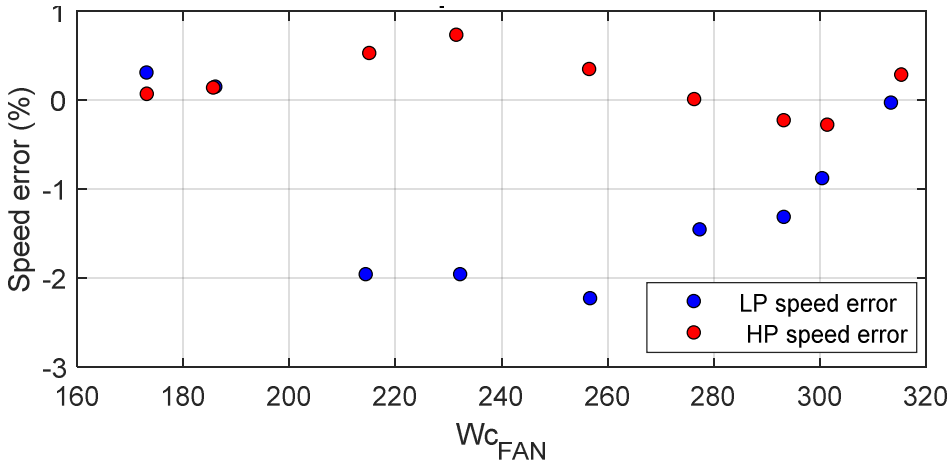


Figure 4-37 Simulation error for shaft speeds

Figure 4-38 and Figure 4-39 show the Specific Fuel Consumption (SFC) and its simulation error compared to the correlation test report. The error at low-speed settings is mainly due to the use of generic maps with different efficiency values compare to the engine maps as well as the use of a single map at various VBV and VSV openings. SFC starts to decrease from 100kN to 90kN due to the increase in HPC efficiency. While between 90kN to 65kN of thrust, the HPC operation point hits its maximum efficiency at 87% (see Figure 4-35). Below 65kN of thrust, the VBVs start to act, decreasing the SFC for 65kN to 45kN of thrust and increasing it below 55kN of thrust.

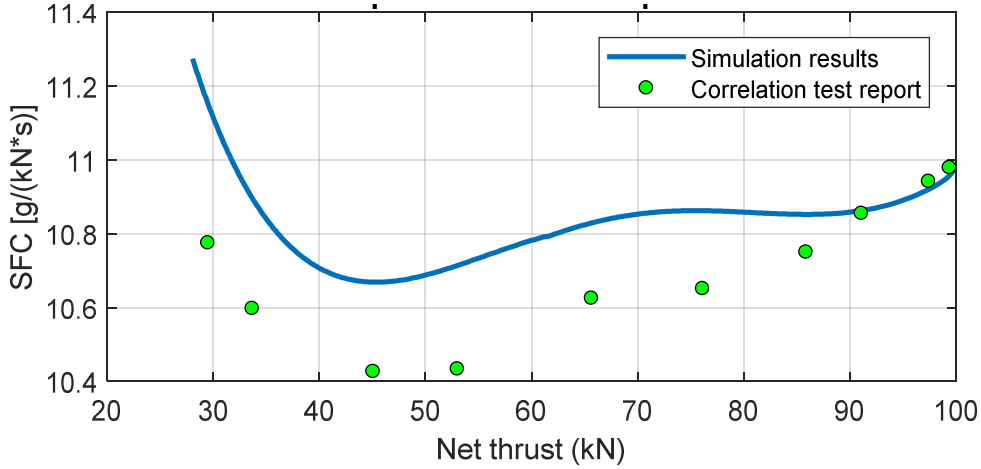


Figure 4-38 SFC (steady-state idle to full throttle at ISA-SLS condition)

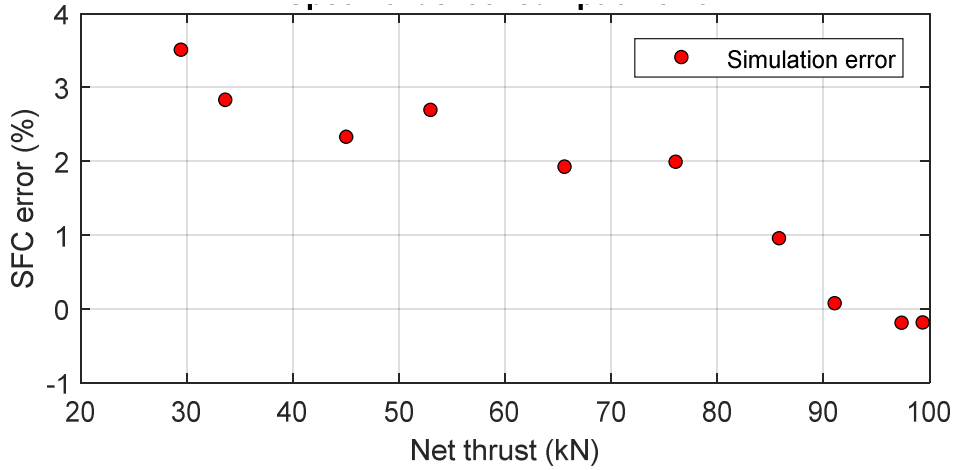


Figure 4-39 SFC error (steady-state idle to full throttle at ISA-SLS condition)

The steady-state error of the simulated engine variables such as speed and fuel consumption presented in this Section is within 1% for the high-speed setting and 3.5% for the low-speed setting. It deems to be acceptable for the electrical power transfer conceptual study.

4.12 Transient simulation results

Burst-chop is one of the typical transient tests for which the engine accelerates from idle to full (burst), followed by the deceleration back to idle (chop). The engine dynamics during severe transients mainly depends on the shaft inertia values. For the CFM56-3 engine, the engine's main controller is on the HP shaft speed. HP shaft speed is scheduled against the PLA and engine inlet temperature [147]. Figure 4-40 shows the HP speed reference, HP speed and LP speed for the acceleration and deceleration of the engine at ISA-SLS. A Bump-less override control system provides smooth HP and LP speed responses. Unfortunately, transient data of the engine performance was not found in the literature to evaluate simulation results. However, as discussed in Section 4.9, up to 30% of error is expected during severe transients such as acceleration and deceleration of the engine. Figure 4-40 illustrates the HPT exit temperature, while it has not hit its limit during acceleration. However, as it can be seen in Figure 4-40, the value of W_f/p_{30} has reached its limit during acceleration and deceleration to avoid exceeding surge margin and lean blowout limits. Typically for surge margins, 10% is the minimum allowable value [31, 139]. The surge limit is not directly controlled, while its limit is met by adjusting the maximum allowable W_f/p_{30}.

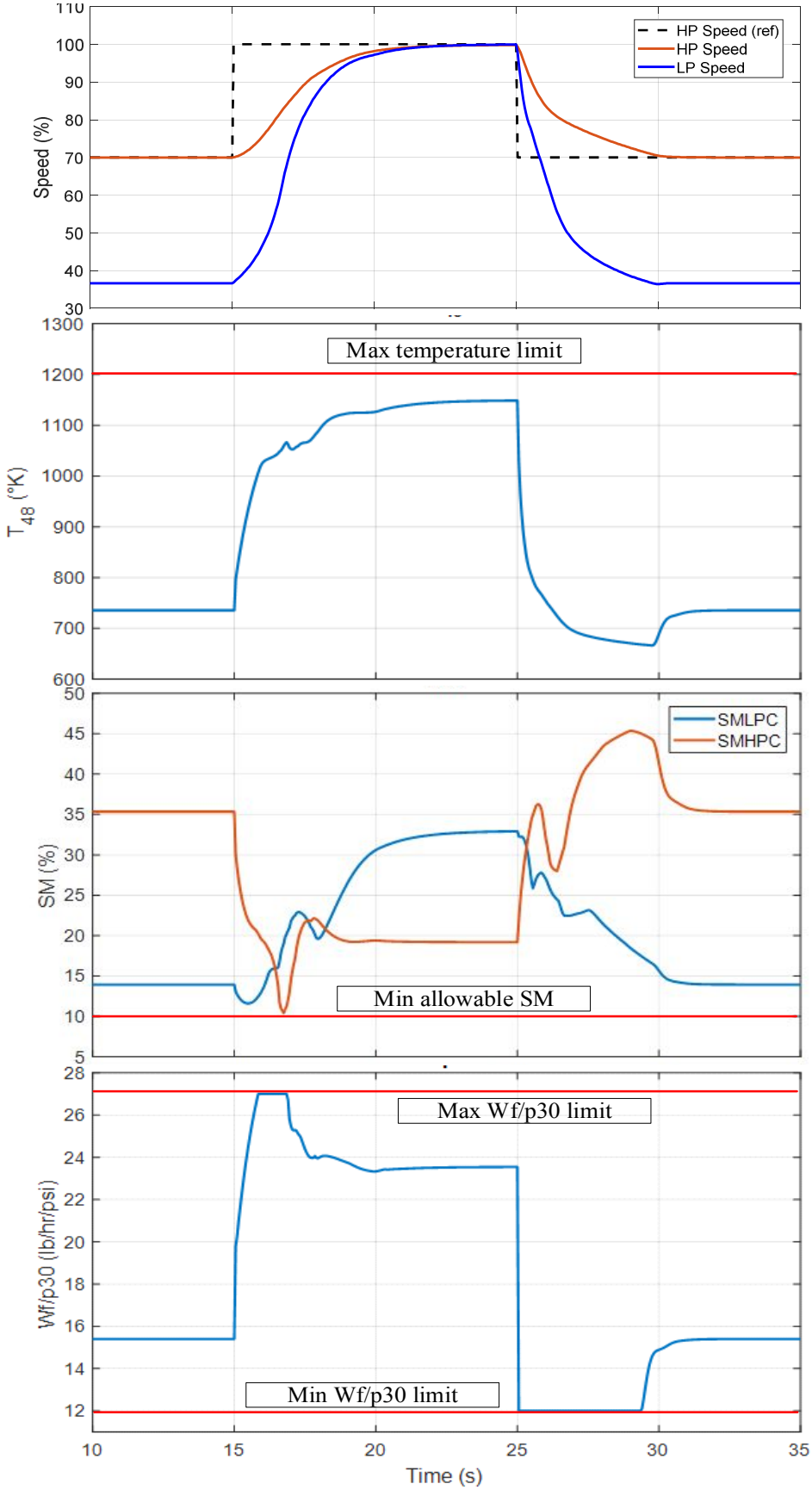


Figure 4-40 Shaft speeds, HPT exit temperature, SMs, W_f/p_{30s} (Burst-Chop maneuver)

Having a narrow region between operating lines for the FAN during burst-chop manoeuvre (see Figure 4-41) highlights the fact that it does not experience extreme dynamic. It can be due to the smooth LP speed response and also no change in its inlet condition. However, for the LPC and HPC in Figure 4-42 and Figure 4-43, respectively, the operations lines demonstrate severe transient with a high degree of nonlinearity. The acceleration operating line for both the LPC and HPC in this engine are closer to the surge line compare to that of deceleration.

For some engines, the deceleration line of the LPC is on top and closer to the surge margin. It depends on the LP shaft inertia and VBVs response, which is involved in engine matching during transient manoeuvres. If the LP shaft speed is less than its matched value, then it cannot provide the requested mass flow by the HPC which causes a lower the pressure ratio than the steady-state operating line for the LPC. In this condition, if the VBVs are closed fast enough, the airflow can be recovered.

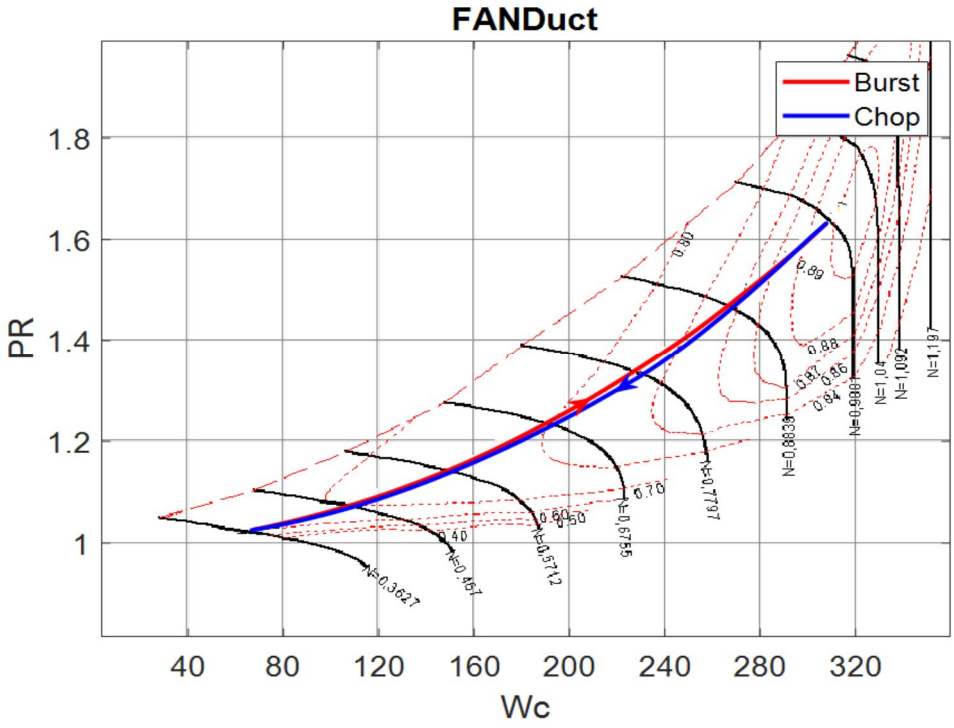


Figure 4-41 FAN transient operating line (Burst-Chop manoeuvre)

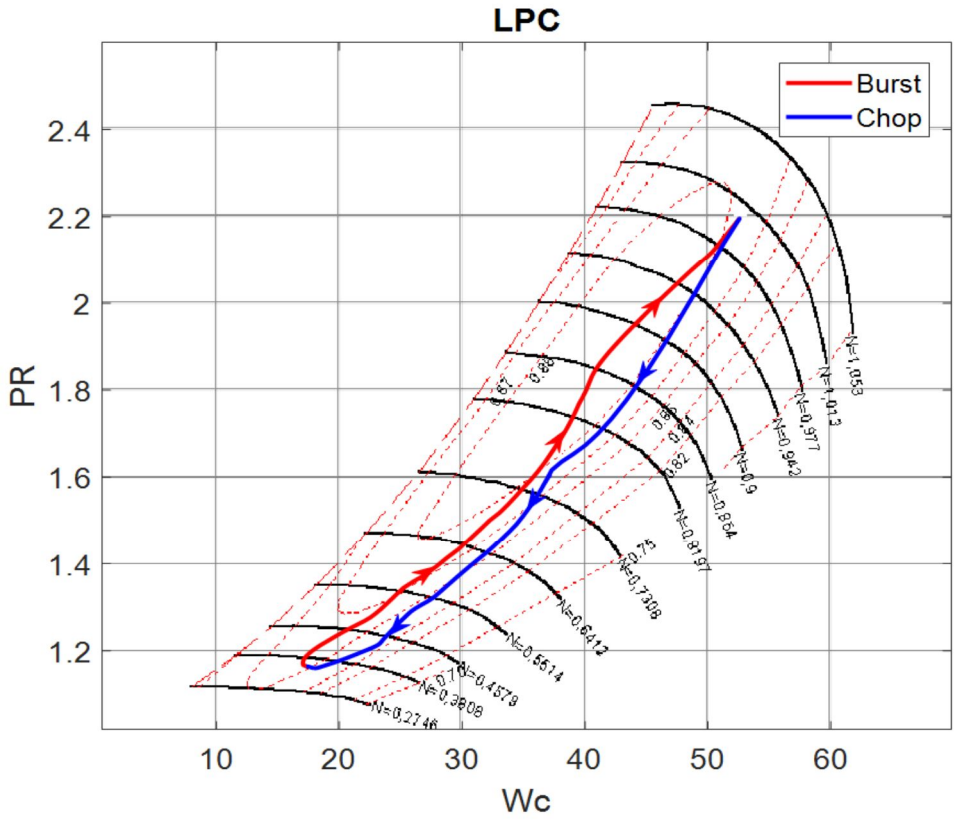


Figure 4-42 LPC transient operating line (Burst-Chop manoeuvre)

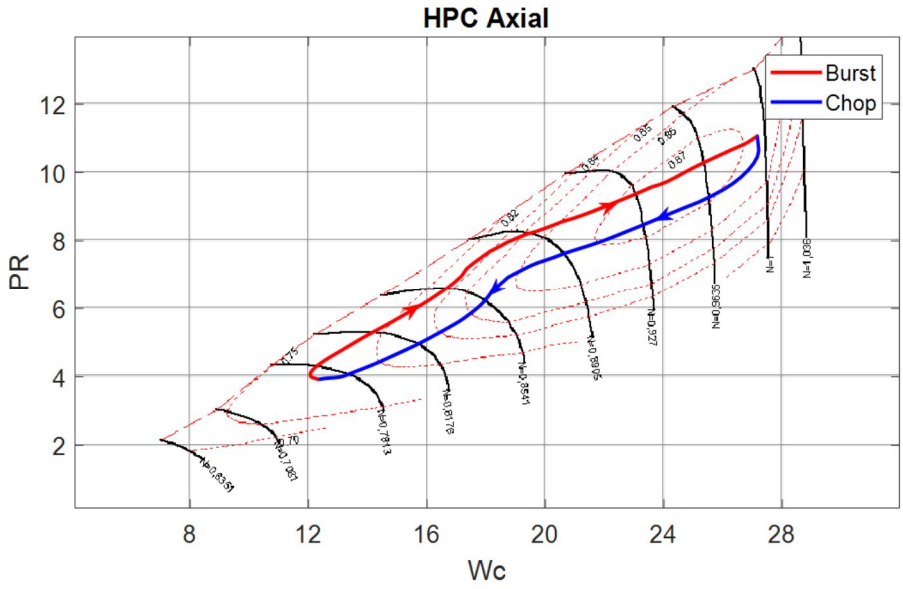


Figure 4-43 HPC transient operating line (Burst-Chop manoeuvre)

4.13 Summary

This Chapter presents the details of a nonlinear model for multi-spool engines, developed for studying power transfer method and engine emulation. The modelling method, details of each module as a lumped system, the implementation of the model in Simulink® are discussed in this Chapter.

The proposed model includes the required dynamics, including shaft dynamics for power transfer between the engine shafts via electrical machines. The great advantage of the model is its modularity, which suggests its application for various engines. It contains the engine maps which are adequate to present the primary thermodynamic behaviour of the engine. However, more details such as heat transfer modules could have been added to the model provided that the engine data were available.

Overall, this Chapter presents:

- a review on the existing multiple-spool engine models
- a review on the ICV method for engine modelling by using the engine maps
- a review on engine map scaling methods
- multiple-spool engine model development by the ICV method
- implementation of the engine model in Simulink
- validation of the engine model and error analysis for CFM56-3 engine
- detailed analytical multi-spool engine performace discussion.

The past works have presented verification and validation of the ICV analysis method, while the current work also touches upon the validation based upon test data on the CFM56-3 engine. For power exchange study, the electrical system model interacts with this model through the shaft inertia modules. Chapter 5 presents detailed studies of power transfer method on the proposed model for the CFM56-3 engine. In Chapter 6, this model is used in dSPACE for the engine emulator rig in conjunction with an integrated power centre.

Chapter 5 Electric Power Transfer

Aero-engines are designed to operate over a wide range of flow and speed to deliver the desired amount of thrust. However, the engine does not always operate at its maximum possible efficiency due to the trade-offs between engine efficiency and operational limits considering the whole flight envelope. Narrow margin for reliable operation around each engine operation point (i.e. low operability) due to the engine limits causes performance inflexibilities. These inflexibilities adds to the engine design complexity as well. This Chapter deals with the investigation into the opportunities offered by the Electric Power Transfer (EPT) between the engine shafts to increase the engine performance flexibility (i.e. operability), efficiency and stability while considering the engine operational limits.

This Chapter elaborates on impacts of the EPT on engine performance (mainly fuel consumption and compressor Surge Margin (SM)) through intensive simulations using the engine model developed in the previous Chapter. A brief analytical overview on the engine performance in terms of SM and efficiency is given first to explore the possible improvements of engine operation by implementing the EPT system. After this, a novel ***EPT adopted design (EPTAD)*** of the baseline engine is introduced to further utilize the EPT system benefits. Followed by the introduction of EPTAD, simulation results are presented for the impact of the EPT on baseline and EPTAD engines at various flight scenarios.

5.1 Engine performance criteria

The engine design is quite challenging since each operation point, within a wide speed range and environmental conditions, demands specific requirements and imposes specific limitations. For instance, SM is the main limit for compressors and maximum

tolerable temperature for turbines. SM and engine efficiency, which are subject to trade-off during engine design, are elaborated in the following Sections.

5.1.1 *Surge Margin (SM)*

Operating the engine at higher efficiency implies operation closer to surge line, wherein a minimum SM is defined as not to be violated [43]. The required SM varies for different applications. For compressors of an aero-engine, the SM depends mainly on the engine configuration, transient requirements such as acceleration rate, inlet distortion, compressor type (LP, HP, centrifugal, axial), etc. In addition, for each engine there are various effects contributing into SM uncertainty which are listed in Table 5-1. Surge line can also deteriorate due to various effects, such as compressor deterioration, thermal effects and vibration. The percentages of each item can change from engine to engine and for different compressors. For instance, the inlet distortion contributes 5% to the total fan SM. The operating line is also prone to the aforementioned effects.

By taking into account these effects, typical minimum values of SM are in the order of 10-20% for fans, 10-25% for LP compressors, and 20 to 25% for HP compressors and depends on the type of application [31, 156].

Table 5-1 SM uncertainty for the HPC [31, 157]

SM uncertainty elements	%
Reynolds number effect	1
Operating line deterioration	2
Surge line deterioration	4
Inlet distortion	1

5.1.1.1 **HPC SM**

Assuming no bleeding between the HPC and HPT, in order to keep the mass flow consistent through the combustor, the control volume block gives;

$$W_{41} - W_{30} - W_{fuel} = \frac{RT}{V}\frac{dp}{dt} \tag{5-1}$$

where W, p, R, T, V are massflow, pressure, gas specific constant, temperature and volume. By ignoring the flow dynamic between the HPC and HPT, using the equations (4-33) and (4-7) for the corrected mass flow and fuel to air ratio (FAR), and assuming no pressure loss in the combustion chamber ($p_{41} = p_{30}$), equation (5-1) can be rewritten in terms of HPC's pressure ratio and corrected mass flow as below:

$$\frac{p_{30}}{p_{24}} = \left[\frac{(1+FAR)}{W_{c,HPT}}\right]\sqrt{\frac{T_{41}}{T_{24}}}W_{c,HPC} \tag{5-2}$$

The HPT is choked for most of EOMs, meaning that $W_{c,HPT}$ is constant over the pressure ratio changes. The quantities in the bracket are then constant for a constant speed, which means that equation (5-2) is the operating line on the HPC map. The line slope depends on $\frac{T_{41}}{T_{24}}$ for a fixed geometry turbine which normally causes smaller HPC SM at lower HPC corrected speed.

At cruise condition, electric power transfer from the LP to HP shaft would increase the HPC speed, while the combustion temperature remains almost constant. From equation (5-2), both the pressure ratio and corrected flow shift to a new operating point which is lower than the steady state operation line as it is shown in Figure 5-1. Hence, EPT from the LP to HP shaft leads to increase in the available HPC SM.

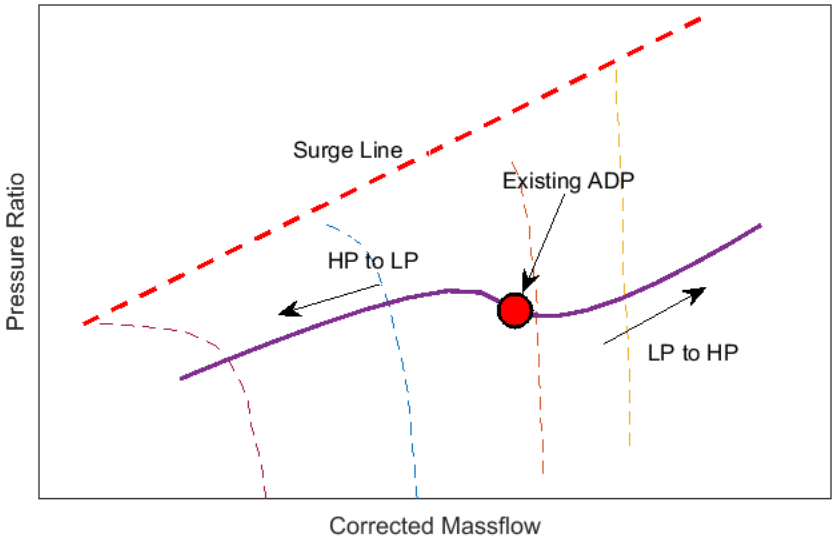


Figure 5-1 Operation line on the HPC map with the effect of power transfer (cruise)

5.1.1.2 **LPC surge**

The corrected speed of the HPC determines the outlet condition to the LPC. Provided that, the combustor is replaced by the HP spool, the LP spool can be described by relations analogous to equation (5-2), as below:

$$\frac{p_{48}}{p_{21}} = \left[\frac{(1+FAR)}{W_{c,LPT}}\right]\sqrt{\frac{T_{48}}{T_{21}}}\left(W_{c,LPC} - W_{BLD}\frac{\sqrt{T_{21}}}{P_{21}}\right) \tag{5-3}$$

By rewriting the left side of the equation (5-3) as below:

$$\frac{p_{48}}{p_{21}} = \frac{p_{24}}{p_{21}}\frac{p_{30}}{p_{24}}\frac{p_{41}}{p_{30}}\frac{p_{48}}{p_{41}} \tag{5-4}$$

Equation (5-3) can be rewritten as below:

$$\frac{p_{24}}{p_{21}}\sqrt{\frac{T_{21}}{T_{24}}} = \left[\frac{W_{c,HPT}}{W_{c,LPT}}\right]\frac{p_{41}}{p_{48}}\sqrt{\frac{T_{48}}{T_{41}}}\frac{\left(W_{c,LPC} - W_{BLD}\frac{\sqrt{T_{21}}}{P_{21}}\right)}{W_{c,HPC}} \tag{5-5}$$

Ignoring the cooling flow and using equations (4-42) and (4-52) for entropic process the equation below is obtained:

$$\frac{p_{24}}{p_{21}} = \left(\frac{2\eta\gamma}{(2\eta-1)\gamma+1}\right)_{LPC}\sqrt{\left(\left(\frac{T_{41}}{T_{48}}\right)^{\frac{\gamma}{\eta(\gamma-1)}-\frac{1}{2}}\right)_{HPT}\frac{\left(W_{c,LPC} - W_{BLD}\frac{\sqrt{T_{21}}}{P_{21}}\right)}{W_{c,HPC}}} \tag{5-6}$$

As it can be seen, the pressure between LPC and HPC (p_{24}) is established based on compressors matching and flow requirement of HPC, wherein by increasing W_{BLD} and $W_{c,HPC}$, the pressure ratio of the LPC drops. Equation (5-6) also proves the fact that p_{24} is affected by mass flow balance between the LPC and HPC.

The HPC swallows and pass the flow delivered by the LPC once the HPC speed is properly matched with the LPC one. For the same LPC speed line, the HPC demands less mass flow if the HPC speed is less than the matched value.. Hence, it acts as a blockage for the rear side of the LPC, pushing the LPC to decrease its mass flow on the same speed line. As is shown in Figure 5-2, the pressure ratio of the LPC increases and the operation point of the LPC gets closer to surge.

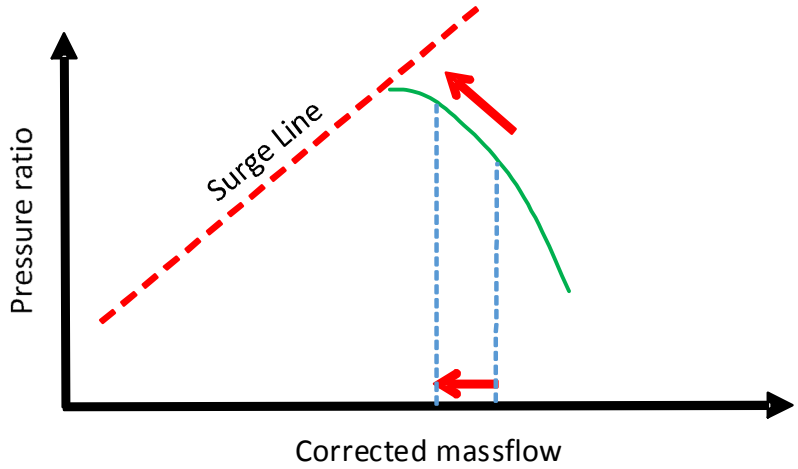


Figure 5-2 Operational speed line on compressor map

At cruise condition, the HPT power is enough to drive the HPC, building up to a matched speed with the LPC speed to swallow and pass the airflow properly without

any bleeding ($W_{Bleed} = 0$). This in fact establishes p_{24} and a core massflow to provide operation points on the compressor maps with an adequate SM. Whereas at lower speed settings, the HPC speed is lower than the desired matched value due to the thermodynamic coupling of shaft speeds. In this case, the HPC accepts less airflow causing the LPC discharge pressure to increase, which in turn increases a risk of LPC surge.

Higher LPC back pressure causes the entry flow speed to decrease which may lead to stall on the first blade rows of the HPC. To prevent this, VBVs are located between the LPC and HPC and their function is to regulate the primary flow entering the HPC and to bypass excess air from the core flow to the fan discharge duct. VBVs act primarily at low speeds where the SM of the LPC is lower. Since the bleeding of compressed air is a loss of energy, VBVs are opened no more than the value required to match the LPC and HPC flows. The VBV position is scheduled to increase bleeding as the HPC's speed decreases.

Power transfer between engine shafts can improve or worsen this condition for cruise as it is shown in Figure 5-3. EPT from the LP to HP shaft will increase the HPC speed and corrected flow which subsequently drops the pressure between the LPC and HPC. Hence, EPT from the LP to HP shaft lowers the operation point of the LPC away from the surge line, increasing the LPC SM.

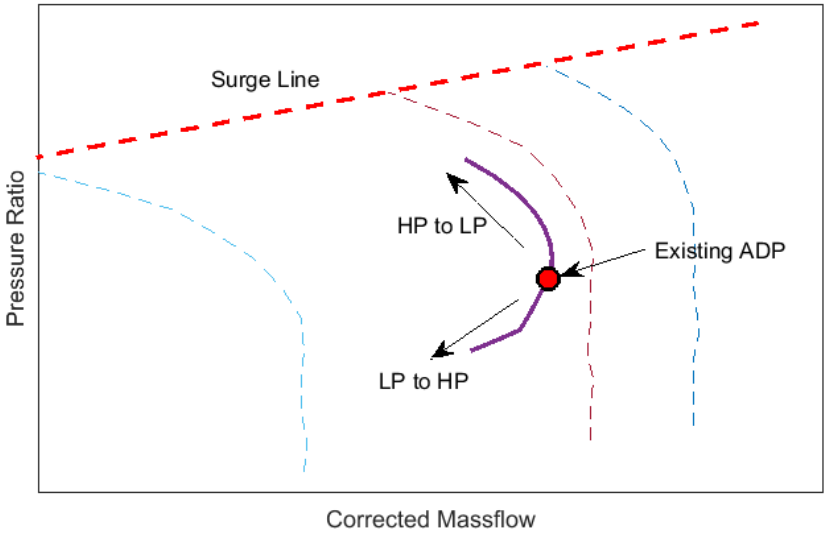


Figure 5-3 Operation line on the LPC map with the effect of power transfer (cruise)

5.1.2 *Overall efficiency*

After discussing surge margin and the impact of EPT on HPC and LPC, this Section discusses the engine efficiency. For an ideal Brayton cycle, efficiency is correlated with the compressor pressure ratio, π, as below [131]:

$$\eta_c = 1 - \frac{1}{\pi^{\frac{\gamma-1}{\gamma}}} \tag{5-7}$$

This principle also applies for the multi-spool turbofans, where ***efficiency increases with higher core pressure ratio.*** By assuming isentropic process in all components, Figure 5-4 shows the T-S (temperature-specific entropy) diagram [131], where enthalpy-drop to increase the flow's speed in the nozzles can be considered as the net power.

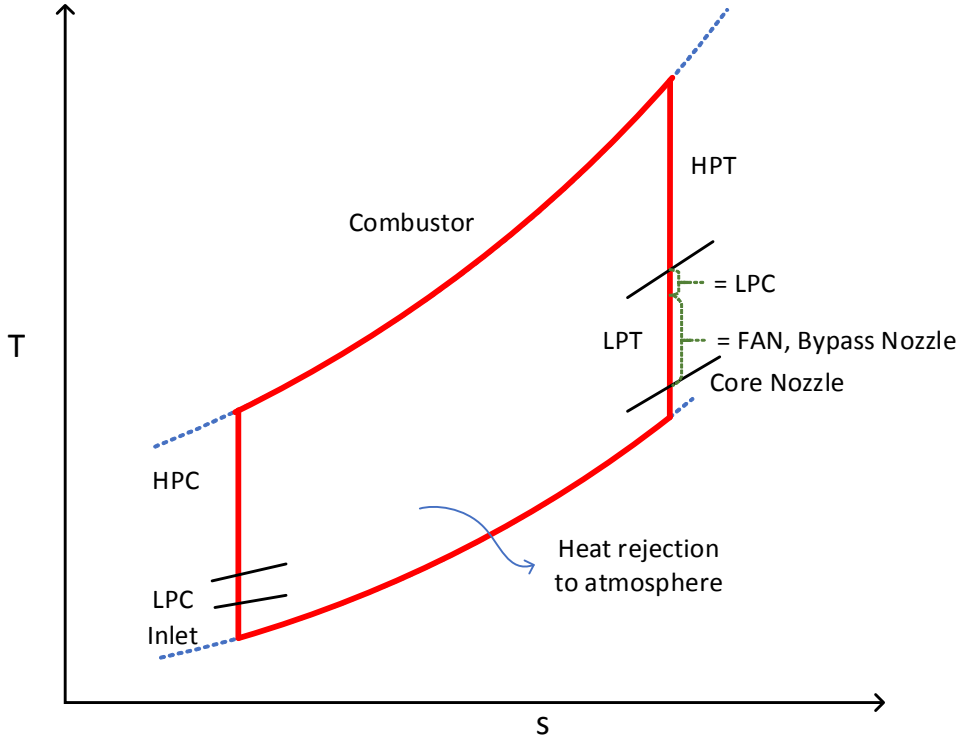


Figure 5-4 Turbofan's core T-s diagram

By assuming isentropic process and same specific heat in constant pressure,c_p in all components:

$$\eta_c = \frac{Net\ work}{Heat\ in} \cong \frac{\left[\dot{m}_{core}(T_{41} - T_{30}) - \dot{m}_{core}\left(T_{exit,core} - T_{inlet}\right) - \dot{m}_{duct}\left(T_{exit,bypass} - T_{inlet}\right)\right]}{\dot{m}_{core}(T_{41} - T_{30})} \tag{5-8}$$

Due to low fraction of $\frac{\dot{m}_{duct}\left(T_{exit,bypass}-T_{inlet}\right)}{\dot{m}_{core}\left(T_{exit,core}-T_{inlet}\right)}$, less than 5% for CFM56-3 with BPR=5, equation (5-8) can be rewritten as below:

$$\eta_c \cong 1-\frac{T_{inlet}\left(\frac{T_{exit,core}}{T_{inlet}}-1\right)}{T_{30}\left(\frac{T_{41}}{T_{30}}-1\right)} \tag{5-9}$$

Assuming no pressure loss in the combustion chamber gives:

$$\frac{P_{41}}{P_{exit,core}}=\frac{P_{30}}{P_{inlet}} \rightarrow \left(\frac{T_{41}}{T_{exit,core}}\right)^{\frac{\gamma-1}{\gamma}}=\left(\frac{T_{30}}{T_{inlet}}\right)^{\frac{\gamma-1}{\gamma}} \tag{5-10}$$

From equations (5-9) and (5-10), the cycle efficiency of the engine can be given as:

$$\eta_c \cong 1-\frac{T_{inlet}}{T_{30}} \tag{5-11}$$

which can be expressed in terms of engine's overall pressure ratio ($OPR = P_{30}/P_{inlet}$) as below:

$$\eta_c \cong 1-\frac{1}{OPR^{\frac{\gamma-1}{\gamma}}} \tag{5-12}$$

The discussion above highlights the importance of the OPR together with the efficiency of each individual component on engine efficiency. As it is shown in Figure 5-5, engine designers have been trying to accommodate higher pressures as a primarily design target, reaching an OPR of 50 [28].

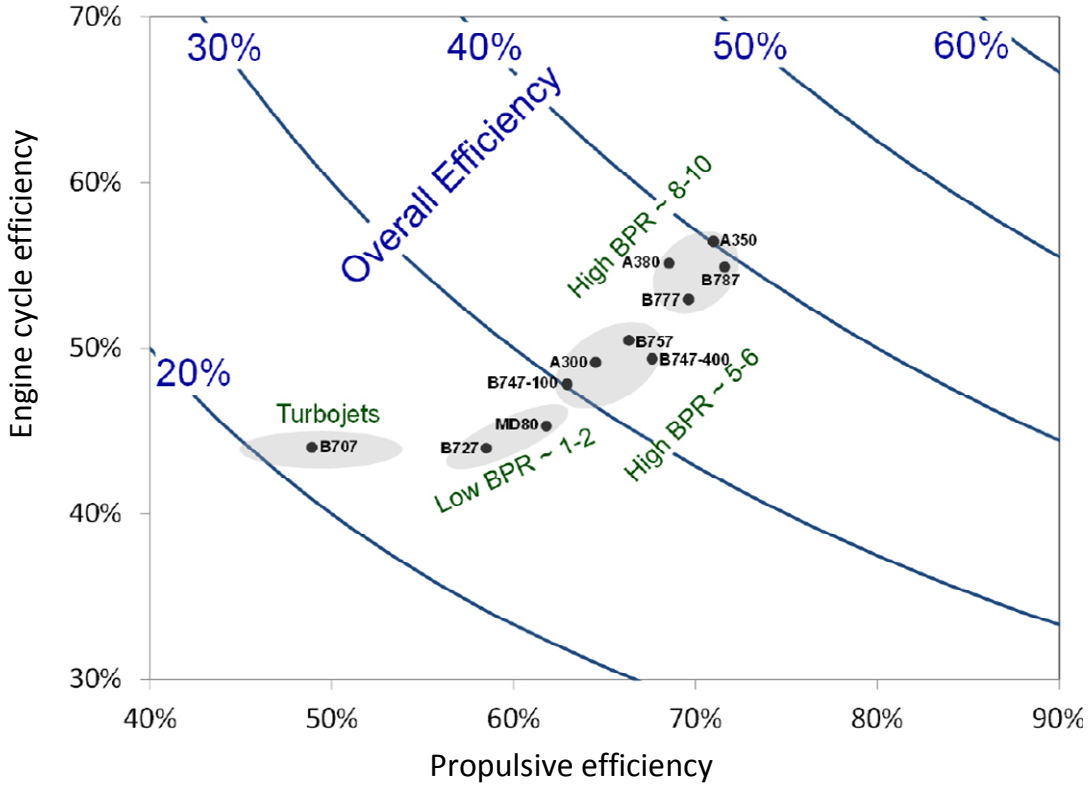


Figure 5-5 Commercial aircraft gas turbine engine efficiency trend [158, 159]

Typically for the aero-derivative engines the overall efficiency, η, is split into two parts; cycle efficiency, η_c, and propulsive efficiency, η_p, as per equations (5-13), (5-14) and (5-15). Basically, η_c represents the change in the kinetic energy of the air obtained from the fuel power and η_p expresses the propulsive power out of that change in kinetic energy.

$$\eta = \eta_c . \eta_p \tag{5-13}$$

$$\eta_c = \frac{\left(\left(\frac{W.V^2}{2}\right)_{exit} - \left(\frac{W.V^2}{2}\right)_{inlet}\right)}{W_{fuel}.LHV} \tag{5-14}$$

$$\eta_p = \frac{FV_0}{\left(\left(\frac{W.V^2}{2}\right)_{exit} - \left(\frac{W.V^2}{2}\right)_{inlet}\right)} \tag{5-15}$$

where LHV, W and V are the lower heating value, flow and airspeed. The thrust value, F, in equation (5-15) can be replaced from equation (4-59), resulting in the relation below for the propulsive efficiency:

$$\eta_p = \frac{W(V_{exit} - V_0)V_0}{\frac{W}{2}(V_{exit}^2 - V_0^2)} = \frac{2}{1 + \frac{V_{exit}}{V_0}} \tag{5-16}$$

where V_0 is aircraft speed.

For the CFM56-3 engine, the core nozzle's flow speed is $100\,m/s$ higher than that of bypass nozzle. Equation (5-16) manifests higher propulsive efficiency of the high-bypass turbofans due to lower V_{exit} of higher portion of the flow (i.e. duct airflow).

From equations (5-13) to (5-15), the overall efficiency of a turbofan is comprised of the core and bypass efficiency as below:

$$\eta = \frac{F.V_0}{W_{fuel}.LHV} = \frac{\left[\left(W(V_{exit} - V_0)\right)_{core} + \left(W(V_{exit} - V_0)\right)_{bypass}\right]V_0}{W_{fuel}.LHV} \tag{5-17}$$

If total pressure and temperature values are used, then the aircraft speed, V_0, is already considered in calculation of exit speeds as below:

$$\eta = \frac{\left[(W.V_{exit})_{core} + (W.V_{exit})_{bypass}\right]V_0}{W_{fuel}.LHV} \tag{5-18}$$

Using equations (5-18) and (4-58), the overall efficiency can be expressed in terms of the flow rate, temperature and pressure, as below:

$$\eta = \frac{\left[\left(W^2 \frac{RT_{exit}}{Ap_{exit}}\right)_{core} + \left(W^2 \frac{RT_{exit}}{Ap_{exit}}\right)_{bypass}\right] V_0}{W_{fuel}.LHV} \tag{5-19}$$

where p_{exit} is the atmospheric total pressure at the corresponding altitude of the aircraft for both the core and duct nozzles. Then, η is a function of exit temperature and square of massflow for the core and duct of the engine. The duct mass flow and exit temperature are mainly functions of fan speed while the core mass flow and temperature are subject to the performance of the engine core components including the HPC, LPC, HPT and LPT.

The corrected speed lines on the compressor maps become more vertical at higher shaft speeds. Hence, the core mass flow at high shaft speeds mainly depends on the speed of the HPC and LPC although higher back-pressure tend to slightly decrease the mass flow for a given corrected speed.

The exit temperature of the core nozzle depends on the power extracted by the HPT and LPT. The exit temperature of hot (core) and cold (bypass) nozzles can be represented in terms of temperature ratios as below:

$$T_{exit,core} = \frac{T_{exit}}{T_{50}} \frac{T_{50}}{T_{48}} \frac{T_{48}}{T_{41}} \frac{T_{41}}{T_{30}} \frac{T_{30}}{T_{24}} \frac{T_{24}}{T_{inlet}} T_{inlet} \tag{5-20}$$

$$T_{exit,bypass} = \frac{T_{exit}}{T_{13}} \frac{T_{13}}{T_{inlet}} T_{inlet} \tag{5-21}$$

For turbines, the equation (4-52) can be rewritten as a polytropic process as below:

$$\frac{T_{out}}{T_{in}} = 1 + \eta_T \left(\pi^{\frac{\gamma-1}{\gamma}} - 1\right) \cong \pi^{\frac{k-1}{k}} \tag{5-22}$$

where the polytropic index for expansion is:

$$k = \frac{\gamma}{\gamma - \eta(\gamma - 1)} \tag{5-23}$$

For compressors the compression can be rewritten as polytropic process as below:

$$\frac{T_{out}}{T_{in}} = \frac{\pi^{\frac{\gamma-1}{\gamma}} - 1}{\eta_C} + 1 \cong \pi^{\frac{k-1}{k}} \tag{5-24}$$

where the polytropic index for compression is:

$$k = \frac{\gamma}{\gamma - \frac{1}{\eta}(\gamma - 1)} \tag{5-25}$$

Substituting equations (5-23) and (5-25) in (5-20) and (5-21), the relation for the outlet temperature can be derived as follows:

$$T_{exit,core} = \left(\pi^{\frac{k-1}{k}}\right)_{Nzl,core} \left(\pi^{\frac{\eta(\gamma-1)}{\gamma}}\right)_{LPT} \left(\pi^{\frac{\eta(\gamma-1)}{\gamma}}\right)_{HPT} \left(\pi^{\frac{\gamma-1}{\eta\gamma}}\right)_{HPC} \left(\pi^{\frac{\gamma-1}{\eta\gamma}}\right)_{LPC} \frac{FAR.LHV + (c_p)_{30}}{(1+FAR)(c_p)_{41}} T_{in} \quad (5\text{-}26)$$

$$T_{exit,bypass} = \left(\pi^{\frac{k-1}{k}}\right)_{Nzl,bypass} \left(\pi^{\frac{\gamma-1}{\eta\gamma}}\right)_{FAN} T_{inlet} \quad (5\text{-}27)$$

The core thrust is then given by the equation below:

$$F_{core} = \left(W^2 \frac{RT_{exit}}{Ap_{exit}}\right)_{core} = \frac{R}{A} T_{inlet} W_{c,core}^2 \frac{P_{24}^2}{T_{24}} \frac{FAR.LHV + (c_p)_{30}}{(1+FAR)(c_p)_{41}} \left(\pi^{\frac{\eta(\gamma-1)}{\gamma}}\right)_{Nzl,core} \left(\pi^{\frac{\eta(\gamma-1)}{\gamma}}\right)_{LPT} \left(\pi^{\frac{\eta(\gamma-1)}{\gamma}}\right)_{HPT} \left(\pi^{\frac{\gamma-1}{\eta\gamma}}\right)_{HPC} \left(\pi^{\frac{\gamma-1}{\eta\gamma}}\right)_{LPC} \quad (5\text{-}28)$$

and the bypass thrust is given by:

$$F_{bypass} = \left(W^2 \frac{RT_{exit}}{Ap_{exit}}\right)_{bypass} = \frac{R}{A} P_{inlet}^2 W_{c,duct}^2 \left(\pi^{\frac{\eta(\gamma-1)}{\gamma}}\right)_{Nzl,bypass} \left(\pi^{\frac{\gamma-1}{\eta\gamma}}\right)_{FAN} \quad (5\text{-}29)$$

Each of the engine components including compressors and turbines have a dedicated isentropic efficiency value which contributes to the engine efficiency.

Next Section provides a preliminary analysis on the impact of EPT on various engine variables such as component efficiencies and their contribution into the engine efficiency by using the equations derived in this Section.

5.2 EPT impact on baseline engine's efficiency

Having been designed for optimum performance at cruise condition, turbofan components' operating points have their maximum possible efficiency, while also providing maximum thrust for take-off and climb conditions. Within the wide range of operation, the engine limits, including the permissible minimum surge margin of compressors, maximum Turbine Inlet Temperature (TIT) and maximum shaft speeds, should not be violated. In this case, designers should consider a trade-off between component efficiencies at cruise and excessive safety margins at other critical flight scenarios. For this reason, normally the HP speed at cruise is within the range of 93-95% while being at 100% at MTO. As already discussed in Section 5.1.2, turbofan efficiency increases with the increase in pressure ratio. While 5% fall in HP speed results in under-utilization of pressure ratio and engine efficiency.

For the baseline engine, EPT can be from the LP to HP shaft to increase the core pressure ratio. Equations (5-28) and (5-29) provide initial insight into the factors contributing to the engine efficiency to assess the impact of EPT. As it is presented on the component maps, W_c, π and η for all components are functions of the LP and HP speeds. Any variation in shaft speeds due to the EPT will affect the component efficiencies. Increasing the efficiency of one component can lead to decrease in that of other components. In order to consider the efficiency of all components, drive efficiency is defined as the amount of power which is used to increase pressure ratio in the compressors to the amount of power that can be extracted from the turbines. In this aspect, not only components' efficiency, but also their Power Split Ratios (PSRs) play important roles for engine efficiency. PSR can be defined as:

$$PSR_{Component} = \frac{Component\ power}{Available\ Engine\ Power} \tag{5-30}$$

Available engine power is the total amount of power produced by the turbines. Then, $PSR \times \eta$ is the contribution of each compressor to create an engine pressure ratio. As a result, the engine efficiency, η_{Engine}, can be calculated as:

$$\eta_{drive} = \frac{-\sum(PSR \times \eta)_{Compressor}}{\sum(PSR/\eta)_{Turbine}} \tag{5-31}$$

Based on the drive efficiency curve around the design point the favourable direction of power transfer to increase engine efficiency may differ. Depending on the operation mode, power circulation can be modified to optimize the engine for either higher efficiency or wider SMs or both of them. Moreover, by power transfer from the LP to HP shaft, there is a trade-off between higher core pressure ratio (by increasing HP speed) while losing thrust due to lower LP speed (i.e. FAN speed).

The impact of core pressure ratio and components efficiency on overall efficiency are considered in the next Section that introduces the EPTAD engine to exploit higher pressure ratio at various flight scenarios.

5.3 Electric Power Transfer Adopted Design (EPTAD)

With the privilege of controlled power circulation between shafts, operating points of the LP and HP shaft components can be manipulated independently. Being able to transfer power from the HP to LP can allow designers to upgrade component efficiencies by surpassing the excessive safe margins at cruise while reviving it for

take-off and climb scenarios. Due to a fast response of the electrical system in the case of any disturbance in engine performance, SMs can be quickly recovered.

In this manner, EPT can provide more flexibility by suggesting EPTAD engine to utilize the maximum available core pressure ratio at ADP. With a re-design of the engine, if the HPT pressure ratio is increased in order to change the power split ratio between the HPT and LPT of the engine, the HP speed at cruise can shift from 95% up to 97% (see Figure 5-6). Then, power transfer from the LP to HP shaft can further increase the HP shaft speed to 100% to reach the maximum available core pressure ratio. Higher HP speed improves compressor's surge margin as HPC can swallow more airflow. Figure 5-6 shows the operating points for the baseline and EPTAD designs. The operating points are obtained from initial simulation iteration.

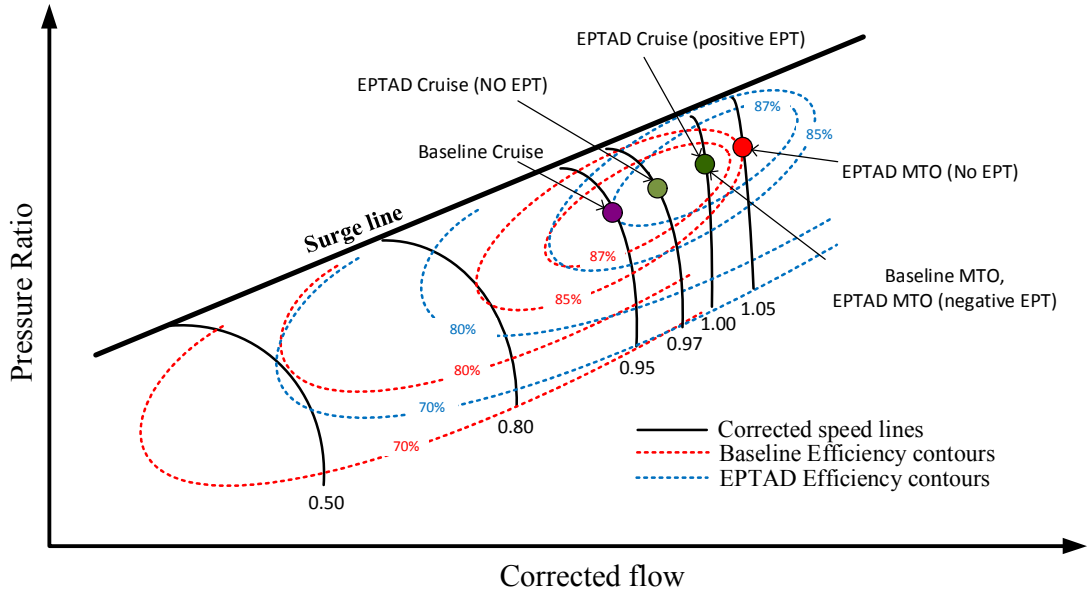


Figure 5-6 Baseline and EPTAD engines' cruise and MTO operation points on the HPC map

For the same thrust as baseline engine, the LP speed of the EPTAD engine remains approximately the same. LP shaft speed is controlled to provide thrust for high BPR turbofans.

As it is shown in Table 5-2, higher HPT pressure ratio will lead to over-speed of the HP shaft at MTO which can be compensated by power transfer from the HP to LP shaft. The matching between the LPC and HPC remains the same at MTO due to the same compressor power split ratio for the EPTAD engine. Thus, at 100% of speed for both HP and LP speed, surge margins of the HPC and LPC remain the same as the baseline engine.

Table 5-2 Shaft speeds of the baseline and EPTAD engines

EOM	Baseline: LP-HP	EPTAD: LP-HP	
Cruise	90%-95%	90%-100%	EPT LP to HP
MTO	100%-100%	100%-100%	EPT HP to LP

The HPT have higher efficiency at higher speeds which is expected to increase engine efficiency by equation (5-31). In order to further increase the efficiency, the highest efficiency design point of the HPC can move to higher speeds as it is shown in Figure 5-6. Negative EPT refers to EPT from the HP to LP shaft and positive EPT refers to EPT from the LP to HP shaft.

The LP speed at cruise condition remains unchanged in the EPTAD engine compared to that of the baseline engine. With the higher HP speed for the same LP speed, the flow matching between the compressors will change, leading to much higher LPC SM and small increase in HPC SM. At low speed setting, the HP speed is also more than its baseline values which results in higher SMs. At MTO, the compressors PSR of the EPTAD engine remains the same as the baseline engine, by having the same shaft speed values after negative EPT. In this case, the compressors have the same matching and SMs as the baseline engine. Slight changes in fuel consumption and TIT are expected due to the losses through EPT.

5.4 Simulation studies

The opportunities of the power exchange in terms of fuel consumtion reduction and surge margin increase are investigated in this Section using the engine model developed for CFM56-3 engine in Chapter 4. For the purpose of EPT, a functional model has been implemented in initial phase of study to purely assess the effect of EPT on the engine performance for steady-state simulation. The functional model has assumed an efficiency for EPT channel between 90-95%, considering the efficiencies to be; 98-99% for the gearbox, 97-98% for each of the electrical machines and 97-98% for the converter.

It should be noted that, negative EPT corresponds to the power flow direction from the HP to LP shaft and vice versa, and per-unit quantities are fractions of their amount during engine maximum available thrust at ISA-SLS. The EPT channel power capability of ±500kW (from initial stuidies iteration) is assumed, which is quite a significant amount since it is approximately 6.5% and 7.5% of the HP and LP shaft power respectively, for CFM56-3 at cruise conditions.

In this Section, simulation results with the EPT system are provided for the cases below:

- the baseline engine design
  - ✓ at a reference cruise condition
  - ✓ at various cruise condition compare to the reference condition
  - ✓ at various EPT efficiency cases
  - ✓ for degraded engines
- the EPTAD engines with two levels of power transfer (500kW and 1150kW)
  - ✓ cruise condition at reference point
  - ✓ MTO condition
- off-design analysis for the baseline and EPTAD engines
  - ✓ VBVs schedule modification
  - ✓ take off condition
  - ✓ climb condition
  - ✓ idle conditions
  - ✓ touch and go

Last but not least, weight penalty and fuel consumption analysis are presented to discuss possible outcomes in terms of propulsive efficiency.

5.4.1 *Baseline engine at cruise condition*

For most passenger aircraft, the cruise phase consumes most of the aircraft's fuel. This lightens the aircraft and raises the optimum altitude for fuel economy. For traffic control reasons, it is usually necessary for an aircraft to stay at the cleared flight level. On long-haul flights, the pilot may ask air traffic control to climb from one flight level to a higher one, in a manoeuvre known as step climb. Other factors affecting optimum cruise altitude include payload, centre of gravity, air temperature, humidity, and speed. At this altitude, the increase in aerodynamic drag power due to the higher ground speeds, and the decrease in engine thrust and efficiency due to lower air density are balanced.

Table 5-3 is listed by altitude and gross weight for Boeing 737 aircraft with most optimum performance in blue. At each combination, there is performance values such as: Average N1 (LP speed) and Mach number. The flight distance determines the approximate gross weight, which corresponds to an altitude and cruise speed that provide the best efficiency. The cruise point at 39kft and 125klb, with 88.3%N1 and

0.789 for Mach number, is selected to be the reference point for the rest of study in this Chapter (highlighted in red in Table 5-3).

For short flights of less than 250 nautical miles, the maximum altitude is generally below 30,000 feet with the most flights occurring from 20,000-25,000 feet. For flights from 250-500 nautical miles the altitude may range from 25,000 to 40,000 feet, while for flights above 500 nautical miles the maximum altitude can be considered above 30,000 feet [160].

The data from Table 5-3 is used as the input data for the engine model at cruise condition at different altitudes with different payloads. The next Section provides simulation studies at various cruise conditions.

Table 5-3 Optimum flight and engine speed for 737 aircraft [161]

Altitude		135 klb (61.2 kg)	130 klb (59.0 kg)	125 klb (56.7 kg)	120 klb (54.4 kg)	115 klb (52.2 kg)	110 klb (49.9 kg)
41 kft (12.5 km)	N1 (%)			91.6	90.2	88.9	87.8
	Mach			0.795	0.794	0.791	0.786
39 kft (11.9 km)	N1 (%)	90.6	89.4	88.3*	87.4	86.5	85.7
	Mach	0.795	0.793	0.789*	0.785	0.78	0.774
37 kft (11.3 km)	N1 (%)	87.6	86.8	86	85.3	84.6	83.7
	Mach	0.787	0.783	0.778	0.773	0.766	0.756
35 kft (10.7 km)	N1 (%)	85.9	85.3	84.5	83.7	82.8	81.7
	Mach	0.776	0.771	0.764	0.754	0.742	0.726
33 kft (10.1 km)	N1 (%)	84.7	83.9	83	82.1	81	80
	Mach	0.76	0.751	0.738	0.723	0.706	0.69
29 kft (8.8 km)	N1 (%)	81.5	80.6	79.6	78.7	77.8	77
	Mach	0.698	0.684	0.67	0.658	0.647	0.683

5.4.1.1 Engine Performance analysis for the reference point (39kft, 125klb)

As already discussed in Section 2.3, due to various reasons the engine efficiency may shift from its primarily designed maximum efficiency to lower efficiency at ADP. This means, there is still an opportunity to retrieve the efficiency by added flexibility offered by EPT. Keeping this in mind, the target of power transfer can be "moving the engine's operation point closer to its maximum achievable efficiency within the engine limits".

In this Section, the engine performance for the reference point is studied in detail to show the impact of power transfer on various engine variables. The constraint is to

keep the calculated thrust at the value set for the reference cruise condition. The engine has already been designed to deliver this amount of thrust to create optimum flight speed for maximum propulsion efficiency of the aircraft at cruise condition. For the purpose of comparison of the engine performance with and without EPT, a controller has been designed for the engine model to keep the calculated thrust at its fixed ADP value while power is being exchanged between the shafts. The following present and discuss the results of the EPT impact studies and effects on various engine variables such as shaft speeds and core flow and performance indexes such as surge margins.

a) Shaft speeds

Figure 5-7 shows the speed shift for each shaft depending on the amount of power transfer. It can be seen that HP shaft speed variation is much wider than that of the LP shaft, because the controller maintains the thrust value which changes mainly with the LP speed. It should be also noted that EPT is limited at +200kW wherein the HP speed reaches its allowable maximum value of 100% (14335rpm from Table 4-3). If the speed increases beyond 100%, it will damage the bearings, and the centrifugal stress of the blade roots will exceed the limit. As it is shown in Figure 5-7, turbine PSR for the studied turbofan is 57.5/42.5, close to typical crude 60/40 of turbofans, which approximately remains fixed during power circulation between shafts).

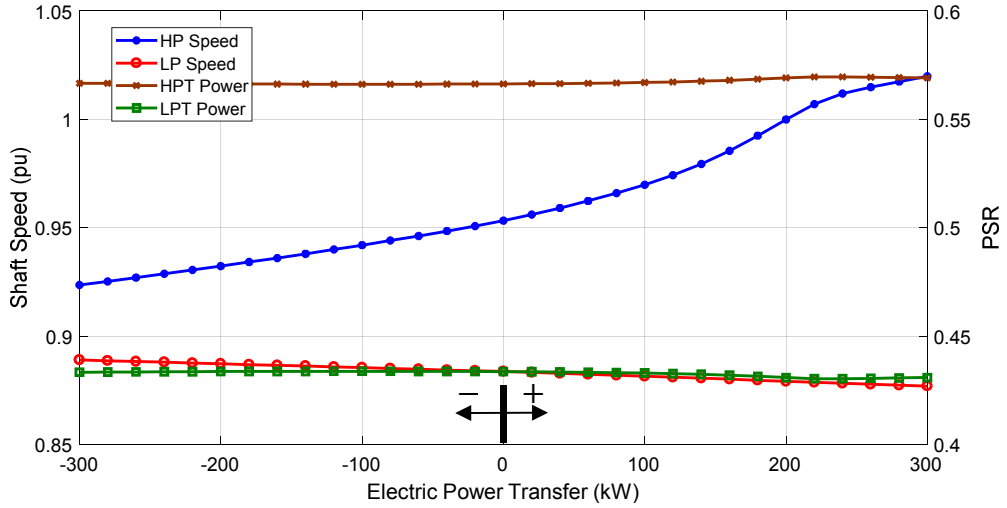


Figure 5-7 Shaft speeds and turbine PSR vs EPT (cruise)

b) Core flow and HPT exit temperature (T_{48})

Figure 5-8 illustrates the change in airflow and T_{48}. For the studied engine, positive EPT increases core airflow which can be interpreted as increasing the HPC capacity to swallow the maximum possible air flow around the ADP. By negative EPT, the HPC

speed drops and as a result the airflow decreases where the HPC cannot swallow the provided flow by the LPC.

The change in air mass flow affects T_{48} which is an indicator of the HPT inlet temperature (TIT). Clearly, by increase in the airflow, TIT decreases for the same amount of thrust.

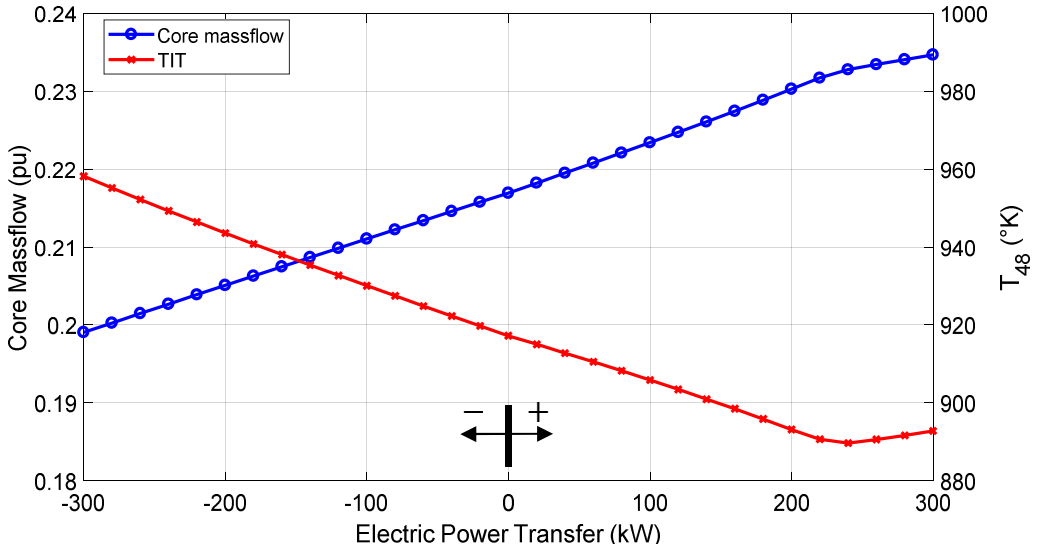


Figure 5-8. Core mass flow and T_{48} vs EPT (cruise)

c) Efficiency

Compressor efficiencies vary depending on sources of losses which include, profile loss, end wall loss, secondary flow loss, tip clearance loss, shock loss and shock boundary layer interaction. As discussed in Section 5.1.2, normally compressors are at their maximum efficiency for the reference cruise design point. Figure 5-9 illustrates efficiency increase by transferring power from the LP to HP shaft while the turbines' operation point moves to maximum efficiency. Positive EPT increases the HPT efficiency while HPC remains almost constant at its maximum value. The efficiency of LPT decrease due to the fall in its speed. While compressors' maximum efficiency contour is more or less constant around cruise design point.

By moving to higher HP speeds, efficiencies of the HPC, LPC and LPT start to decrease. In this case, by considering the efficiency of EPT as well, an optimum value of power transfer is found at around 250kW which creates a knee on engine variables in this section. The engine efficiency calculated by implementing equation (5-31) is also shown on Figure 5-9 where it varies by up to 1.25% (72.75-74 %). It is maximum at around 250kW with 0.5% increase compare to the baseline ADP and starts to decrease again beyond 250kW.

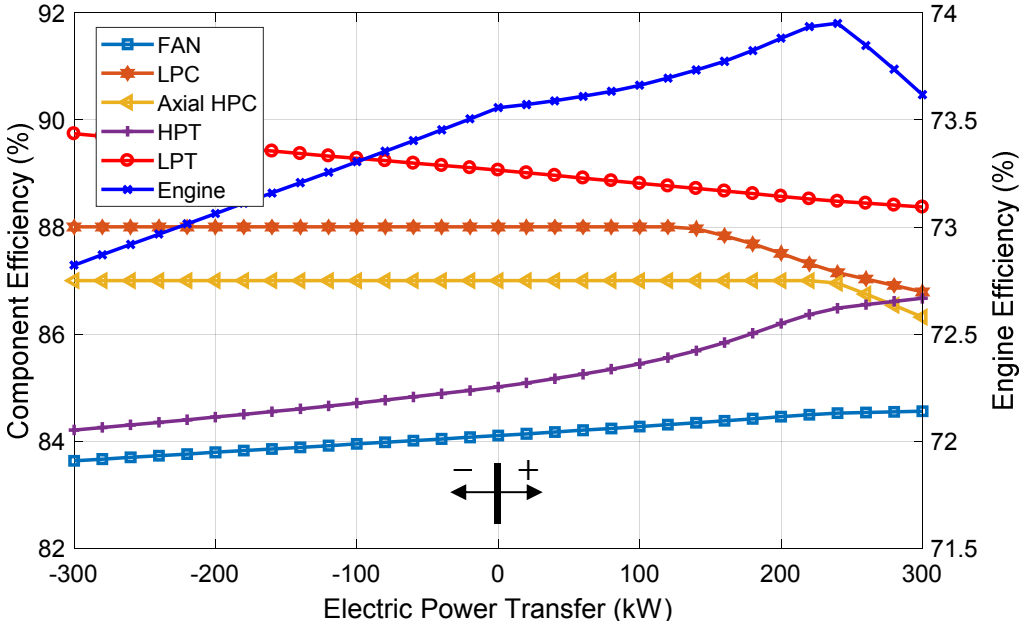


Figure 5-9. Component and engine efficiency vs EPT (cruise)

Figure 5-10 shows that when the HP shaft speed decreases the HPC acts as a blockage for the engine air flow, hence the LPC pressure ratio increases. However, the core compression ratio (p_{30}/p_{21}) decreases due to the drop in HPC pressure ratio. By increasing the HP speed by positive EPT, the core compression ratio increases continuously. Considering Figure 5-10, Figure 5-9 emphasizes the fact that for a designed engine the increase in pressure ratio by EPT does not necessarily increases the engine efficiency.

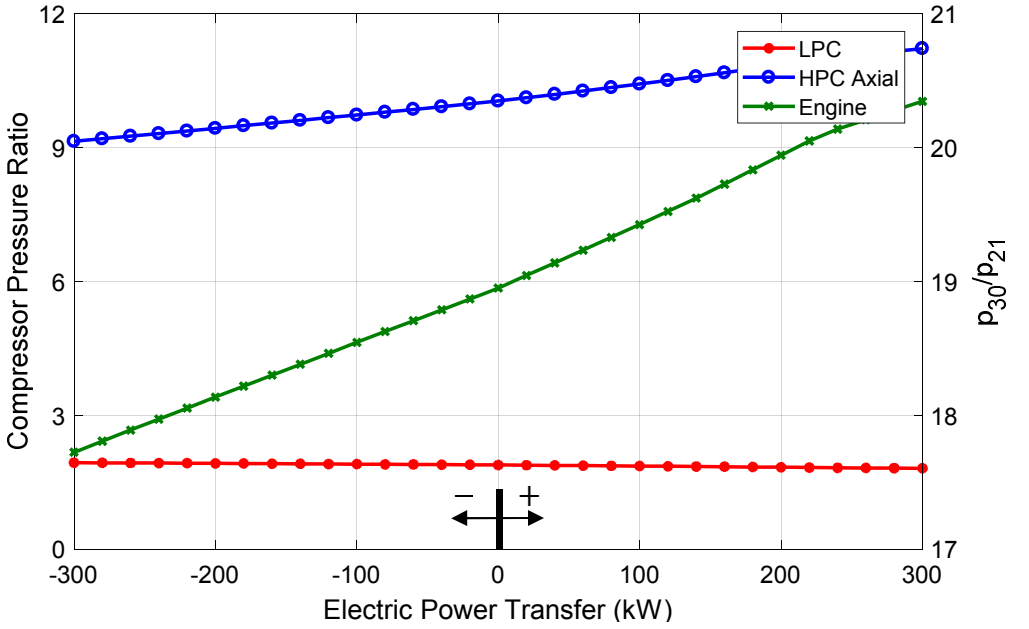


Figure 5-10. Compressors pressure ratio and (p_{30}/p_{21}) vs EPT (cruise)

d) Fuel consumption

Fuel Consumption for constant thrust is plotted in Figure 5-11 together with the fuel error. To assess the impact at cruise, the change in fuel consumption around the ADP for a fixed amount of thrust with ±300kW of EPT between the shafts is up to 2%. The change compare to the baseline ADP is 1.6% to -0.4% for the negative and positive EPT, respectively. Assuming the baseline ADP to be consistent with the real engine ADP, positive EPT up to 210kW reduces the fuel consumption up to 0.36%. However, due to maximum HP speed limit (100%) reached by +200kW of EPT, the fuel reduction is 0.27%.

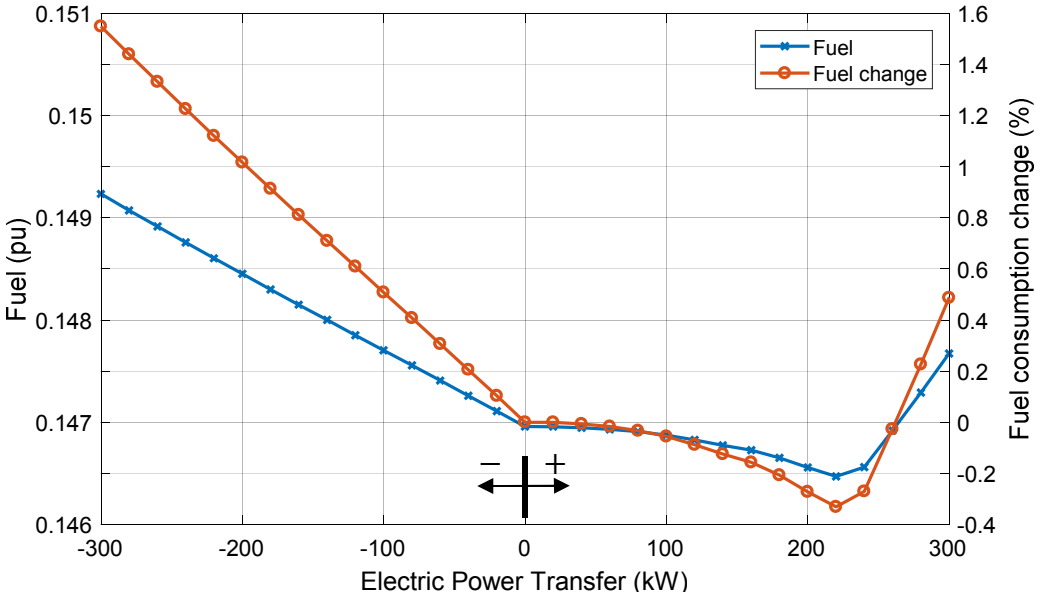


Figure 5-11. Fuel change and per-unit thrust vs EPT (cruise)

e) Surge margin

Figure 5-12 shows that the increase in engine efficiency due to positive EPT is accompanied by increase in SM of the LPC and HPC by 30% and 3%. The HPC SM does not change significantly because it relies more on the downstream components performance which do not experience too much change by EPT.

It is also shown that the fuel ratio unit (which is W_f/p_{30}, i.e. fuel flow/combustion pressure), as an indicator of surge, decreases. This parameter can be used to implement limit controllers to protect the engine against surge and over-temperature while circulating power between shafts at different scenarios.

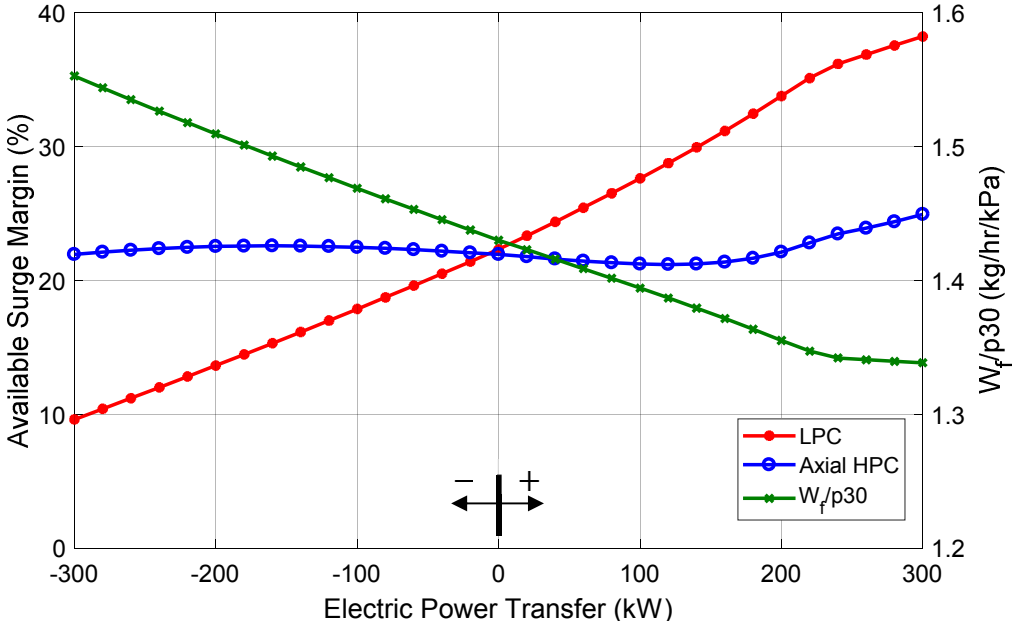


Figure 5-12. Available SM and (W_f/p_{30}) vs EPT (cruise)

Results presented in this Section were derived for the reference cruise condition. However, optimum cruise point may change depending on the payload and requirements from air traffic control. The next Section elaborates the EPT impact on various cruise points, provided in Table 5-3.

5.4.1.2 Fuel consumption change at various cruise conditions

If the engine is designed for one cruise point (reference point), the efficiency can be decreased for other cruise points. Figure 5-13 shows simulation results for fuel consumption change upon various cruise conditions taken from Table 5-3. Fuel consumption decreases by higher values of positive EPT at higher altitudes. This highlights the fact that EPT should also be optimized for each operation point. The amount of desired EPT for cruise points is 0-300kW. These figures are obtained by assuming the EPT efficiency to be 90%. The next Section discusses the impact of EPT efficiency on the fuel consumption change.

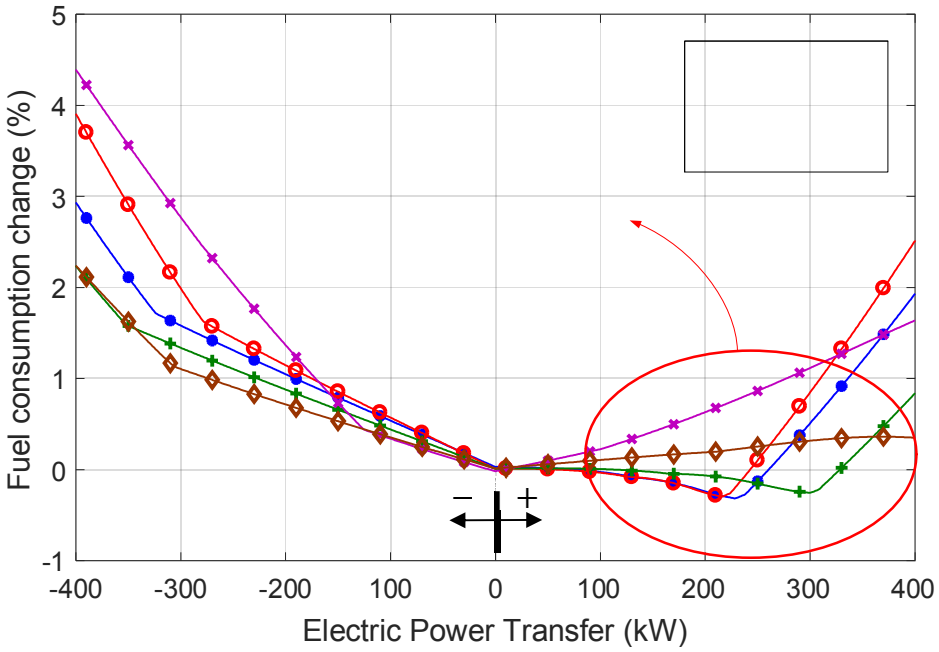


Figure 5-13 Fuel consumption change vs EPT, for various cruise conditions

5.4.1.3 EPT efficiency the impact on fuel error

The discontinuity in the shape of figures around zero EPT is due to EPT channel losses. The efficiency of EPT depends on various factors including machine type, machine and converter design, cable length, gearbox design, etc. The study of system efficiency is out of the scope of this thesis. Figure 5-14 presents the results for the reference point at different EPT efficiency values to assess the effect of losses due to EPT itself.

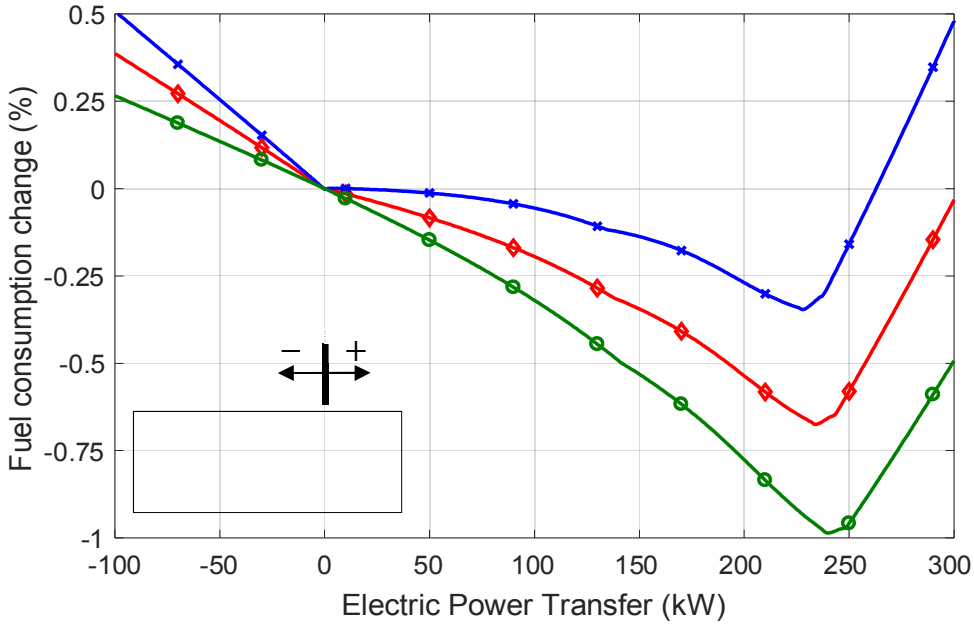


Figure 5-14 Fuel consumption change at various EPT system efficiency

In order to evaluate the impact of EPT efficiency on fuel consumption, the results on Figure 5-14 are given at 100%, 95% and 90% of EPT efficiency. At 100% EPT efficiency, the reduction in fuel consumption at cruise condition is almost 1%, compare to that of almost 0.3% with the 90% efficiency considered for this study. It is also shown that if the EPT efficiency increases from 90% to 95%, fuel consumption can further decrease from 0.3% to 0.7%.

5.4.1.4 Aging of the HPT

The results presented in previous Sections are for off-the-shelf engine. While gas turbine components are prone to degradation due to harsh working environment at high pressure and high temperature. The main deterioration effects include increased tip clearances, changes in airfoil geometry and surface quality. Degradation pushes the compressor and turbine stages to off-optimum operation points at lower SM and efficiency which results in reduced corrected flow capacity and pressure ratio of the compressors. The EPT approach is expected to improve the engine performance by manipulating the shaft speeds depending on the degradation level of the components.
For a compressor, degradation shifts the operating points on a constant corrected speed to lower corrected flow at reduced efficiency values for whole compressor map. As discussed in Section 4.7, the pressure ratio-flow relationship for the HPC is a function of HPT performance, which means the operating line of the HPC remains unchanged if only the HPC is deteriorated. However, due to decrease in the HPC efficiency, the HP shaft should run at higher speeds to provide the same flow rate and pressure ratio for the engine core.
In service, due to regular overhauls the change in compressor efficiency is not significant compared to that of the turbines. Typically, the HPT can experience either decrease or increase in its flow capacity due to degradation in the effective throat area. Efficiency of HPT can also be reduced due to fouling or change of operation point due to other effects [45-47]. The combustion system does not experience severe changes in efficiency compare to that of rotary parts such as compressor and turbines [44, 45].
In order to study the effect of aging on the engine performance, the LP shaft components and the combustor are assumed not to encounter any change in their performance. Whereas the HPT's efficiency and mass flow are changed ±5% and -2%

respectively. Figure 5-15 and Figure 5-16 show the impact of EPT on the performance of off-the-shelf and degraded engine.

As expected, due to the decrease in efficiency of the degraded engine, the fuel consumption for the baseline engine (zero EPT), has increased by approximately 1.1% for degraded engine with lower HPT capacity (green line in Figure 5-15) and 2.6% for degraded engine with higher HPT capacity (red line in Figure 5-15). As it is illustrated in Figure 5-15, 200kW and 300kW of EPT can help decrease the change in fuel consumption by 0.2% for the lower and higher HPT capacity cases respectively.

The SM values for the degraded engines have also experienced positive and negative changes compare to off-the-shelf engine. The LPC SM decreases with degradation while the HPC SM increases with increase in HPC capacity. Similar to off-the-shelf engine, positive EPT can help to redeem severe changes in the SM up to 10% by 500kW EPT for the HPC.

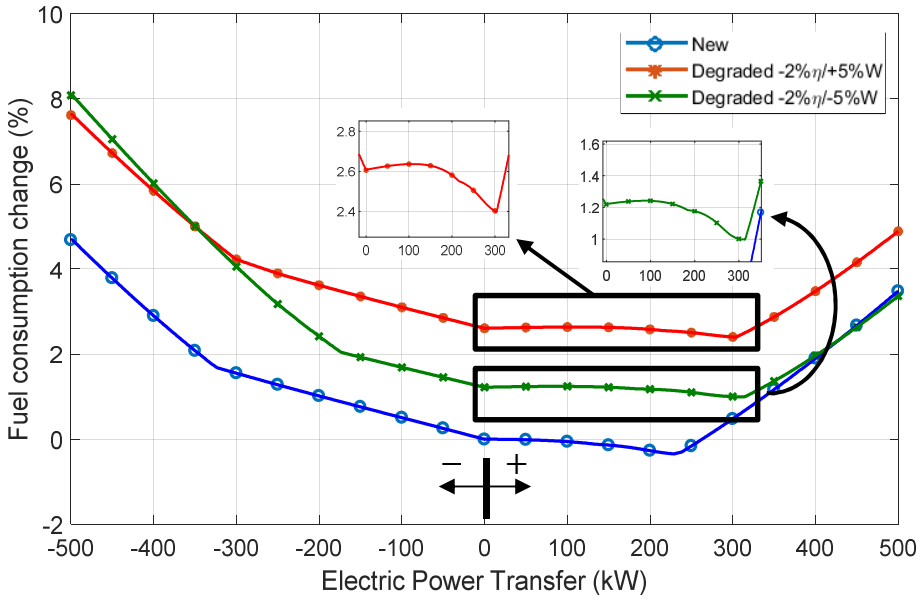


Figure 5-15 Fuel consumption change vs EPT for the degraded engine

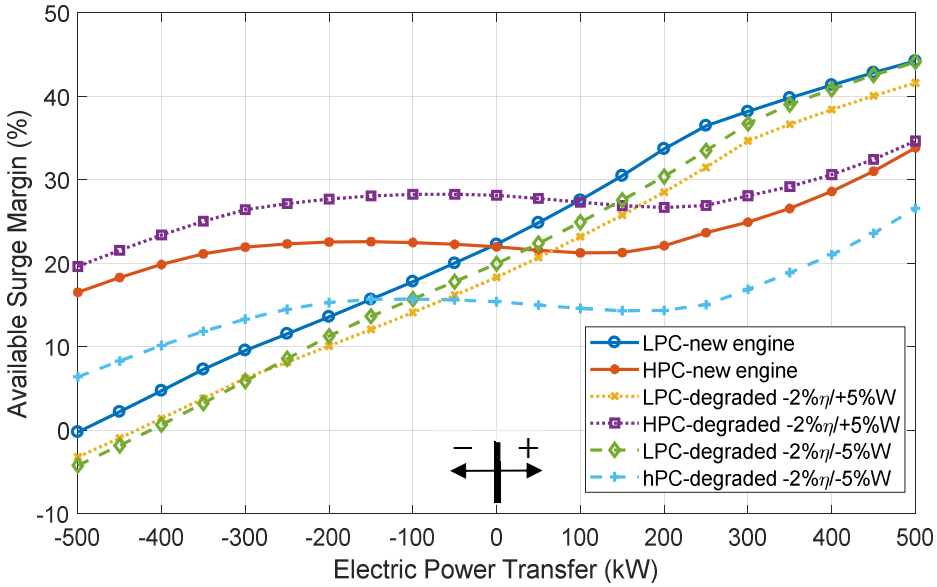


Figure 5-16 Available SM vs EPT for the degraded engine

Summary of EPT effects for the baseline engine

Key benefits of the EPT system for the baseline engine from this Section are as below:

- Optimizing engine performance for various cruise points
- Up to 0.27% fuel reduction for cruise operation with 250kW EPT
- Improvement in SMs at cruise condition
- Redeeming SMs of the degraded engine

5.4.2 *EPTAD engine with 1150kW of EPT (EPTAD-1150)*

For the baseline engine, only positive EPT can improve the engine performance. In this Section, in order to exploit both positive and negative EPT, EPTAD is proposed. As discussed in Section 5.3, the aim of turbines' re-design is to run the engine core at maximum allowable speed (i.e. 100%) at both cruise and take off condition. For the EPTAD engine, the maximum efficiency contour of the HPC moves to 100% HP speed while keeping the maximum efficiency level. In order to have 100% HP speed at 90% LP speed at cruise condition (instead of baseline engine's 95% HP speed at 90% LP speed), the power split ratio between the HPT and LPT should be modified. In order to change the power split ratio between the LPT and HPT, the pressure ratio of the HPT should increase. As discussed in Section 4.7, the pressure ratio of turbines is function of LPT corrected flow and HPT pressure ratio. Hence, the LPT nozzles and HPT blades should be re-designed to increase HPT to LPT power ratio.

However, by increasing the HPT power, when the LP speed reaches 100% during MTO, the HP speed exceeds 100% limit and the engine parameter limits such as TIT, SMs and p_{30s} are also violated. Negative EPT is implemented in this scenario to push the HP speed back to allowable value of 100%, while the fuel controller maintains the LP speed at maximum value of 100%.

As it is shown in Table 5-4, in order to have a better comparison in terms of propulsive efficiency, thrust is fixed for the EPTAD and baseline engines. By keeping this constraint, in order to move the HP shaft speed from 95% to 100% at cruise condition, 9% increase in the corrected flow of the LPT is required to increase the HPT expansion ratio adequately.

In order to address over-speed of the HP shaft at MTO, negative EPT from the HP to the LP shaft is required. For CFM56-3, the amount of required EPT is -1150kW which is approximately 5% and 26% of HP shaft power at MTO and cruise condition respectively. It is important to keep the EPTAD engine within the same operational limits of the baseline engine. As it is stated in Table 5-4, the turbine PSR for EPTAD-1150 engine has changed by roughly 3% at almost the same HPC pressure exit for MTO condition. In MTO, TIT experiences 3°C increase due to increase in fuel consumption, because of EPT losses, to deliver the same amount of thrust at 100% of LP and HP speeds.

The matching between the LPC and HPC remains the same at MTO due to the same compressor power split ratio. The LPC SM improves by 11% at cruise condition and the HPC SM is not lower than the baseline values at cruise and MTO condition.

Table 5-4 Comparison between the baseline and EPTAD-1150 engines

	Baseline cruise	EPTAD-1150 cruise	Baseline MTO	EPTAD-1150 MTO
EPT	0	0	0	-1150 kW
Thrust (kN)	21.92	21.92	102.6	102.6
PSR (HPT/LPT)	56.65/43.35	59.51/40.49	54.39/45.61	57.23/42.77
HP speed (%)	0.95	1.00	1	1.00
LP speed (%)	0.88	0.88	1	1.00
TIT (°K)	1206	1180	1533	1536
P30 (bar)	5.6	5.88	24.40	24.51
PR	10.0	10.8	11.1	11.1
Fuel (kg/s)	0.2222	0.2191	1.137	1.144
LPC SM (%)	22.3	33.9	33.0	33.6
HPC SM (%)	22	22.6	19.0	19

The benefit of EPTAD-1150 engine is 1.4% of fuel consumption reduction at cruise condition. TIT also decreases by 2.1% at cruise condition which is good in terms of engine life.

5.4.3 *EPTAD engine with 500kW of EPT (EPTAD-500)*

In the previous Section, the HP speed design point at cruise condition is moved to 100% at zero EPT, which at MTO condition requires -1150kW EPT. In order to decrease the amount of EPT, a trade-off can be considered by moving the HP speed design point to 97% and further increasing it to 100% by positive EPT, which at MTO requires -500kW EPT.

The turbine PSR is increased to have higher HP speed at cruise condition as it is shown in Figure 5-17. In this design, +111kW is required to increase the HP speed to 100% at cruise condition. At cruise condition, this decreases the fuel consumption by 0.64% and increase the LPC SM by 10% with 2% decrease in TIT (see Table 5-5). The turbine PSR changes by 1.5% while keeping the engine limits by negative EPT at MTO condition.

Table 5-5 Comparison between the baseline and EPTAD-500 engines at ADP

	Baseline cruise	EPTAD-500 cruise	Baseline MTO	EPTAD-500 MTO
EPT (kW)	0	+111	0	-500
Thrust (kN)	21.92	21.92	102.6	102.6
PSR (HPT/LPT)	56.65/43.35	58.05/41.95	54.39/45.61	55.70/44.30
HP speed (%)	0.95	1.00	1.00	1.00
LP speed (%)	0.88	0.88	1.00	1.00
TIT (°K)	1206	1180	1533	1534
P30 (bar)	5.6	5.88	24.40	24.50
PR	10	10.8	11.1	11.1
Fuel (kg/s)	0.2222	0.2205	1.137	1.139
LPC SM (%)	22.3	33.8	33.0	33.6
HPC SM (%)	22.0	22.3	19.0	19.2

By changing the turbine PSR by 1.5%, the HP speed at cruise point increases by 2% with no EPT and exceeds 100% beyond +111k as it is shown in Figure 5-17. The LP speed remains almost the same due to the same thrust requirement.

Figure 5-18 depicts fuel consumption change due to drive efficiency change for various EPT values. Positive EPT is favourable up to 130kW, almost at maximum reachable efficiency. The drive efficiency declines beyond 150kW since the HPC efficiency drop is more than the HPT efficiency rise at higher HP speeds. However, EPT is not allowed to exceed +111kW to avoid HP over-speed. The fuel consumption reduces by 0.64% at +111kW.

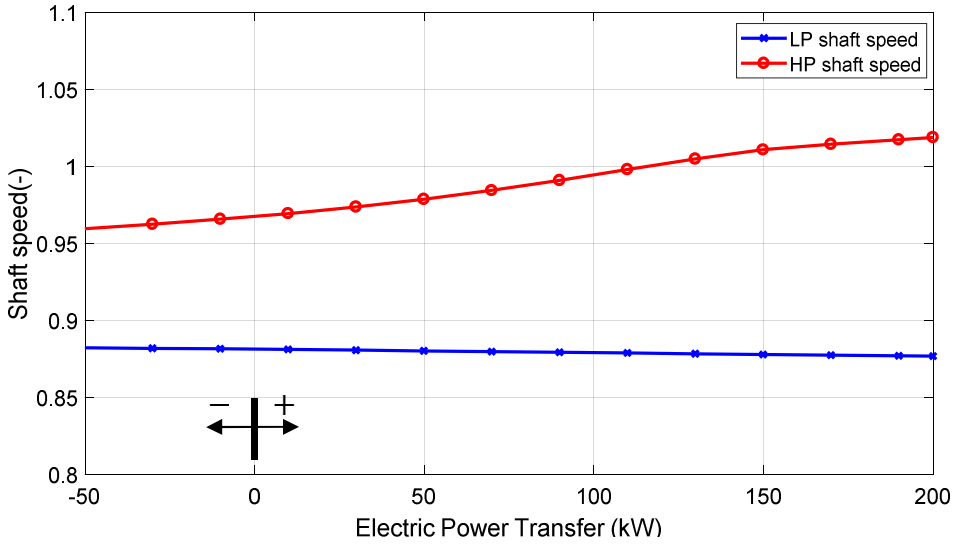


Figure 5-17 Shaft speed change vs EPT for EPTAD-500 engine

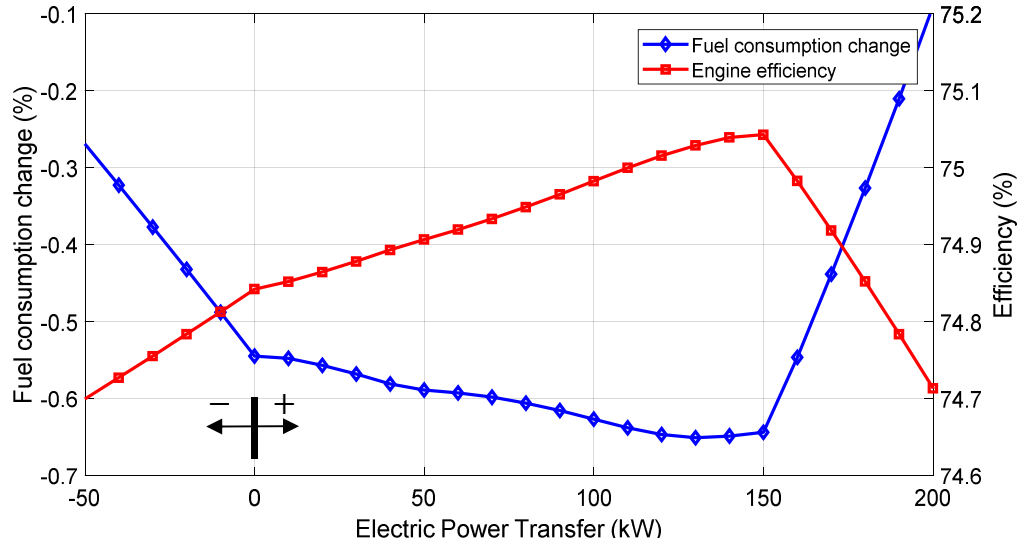


Figure 5-18 Cruise fuel consumption change for the EPTAD-500 engine

Summary on EPT effect for the EPTAD engines

Key benefits of the EPT system for the EPTAD engine from this Section are as below:

- Increasing the engine efficiency by introducing new conceptual design
- Keeping the engine limits at MTO condition for the EPTAD engines
- Up to 1.4% fuel reduction for cruise operation for the EPTAD engines
- Improvement in SMs at cruise condition

The optimum EPT system in terms of the amount of EPT value, either 1150kW system or 500kW system, has weight penalties which affects the propulsive efficiency. A crude system weight analysis and propulsion efficiency are provided at the end of this Chapter.

5.4.4 *Off-design condition*

Since the HPC receives the airflow from the LPC, it is always favourable if HPC operates at higher speeds. At idle setting, the HPC speed can be increased by taking power from the LP shaft and feeding it to the HP shaft.

In order to provide an insight for the idle performance of the baseline and EPTAD engines, their steady-state operating line from full throttle to idle speeds at ISA-SLS condition are shown in Figure 5-32 and Figure 5-20 for the LPC and HPC respectively. The VBVs schedule is kept unchanged for these results.

A PI controller has been implemented to regulate the amount of EPT to increase the HP speed to its maximum permissible value. The required EPT is reduced at lower thrust set-points with decreased HPT power which results in HP speed drop thermodynamically as well.

The “blue” operating lines correspond to the baseline engine without EPT system from idle to full throttle setting. The “red” operating line shows that positive power transfer from 0 to +500kW improves the baseline engine’s compressor stability by lowering the operating line, thus increasing the surge margin. The “green” lines are for the EPTAD-500 engine with EPT from -500kW to +500kW. For the baseline engine, EPT is not required for full throttle setting (100% LP and shaft speed), while for the EPTAD-500 and EPTAD-1150 engines -500kW and -1150kW of EPT is required respectively to keep 100% LP and HP shaft speeds. As it is shown by the “purple” line in Figure 5-20, the EPTAD-1150 engine keeps the HP speed at its maximum value by EPT from -1150kW to +950kW.

The operating line of the HPC, shown in Figure 5-20, is improved significantly by moving away from surge line at narrower speed range. The LPC operating line is also shifts away from the surge line, however, at lower pressure ratio and efficiency. The shape of LPC operating lines highly suggests decrease in VBVs opening which is discussed in the next Section.

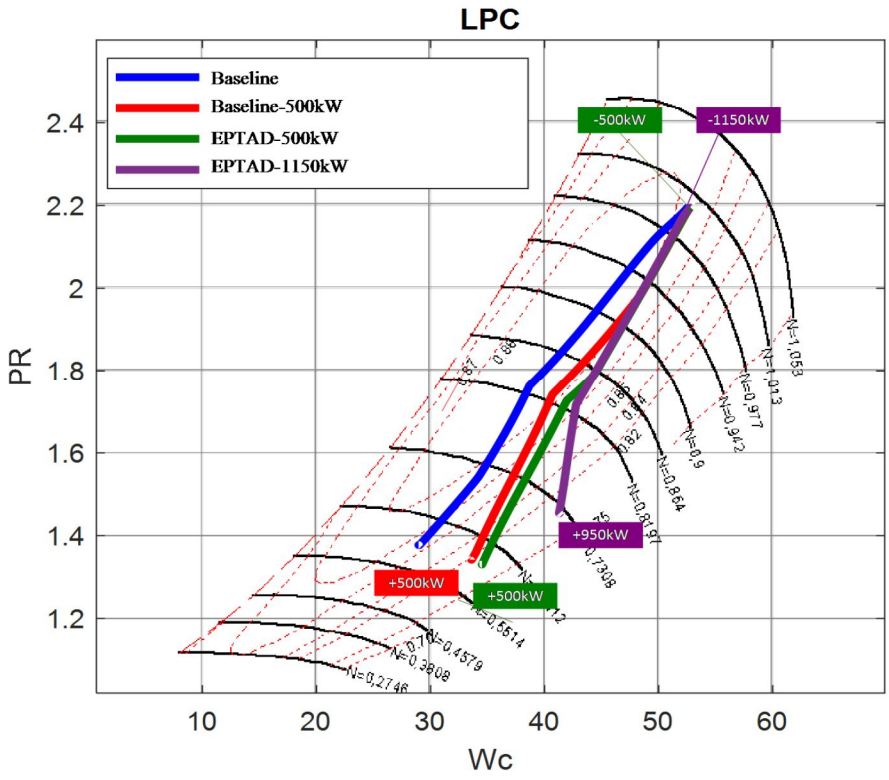


Figure 5-19 LPC's steady-state operating lines at ISA-SLS (baseline VBV schedule)

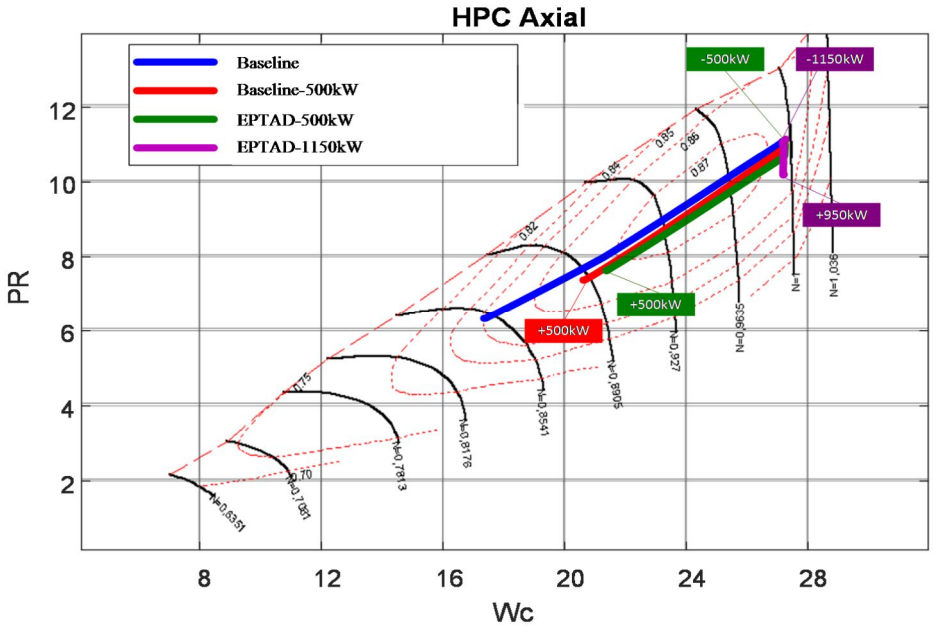


Figure 5-20 HPC's steady-state operating lines at ISA-SLS (baseline VBV schedule)

5.4.5 *VBVs schedule modification*

If the speed of the HPC is properly matched with the LPC value at low speed settings, there will be no need for air bleeding. Therefore, VBVs can be removed without any

concern about airflow limits. By positive EPT the idle speed of HP shaft increases considerably which suggest decrease or removal of the air bleedings, depending on the amount of EPT. In equation (4-75) for the determined value of W_{Bleed}, p_{24} changes up to a point to have equilibrium point in the control volume between the HPC and LPC. By positive EPT the HP speed and HPC corrected flow increases while the LPC corrected flow remains unchanged.

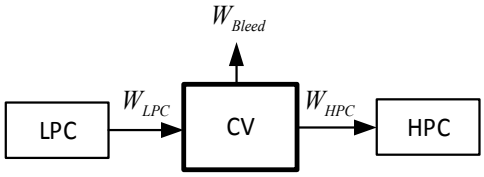


Figure 5-21 Control volume between the LPC and HPC

The VBV schedule should be modified for the EPTAD engine with EPT due to different compressor matching. The LPC SM is very high in the EPTAD engine (see Figure 5-19) which suggests decrease in the opening of the VBVs. In order to re-schedule the VBVs, a typical PI controller for industrial applications is applied, as shown in Figure 5-22, to regulate the VBVs, while the engine's main LP speed controller regulates the LP speed on the steady-state operating line. VBVs controller should keep the LPC operating line below the baseline engine's LPC operating line by adjusting the LPC flow for various LP speeds.

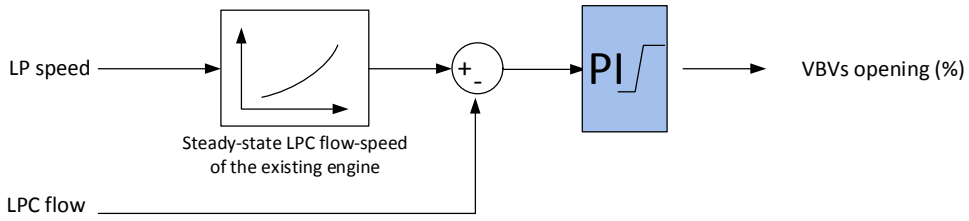


Figure 5-22 VBVs PI controller

The controller's output against either the LP or HP speed gives the new VBV schedules, shown in Figure 5-23. VBVs' opening depends on the HP speed increase by EPT where results show that by +500kW of EPT for the baseline and EPTAD-500 engines it can be decreased by 58% and 65% respectively, while by +1150kW of EPT for the EPTAD-1150 engine it can be removed .

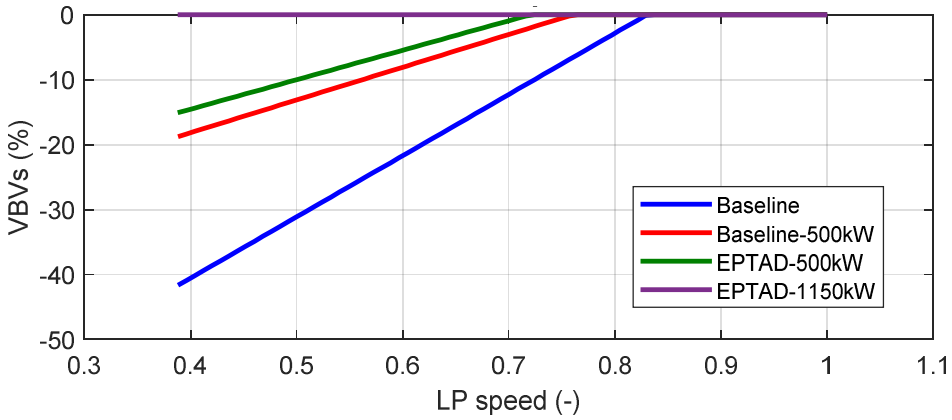


Figure 5-23 VBV schedule for the baseline and EPTAD engines

The EPT PI controller regulates the amount of EPT to increase the HP speed to its maximum permissible value. As it is shown in Figure 5-24, for the baseline engine positive EPT keeps the HP speed at its maximum value for LP shaft speed between 1-0.93. For the EPTAD engines, negative EPT is implemented by EPT controller to avoid HP speed exceeding its maximum value for high LP shaft speeds, at low LP speed positive EPT is implemented to increase the HP speed. For the baseline engine, the HP speed range is 0.74-1.00, while the EPTAD-1150 engine narrows down the HP speed range (from 0.9-1) for the same LP speed (0.4-1).

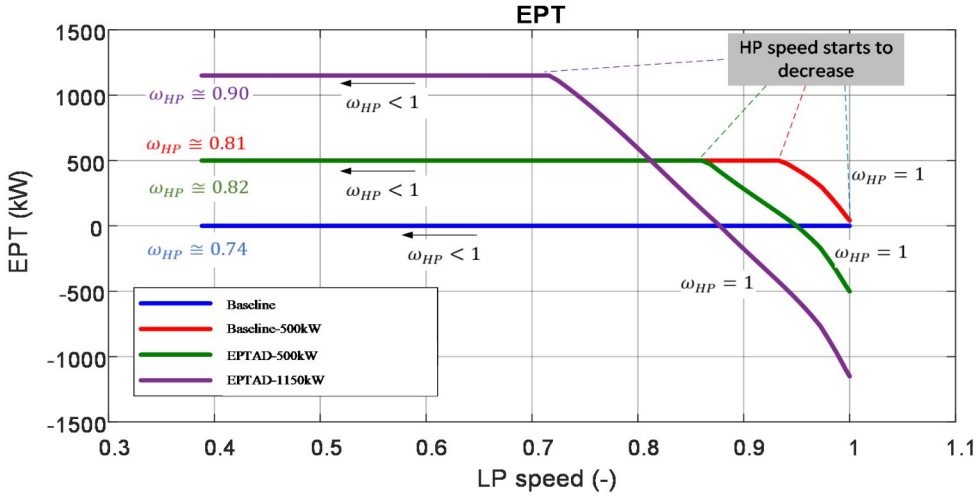


Figure 5-24 Steady-state shaft speeds at ISA-SLS (re-scheduled VBVs)

The operating line on compressor maps are shown in Figure 5-25 and Figure 5-26. The baseline LPC SM is not violated by re-scheduling of the VBVs. At maximum speed negative EPT has been implemented to avoid the HP speed exceeding its maximum permissible value (100%). At low speed settings positive EPT has been implemented to increase the HP speed. The corresponding operating points with the same LP speed for the baseline and EPTAD engines are shown on the operating lines. The HPC operating points move to higher speeds with higher corrected mass flow. Higher HP

speed at idle condition also suggests elimination of VSVs. However, this has not been modelled in this study due to lack of data regarding map changes with VSVs.

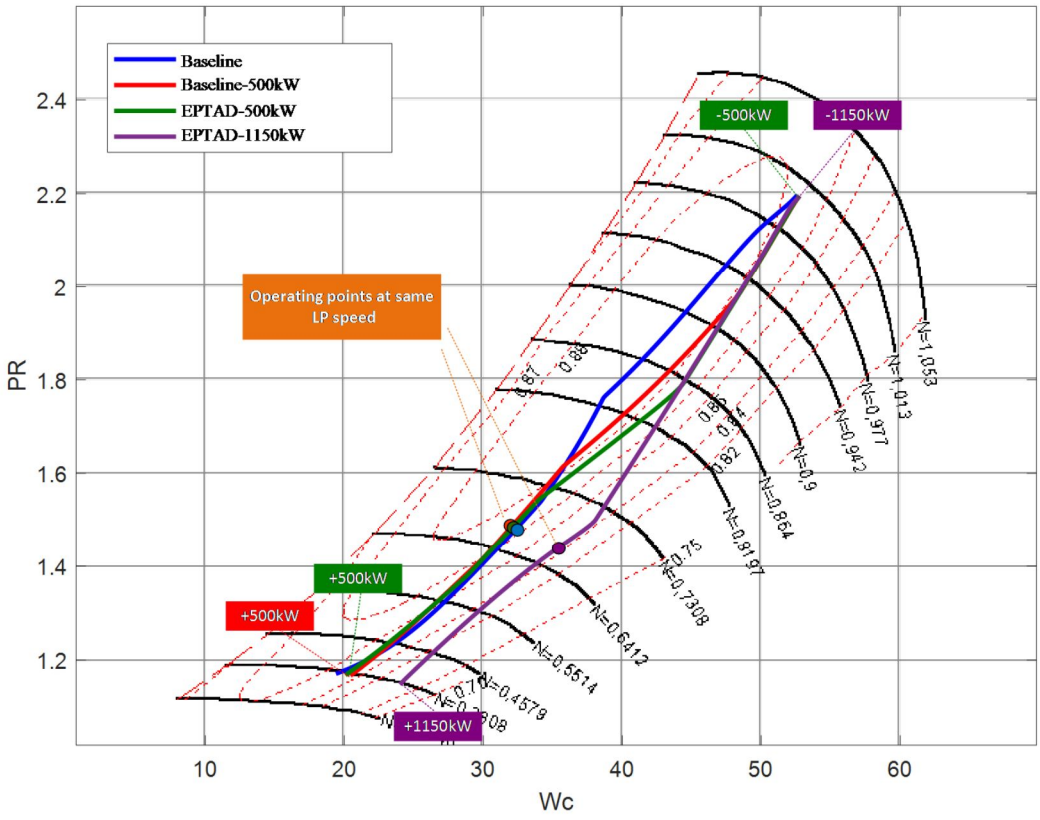


Figure 5-25 LPC steady-state operating lines at ISA-SLS (re-scheduled VBVs)

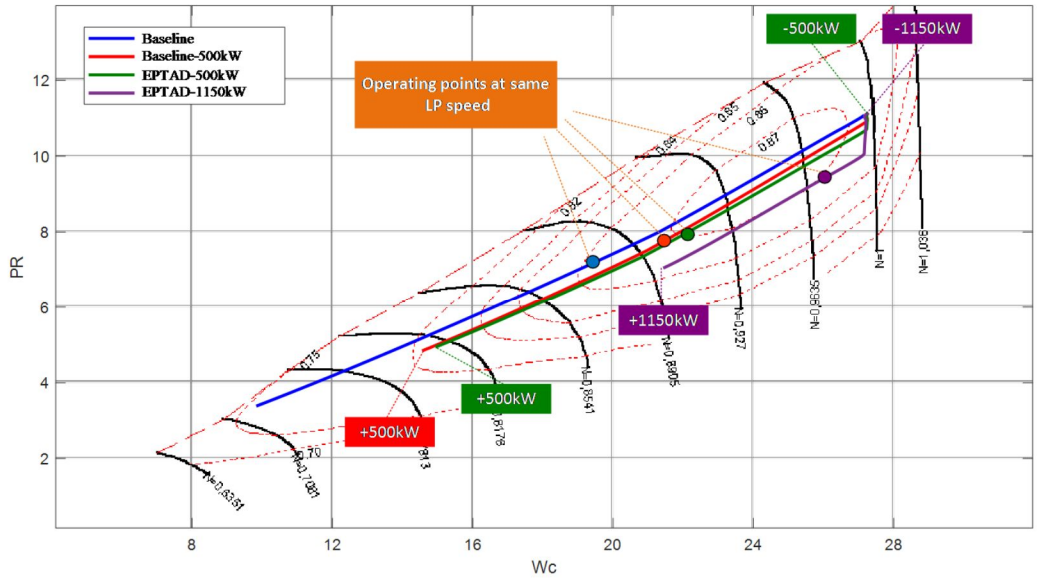


Figure 5-26 HPC steady-state operating lines at ISA-SLS (re-scheduled VBVs)

In order to have a better comparison of surge margins, Figure 5-27 and Figure 5-28 highlight the fact that the surge margins of baseline and EPTAD engines have improved.

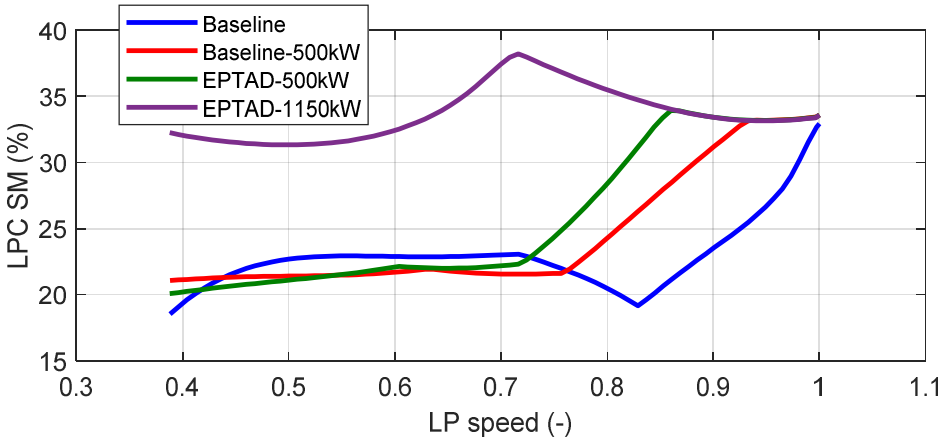


Figure 5-27 LPC SM at steady-state operating lines at ISA-SLS (re-scheduled VBVs)

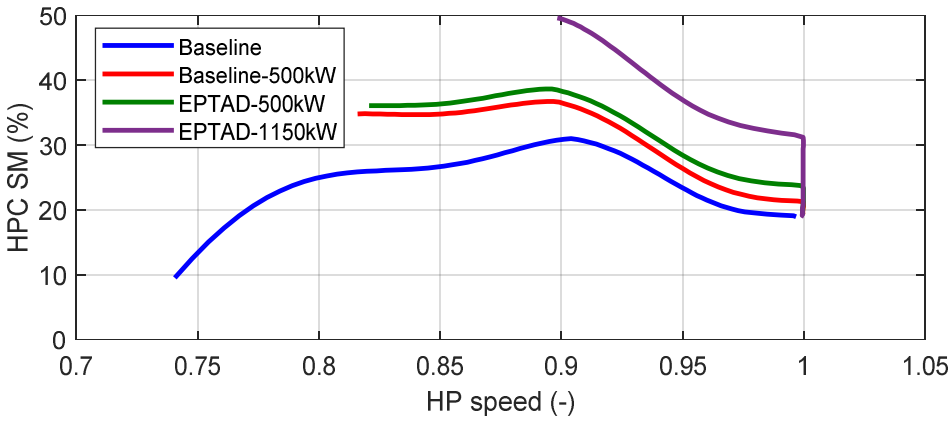


Figure 5-28 HPC SM at steady-state operating lines at ISA-SLS (re-scheduled VBVs)

Normally, core pressure ratio and mass flow are mainly produced by the HPC. Figure 5-29 and Figure 5-30 show the engine's core pressure ratio and mass flow over their values at MTO condition. The pressure ratio and mass flow increase significantly for the EPTAD engines with EPT compare to the baseline engine. In this manner, the EPTAD engines can recover full thrust faster than the baseline engines. If the same thrust response is targeted, engine's idle speed can be decreased to decrease idle fuel consumption which is discussed later in idle scenarios.

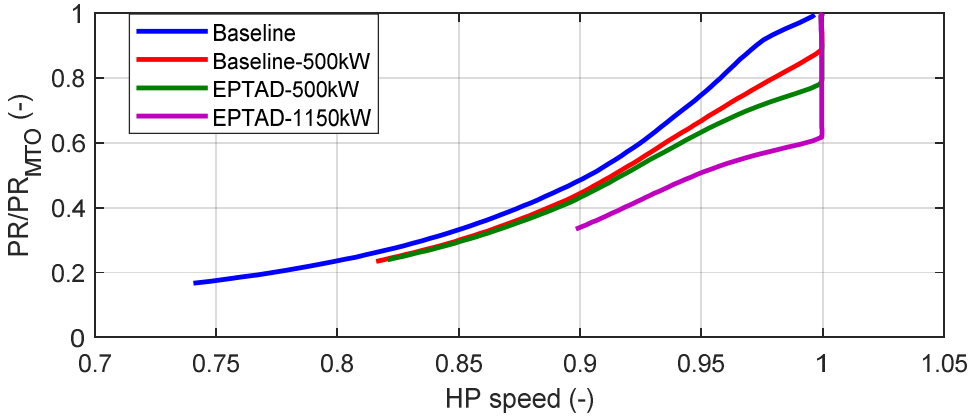


Figure 5-29 Core pressure ratio at steady-state operating lines at ISA-SLS (re-scheduled VBVs)

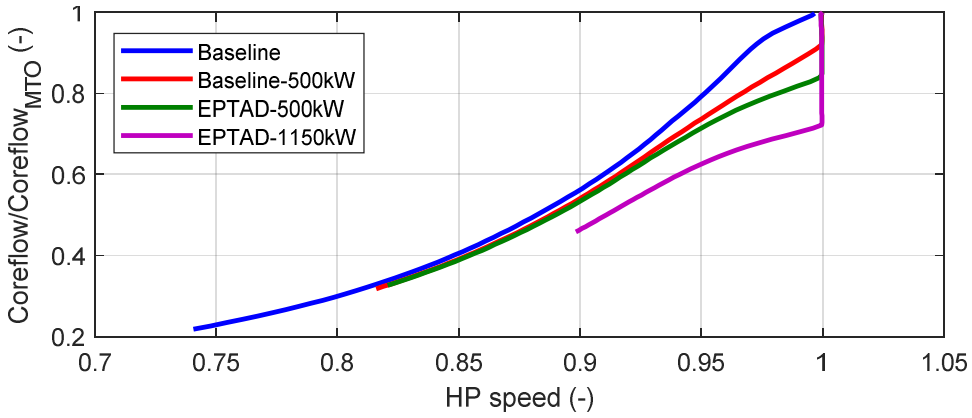


Figure 5-30 Core mass flow at steady-state operating lines at ISA-SLS (re-scheduled VBVs)

Depending on the setting for low speed scenarios in which some thrust can be required for taxing or minimum HP speed for idle operation, fuel consumption can be decreased or increased by means of EPT. However, the results for fuel consumption at low speed setting are not of high accuracy due to lack of map data at various bleeding schedules. After providing the general trend in shaft speeds and SMs for both the baseline and EPTAD engines, the following Sections discuss various flight scenarios in detail to investigate possible achievements in terms of aircraft operation such as fuel consumption reduction, SMs and thrust recovery.

5.4.6 *Take off condition for EPTAD engines*

The required thrust for take-off is normally between 80-100%, mainly depending on the runway length and ambient temperature. Table 5-4 and Table 5-5 for the MTO conditions (on pages 137 and 138) show that the fuel consumption increases by 0.007kg/s for the EPTAD-1150 engine and by 0.002kg/s for the EPTAD-500 engine respectively. The fuel consumption increase is mainly due to the EPT losses. The EPTAD engine's performance is also investigated at 90% of the MTO thrust condition.

Engine variables are presented over various EPT values to find the most optimum operation point in terms of fuel consumption or SMs. Figure 5-31 shows shaft speed changes by EPT, wherein the minimum required negative EPT to keep the HP speed below its maximum permissible value is -620kW and -80kW for the EPTAD-500 and EPTAD-1150 engines. For the baseline engine, EPT over +380kW is not permitted to avoid exceeding the maximum allowable HP speed. The LP speed is small (0.5% change) compare to that of HP speed (4% change) since LP shaft provides most of the thrust by the fan.

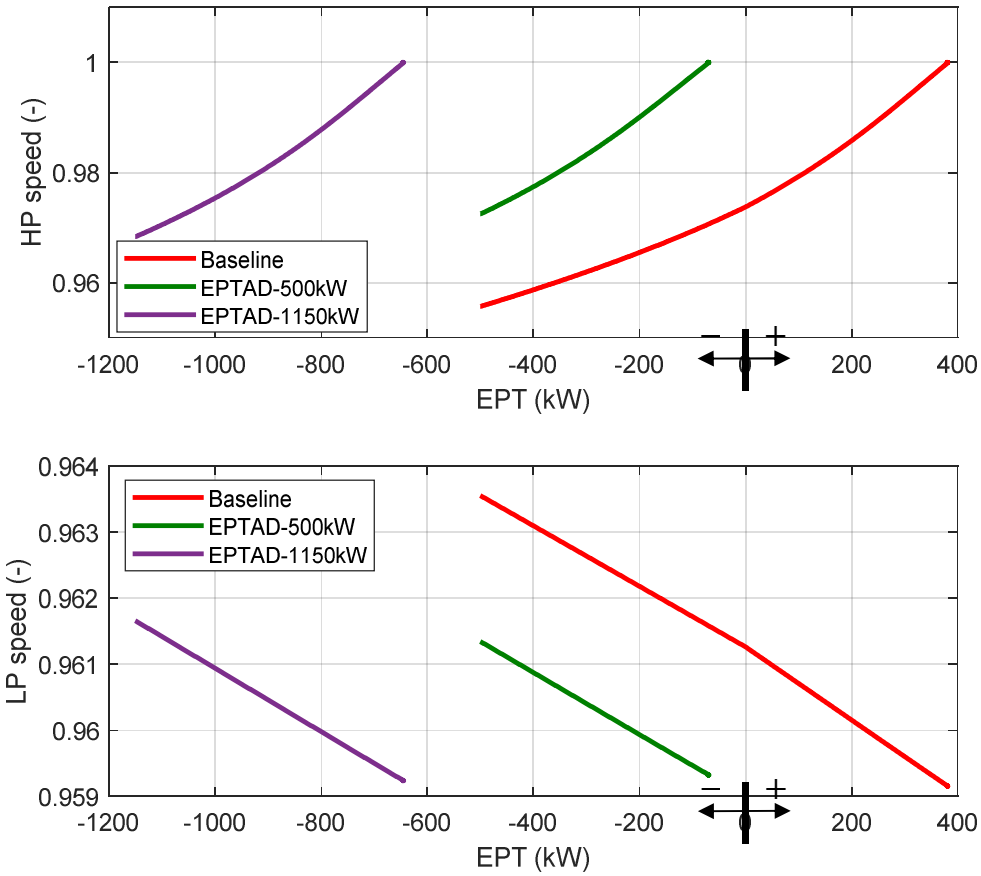


Figure 5-31 Shaft speeds at 90% of MTO at ISA-SLS condition

The fuel consumption change is compared between the baseline and EPTAD engines at 90% of the MTO in Figure 5-32. For the baseline and EPTAD engines, negative EPT increases fuel consumption due to lower core pressure ratio and efficiency. In comparison to the baseline engine with no EPT, the fuel consumption reduction is approximately 0.0025kg/s by +380kW of EPT for the baseline engine, 0.06kg/s with -80kW of EPT for the EPTAD-500 engine and 0.003kg/s with -620kW of EPT for the EPTAD-1150 engine.

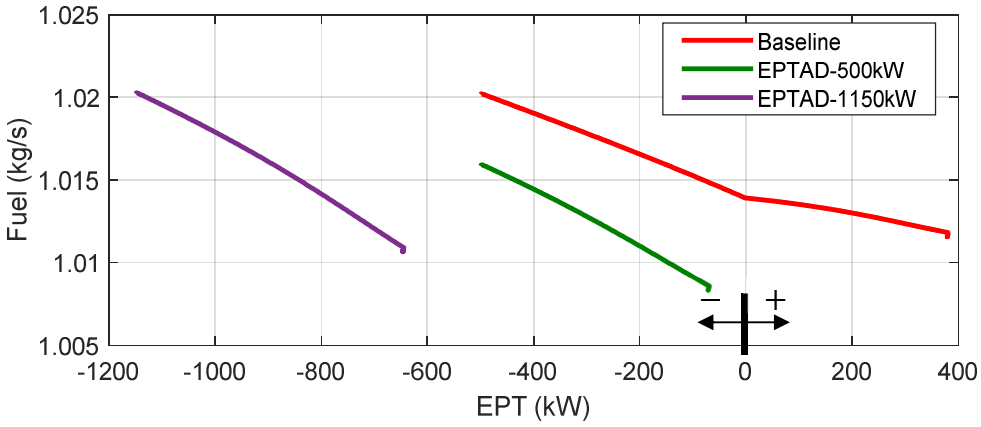


Figure 5-32 Fuel consumption at 90% of MTO at ISA-SLS condition

As it is shown in Figure 5-33, the HPC SM remains approximately the same (1% change) while the LPC SM increases more than 7% by the optimum values of EPT for fuel reduction (+380kW, -80kW and -620kW for the baseline and EPTAD engines). This Section highlights the fact that reducing negative EPT until reaching the maximum allowable HP speed reduces fuel consumption and increases surge margins.

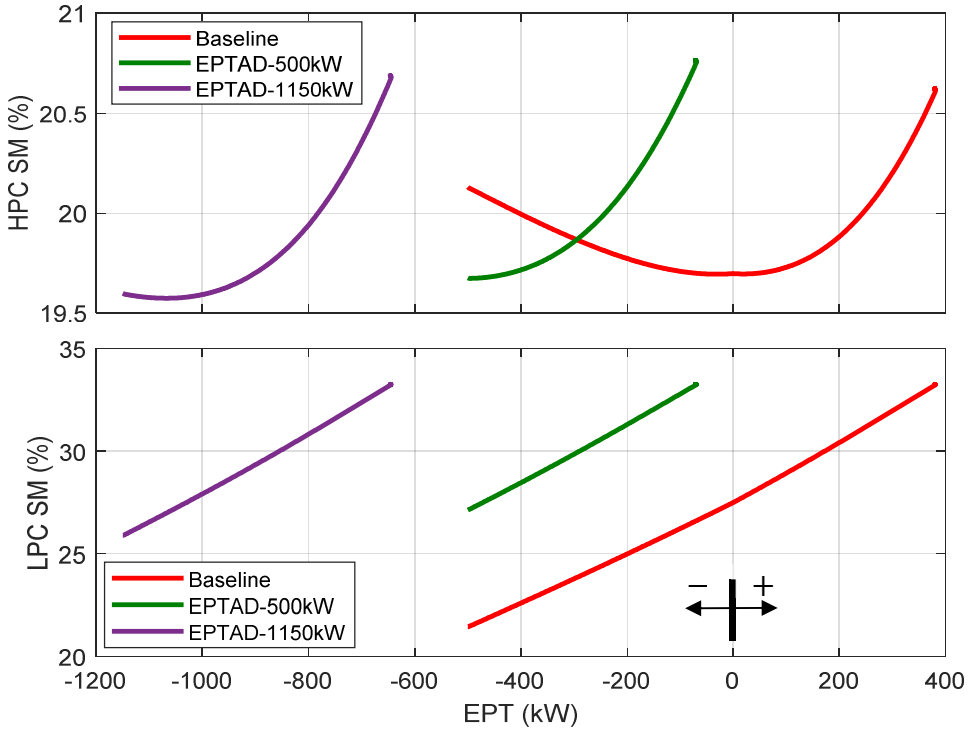


Figure 5-33 Surge margins at 90% of MTO at ISA-SLS condition

5.4.7 *Climb*

In this Section, the engine performance at the beginning and top of climb condition are investigated. The operation points selected for this purpose are:

- climb at 5kft with Mach=0.5 with 100% throttle (99% of MTO thrust)

- climb at 35kft with Mach=0.75 with 100% throttle (35% of MTO thrust)

In order to compare engine performance, a controller keeps the thrust at the baseline engine's thrust level. The engine variables for the baseline and EPTAD engines are shown in Table 5-6 and Table 5-7. Similar to previous Section, EPT has been implemented to increase the HP speed to 100%. The required EPT has decreased due to lower power of engine shafts at lower air density. Surge margins are within the same range since shaft speeds are the same for the baseline and EPTAD engines. However, the fuel consumption increases mainly due the EPT losses. The change in fuel consumption at 5kf are 0.0022kg/s and 0.0063kg/s for the EPTAD engines with 500kW and 1150kW EPT systems respectively while at 35kf they decrease to 0.0008kg/s and 0.0021kg/s respectively. The fuel consumption analysis for a flight envelope is given in Section 5.5. The increase in TIT in due to higher fuel flow rate.

Table 5-6 Engine variables beginning of climb (100% throttle, 5kft, Mach=0.5)

	Baseline	EPTAD-500	EPTAD-1150
Thrust (pu)	0.99	0.99	0.99
EPT (kW)	0	-490	-1135
HP speed (pu)	1	1	1
LP speed (pu)	1	1	1
LPC SM (%)	32.8	33.6	33.6
HPC SM (%)	19	19.2	19.1
TIT (°)	1597	1597	1599
Fuel (kg/s)	1.1368	1.1390	1.1431

Table 5-7 Engine variables top of climb (100% throttle, 35kft, Mach=0.75)

	Baseline	EPTAD-500	EPTAD-1150
Thrust (pu)	0.35	0.35	0.35
EPT (kW)	0	-165	-368
HP speed (pu)	1	1	1
LP speed (pu)	1	1	1
LPC SM (%)	33.2%	33.6	33.6
HPC SM (%)	18.6%	18.7	18.6
TIT (°)	1355	1356	1359
Fuel (kg/s)	0.3577	0.3585	0.3598

100% throttle for climb is set at high altitude and high temperature condition, while for normal condition, climb throttle is between 80-90% [162]. Table 5-8 and Table 5-9 show the fuel consumption at 85% throttle (≈94% LP speed) for the baseline and EPTAD engines at 5kft and 35kft, respectively. The HP speed of the engine is increased by EPT for the baseline and EPTAD-500. For the EPTAD-1150, the amount of negative EPT has decreased compare to 100% throttle to keep the HP speed below maximum speed. The increase in the HP speed increases the surge margins and reduces the fuel consumption. The change in fuel consumption at 5kf are -0.0025 kg/s, -0.0071kg/s and -0.0065kg/s for the baseline and EPTAD-500 and EPTAD-1150

engines respectively while at 35kf they decrease to -0.0006kg/s, -0.0020kg/s and -0.0017kg/s respectively.

Table 5-8 Engine variables beginning of climb (85% throttle, 5kft, Mach=0.5)

	Baseline No EPT	Baseline with EPT	EPTAD-500	EPTAD-1150
Thrust (pu)	0.85	0.85	0.85	0.85
EPT (kW)	0	492	73	-461
HP speed (pu)	0.967	1	1	1
LP speed (pu)	0.94	0.937	0.937	0.937
LPC SM (%)	25.8	33.2	33.2	33.2
HPC SM (%)	20.4	21.2	21.4	21.4
TIT (°)	1523	1505	1501	1501
Fuel (kg/s)	0.9586	0.9561	0.9515	0.9521

Table 5-9 Engine variables top of climb (85% throttle, 35kft, Mach=0.75)

	Baseline No EPT	Baseline with EPT	EPTAD-500	EPTAD-1150
Thrust (pu)	0.29	0.29	0.29	0.29
EPT (kW)	0	149	17	-152
HP speed (pu)	0.968	1	1	1
LP speed (pu)	0.94	0.937	0.938	0.938
LPC SM (%)	26.1	33.2	33.2	33.2
HPC SM (%)	19.8	20.6	20.8	20.8
TIT (°)	1294	1278	1275	1276
Fuel (kg/s)	0.3017	0.3011	0.2997	0.3000

5.4.8 *Idle scenarios*

The engine idle system control is designed to produce three levels of variable idle speeds identified as "Minimum Idle", "p_{30} Idle Range" and "Approach Idle". Since idle ratings are shaft speed related, the HP shaft speed is used as the idle speed set-point which normally increases with air density decrease [42]. At minimum idle rating the HP shaft speed is at its lowest possible to minimize the generated thrust. Normally during ground and flight idle, minimum idle is used unless the supply pressure for the aircraft pneumatic system and environmental control system is too low. In this case, the idle setting switches to p_{30} idle range to meet the required pressure calculated by the Electronic Engine Control (EEC) wherein the HP shaft speeds are between minimum idle and approach idle. "Approach Idle" is applied only when "anti-icing" is selected or the aircraft has flaps configured for an imminent landing for immediate availability of engine high power setting for the anti-icing system or thrust demand [42].

Regarding variable idle speeds in engine control system the criteria to determine these can be:

- rapid recovery of thrust during a balked landing manoeuvre (approach idle)

- p_{30} level to supply pressure for the environmental control system
- core mass flow should be maintained higher than the minimum level for sustainability of the engine
- enough SM for compressors

5.4.8.1 p_{30} Idle

During descent, flight idle mode is selected where the engine needs to operate at a high enough power to keep the bleeding pressure higher than a minimum for its application in the ECS. In order to keep the engine operation within its limits, while allowing immediate recovery of thrust during power transfer, the controller must maintain HP speed at its default minimum idle setting which has also been assumed to be 80% of its nominal value. p_{30} limit controller protects against the supply pressure for ECS [42] which has been assumed to be 250kPa for this engine. Results for flight idle, at 30kft with Mach number of 0.6, are presented in this Section.

Figure 5-34 shows that by positive EPT, speed of the HP shafts increases to provide the pressure of 250kPa by the HPC. As it is plotted in Figure 5-35, +225kW EPT decreases the fuel consumption by 0.015kg/s for the baseline and EPTAD engines. For EPT over +250kW the model is not valid due to lack of sub-idle performance data. The decrease in fuel consumption is due to the fact that, operating HPC at higher speed is more efficient to produce the required pressure for the ECS usage. SMs, shown in Figure 5-36, are also more than their baseline values by minimum 10% due to positive EPT for the baseline and EPTAD engines.

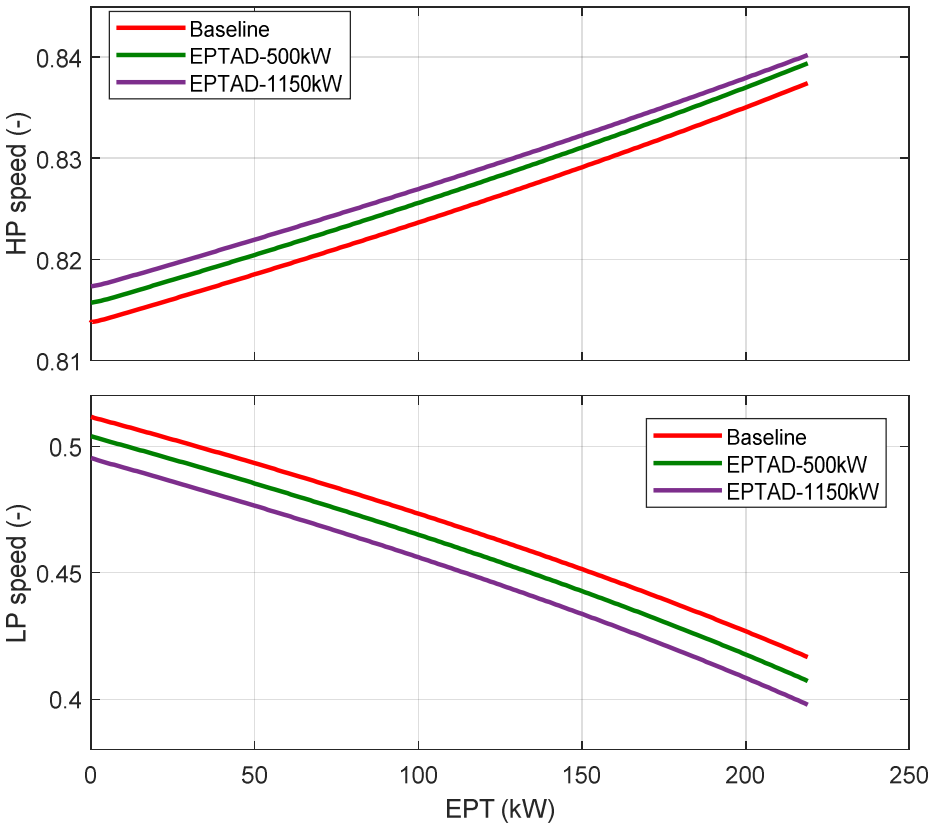


Figure 5-34 Shaft speeds vs EPT at p_{30} Idle

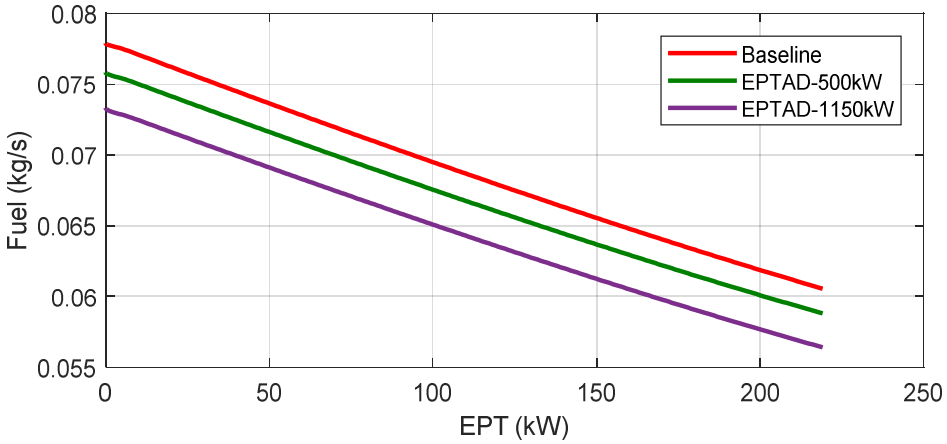


Figure 5-35 Fuel consumption change vs EPT at p_{30} Idle

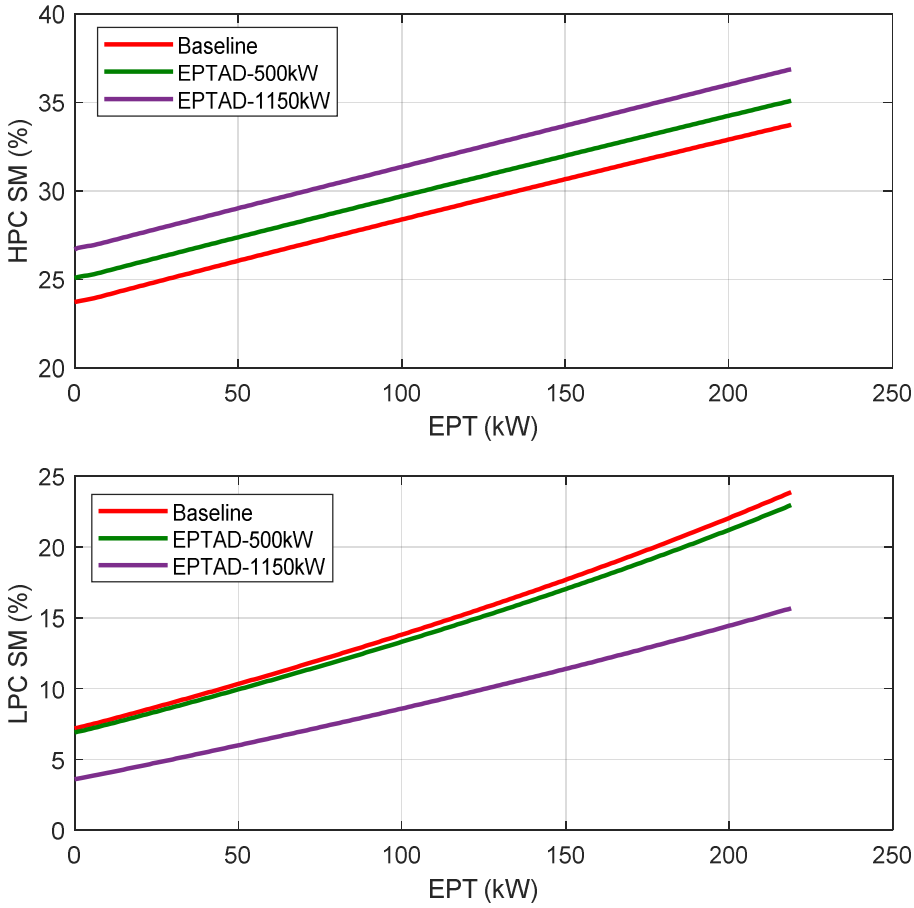


Figure 5-36 SMs vs EPT at p_{30} Idle

5.4.8.2 **Flight idle**

During flight idle, a minimum HP speed controller is activated to keep the engine ignition with adequate core flow and surge margins. In order to compare the baseline and EPTAD engines, the HP speed is kept in its constant value (80%) by the speed controller at 5kft with Mach=0.4. As it can be seen in Figure 5-37, the LP speed drops in the EPTAD engines and also by positive EPT it decreases as well. The fuel consumption, shown in Figure 5-38 also drops significantly, more than 20% by +400kW EPT. Figure 5-39 illustrates SMs which experiences boosts due to positive EPT as expected.

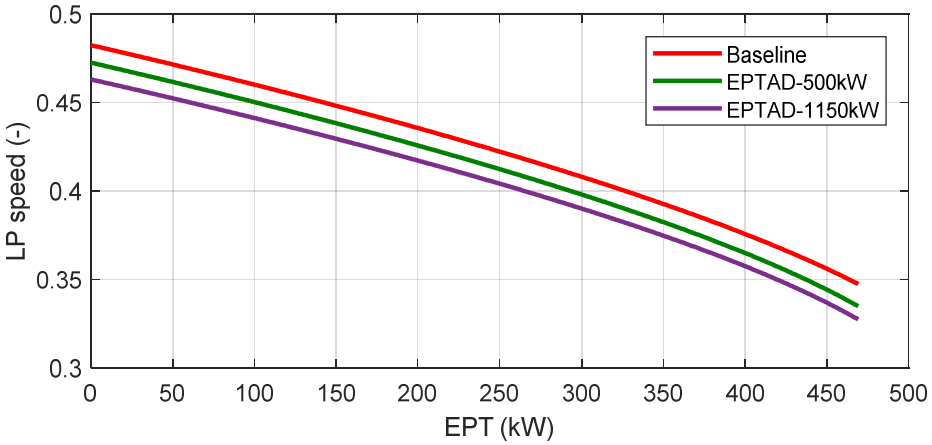


Figure 5-37 LP speed vs EPT during flight idle

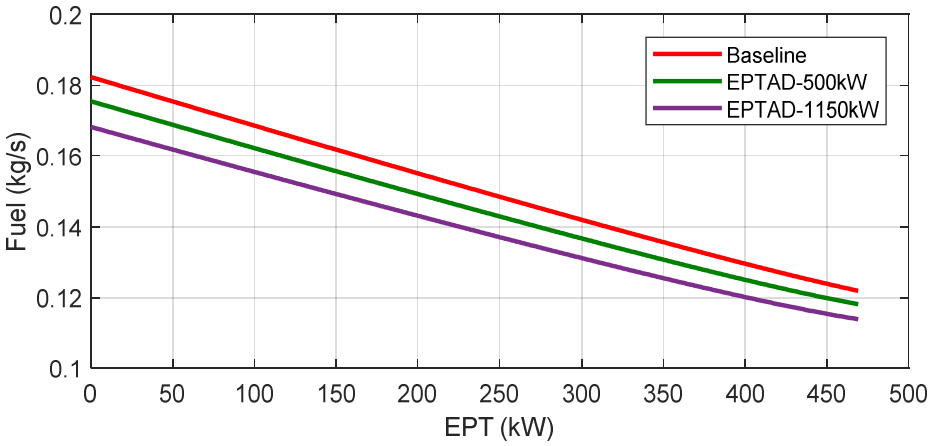


Figure 5-38 Fuel consumption vs EPT during flight idle

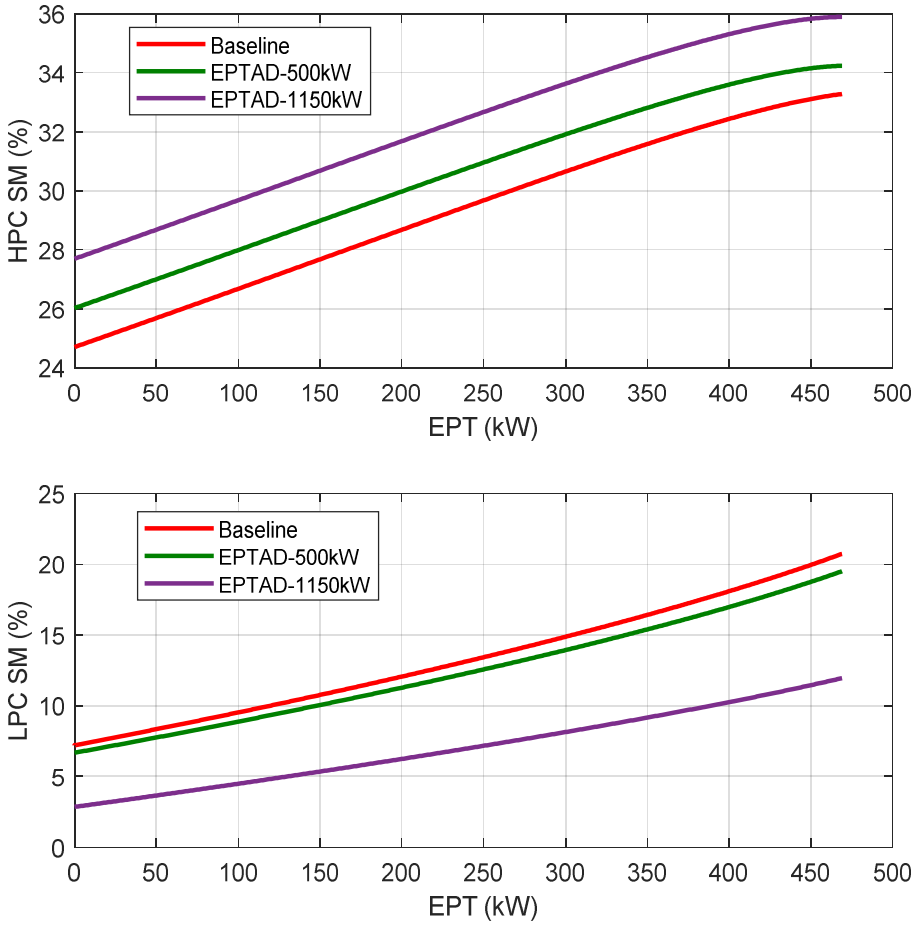


Figure 5-39 SMs vs EPT during flight idle

5.4.8.3 **Taxiing**

For taxiing manoeuvre, 10% of engine thrust is required based on International Civil Aviation Organization (ICAO) values in [162] which can be less or more due to runway slope and friction, wind, etc. For the purpose of comparison, a controller keeps the thrust at 10% of the baseline maximum thrust. Since the fan provides most of the required thrust, by positive EPT, the controller increases the fuel rate to the combustion chamber to keep the LP speed unchanged.

Due to higher turbine PSR, HPT power is higher for the EPTAD engines compare to the baseline engine which increases the HP speed for the same amount of thrust by the fan. Plotted in Figure 5-40, fuel consumption increases by positive EPT since power is extracted from the fan which is the main source of thrust. Figure 5-41 shows that HPC SMs increase which is the advantage of EPT during taxiing and the LPC SMs decrease which can be acceptable at very low speed of the LP shaft. On the other hand, negative EPT is not allowed because it further decreases the HPC and LPC SMs. Thus,

as a compromise between the fuel consumption, no EPT for the baseline and EPTAD engines is recommended during taxing.

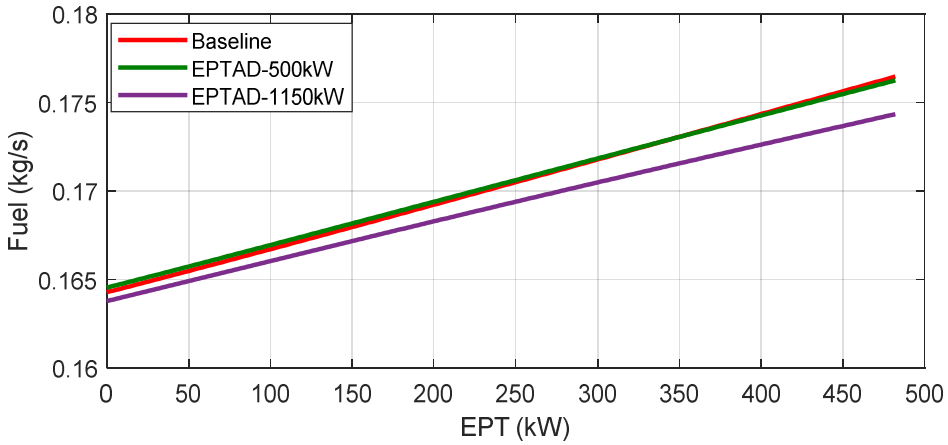


Figure 5-40 Fuel consumption change vs EPT during taxing

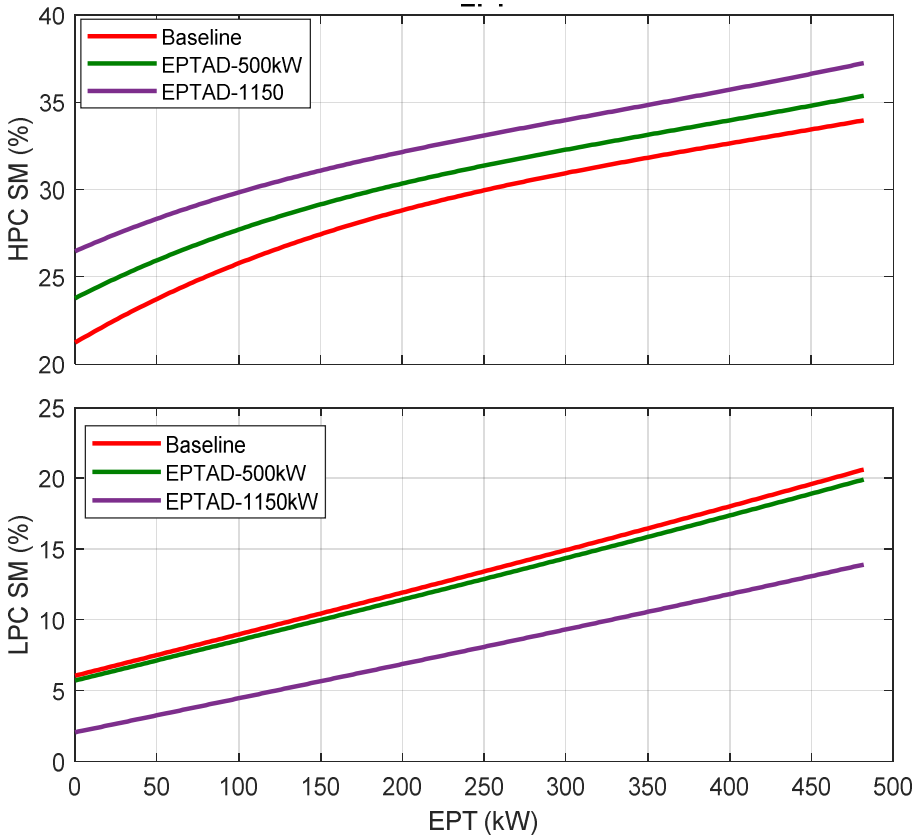


Figure 5-41 SMs vs EPT during taxing

5.4.8.4 Touch and go

In aviation, a touch-and-go landing (TGL) [1] or circuit is a manoeuvre that is common when learning to fly a fixed-wing aircraft. It involves landing on a runway and taking off again without coming to a full stop. Usually the pilot then circles the airport in a defined pattern known as a circuit and repeats the manoeuvre. This allows many

landings to be practiced in a short time [2]. Touch-and-go landings are also crucial when a plane lands with not enough space to come to a complete stop, but has enough space to accelerate and take off again to carry out a go-around. In this manoeuvre the acceleration time of the engine comes to play an important role, since acceleration faster means shorter required runway. During the approach phase, the idle speed setting is normally higher to provide immediate recovery of thrust in case of a TGL manoeuvre. Typically thrust value for is also set at 20% for landing manoeuvres at Mach=0.4 at zero altitude [162].

The method of power exchange provides the ability to decrease the engine set-point to burn less fuel during approach phase while accelerating the engine as fast and safe as the baseline design. The limits of the engine such as surge/stall, over-temperature, over-speed and over-pressure define acceleration rate of the engine.

The model is expected to have 30% of error during severe transients due to lack of heat transfer model as discussed in Section 4.9. However, it can be used to compare the EPTAD and baseline designs. The electrical system dynamics has been ignored in this Section due to very fast response of it, compare to that of engine. Figure 5-43 to Figure 5-46 show engine performance during acceleration from idle to full throttle setting.

A time constant represents the EPS lag in this Section for transient response. The idle setting is assumed to be with +500kW EPT and +1150kW for the EPTAD-500 and EPTAD-1150 engines respectively. The full throttle setting is with -500kW and -1150kW for the EPTAD-500 and EPTAD-1150 engines respectively (see Figure 5-42).

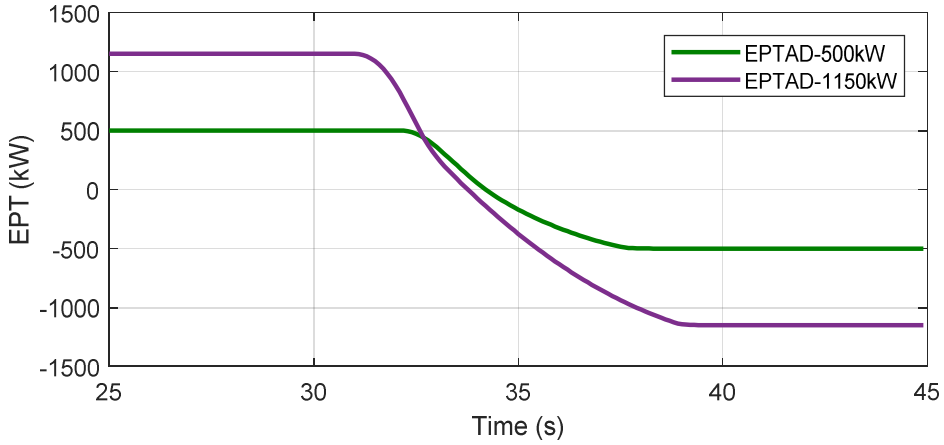


Figure 5-42 EPT values during TGL manoeuvre

In Figure 5-43, HPT exhaust temperature is lower at idle setting due to lower idle speed, while following the same trend during acceleration. Once TIT hits its limit fuel control system switches to TIT limit controller and the acceleration rate decreases.

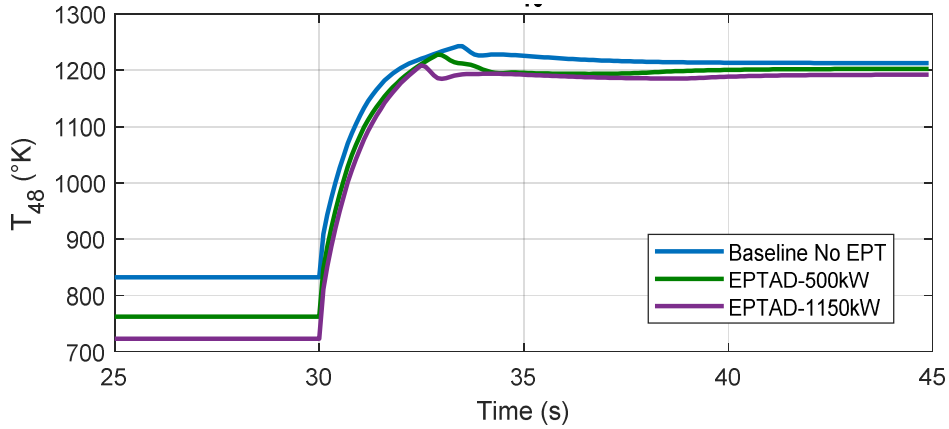


Figure 5-43 HPT exhaust during acceleration from idle to full throttle setting

Fan speed and thrust (shown in Figure 5-44 and Figure 5-45), are retrieved quite fast from their lower value at idle setting. With power exchange, HP speed is higher which means it is closer to its full throttle value. This helps the core airflow to be higher, thus increasing fuel flow during acceleration for the same temperature limit. As a result, fan speed reaches its full throttle as fast as the baseline engine.

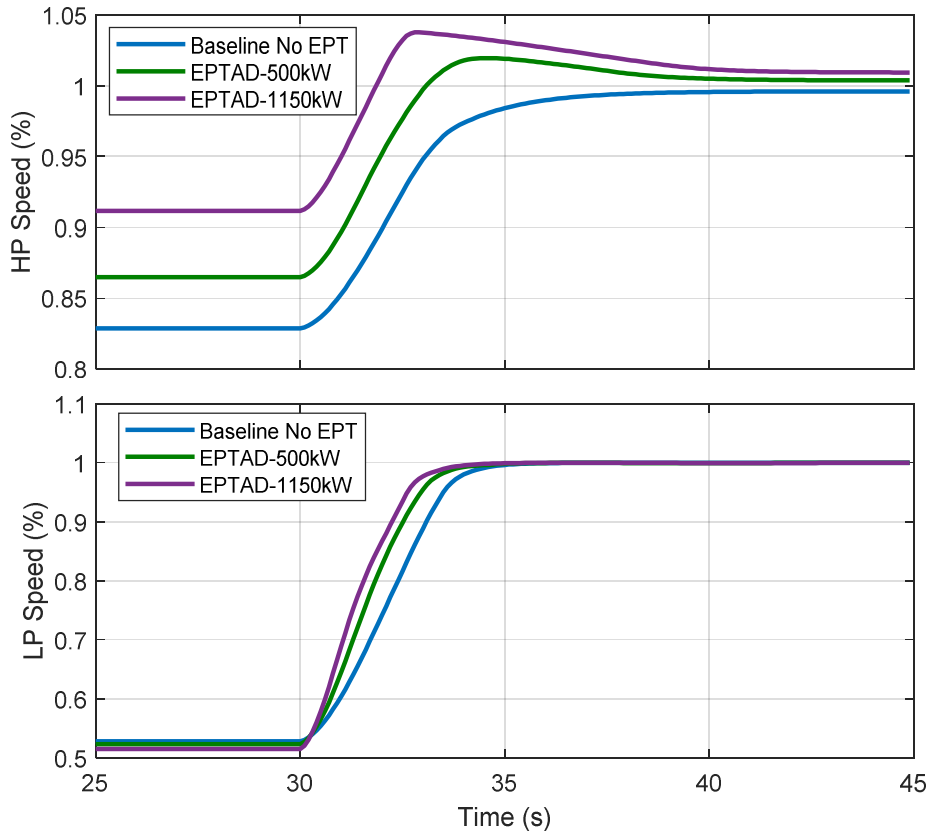


Figure 5-44 Shaft speeds during acceleration from idle to full throttle setting

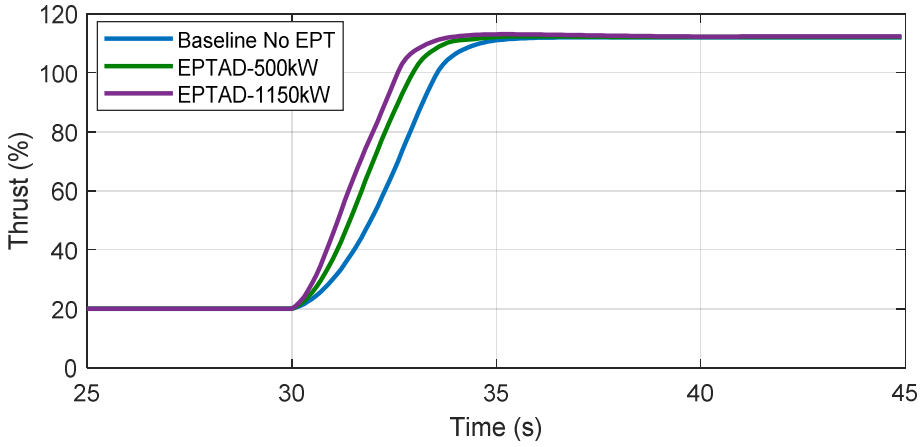


Figure 5-45 Calculated thrust during acceleration from idle to full throttle setting

There is initial shift in SM before acceleration, due to EPT (see Figure 5-46). Different fluctuation patterns during acceleration in SM for HPC and LPC are due to different VBVs schedule and speed matching between LP and HP shaft with EPT compare to current configuration without EPT. In general, higher SM highlights the fact that the method of EPT provides the ability to accelerate the engine faster while keeping the engine's surge margin limits.

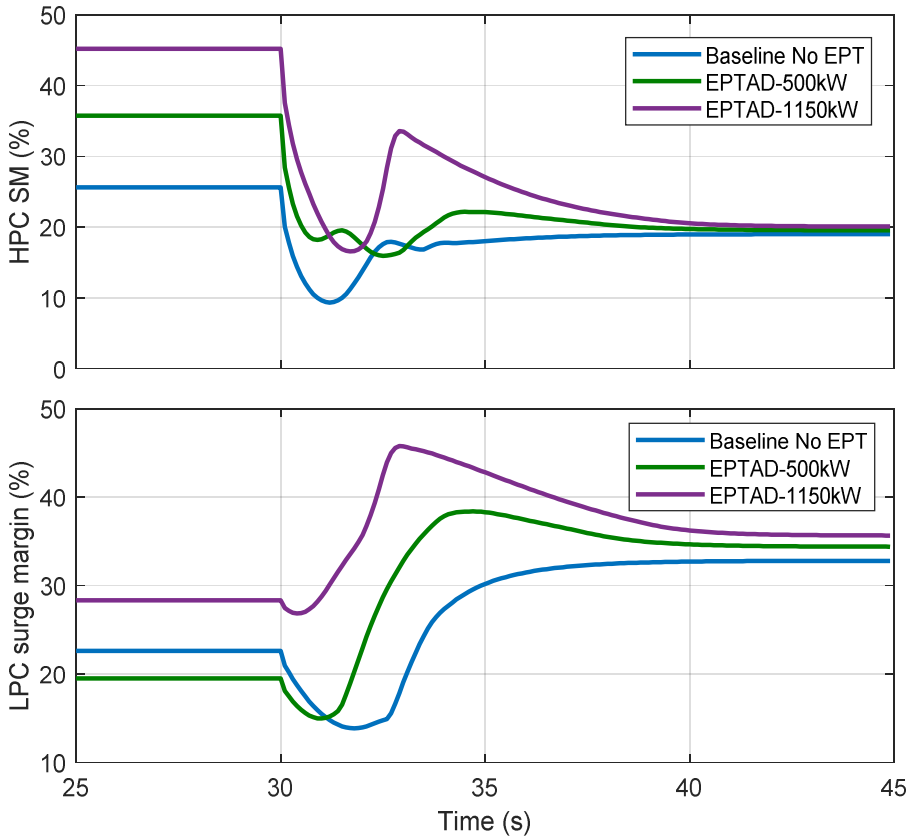


Figure 5-46 SMs during acceleration from idle to full throttle setting

5.4.8.5 Minimum Idle Mode

Minimum idle mode is the very bottom end of engine speed setting for self-sustained operation. The LPT available power is very low in this case just to overcome frictions in bearings of the fan and LPC. The HPT power, however, should be enough to run the HPC to create enough airflow and pressure for combustion purpose.
The minimum idle cannot be modelled due to lower LP speed than the minimum speed on the LPC map. While Similar to Section 5.4.8.2, the EPTAD engines are expected to decrease the fuel consumption due to higher turbine PSR.

Summary on EPT effects for off-design conditions

Key benefits of the EPT system for the off-design performance from Section 5.4.8 are as below:

- Increasing the engine efficiency and SMs if minimum speed is required for the engine operation
- Increasing the SMs with lower efficiency if low thrust value is required for taxiing
- Ability to decrease the engine minimum idle speed, while keeping the engine ready for abrupt recovery of thrust

5.5 Fuel consumption analysis

After studying various flight modes including cruise, taxiing and flight idle, in this Section the fuel burn benefit is assessed by comparing the baseline and EPTAD engines. This investigation includes the differences in fuel burn due to the EPT system and additional fuel burn due to the EPT system weight. For other flight scenarios detailed aircraft performance model is required to calculate the impact of weight on mission fuel burn. It should be noted that the data presented in this Section are crude estimations.
A typical flight time is presented in Table 5-10 from [162]. From the simulation results in the previous Section, the expected average fuel consumption change by the EPT system at various flight phases are shown in Table 5-10. The time of each manoeuvre is also obtained from [162] for an 8-hours flight. The time of each manoeuvre is also obtained from [162] for an 8-hours flight.

Table 5-10 Average fuel consumption for CFM56-3 engine for an 8-hours flight

	Time	fuel	Fuel consumption change		
		Baseline No EPT	Baseline 500kW	EPTAD-500	EPTAD-1150
TAXIING	5 min	9.90 kg/min	0.00 kg/min	0.00 kg/min	0.00 kg/min
CLIMB	30 *min*	37.81 *kg/min*	-0.09 kg/min	-0.28 kg/min	-0.25 kg/min
CRUISE	375 *min*	13.33 *kg/min*	-0.03 kg/min	-0.10 kg/min	-0.19 kg/min
DESCENT	25 *min*	7.66 kg/min	-0.90 kg/min	-1.02 kg/min	-1.20 kg/min
TAXING	5 min	9.90 *kg/min*	0.00 kg/min	0.00 kg/min	0.00 kg/min
Flight envelope	440 *min*	6419.60 *kg*	-36.45 *kg*	-72.03 *kg*	-107.13 *kg*

Continuous advancement in electrical machines and power electronics technologies and electrical and magnetic materials allow design and fabrication of high-power density motor drives and generation units with higher reliability and efficiency. The predicted power density of the proposed back-to-back motor generator set including power electronics, cables and switchgear is predicted to be ~20kW/kg by 2035 [16, 163, 164]. In this case, the total estimated weight of the power exchange system is provided in Table 5-11, which adds additional fuel consumption by the engine. The weight reduction due to VBVs removal is not considered in the weight analysis due to lack of VBVs weight data.

By assuming maximum take-off weight (MTOW) of 57,000kg for B737-300 [161], the fuel consumption for a 7 hours flight is around 5600kg which is less than 20% of the aircraft MTOW. By assuming constant weight of the aircraft during cruise, the fuel consumption at reference cruise (provided in Table 5-3) for each engine is 0.014kg of fuel per hour per weight of the aircraft (kg/(kg.hr)). By assuming linear ratio between aircraft added weight and fuel consumption, the added fuel consumption due to weight and fuel saving of the EPT system are given in Table 5-11. A rule-of-thumb is that a reduction in fuel consumption of about 0.75% results from each 1% reduction in weight [165]. The added fuel consumption due to weight and fuel saving of the EPT system with this assumption are also given in Table 5-11. The values in Table 5-11 are per engine. Table 5-12 presents the fuel saving with various power density values to have a better insight into the future of this system.

After subtracting the added fuel consumption due to EPT weight from the fuel reduction in Table 5-11, up to 1.5% and 2.0% of fuel savings are achieved for the long and short flights with the assumption of ~20kW/kg for the electrical system. The significant fuel saving by the EPT system suggests the implementation of the EPT system for future engines.

Table 5-11 EPT system weight analysis for B737 with CFM56-3 engine

		Baseline-500	EPTAD-500	EPTAD-1150
Fuel saving with EPT system	7-hours flight	36.4 kg	72.0 kg	107.1 kg
EPT System weight (20 kW/kg)		50.0 kg	50.0 kg	115.0 kg
Added fuel consumption due to EPT weight-linear assumption		5.0 kg	5.0 kg	11.4 kg
Fuel saving- linear assumption		31.4 kg (0.48%)	67.0 kg (1.04%)	95.7 kg (1.49%)
Added fuel consumption due to EPT weight- (1%-0.75%) rule		4.2 kg	4.2 kg	9.7 kg
Fuel saving- (1%-0.75%) rule		32.2 kg (0.50%)	67.8 kg (1.06%)	97.4 kg (1.52%)
Fuel saving with EPT system	2-hours flight	27 kg	40 kg	49 kg
EPT System weight (20kW/kg)		50.0 kg	50.0 kg	115.0 kg
Added fuel consumption due to EPT weight-linear assumption		1.5 kg	1.5 kg	3.4 kg
Fuel saving- linear assumption		25.5 kg (0.48%)	38.5 kg (1.04%)	45.6 kg (1.49%)
Added fuel consumption due to EPT weight- (1%-0.75%) rule		1.4 kg	1.4 kg	3.3 kg
Fuel saving- (1%-0.75%) rule		25.6 kg (1.15%)	38.6 kg (1.73%)	45.7 kg (2.01%)

Table 5-12 EPT system weight analysis for B737 with CFM56-3 engine (3 hours flight)

	Baseline-500	EPTAD-500	EPTAD-1150
Fuel saving with EPT system	29 kg	46 kg	60 kg
Fuel saving (1%-0.75%) (20 kW/kg)	27.0 kg (0.90%)	44.0 kg (1.46%)	55.4 kg (1.84%)
Fuel saving (1%-0.75%) (10 kW/kg)	25.1 kg (0.83%)	42.1 kg (1.40%)	50.9 kg (1.69%)
Fuel saving (1%-0.75%) (5 kW/kg)	21.0 kg (0.70%)	38.0 kg (1.26%)	41.7 kg (1.38%)

5.6 Summary

This Chapter presents a preliminary study into the impact of EPT on the turbofan performance including compressor surge and fuel consumption through simulations. A conceptual EPTAD re-design of the engine to utilize the EPT system benefits is offered and discussed in detail. The simulation results for CFM56-3 baseline and EPTAD-500 and EPTAD-1150 engines with two levels of EPT system (500kW and 1150kW) are presented.

Overall, this Chapter presents the items below:

a) for the baseline engine:

- Optimizing engine performance for various cruise points
- Up to 0.27% fuel reduction for cruise operation with 250kW EPT, depending on the component efficiencies a knee is created on fuel consumption curve which may change for various engines.
- Improvement in SMs at cruise condition
- Redeeming SMs of the degraded engine
- Reduced VBVs opening

- Significant fuel consumption reduction at low speed settings
- Significant surge margin increases at low speed settings
- Improved transient response

b) for the EPTAD-500 engine:

- Keeping the engine limits at MTO condition
- Up to 0.64% fuel reduction for cruise condition
- Improvement in SMs at cruise condition
- Reduced VBVs opening
- Significant fuel consumption reduction at low speed settings
- Significant surge margin increases at low speed settings
- Improved transient response

c) for the EPTAD-1150 engine:

- Keeping the engine limits at MTO condition
- Up to 1.4% fuel reduction for cruise operation
- Improvement in SMs at cruise condition
- VBVs removal
- Significant fuel consumption reduction at low speed settings
- Significant surge margin increases at low speed settings
- Improved transient response

The EPT system will always improve the engine performance and provide many opportunities at various operating modes of the flight mission. A crude estimation on the weight of the system is provided to see the overall impact of the EPT on fuel consumption. The achievements represented by this novel configuration, however, should be further evaluated to determine the optimum amount of power transfer, considering the impact of system weight and space on propulsion efficiency.

Chapter 6 Experimental Studies by Engine Emulation

As discussed in Chapter 3, one of the main areas of research for the MEA is mounting a generator on the LP shaft in addition to the starter/generator mounted on the HP shaft. Given that there are electrical machines on both the LP and HP shafts, there is an "electrical bridge" to establish power exchange between the shafts. Potential improvements in the engine performance under such transfer have been studied and discussed in this Thesis. Preliminary results in Chapter 4 show great benefits in terms of fuel consumption, engine stability and compatible thrust with flight mission at various flight scenarios.

In order to prove the concept and demonstrate the practicality of power transfer, an engine emulator has been constructed. The emulator will replicate basic behaviour of the engine by using defined scaling factors and will allow for conducting tests in a scaled environment without the need for an actual physical engine. Hence, the emulator will provide an opportunity to study the integrated system behaviour under various scenarios, including the engine-generator-electrical system interactions. The emulator can evaluate steady-state and transient operations and the impact of engine instabilities such as surge and fault scenarios in an electrical system such as short-circuit and open circuit. A unique time scaling technique is implemented to synchronize the time of the engine model and the test rig. This enables scalable flexible engine emulation at different power generation ratings.

This Chapter gives a brief introduction to the Hardware-in-the-Loop (HIL), followed by its implementation for engine emulation. Then, the developed engine emulator is described, and finally, the experimental results are reported to demonstrate and further discuss the feasibility of electric power transfer between the engine shafts.

6.1 Hardware-in-the-Loop (HIL) technique

HIL technique, which is the simultaneous implementation of simulation and real equipment is commonly employed in experimental demonstrators, to examine future cross-disciplinary applications [166-170]. HIL systems are typically composed of a digital, Real-Time Platform (RTP), physical hardware pieces and signal interfaces. The RTP should be capable of performing a real-time simulation of the model of the system being emulated (e.g. an engine). It imposes a limit on the complexity of the model, depending on the processing capabilities of the simulator. Two primary types of HIL simulations include; Controller Hardware-in-the-Loop (CHIL) and Power Hardware-in-the-Loop.

CHILs are used to enable the evaluation of control algorithms implemented on industrial control platforms before test work on a physical power system (e.g. a converter) [171]. The interface signals, shown in Figure 6-1, only involve -to-digital and digital-to-analogue converters, operating at low power and voltage levels (+/-15V, mA) [172-174]. The physical control hardware includes the control algorithm and hardware devices (e.g. protection relays [171]), and the real-time simulation of the system model (e.g. power electronic circuits) is performed in the RTP [166]. In CHIL, the physical hardware commands the system model in the RTP.

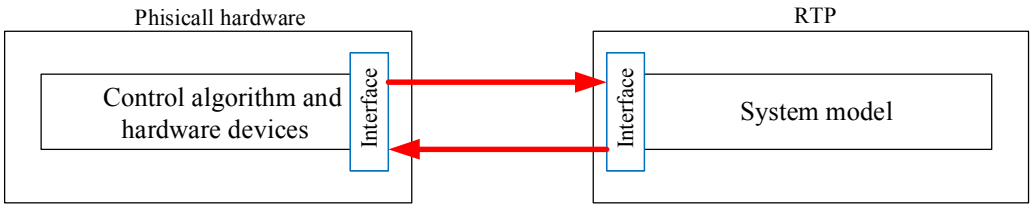


Figure 6-1 Overview of CHIL [166]

PHIL techniques form the basis of modern emulation systems [173]. As shown in Figure 6-2, a piece of the hardware (e.g. a motor) replicates the behaviour of a different system (e.g. an engine). The model of the system which is not physically available is run in the RTP [173]. A candidate sub-system (e.g. generators and dc bus architecture) is also included in the physical hardware, which is the main focus of study. In this case, real power is virtually exchanged between the simulation and the hardware part of the PHIL [173]. Rapid control prototyping is another application of PHIL, wherein power hardware components are linked to the controllers in the RTP through a much more complex interface [166, 174].

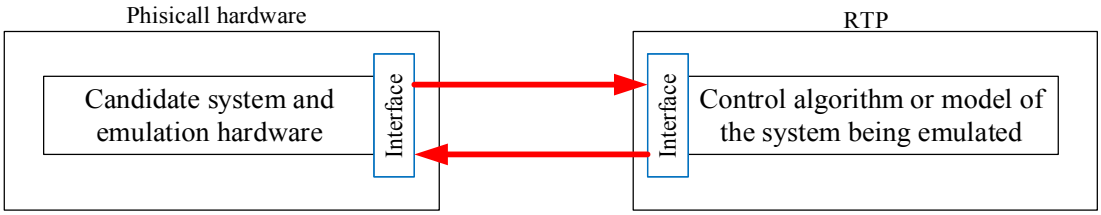


Figure 6-2 Overview of PHIL [166]

It is a common practice to emulate mechanical systems [175], sources or loads for various range of technologies including mechanical, hydraulic [176] and electric drive systems [166]. Various systems can be emulated over a subset of speed, torque and inertia owing to the PHIL development together with the well-established control methods [177]. For instance, wind turbine emulation has been widely implemented as an electrical drive-based emulation system, some of which are discussed in [168, 178-181]. As shown in Figure 6-3, the RTP runs the simulation model of the wind turbine and provides the current and frequency demand for the induction motor which emulates the wind turbine behaviour in terms of torque and pitch control [179, 182, 183]. The generator can be a real generator or a scaled generator to evaluate advanced control or alternative design of the generator.

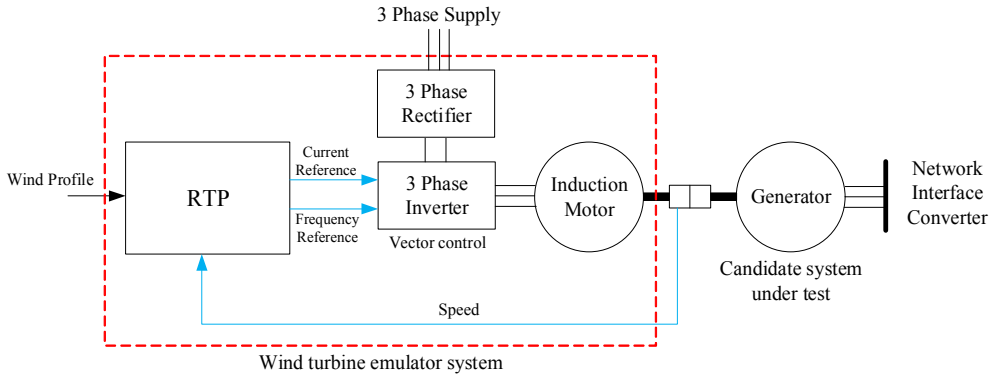


Figure 6-3 System structure of the wind turbine emulator

6.2 Overview of gas turbine engine emulation systems

Electrical drive systems are employed to emulate single-shaft or multi-spool gas turbine engines as well. Correa et al. in [114] have implemented a parameterized, twin-shaft gas turbine engine model consisting of a gas-generator and a free turbine, represented in 4.1, in an RTP to emulate the steady-state and transient dynamics. Two identical 15kW induction machines are coupled to a torque transducer on a common shaft.

A 100kW facility based on HIL techniques has also been developed in the Rolls-Royce University Technology Center at The University of Manchester, focusing on electrical systems of the MEA [184]. The so-called Intelligent Electrical Power Network Evaluation Facility (IEPNEF) includes the emulated twin-spool engine in an RTP [184], commanding two 115kW variable-speed induction machine drives [166]. The LP shaft's emulation motor is coupled to a 70kW 3000rpm PM generator [185], and the HP shaft's emulation motor is coupled to a 30kW 15000rpm SR starter/generator [186]. The output power of the generators is fed to a 540V DC bus architecture. In addition to power from the generator, a 1MJ supercapacitor based energy storage system has also been implemented to evaluate the performance of advanced power management schemes at electrical load transients [187].

An Electrified Aircraft Propulsion (EAP) real-time simulator has also been developed to demonstrate Turboelectric Distributed Propulsion (TeDP) [188, 189] in the NASA Glenn Research Center (GRC) [170, 190]. In the TeDP, generators extract power form turboshaft engines and feed the power to motors which drive propulsive fans [170, 191]. Actual engines, fans, motors and generators are all emulated by thin-gap PM motor drive systems, which are capable of up to 1.5kW at 400rpm [170]. A single shaft 48MW gas turbine model (developed based on Rowen model [112]) together with the fan maps and generator characteristics and, loads are implemented in the dSPACE control system to provide speed reference from the engine.

For engine emulation concepts discussed above, electric motor drives have replaced the actual gas turbine to drive the generators which are meant to extract power from the engine shafts. As shown in Figure 6-4, the RTP should be able to accurately run the engine simulation model and provide real-time shaft speed signals for the motors. The inputs to the engine model are throttle and Ambient Temperature and Pressure (ATP), and the measured torque value from the torque sensor. The emulation motor operates in speed control mode so that it tracks the engine' shaft speed, and the PO generator operates in torque control mode to determine the amount of power offtake.

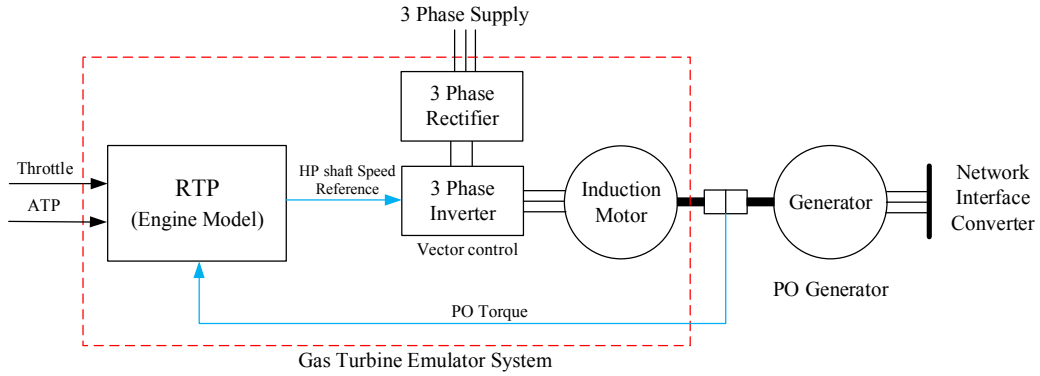


Figure 6-4 System structure of the gas turbine emulator (single-shaft emulator)

Typically, a scaling module is needed if the PO generator's rating is less than a real generator on the engine shaft. For instance, for EPT studies in this Thesis, the required power is 500kW while the emulator is designed for a maximum of 50kW. The scaling module scales up the torque from the emulator rig to the required EPT. The same applies to the speed if the PO generator and emulator speeds are different.

The gearbox module should also be included in the RTP if there is a gearbox (e.g. AGB) between the PO generator and engine shaft in the actual system. As shown in Figure 6-5, the shaft modules which contain the shaft speed states are solved within the RTP with torque inputs from engine modules including the compressor and turbines, and the torque transducer presenting power offtake from the generator.

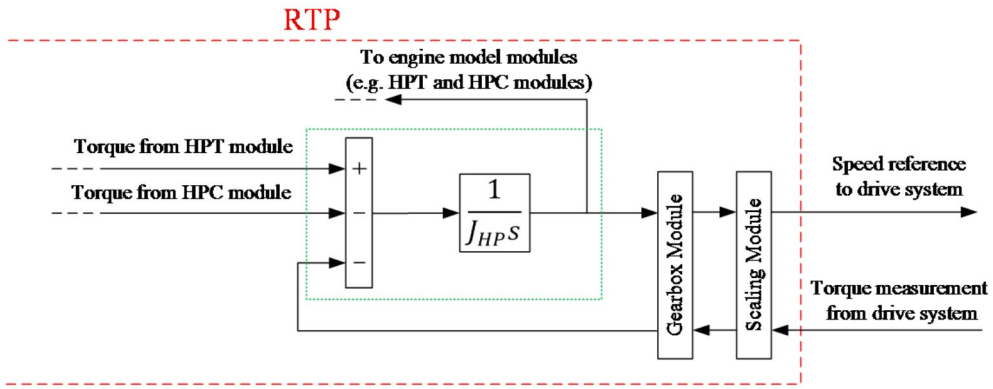


Figure 6-5 Torque-speed block diagram of the emulator

The engine emulator designed for EPT and future power system studies is similar to the existing engine emulators discussed above. The next Section presents a detailed design of the constructed emulator.

6.3 Twin shaft engine emulator setup

An Advanced Integrated Power Centre (AIPC) is under development in the University of Nottingham to look at design and development of a highly innovative integrated

electric power centre for future aircraft platforms. This considers the engine as a part of the overall electrical energy generation system, together with the driven generators, one from the LP shaft and another one from the HP shaft, and the power electronic converters. Figure 6-6 presents the layout of the engine emulator setup and Figure 6-7 shows the engine emulator components which is elaborated in the next Sections.

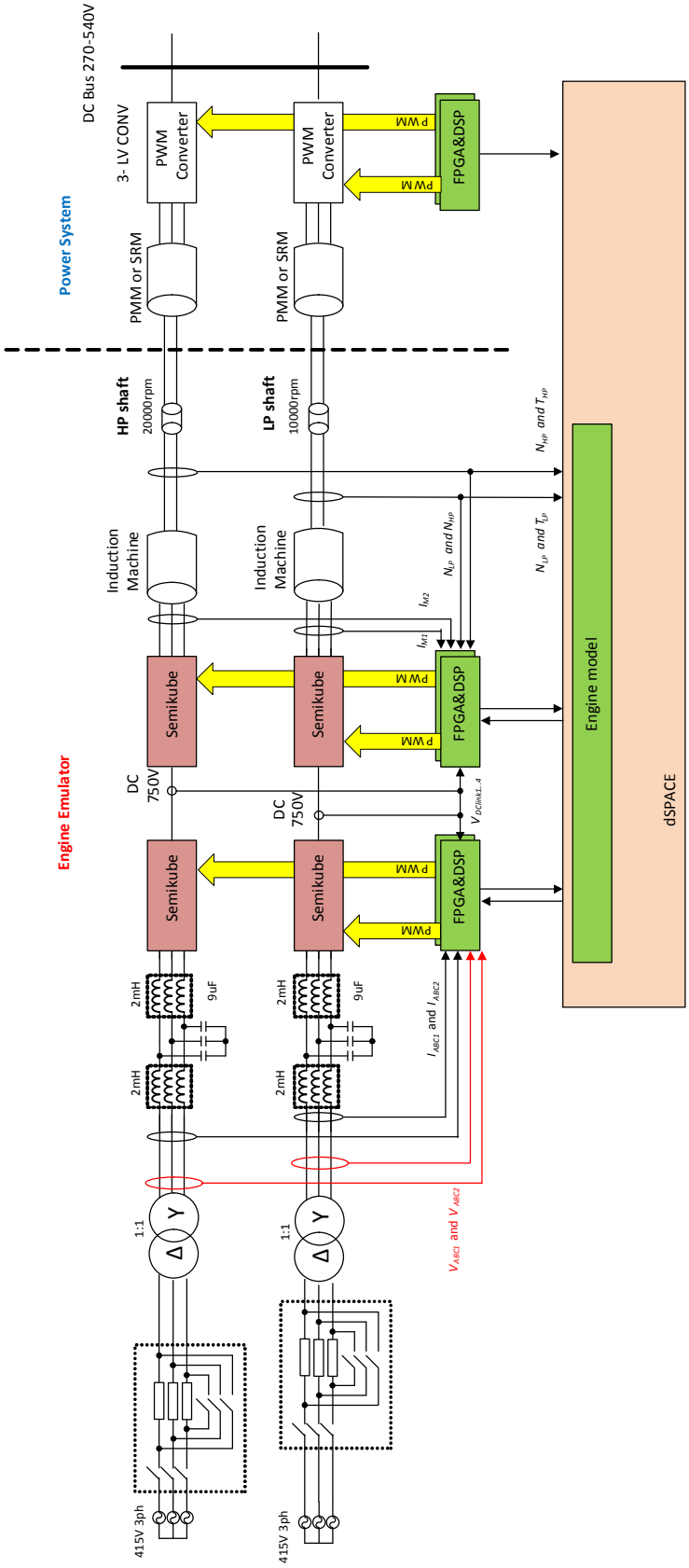


Figure 6-6 Emulator's setup layout plan

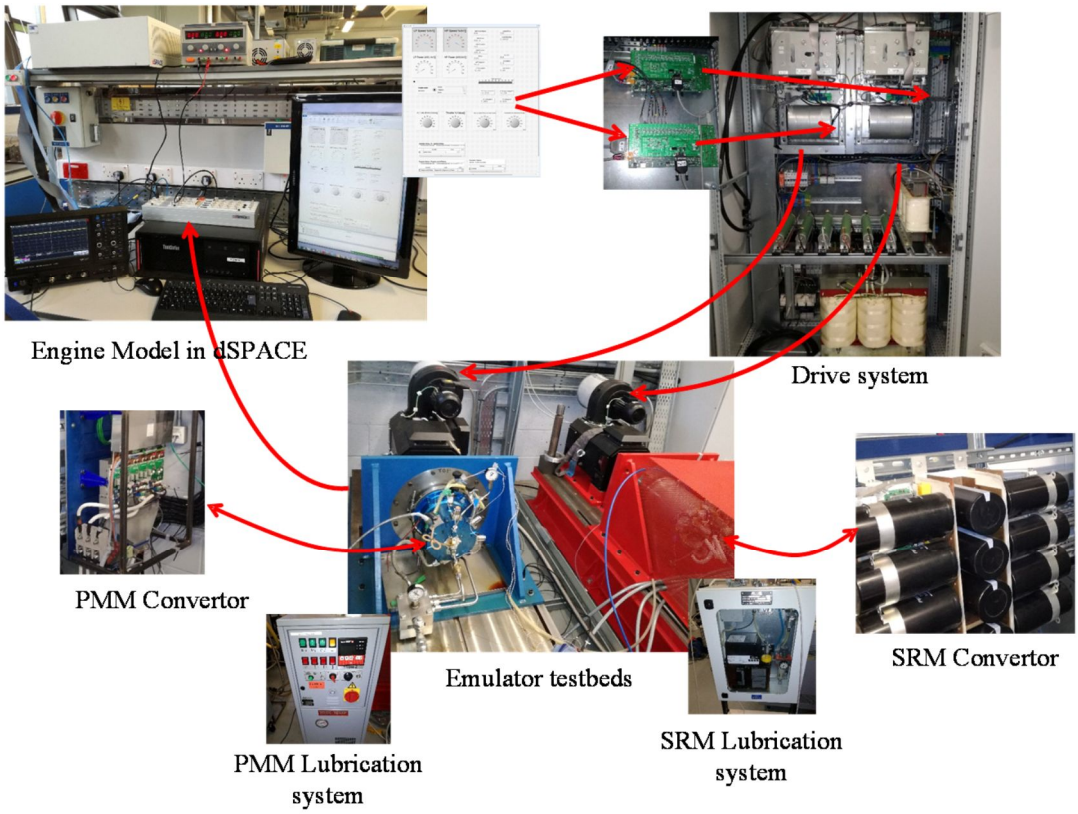


Figure 6-7 Engine emulator components

6.3.1 *dSPACE*

The twin-spool turbofan real-time model is run by the dSPACE control system, used for the HIL implementation [192]. The dSPACE control platform is used for the implementation and online simulation of the complex nonlinear aircraft engine model developed in Chapter 4. The engine model in the Simulink environment is downloaded into the dSPACE to be calculated in real-time. Torque measurements from both LP and HP shafts' torque transducers are fed to the engine model through dSPACE interface board (see Figure 6-8).

The engine model provides the speed references to the emulator drive systems. The engine's HP and LP shaft speed set-points, generated by dSPACE, are sent to two induction motor drives to mimic the speed-torque characteristic of the power offtake shafts. The speed reference signal is fed to the FPGA board from the dSPACE through an interface board shown in Figure 6-8. The drives have their fast speed control loop to guarantee to track the reference speed provided by the dSPACE system.

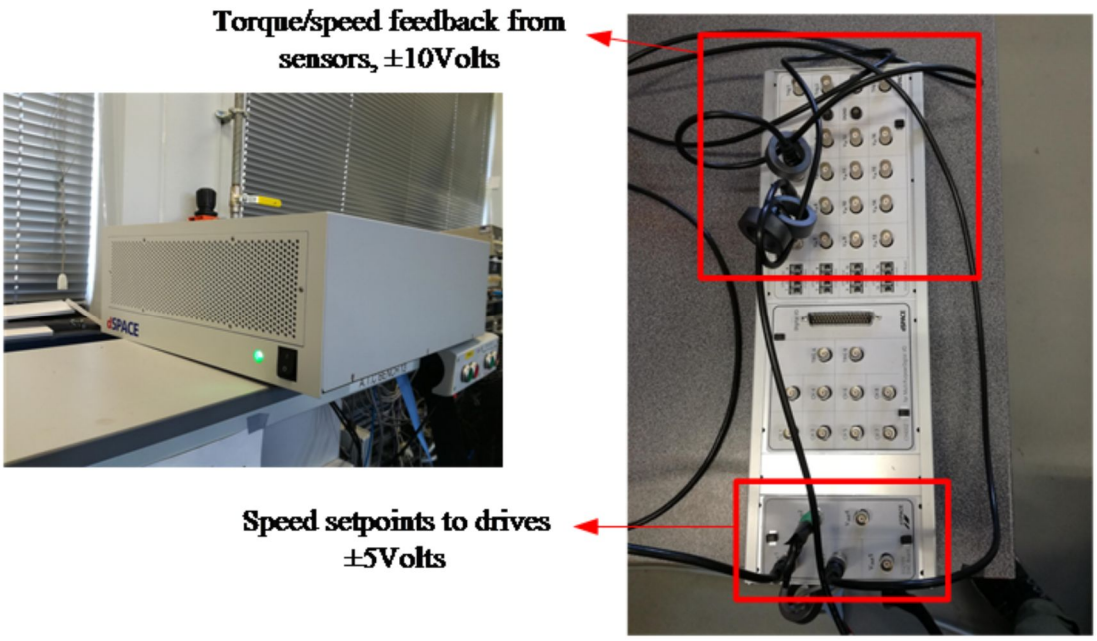


Figure 6-8 dSPACE and its interface board

6.3.2 *Drives*

For the drive system of the induction machines, four bidirectional AC/DC power converters (SEMIKRON's IGBTS Power Stack-SEMIKUBE: SKM400GB12E4 [193]) are used, two of them as the interface between the grid and the DC link 750V and two of them between the DC link 750V and the machines (see Figure 6-6). The DSP/FPGA control board commands the converters through an interface board. All data computation is done on the DSP, while the FPGA fulfils logic and signal acquisition functions. The FPGA board receives the sensor signals (voltage sensor/current sensor) from the sensor boards of the drive system. Figure 6-9 shows the drives' cabinet.

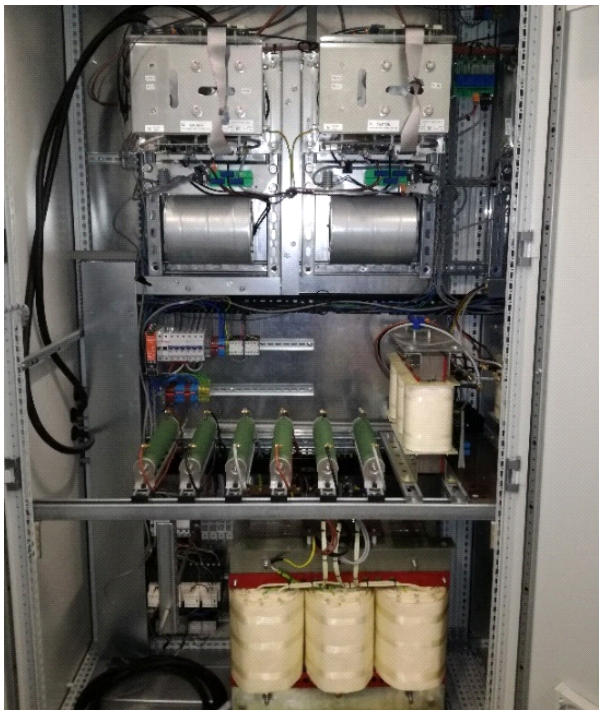


Figure 6-9 Induction machines' drive cabinet

6.3.3 *ControlDesk*

An HMI graphical interface can remotely operate the emulator, implemented using ControlDesk software, which runs on a Windows Operating System. ControlDesk is the dSPACE experiment software which performs all the necessary tasks and sets a single working environment, from the start of experimentation right to the end [192]. Figure 6-10 shows the control module of the engine emulator in ControlDesk, which includes engine throttle, start-up ramps, altitude, Mach number, etc. ControlDesk provides the ability to change or modify variables of the engine such as throttle, altitude.

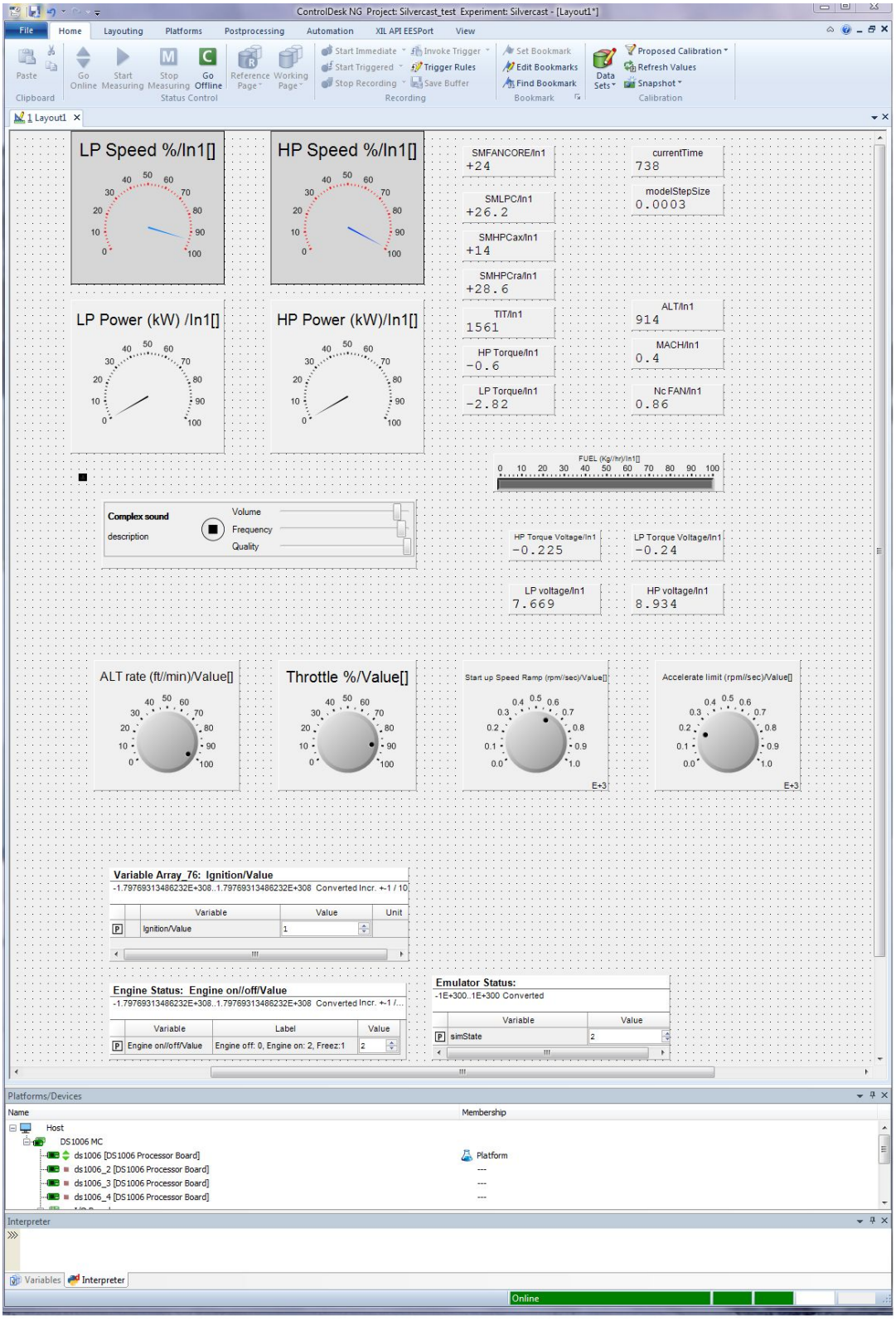


Figure 6-10 Engine model control in ControlDesk environment

ControlDesk also provides monitoring of engine model parameters such as surge margins and measured signals from sensors such as shaft speeds in real-time as it is shown in Figure 6-11.

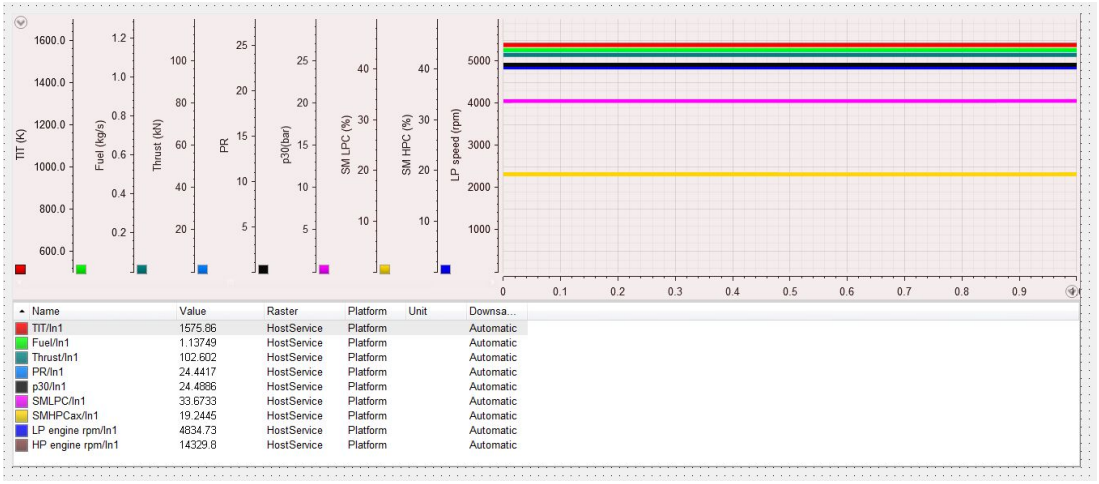


Figure 6-11 Monitoring in ControlDesk environment

6.3.4 *Machines*

The engine emulator comprises of two Oswald induction machines (Appendix A) with two front-end drives of 40 kW. The system can deliver a peak power of 50 kW per shaft. The drives control the induction machines to mimic the HP and LP engine characteristics for the full speed range of the engine from 2000 to 20000rpm.

The induction machines are mechanically coupled with the engine LP and HP generators. On the emulator testbeds, as illustrated in Figure 6-12, high-speed 45kW starter-generators [19]), designed and fabricated in the University of Nottingham, are connected to the LP and HP shaft emulators respectively. T40B torque transducers [194] have been mounted on the shafts to measure speed and torque of the emulator shafts.

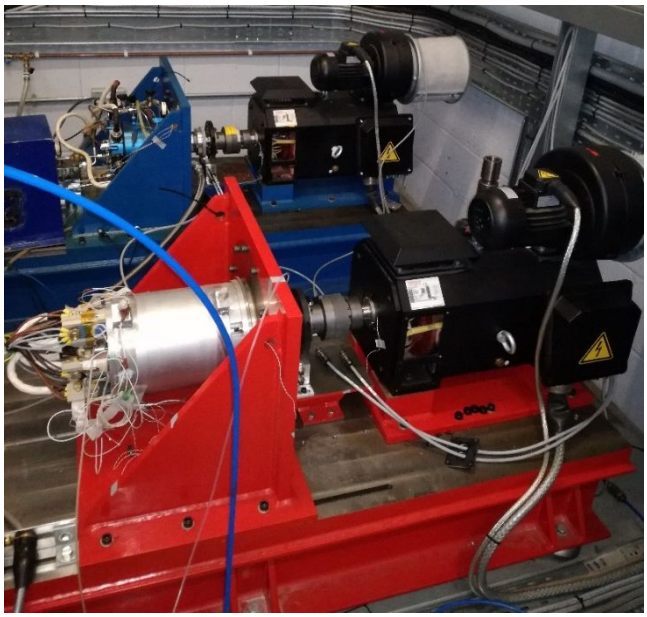


Figure 6-12 Emulator's HP and LP testbeds

The outputs of PMMs are connected to the aircraft DC power system through bidirectional power converters. In this way, power can be transferred between engine shafts through the DC bus to demonstrate the power transfer concept between the HP and LP shafts.

6.4 Engine emulator dynamics

After reviewing the emulator setup, this Section discusses the engine emulator dynamic behaviour, which includes scaling of the emulation system by similarity analysis, control systems for electrical machines and speed tracking performance of the emulator spools.

6.4.1 *Similarity analysis*

The amount of power to study the benefits from EPT on the engine performance is set to 500 kW (from Chapter 5), while the emulator shaft, power test capability is 50 kW. As shown in Figure 6-13, the emulator rig data are scaled up in order to communicate with the dSPACE. In order to scale the system, similarity analysis has been done in this Section.

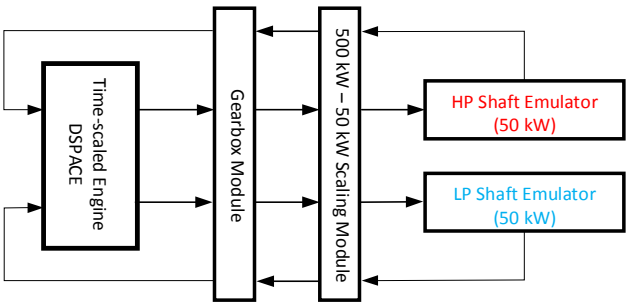


Figure 6-13 Schematic of emulator rig simulation modules

The specifications of the PMM used on the emulator rig (AEGART [19]) and a 500kW PMM (scaled from AEGART in MotorCad software) is presented in Table 6-1.

Table 6-1 Specifications of PMMs

Parameter	Symbol	Model (1)	Experiment (2)
Power	P	500 kW	50 kW
Phase resistance	R_s	5.3 $m\Omega$	1.06 $m\Omega$
Machine inductance	L_d, L_q	36.1 μH	99 μH
Permanent magnet flux linkage	φ_m	0.081 Wb	0.036 Wb
Number of pole pairs	p	3	3
Speed	ω	12000 rpm	12000rpm
DC bus voltage	V_{DC}	540 $volt$	270 $volt$
Inertia	J	0.0504 kgm^2	0.0046 kgm^2

The electrical system model is presented in rotating reference, (or dq) frame [195]. If the *d*-axis is aligned with phase *a* ($x_d = x_a$) as a reference point for both frames, the dynamic equations for PMM machines are:

$$L_d \frac{di_d}{dt} = v_d - Ri_d + L_q p\omega_r i_q \tag{6-1}$$

$$L_q \frac{di_q}{dt} = v_q - Ri_q - (L_d p\omega_r i_d + \varphi_m p\omega_r) \tag{6-2}$$

where v_d, v_q, i_d and i_q are the d and q-axis voltage and current components, and the positive current is the current following into the machine. R_s, L_d and L_q are the stator resistance and inductances, ω_r is the mechanical rotor speed, p is the number of pole pairs and φ_m is the permanent magnet flux. The machine torque is also given as:

$$T = \frac{3}{2} p(\varphi_m i_q + i_d i_q (L_d - L_q) \tag{6-3}$$

$$T = J \frac{d\omega_r}{dt} \tag{6-4}$$

Dividing equations (6-1) and (6-2) by v_d, v_q, and (6-3) and (6-5) by T respectively, the equations below are obtained;

$$1 - \frac{L_d}{v_d}\frac{di_d}{dt} - \frac{Ri_d}{v_d} + \frac{L_q p\omega_r i_q}{v_d} = 0 \tag{6-5}$$

$$1 - \frac{L_q}{v_q}\frac{di_q}{dt} - \frac{Ri_q}{v_q} - \frac{L_d p\omega_r i_d + \varphi_m p\omega_r}{v_q} = 0 \tag{6-6}$$

$$1 - \frac{3}{2}\frac{p(\varphi_m i_q + i_d i_q (L_d - L_q)}{T} = 0 \tag{6-7}$$

$$1 - \frac{J}{T}\frac{d\omega_r}{dt} = 0 \tag{6-8}$$

Considering two PMM in Table 6-1, since the phenomena are similar, the parameters can be related by scale factors (*m*) as below:

$$t_1 = m_t t_2, R_1 = m_R R_2, \ldots \tag{6-9}$$

The same is applied to L_d, L_q, p, φ_m, J, T, v_d, v_q, i_d and i_q.

By substituting equation (6-9) into (6-5), the equation below is obtained:

$$1 - \frac{m_{Ld} m_{i_d}}{m_{v_d} m_t}\frac{L_{d_2}}{v_{d_2}}\frac{di_{d_2}}{dt_2} - \frac{m_R m_{i_d}}{m_{v_d}}\frac{R_2 i_{d_2}}{v_{d_2}} + \frac{m_{L_q} m_p m_{\omega_r} m_{i_q}}{m_{v_d}}\frac{L_{q_2} p_2 \omega_{r_2} i_{q_2}}{v_{d_2}} = 0 \tag{6-10}$$

The same is applied for q-axis equation (6-6) and torque equations (6-7) and (6-8), which results in the relation below:

$$1 = \frac{m_J m_{\omega_r}}{m_T m_t} = \frac{m_p m_{\varphi_m} m_{i_q}}{m_T} = \frac{m_{Ld} m_{i_d}}{m_{v_d} m_t} = \frac{m_R m_{i_d}}{m_{v_d}} = \frac{m_{L_q} m_p m_{\omega_r} m_{i_q}}{m_{v_d}} = \frac{m_{Lq} m_{i_q}}{m_{v_q} m_t} = \frac{m_{L_d} m_p m_{\omega_r} m_{i_d}}{m_{v_q}} = \frac{m_{\varphi_m} m_p m_{\omega_r}}{m_{v_q}} \quad (6\text{-}11)$$

Replacing the scale factors by the ratios of corresponding parameters, the relation below is obtained:

$$\frac{{}^{J_1}/_{J_2}\ {}^{\omega_{r1}}/_{\omega_{r2}}}{\left({}^{T_1}/_{T_2}\right)\left({}^{t_1}/_{t_2}\right)} = 1, \ldots \quad (6\text{-}12)$$

The dependent values must be taken at corresponding moments of time. In the present case, from equation (6-12), the corresponding moments of time of the 50kW (2) and 500kW (1) have the relation below:

$$t_1 = 1.1 t_2 \quad (6\text{-}13)$$

which means the experiment (50kW machine) is 1.1 times faster than model (500 kW machine). From equation (6-12), the steady-state relation between independent parameters are also obtained as below:

$$i_{q,1} = 4.44 i_{q,2},\ v_{d,1} = 1.62 v_{d,2} \quad (6\text{-}14)$$

This section provided similarity analysis to enable studying EPT with the constructed experiment setup (50kW), by scaling it up to the required power (500kW). Transients are also investigated by scaling the time in addition to steady-state responses. The next Section discusses the implementation of time in the emulator.

6.4.2 *Engine model time scale*

The modulated multi-spool turbofan model that is developed in SIMULINK environment, using the ICV method in Chapter 4, has been implemented in the dSPACE. A bump-less override control structure (from Section 4.6) has also been implemented, for the turbofan with limit controllers, for over-temperature, surge and bleeding pressure for the Environmental Control System (ECS).

Shaft dynamics for the real system can be expressed as below:

$$T_{HPT} - T_{HPC} - T_{EHP} = J_{HP} \dot{\omega}_{HP} \quad (6\text{-}15)$$

$$T_{LPT} - T_{FAN} - T_{LPC} - T_{ELP} = J_{LP} \dot{\omega}_{LP} \quad (6\text{-}16)$$

where T_{HPT} and T_{LPT} are the generated torques by the HPT and LPT, respectively; and T_{HPC} and T_{LPC} are the consumed torques by the HPC and LPC respectively. For

application in the emulator, component modules of the engine model (from Section 4.5) are solved in real-time to provide T_{HPT}, T_{LPT}, T_{HPC} and T_{LPC} for the LP and HP shaft modules. T_{EHP} and T_{ELP} are the scaled values of torque measurements from the torque transducers of the HP and LP shafts respectively. The real-time outputs of shaft dynamic modules after solving equations (14) and (15) are the HP shaft speed, ω_{HP}, and the LP shaft speed, ω_{LP}, which, after scaling, are fed to the drives of the Induction Machines (IMs).

For the ICV engine modelling approach, the state space differential equation of the model is:

$$\frac{dX_1}{dt_1} = A(X_1).X_1(t_1) + B(X_1).U_1(t_1) \tag{6-17}$$

$$Y_1 = C(X_1).X_1(t_1) + D(X_1).U_1(t_1) \tag{6-18}$$

where X is the states' vector, U is the model input and Y is the model output and A, B, C and D are state dependent matrixes.

The engine model runs in real-time in dSPACE, for which based on equation (12), its simulation time should be scaled. If the real-time is symbolled as t, since the physical emulator rig runs in real-time then, $t_2 = t$ and $t_1 = m_t t$.

If the engine model is scaled, in a similar fashion to Section 6.4.1,

$$X_1 = m_X X_2,\ U_1 = m_X U_2,\ t_1 = m_t t \tag{6-19}$$

Substituting (17) into (16), the state space equation in real-time is:

$$\frac{m_X dX_2}{m_t dt} = A(m_X X_2).m_X X_2(t) + B(m_X X_2).m_U U_2(t) \tag{6-20}$$

$$m_Y Y_2 = C(m_X X_2).m_X X_2(t) + D(m_X X_2).m_U U_2(t) \tag{6-21}$$

The engine model is preferred to be scaled only in time and not in other parameters, due to its nonlinear behaviour, which results in the relations below:

$$m_X = m_U = m_Y = 1 \tag{6-22}$$

while the states corresponding to the shaft speeds are scaled separately with scale factor, m_ω, and the torque inputs to the engine are scaled with the scale factor, m_T, to match real engine performance. As a result, the state space equations are scaled only in time as below:

$$\frac{dX_2}{dt_2} = m_t\big(A(X_2).X_2(t) + B(X_2).U_2(t)\big) \tag{6-23}$$

$$Y_2 = C(X_2).X_2(t) + D(X_2).U_2(t) \tag{6-24}$$

In order to implement the time scaling, shown in equation (20) in the ICV approach, the time scale factor block, m_t, is added before each state's derivative in Simulink as shown in Figure 6-14.

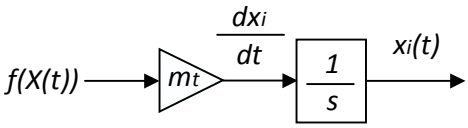


Figure 6-14 Time scale block for Simulink state blocks

X is the state vector and x_i is the corresponding state. For the shaft speeds states, applying the time scale m_t can basically be interpreted scaling the shaft inertia to J_{scaled} , which is calculated from the equation below:

$$J_{scaled} = \frac{J}{m_t} \tag{6-25}$$

Note that, model inputs which are a function of time such as throttle, should be scaled in time as well. After assessing the capability of the emulator rig for scaling up to 500kW, the next Section discusses EPT emulation.

6.4.3 *Electric power transfer emulation*

As discussed in Chapter 5, there is a great interest in controllable power transfer between the shafts, to relatively decouple shaft speeds and improve engine performance. A well-known architecture of the MEA power system is the single dc bus architecture, which is elaborated in Section 3.2.4. In this architecture, the machine outputs are connected to the dc bus through bidirectional converters, as shown in Figure 6-15. It provides the opportunity to circulate controllable power between shafts through the electrical machines. The common dc bus architecture's structure and control schemes, including torque and DC link voltage are presented in Appendix B. The power circulation between shafts can simply be expressed as below:

$$T_{ELP} \times \omega_{LP} + T_{EHP} \times \omega_{HP} + P_{EPS} + P_{loss} = 0 \tag{6-26}$$

where T_{EHP} and T_{ELP} are the torques of the electrical machines that are connected to the HP and LP shafts with the corresponding speeds of ω_{HP} and ω_{LP}. P_{EPS} is the electrical load power on the dc bus and P_{loss} is the power loss of the system.

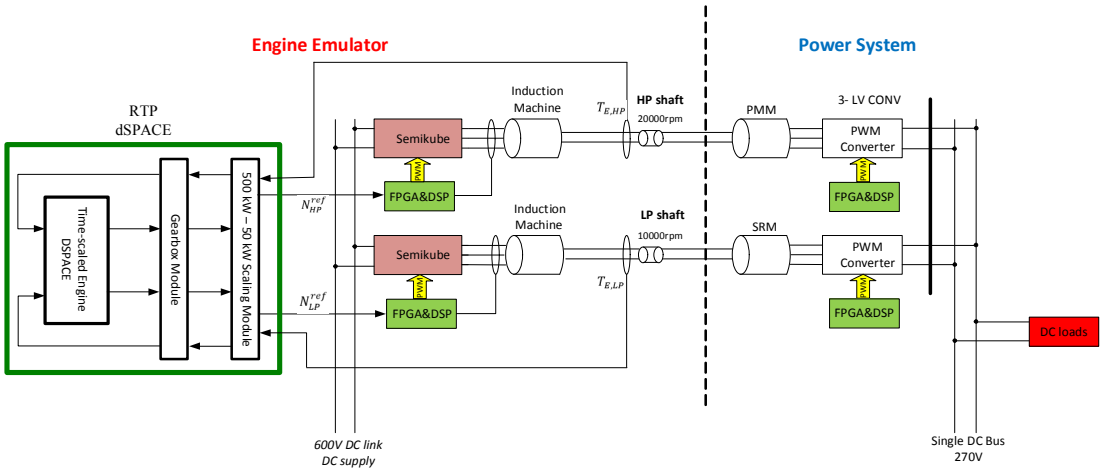


Figure 6-15 Configuration of the engine emulator for electric power transfer

The grid side of the emulator is not in focus this study; therefore, a 600V DC supply is used to provide DC power for the induction machine converters. The IMs operate in speed control mode to represent the LP and HP shaft speeds. The speed reference is received from the dSPACE and compared with speed measurements from the induction machine encoder measurements within the DSP/FPGA board. Figure 6-16 shows the control loop of the IM. The IM motor drive, speed control loop bandwidth is 10 rad/s, and the current control loop bandwidth is 600 rad/s, and the switching frequency of the motor drive inverter is 2.5 kHz. Positive or negative torque is imposed on the induction machines by the coupled PMMs.

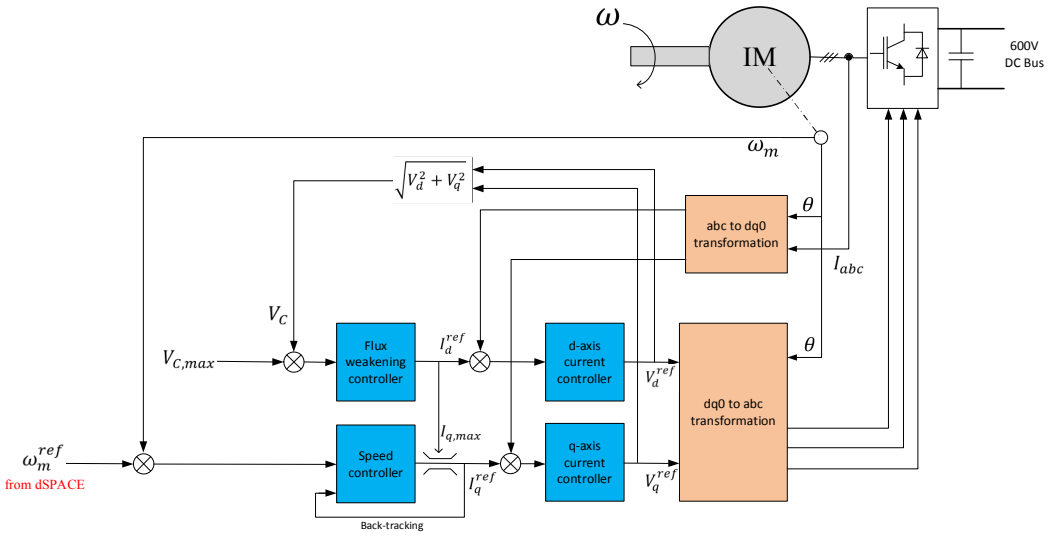


Figure 6-16 Control structure of the IM

The PM generator can operate in voltage or current control mode, to regulate the dc link voltage or amount of EPT. The control loop of the PM generator is provided in Appendix B.

6.4.4 *Speed tracking performance*

In order to be able to emulate transients, the electrical drive bandwidth should exceed that of the scaled engine model in the RTP [196, 197]. Typically, the PI speed controller is designed for the motor to allow speed tracking of the engine shaft speeds [166, 173, 198].

Shaft inertia of the actual system is a critical parameter for prime mover emulation systems. For high-inertia prime movers such as wind turbines, the substitution of a motor is relatively straightforward due to significantly lower shaft inertia in comparison to that of the actual wind turbine at the same power rating [114, 178, 179]. The inertia ratio of an actual gas turbine with the mega-watt power to emulation motor with kW range power is around 1:600 [114].

If the ratio of shaft inertia of the actual engine to the emulator is less than 10:1, the drive torque oscillations considerably affect the emulation dynamics performance [114]. In this case, mitigation techniques such as feedforward compensators are implemented to cancel the emulation system dynamics [198-200]. It enables emulation of mechanical systems over a wide range of speed, power and bandwidth [166].

Table 6-2 shows the mechanical parameters of the engine model and the emulator system. The shaft inertia values for CFM56-3 engine are estimated by inertia scaling method discussed in Section 4.4, and equation (6-25) is used to calculate the inertia of the time-scaled model.

Table 6-2 Mechanical parameters of the emulation system

Parameters	CFM56-3	Scaled model	Spool emulators
HP electrical machine	500kW	50kW	10kW
LP electrical machine	500kW	50kW	10kW
HP speed range	8000:15000 rpm	8000:15000 rpm	6500:20000 rpm
LP speed range	2500:5000 rpm	2500:5000 rpm	4000:10000 rpm
HP shaft inertia	28.00 $kg.m^2$	$28/1.1$	0.10 $kg.m^2$
LP shaft inertia	50.00 $kg.m^2$	$50/1.1$	0.10 $kg.m^2$

For the jet engine emulation, the torque sensor on each shaft sends the torque signal to dSPACE which is fed to shaft module as LP and HP PO torques integrated with turbine and compressor torques of engine's LP and HP shafts. This means that turbine-

compressor equilibrium is solved in the shaft module in the RTP, which also receives the torque feedback from the physical emulator shaft (see Figure 6-5).

The simulation block for the gear ratio and scale factors for speed and torque between the engine and the emulator rigs are shown in Figure 6-17. A communication delay between the RTP and the emulator drive system exists and is considered.

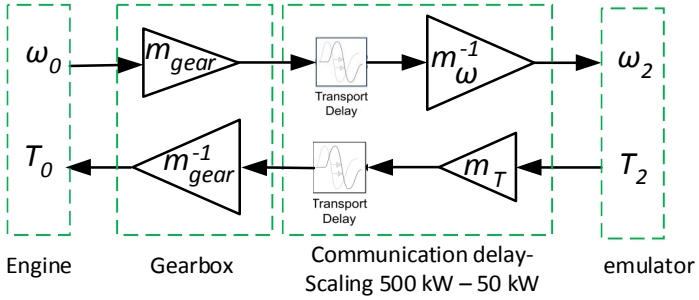


Figure 6-17 Speed and torque communication between DSPACE and the emulator rig

The equation below gives the engine and HP emulator shaft dynamics;

$$T_{HPT} - T_{HPC} - \frac{m_T}{m_{gear}} T_{Gen} = \frac{J_{HP}}{m_t} \dot{\omega}_{HP} \tag{6-27}$$

$$T_{PM} - T_{Gen} = J_{em} \frac{m_{gear}}{m_\omega} \dot{\omega}_{HP} \tag{6-28}$$

where T_{HPT}, T_{HPC}, T_{PM} and T_{Gen} are torques implemented on the HP shaft by the HPT, HPC, prime mover and generator, respectively, m_T, m_ω are the scaling factors for the speed and torque, respectively, and m_{gear} is the gear ratio between the engine shaft and the emulator. For the designed emulator in this Thesis, from Table 6-2, the coefficients are calculated as below,

$$m_T = \frac{T_1}{T_2} = \frac{500\ kW}{50\ kW} \times \frac{20000\ rpm}{15000\ rpm} = 13.3,\ m_\omega = \frac{15000 rpm}{20000 rpm} = 0.6,\ .m_{gear} = 1,\ m_t = 1.1$$

Then the ratio of $\frac{m_\omega}{m_t . m_{gear}} \frac{J_{HP}}{J_{em}}$ is 152 for the HP shafts. In this case, the engine dynamics is very slow compared to that of the emulator, so that the inertia of the emulator shaft can be ignored. Figure 6-18 presents a simplified block diagram of the engine emulator dynamics. The emulation method is expected to track the speed reference, due to fast response of induction machines on emulator spools, compared to slow dynamics of the engine shafts.

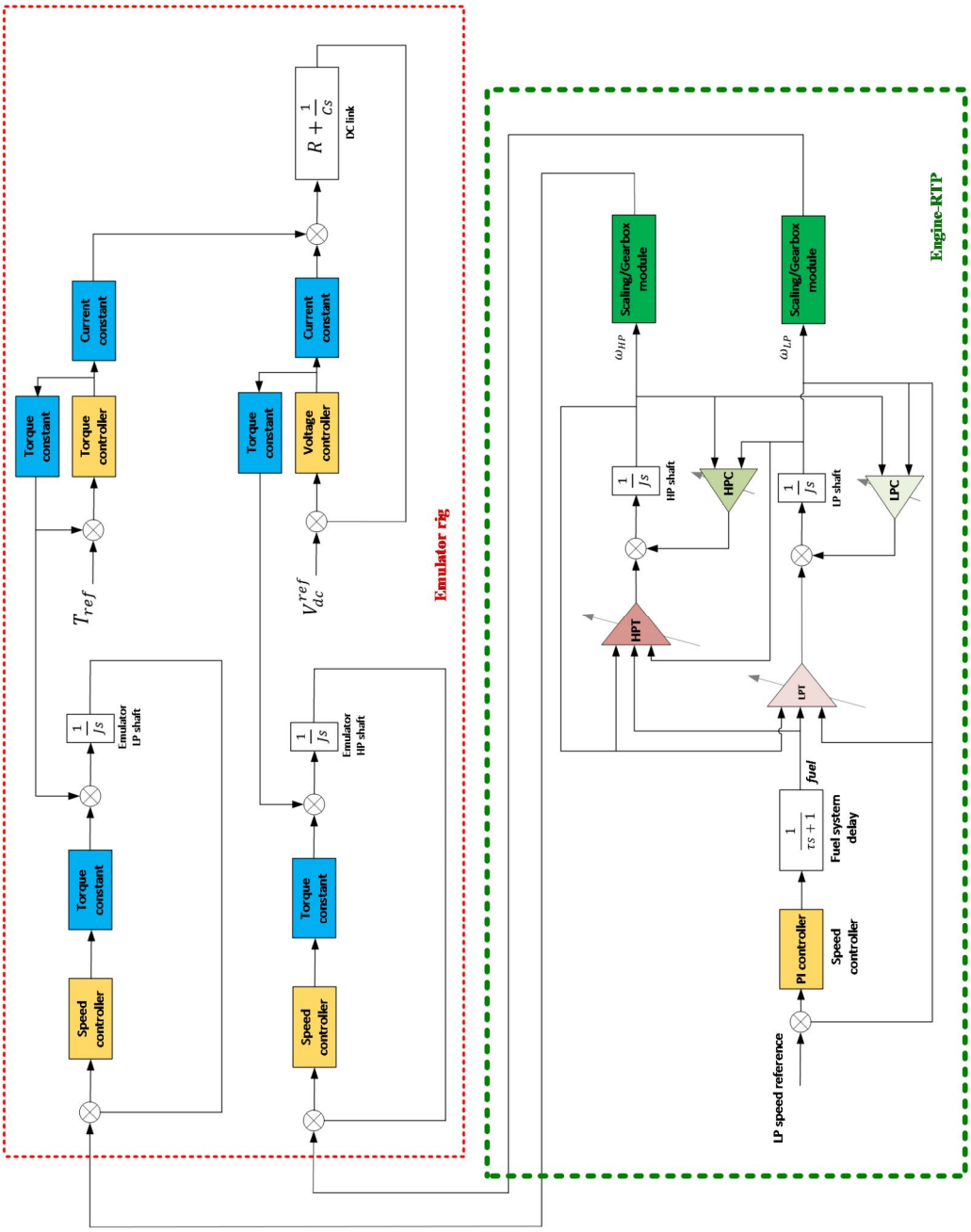


Figure 6-18 Simplified block diagram of the engine emulator dynamics

The tracking performance of the emulator also depends on the IM's speed loop bandwidth, and a maximum acceleration/deceleration rate of the shaft, which is:

$$a = \frac{T_{ava}}{J} \tag{6-29}$$

where T_{ava} is the available torque of the induction machine and it is defined as

$$T_{ava} = T_{peak} - T = \frac{P_{peak} - \mathrm{P}}{\omega} \quad \text{for acceleration} \tag{6-30}$$

$$T_{ava} = -T_{peak} - T = \frac{-P_{peak} - \mathrm{P}}{\omega} \quad \text{for deceleration} \tag{6-31}$$

Figure 6-19 and Figure 6-20 show the IM's peak power and torque diagram. In order to facilitate the full capacity of the AC machine for high-speed emulation, field weakening is implemented. Depending on the power of the PMMs, the available torque and the acceleration or deceleration rate will change.

For the operating point shown in Figure 6-19 and Figure 6-20, the available torque is:

$$T_1 = \frac{P_1}{\omega} \quad \text{for acceleration} \tag{6-32}$$

$$T_2 + T_{peak} = \frac{P_2 + P_{peak}}{\omega} \quad \text{for deceleration} \tag{6-33}$$

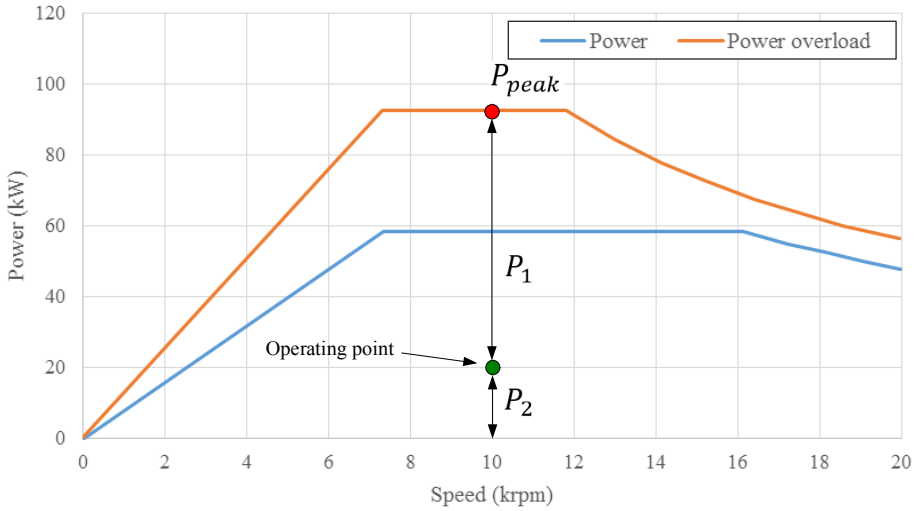


Figure 6-19 Available power for acceleration and deceleration of the emulator shaft [201]

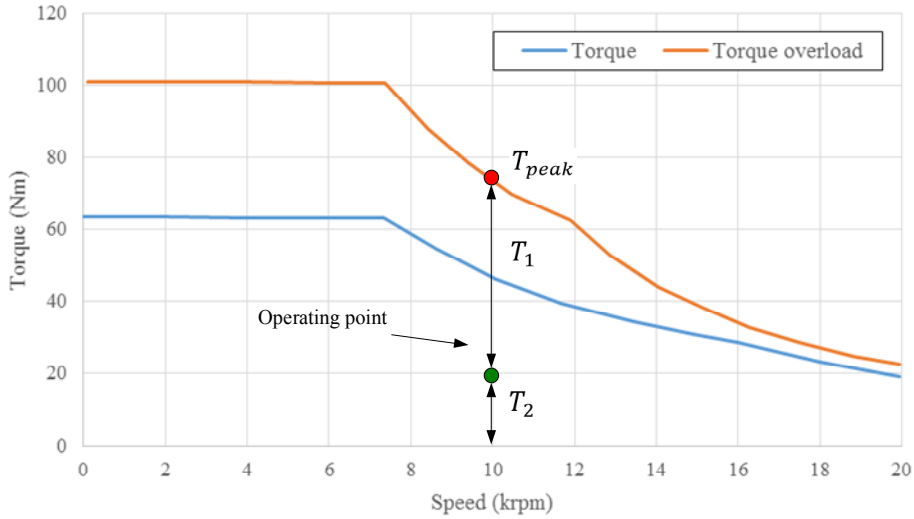


Figure 6-20 Available torque for acceleration and deceleration of the emulator shaft [201]

6.4.4.1 Speed tracking test (acceleration-deceleration at ISA-SLS)

The dynamic performance of the emulator in evaluated, by considering the speed response of the emulation motor, with respect to the reference speed, provided by the gas turbine's model speed reference after scaling. Figure 6-21 presents the HP speed tracking performance when the engine's throttle experiences acceleration and deceleration with a step of 50% of the throttle. It should be noted that the HP speed is scaled from 14250rpm to 11400rpm at 100% throttle ($m_\omega = 1/0.8$). As can be seen in Figure 6-21, the emulator can track the engine speed during acceleration (50% to 100% throttle) and deceleration (100% to 50% throttle).

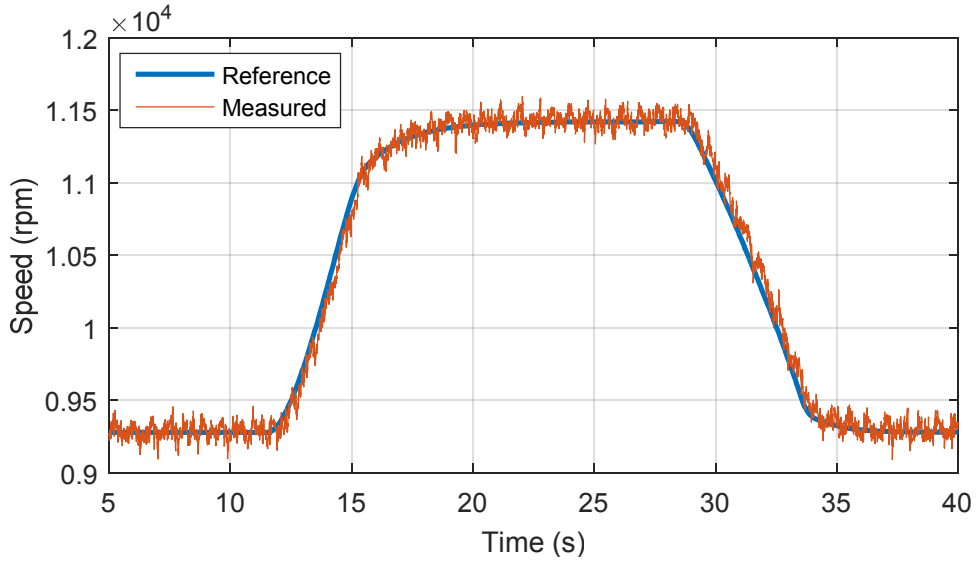


Figure 6-21 Emulator' HP shaft speed tracking performance (steps of 50% throttle at ISA-SLS)

Preliminary analysis on the emulator's dynamic behaviour is presented in this Section; however, transient analysis is out of the scope of this thesis. The focus is on the steady-state performance of the engine emulator to study the impact of EPT on engine parameters, which is provided in the next Section.

6.5 Experimental results

This Section presents the experimental results of the steady-state performance of the engine, obtained by using the engine emulator. The models of the baseline and EPTAD engines are implemented in dSPACE, to confirm the impact of EPT on engine performance upon different flight scenarios. The maximum tested power of electrical machines during experiments is 10kW, and it is scaled to the required power of the

EPT systems. Note, that the efficiency of power transfer channel is not a subject of the conducted experiments.

For the experimental results in this Chapter, based on Figure 6-17 the HP gear ratio is $m_{gear,HP} = 1$, and the HP speed scaling factor is $m_{\omega,HP} = 1/0.8$, the LP gear ratio is $m_{gear,LP} = 2$, and the LP speed scaling factor is $m_{\omega,LP} = 1$.

6.5.1 *HP power offtake emulation (p_{30} idle)*

As discussed in Section 3.1.1, sudden extreme HP PO at idle settings can lead to surge. Due to the engine's low throttle, HP PO can result in noticeable speed drop at idle setting (p_{30} idle) on the top of descent (30kft, Mach=0.6). In this scenario, the engine's controller keeps the minimum bleeding pressure, p_{30}, for the purpose of ECS. Two different PO cases are presented to evaluate the emulator's performance. The HP PO's effect on the engine performance is then studied, by results acquired from the ControlDesk and PMM's control board.

In order to realise sudden load increase, a step of q-axis current reference has been fed to the PMM, as seen in Figure 6-22. Figure 6-23 shows the amount of current corresponding to this torque. The cut-off frequency of the low-pass filter on the torque transducer signal is fixed to 10 Hz. The test is repeated for two different scale factors, for which the amount of power offtake (around 4.5kW) is scaled to 90kW and 180kW with scaling factors of 20 and 40 respectively (see Figure 6-23).

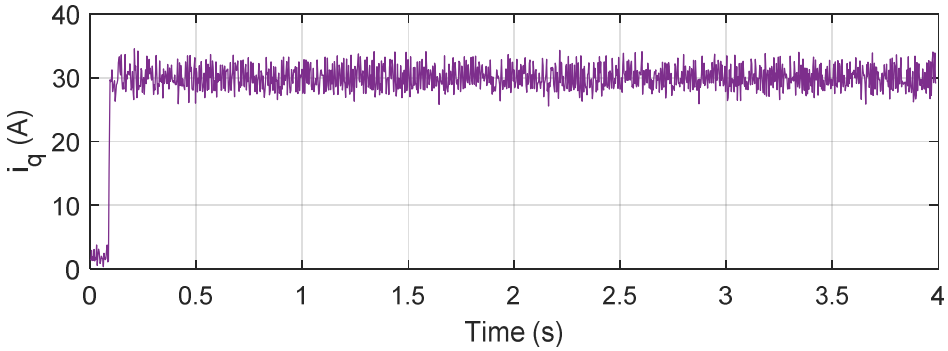


Figure 6-22 q-axis current of the PMM from PMM's control board

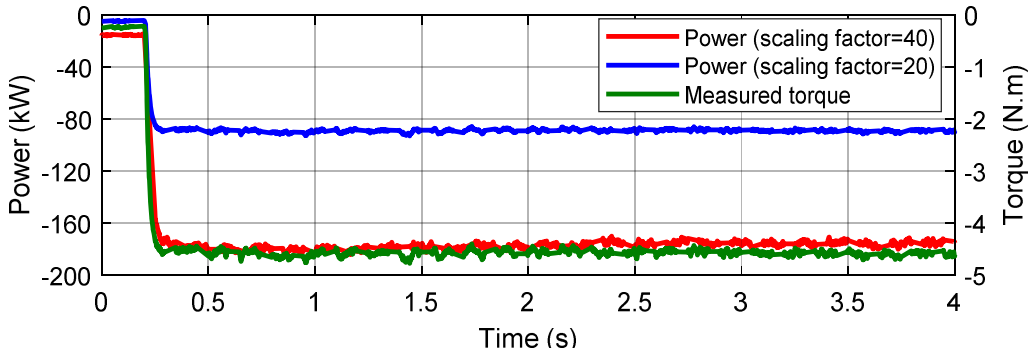


Figure 6-23 Measured torque and corresponding scaled power from ControlDesk

The speed tracking performance of the emulator for two cases of scaling factors is shown in Figure 6-24 and Figure 6-25. There is a steady-state error (less than 50rpm) due to the communication offset between the reference signal from dSPACE and the IM's drive system. This offset can be ignored due to its small value. The emulator shaft has experienced a 110rpm drop and a quick recovery for a step of 4.5kW PO from the generator. It is acceptable for transient studies due to its small value compared to the wide range of speed change of an engine.

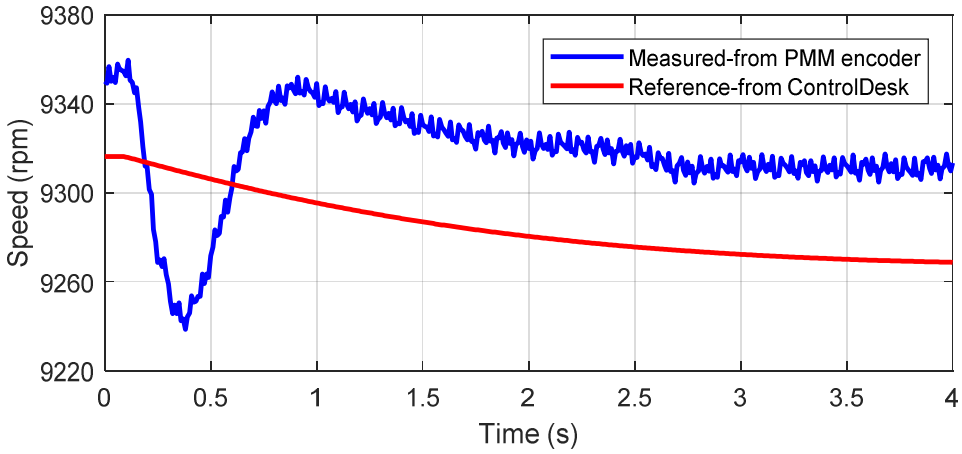


Figure 6-24 Speed tracking performance of the HP shaft (scaling factor=20)

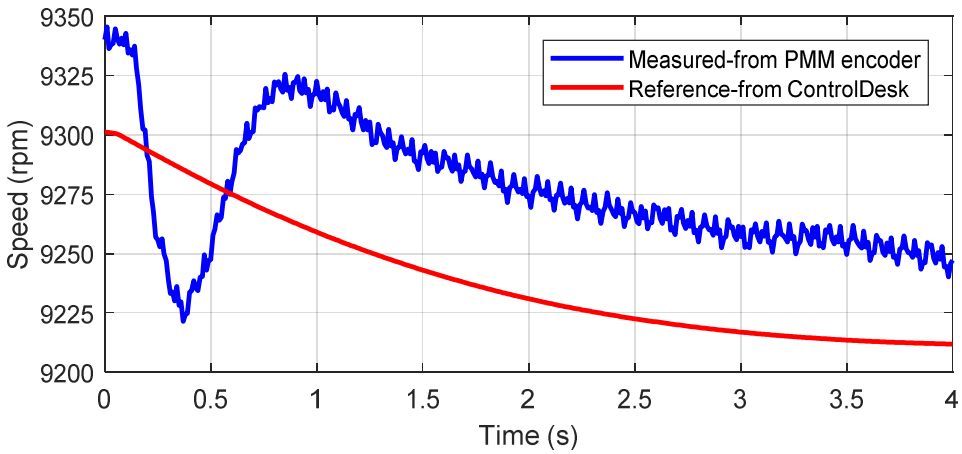


Figure 6-25 Speed tracking performance of the HP shaft (scaling factor=40)

Two transient shifts of the operating point are shown in Figure 6-26 and Figure 6-27 for the operating lines of the LPC and HPC, respectively. Due to higher PO, the operating point gets closer to the surge line. Figure 6-28 represents the surge margin reduction of the HPC due to 90kW and 180kW PO.

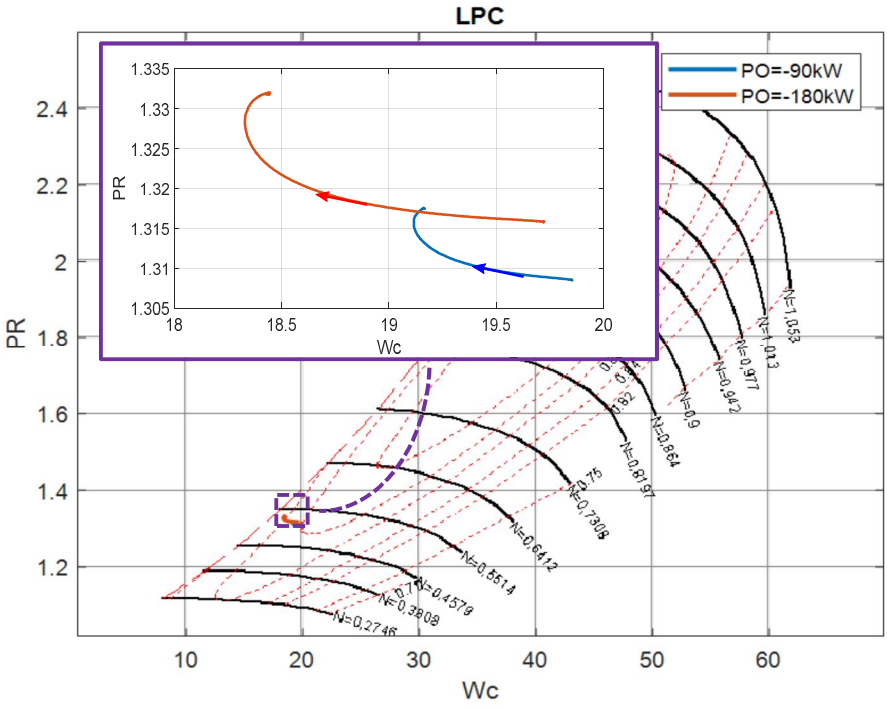


Figure 6-26 Operating line of the LPC due to load steps ($\boldsymbol{p_{30}}$ idle)

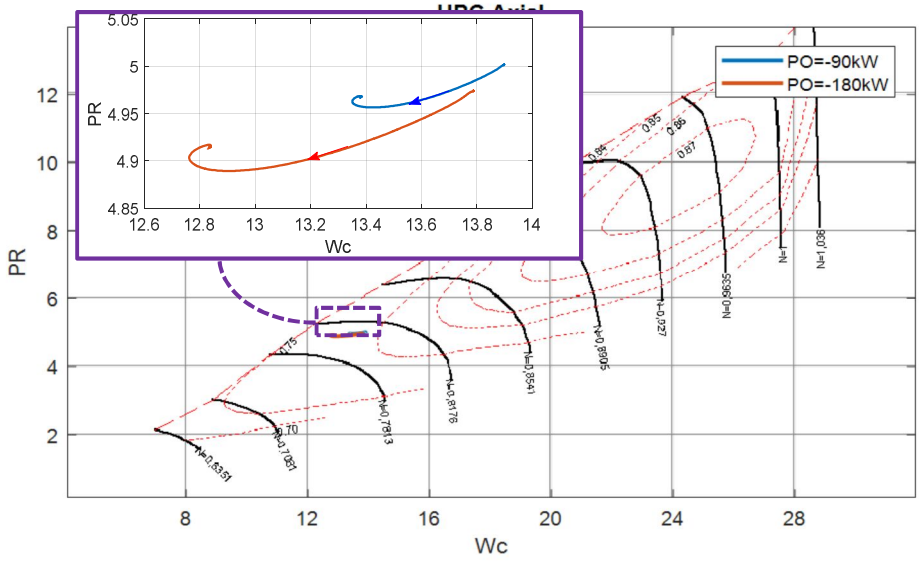


Figure 6-27 Operating line of the HPC due to load steps ($\boldsymbol{p_{30}}$ idle)

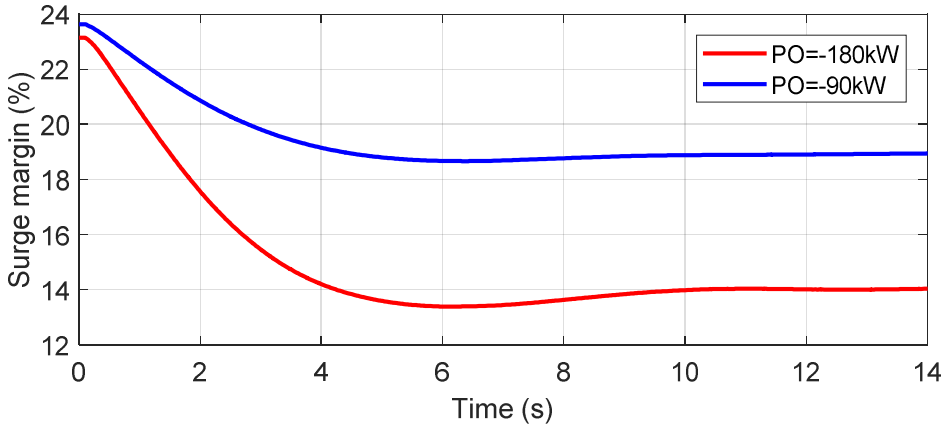


Figure 6-28 HPC surge margin due to load steps ($\boldsymbol{p_{30}}$ idle)

6.5.2 *Baseline engine's EPT emulation (Cruise)*

As already discussed in Section 5.4.1, positive EPT can reduce fuel consumption and increase surge margin during the cruise for the baseline engine. In this scenario, the engine's controller keeps the thrust fixed. It is in order to compare the engine performance with EPT at the same thrust level of the baseline engine, as discussed in Section 5.4.1. Results collected from ControlDesk and processed in Matlab are presented in this Section.

In order to realize EPT, both PMMs on the LP and HP shafts are operating in current control mode, while the dc-link voltage is controlled by the 270V DC supply (Grid-tie Source Sink (GSS)). The steps of implementing EPT, including the power of the LP PMM, HP PMM and GSS are shown in Table 6-3. For EPT, the LP PMM generates 10kW, which is transferred to the HP PMM through the dc link. The torque feedback from LP and HP PMMs are shown in Figure 6-29. The power scaling factor is 20, which scales up the EPT for the LP and HP shafts to 200kW (see Figure 6-29).

Table 6-3 Steps of implementing EPT

Time (s)	Status	LP PMM	HP PMM	GSS power
0-10	Baseline engine	-0.5 kW	0.1 kW	0.4 kW
10-60	LP PMM generating 10kW	0 to -10 kW	0	0.4 to +10 kW
90-130	HP PMM motoring 10kW	-10 kW	0 to +10 kW	+10 to 0 kW
130-210	Positive EPT realised	-10 kW	+10 kW	0 kW
210-230	Removing the load from LP PMM	-10 to 0 kW	+10 kW	0 to -10 kW
240-260	Decreasing the power of HP PMM	0 kW	+10 to 0 kW	-10 to 0.4 kW
260-270	Baseline engine	-0.5 kW	0.1 kW	0.4 kW

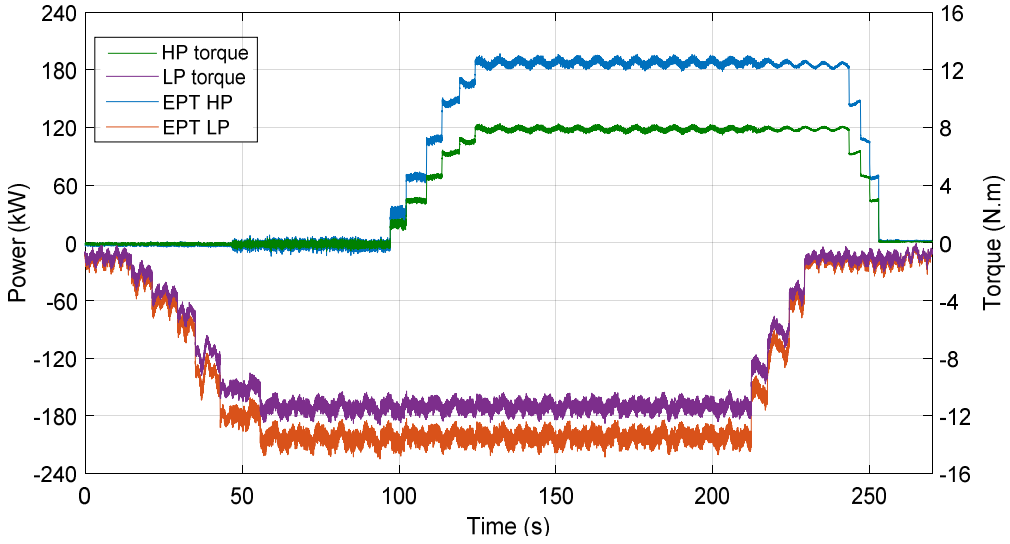


Figure 6-29 Scaled LP and HP shaft power

The transient shift of the operating point due to EPT on the LPC and HPC maps are shown in Figure 6-30 and Figure 6-31 respectively. The time shown on Figure 6-30 and Figure 6-31 refers to the time of Figure 6-29. Due to positive EPT, the operating point of the HPC moves to higher speeds, flow and pressure ratio parallel with the surge line. The operating point of the LPC remains on the same speed line with lower pressure ratio and higher flow, thus moving away from the surge line.

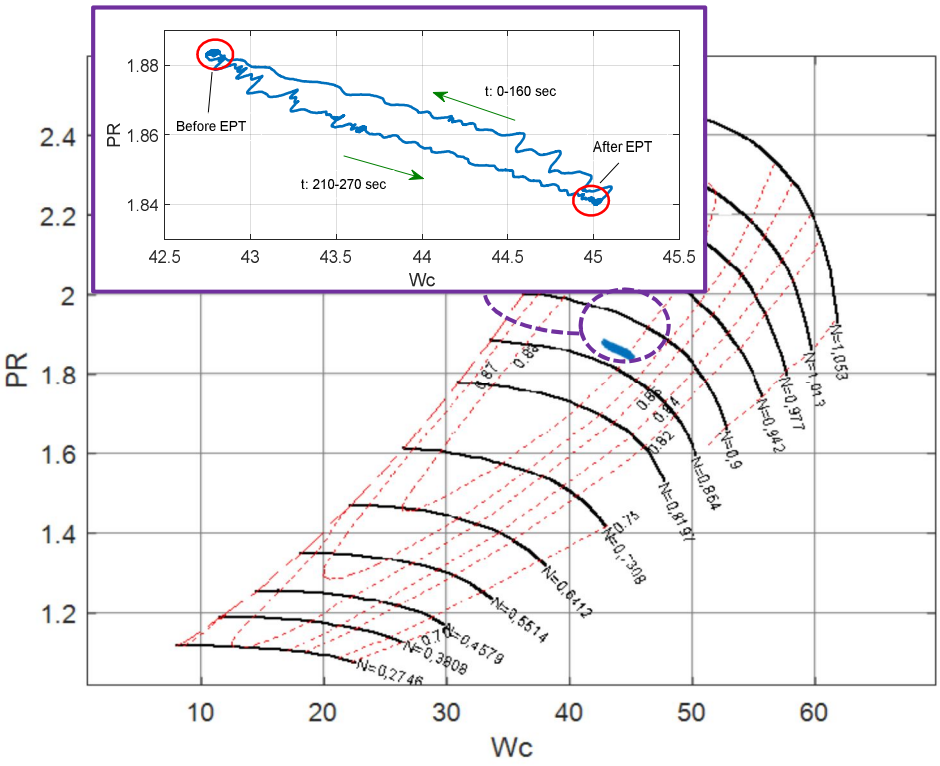


Figure 6-30 Operating line of the LPC due to EPT (cruise)